Applied Computational Electromagnetics Society Journal

March 2025
Vol. 40 No. 3
ISSN 1054-4887

The ACES Journal is abstracted in INSPEC, in Engineering Index, DTIC, Science Citation Index Expanded, the Research Alert, and to Current Contents/Engineering, Computing & Technology.

The illustrations on the front cover have been obtained from the ARC research group at the Department of Electrical Engineering, Colorado School of Mines

Published, sold and distributed by: River Publishers, Alsbjergvej 10, 9260 Gistrup, Denmark

MARCH 2025 REVIEWERS

Alireza Baghai-Wadji
Yiming Chen
Junbing Duan
Javad Ebadi
Kalyan Gattupalli
Bernhard J. Hoenders
Zheng-Yu Huang
Zhan Jin
Rostom Khalef
Ilkyu Kim
lihua Li
Kun Liao
Jake Liu
Mahdi Oliaei
Natarajamani S.
Giovanni Maria Sardi
Luca Scorrano
Varun Singh
Qing Wang
Shihyuan Yeh
Tao Yuan
Xiaoyan Zhang
Ziyang Zhang

THE APPLIED COMPUTATIONAL ELECTROMAGNETICS SOCIETY JOURNAL

Vol. 40 No. 3 March 2025

TABLE OF CONTENTS

Women's History Month Special Article: Interview with Sima Noghanian

Cynthia Furse

Department of Electrical and Computer Engineering
University of Utah, Salt Lake City, UT 84112, USA
cynthia.furse@utah.edu

***Abstract* –** In this Special Article, Cynthia Furse interviews Sima Noghanian, Distinguished Hardware Engineer with CommScope Ruckus Networks in Sunnyvale, California, USA. Noghanian has worked in both industry and academia and is well known for her work in computational electromagnetics applied to antenna design.

***Index Terms* –** Women in applied computational electromagnetics, women in STEM.

I. INTRODUCTION

Doctor Sima Noghanian is a Distinguished Hardware Engineer with CommScope Ruckus Networks in Sunnyvale, California, USA (Fig. 1). She previously worked in academia (Sharif University, University of Manitoba and University of North Dakota). She is well known for her work in computational electromagnetics applied to antenna design (Fig. 2). I had the pleasure of interviewing Dr. Noghanian to learn more about her experiences in the field.

Fig. 1. Sima Noghanian.

II. QUESTIONS AND ANSWERS (Q & A)

Q1: How did you get into engineering, and what is most exciting about it to you?

A1: I am from Iran. At my time, students had to choose a concentration in high school. After that, I had to take a university entrance exam and select a few fields of interest. I was passionate about math, which was a challenging field to get into. Boys and girls attended separate schools and, in my city, there was only one girls' high school that offered a math concentration. However, it was too far from my home. To accommodate me, my high school principal agreed to offer classes for the math concentration if I could find five or six other students interested in joining. I managed to recruit enough students and, to support our learning, I started an after-school math club.

Fig. 2. Sima Noghanian at authors' appreciation event, University of North Dakota [1].

At that time, one of the biggest challenges I faced was the war. My mother was a single parent. This created many difficulties, as there were restrictions on where I could go and what I could do. In the beginning of the war, we had to relocate to another city in the middle of the school year, causing me to lose a year of education. To make up for it, I completed my third year of high school at home over the summer and took the necessary exams at the end of the summer.

Initially, I planned to pursue a math major at the university. I took the entrance exam and achieved a high score. However, my older brother encouraged me to consider engineering, believing I might not enjoy pure math as much and would likely find engineering more engaging. Following his advice, I applied to several engineering programs and some applied math programs. Once I started engineering, I realized he was right—I saw

Submitted On: March 24, 2025
Accepted On: March 24, 2025
https://doi.org/10.13052/2024.ACES.J.400301
1054-4887

how math was applied in the real-world scenarios, how it fueled creativity in problem-solving and how it could be used to innovate. This kept me in electrical engineering, and I'm glad I stayed.

At Sharif University of Technology in Tehran, where I earned my undergraduate degree in Electrical Engineering, I had excellent mentors and role models. My professors encouraged and motivated me. During my studies, I had to choose a concentration. Two professors, Dr. Farzaneh and Dr. Tebyani, were instrumental in guiding me. Dr. Farzaneh taught antennas and microwave engineering, which I found fascinating. His classes sparked my interest in microwaves and antennas. Studying at Sharif University was rigorous, but we had many outstanding professors and practical courses. One particularly valuable course was on RF circuit design, taught by Professor Behnia.

The war had a profound impact on my education. I was determined not to fall behind and get affected by the war. During my first year at the university, there was a risk of staying in Tehran due to ongoing attacks. The classes were canceled, and I didn't want to lose a semester. I considered taking a semester as a guest in Ahvaz to continue my studies, but my mother was reluctant to let me go. To convince her, I went on a three-day hunger strike until she finally agreed. I spent a semester as a guest student at Chamran University, where my aunt worked. It was a difficult time, filled with uncertainty about my family's safety in Tehran. I returned to Sharif University after that semester but, throughout my undergraduate years, we lived with the constant possibility of having to relocate or cancel classes due to the war. It was stressful, but we adapted.

Living in a war zone made me resilient and flexible. I learned to focus on what was within my control—such as making up for lost time with extra effort. It was challenging to juggle responsibilities and sacrifice time with family, but this experience made me stronger when facing future challenges. The unpredictability of war required full mental and emotional strength. I can only imagine the immense stress my mother and other parents endured. I hope that one day, war will no longer exist.

Q2: Can you tell me about your graduate school experience?

A2: As an undergraduate student, I always aspired to go to graduate school. I wanted to learn more and expand my knowledge. At the end of my undergraduate degree, I got married. My husband, also an electrical engineering major, was pursuing a master's in biomedical engineering. He received a scholarship for his PhD studies, which he took at the University of Manitoba in Canada. I also explored master's programs in Canada and reached out to professors conducting research in antennas and RF engineering.

Professor Lot Shafai (Fig. 3) at the University of Manitoba offered me a position in his research group, but it was initially unpaid. I had some savings to cover my tuition for the first year and, afterward, he provided me with a graduate research stipend. Dr. Shafai was an incredible mentor, researcher and educator. Studying under his guidance was the best thing that could have happened to me when I moved to Canada. He not only supervised my master's and PhD research but also taught me invaluable life lessons. He showed me how to be an educator, researcher and problem solver. His guidance helped me develop teamwork skills and a structured approach to tackling complex engineering problems. Even years after graduation, I often sought his advice when facing difficult challenges.

Fig. 3. Professor Abdel Sebak (advisory committee member), Sima Noghanian and Professor Lot Shafai (her advisor) during her thesis defense at the University of Manitoba.

Graduate school taught me more than just technical knowledge—it shaped my problem-solving mindset. I learned how to break down complex problems into manageable components, work effectively in teams and continuously seek opportunities to learn. To this day, I see myself as a student, always eager to explore new ideas. Sometimes, I wish I could return to school. I always encourage my students to cherish their time as learners, because it is a rare and valuable phase of life.

Q3: What are the most important things you have done in your career?

A3: One of the most meaningful aspects of my career is teaching (Fig. 4) and mentoring students (Fig. 5). They are the most valuable outcome of my work. I am grateful that I have had the opportunity to support and guide students, playing a small role in their growth. Not everyone gets this chance, and I appreciate the encouragement

I received from Dr. Shafai to pursue an academic career. Although I left academia a few years ago, I continue to mentor, teach and share my knowledge. Supporting the next generation is crucial—not just for individuals but for society as a whole. Seeing my students grow into professors, engineers or business leaders has been deeply rewarding.

Fig. 4. Sima Noghanian and graduate class students (Luis Gurrieri, Abdel-Halim Mohammad, Abas Sbouni and Mohammad Sehaili).

Fig. 5. Sima Noghanian with Dr. Ala Alemaryeen, Sima's graduate student at the University of North Dakota.

Another important goal for me is lifelong learning. After leaving my academic job, I transitioned into industry to see my work directly impact peoples' lives. I wanted my contributions to be used in real-world applications. Currently, at Ruckus, I work on Wi-Fi access points as an antenna designer. These devices are essential for connectivity, education and information access. Being part of an incredible and talented team that develops innovative products is fulfilling.

In my research, computational electromagnetics has been central to many projects, including implantable and wearable antennas, wireless power transfer and microwave imaging for breast cancer detection (Fig. 6). This field, rooted in mathematical principles, has been a constant in my work. With advancements in artificial intelligence, machine learning, new materials and 3D printing, the possibilities for antenna design and wireless communication continue to expand. I am excited about the future of engineering and the innovations that will make technology more efficient, cost-effective and accessible.

Fig. 6. Sima Noghanian with the Microwave Imaging Research Group at the University of Manitoba.

Q4: What is some important career advice?

A4: Persistence is key. Any meaningful pursuit comes with challenges and, at times, giving up may seem easier. However, if you stay committed, you will find a way forward. Hardships shape us, making us stronger and more capable. I have faced moments of doubt, wondering why certain obstacles were placed in my path. However, by staying positive, I discovered new opportunities where I least expected them. Failures are often stepping stones to success, teaching us valuable lessons along the way.

Q5: What about work-life balance?

A5: Achieving perfect balance is impossible—there is always something left undone. I constantly ask myself: Am I a good mother? A good employee? A good teacher or mentor? But I remind myself that I have to do my best. No matter how much I accomplish, there will always be more to do and ways I could have done better. However, it's important to look back and recognize what I have achieved, even if some things were missed along the way. On days when I feel like I've fallen short, I look at my children and students and see the impact I've made. That motivates me to keep going and give my best effort.

If there were ever a day when I had completed everything on my list, what would be the point of living? Life is about continuous growth—there will always be new challenges, unfinished tasks and opportunities for improvement.

Q5: Do you have role models?

A5: There are many individuals in the ACES and IEEE Antennas and Propagation (AP) Society whom I may not have interacted with directly, but who have served as inspiring role models. There was a time when the number of women in AP was very small. As a student, I saw only a few women in the field. However, witnessing their accomplishments—despite balancing family and other responsibilities—was incredibly motivating.

I remember one particular moment at our annual symposium when a senior female researcher was presenting awards for the student paper competition. Curious, I asked her about her research and she told me she was working on implanted antennas. I found the topic fascinating, and it ultimately became an area I pursued myself. Seeing women actively contributing to our society and excelling in leadership positions was encouraging. Inspired by these experiences, I strive to give back by mentoring and supporting the next generation of engineers.

I especially would like to mention my undergraduate and graduate advisors, Professors F. Farzaneh, M. Tebyani and L. Shafai, for their enormous support and their role in my education and becoming a professional in my field.

Finally, I would like to acknowledge and thank my family (Fig. 7), my husband Dr. Reza Fazel-Rezai and my sons Vahid and Hamed, for their unwavering support, inspiration and understanding.

Fig. 7. Sima Noghanian with Hamed, Vahid and Reza Fazel-Rezai.

III. CONCLUSION

We can be pioneers in many ways. It really is possible. This is why it's good to have the story of women in our society, like this interview and others, to help inspire the next generation of women in electromagnetics.

REFERENCES

[1] S. Noghanian, A. Sabouni, T. Desell, and A. Ashtari, *Microwave Tomography: Global Optimization, Parallelization and Performance Evaluation.* New York: Springer, 2014.

Cynthia Furse is a Distinguished Professor of Electrical and Computer Engineering at the University of Utah, USA. She applies electromagnetics to sensing and communication in complex lossy media such as the human body. She is a Fellow of the Applied Computational Electromagnetics Society, the IEEE and the National Academy of Inventors, and has received numerous teaching and research awards including the 2020 IEEE Chen To Tai Distinguished Educator Award.

Fast FDTD/TDPO Hybrid Method Based on Spatiotemporal Sparse Sampling

Linxi Wang and Juan Chen

School of Information and Communications Engineering
Xi'an Jiaotong University, Xi'an 710049, People's Republic of China
wanglinqian@stu.xjtu.edu.cn, chen.juan.0201@mail.xjtu.edu.cn

Abstract **–** Based on a hybrid method of finite-difference time-domain (FDTD) and time-domain physical optics (TDPO), this study employs a sparse sampling technique in near-to-far-field calculations to improve the efficiency of electrical large target computation. In the conventional hybrid method, the transformation from the near-field of the FDTD region to the far-field of the TDPO region involves the largest amount of computation, which can be reduced by applying the sparse sampling optimization method jointly in spatial and time domain. Compared to the conventional method, our proposed algorithm significantly reduces computation time while maintaining a negligible increase in error. Several examples are provided to demonstrate the accuracy and efficiency of our approach. In particular, a large parabolic antenna whose aperture size is 100 wavelengths is computed. The computation time is decreased by up to 91.52% of the conventional method while the maximum relative error is -21.56 dB. Compared with results of CST software, the method proposed in this work has smaller errors and excellent applicability.

Index Terms **–** Far-field, finite-difference time-domain, hybrid method, parabolic antenna, sparse sampling, time-domain physical optics.

I. INTRODUCTION

Benefiting from the rapid development of computer technology and hardware, transient electromagnetic scattering simulations of composite objects with diverse sizes and material properties are widely applied in fields such as aerospace [1], radar [2] and marine [3]. In practical scenarios, the electromagnetic challenges that need to be addressed are often multiscale in nature [4, 5]. For instance, a large reflector antenna is much larger than a typical wavelength, while its feed structure is an electrical fine structure with respect to a typical wavelength. However, as the electrical scale of the target increases, the demands in computational time and resource requirements by numerical methods become overwhelming.

With the aim of computing the transient electromagnetic scattering accurately and efficiently, hybrid methods have been proposed by researchers to address challenges that cannot be remedied easily by a single method [6–9]. A hybrid schema combining finite-difference time-domain (FDTD) [10] and time-domain physical optics (TDPO) [11], as a representative computational method in time domain, demonstrates significant advantages in broadband calculations [12]. The FDTD method enables accurate simulations across various electromagnetic problems, while the TDPO can reduce memory requirements and enhance computational speed. Yang et al. [13] systematically investigated the hybrid algorithm of FDTD and TDPO, conducting far-field scattering calculations for composite targets comprising dipole and perfect electric conductor (PEC) plates. This method needs small amounts of computer memory and achieves high efficiency compared to a full wave solution. However, the examples in the literature are too simple to demonstrate the efficiency. The antenna models in practical engineering applications tend to be more complex and larger in scale. As discussed in [14], the radiation fields of the large single reflector calculated by a hybrid method parallelized-FDTD and parallelized-TDPO, which demonstrated the ability to simulate a large reflector with dimensions spanning hundreds of wavelengths, included cases where the reflector's feed is offset. Indeed, conventional hybrid methods face significant limitations when addressing multiscale problems, primarily due to excessive computational demands. These challenges often render such methods either impractical or prohibitively slow, especially when the antenna aperture exceeds several hundred wavelengths or the feed structure becomes increasingly complex, frequently necessitating the use of parallel algorithms. Furthermore, there is currently a scarcity of literature offering a comparative analysis of computation time for such hybrid algorithms.

This paper presents an optimization of the conventional FDTD/TDPO hybrid algorithm by employing a sparse sampling technique in both spatial and time domains, which reduces computational workload and enhances efficiency. Our proposed approach achieves the computation of large parabolic antennas fed by various

Submitted On: September 25, 2024
Accepted On: March 4, 2025
https://doi.org/10.13052/2024.ACES.J.400302

sources using a serial algorithm, a task previously limited to parallel algorithms as reported in [14]. Importantly, the computation time is significantly saved without a substantial increase in errors compared to conventional hybrid algorithms.

The rest of this paper is organized as follows. The principle of the hybrid method including the formulation of the coupling between the FDTD method and TDPO method and the implementation process of organization have been presented in detail in section II. Through providing several numerical examples, section III demonstrates the accuracy and efficiency of the proposed hybrid method for large composite targets transient electromagnetic scattering. Finally, conclusions are presented in section IV.

II. BASIC THEORY

When using the FDTD/TDPO hybrid method to study complex composite objects, the computation domain is first divided into sub-domains based on configuration: the FDTD region containing small-size objects with fine structures, and the TDPO region containing large electrical dimensions. Conducting far-field scattering calculations is divided into primary scattering and secondary scattering. The primary scattered field involves direct far-field scattering by the FDTD and TDPO regions, which can be calculated separately using FDTD and TDPO methods. The secondary scattered field is due to the mutual-coupling between the FDTD and TDPO region. The scattered field from one region is considered to be the incident field on the other region.

The key point of the hybrid algorithm lies in the coupling between the two regions, which is also crucial for optimization. Let us take the coupling from the FDTD region to the TDPO region as an example. Firstly, the magnetic fields on the FDTD extrapolation surface are calculated using the FDTD method. Then, the magnetic fields in the TDPO region are computed via near-to-far-field extrapolation. Finally, the far-fields of TDPO region are obtained using the TDPO method.

The near-to-far-field extrapolation technique is based on Kirchhoff's surface integral representation (KSIR) [15]. A cubic surface S is selected as the extrapolation surface. The surface S should be closed, enclosing all sources, and as small as possible. Taking the magnetic field along the x-axis as an example, assuming a point P exists outside the surface S, the extrapolated magnetic field H_x from the FDTD extrapolation surface to the TDPO calculation domain surface element is:

$$H_x(r,t+\tau) = \frac{1}{4\pi}\oint_s \left\{ \begin{array}{l} (\hat{n}'\cdot R)\left[\frac{H_x(r',t)}{R^3}+\frac{1}{cR^2}\frac{\partial H_x(r',t)}{\partial t}\right] \\ -\frac{1}{R}\frac{\partial H_x(r',t)}{\partial z} \end{array} \right\} ds', \tag{1}$$

where $\boldsymbol{r}$ is the position vector of the observation point P, $\boldsymbol{r\prime}$ is the position vector of any point on the closed surface S, $\boldsymbol{R} = \boldsymbol{r}\text{-}\boldsymbol{r\prime}$, $R = |\boldsymbol{R}|$, $\hat{n}'$ is the outward-pointing normal to the FDTD extrapolation surface, τ is the retarded time and c is the speed of light in free space.

At time step $n+1$, the partial derivatives with respect to space and time are represented by second-order center differences:

$$\left.\frac{\partial H_x}{\partial z}\right|_{z=k_0} \cong \frac{H_x^{n+1}(i,j,k_0+1)-H_x^{n+1}(i,j,k_0-1)}{2\Delta z}, \tag{2}$$

$$\left.\frac{\partial H_x}{\partial t}\right|_{t=n+1} \cong \frac{H_x^{n+2}(i,j,k_0)-H_x^{n}(i,j,k_0)}{2\Delta t}. \tag{3}$$

H_x^n represents the value of H_x at time step n, Δt is time-step size, Δz is the grid size in the z-direction. Substituting equations (2) and (3) into equation (1) yields:

$$H_{x,k} = F_1(n)+F_2(n+1)+F_3(n+2), \tag{4}$$

where:

$$F_1(n) = \sum_{i,j} A\frac{H_x^n(i,j,k_0)}{2\Delta t}\Delta_{ij}, \tag{5}$$

$$F_2(n+1) = \sum_{i,j}\left[\begin{array}{l} Ac\frac{H_x^{n+1}(i,j,k_0+1)-H_x^{n+1}(i,j,k_0-1)}{2\Delta z} \\ +BH_x^{n+1}(i,j,k_0) \end{array}\right]\Delta_{ij}, \tag{6}$$

$$F_3(n+2) = \sum_{i,j} A\frac{-H_x^{n+2}(i,j,k_0)}{2\Delta t}\Delta_{ij}, \tag{7}$$

$$A = -1/4\pi cR, \tag{8}$$

$$B = 1/4\pi R^2. \tag{9}$$

Here, Δ_{ij} is the area of Yee's cell on the xy plane at $z = k_0$ and R is the distance from each subsurface Δ_{ij} to the observation point.

To reduce memory usage and enhance computational speed, a sequential transfer method [13] is employed. In this method, for each time step computed by FDTD, the field values on the extrapolation surface of the Yee cell are extrapolated to the surface triangular patches of the TDPO region using KSIR. Then, the contribution from each patch to the far-field observation point can be immediately computed using the TDPO method. The far-field values are summed up based on the time delay between cell-to-patch and patch-to-observation point until the transient process is completed.

However, conventional hybrid algorithms face significant challenges when dealing with large antenna apertures and complex feed structures. Large-aperture antennas are often electrically large, requiring a dense grid to accurately model the electromagnetic behavior, which leads to a high grid count. The complexity of the feed structure further exacerbates this issue by demanding smaller and denser grids to capture the fine details, which results in an increased computational load. Moreover, the smaller time step required to maintain numerical stability in such cases can lead to a further increase in computation time. Moreover, the extrapolation step is the most time-consuming part of the entire calculation process. In each time step, it is necessary to calculate extrapolated field values from each Yee cell on the extrapolation surface of the FDTD region to each triangle on the TDPO region.

Here, we propose two optimization strategies: spatial sparse sampling to reduce grid count and temporal sparse sampling to enable larger time step. These two methods can be applied jointly to significantly enhance computational efficiency.

A. Spatial sparse sampling method

Considering the impact of fine structures on the accuracy, the grid size of the targets within the FDTD region is typically set to be small. Consequently, the number of grids on the extrapolation surfaces becomes very large, resulting in a significant computational burden and extremely long computation times during near-field extrapolation. In general, the number of grids on the extrapolation surfaces K_{sum} is in the order of 10^4 to 10^5, while the order of magnitude of cells in the TDPO region M_{sum} is 10^2 to 10^4. Thus, the total extrapolation time will be $K_{sum} \times M_{sum}$, reaching up to 10^{10} times that of one single extrapolation. Consequently, extrapolation becomes a significant bottleneck in overall computation, particularly when addressing electromagnetic problems with electrically small and intricate structures. As an example, consider a composite target where K_{sum} is 10000 and M_{sum} is 1000. By applying sparse sampling to K_{sum}, where every two grid points are sampled once, K_{sum} can be reduced to 5000. This decreases the total number of extrapolations from 10^7 to 5×10^6, thereby significantly reducing the computational cost.

When conducting near-field extrapolation, it is unnecessary to substitute the value of each cell into equation (1). The spatial sparse sampling method involves sampling on the extrapolation surface and then performing extrapolation. Due to the presence of fine structures in the feed, the grids on the extrapolation surface will be dense. However, these overly dense grids are required because the grid partitioning must fit the structure and shape of the target. Since the field variations in these areas are not drastic, selectively extracting grids at intervals on the extrapolation surface for extrapolation calculations does not affect the collection of field values on the extrapolation surface outside the FDTD region and thus does not significantly impact the final results. Therefore, the extrapolation operation with interval sampling will not affect the accuracy of the results significantly but can effectively reduce the computational load.

Taking the xy-plane as an example, Fig. 1 depicts a schematic diagram of the grid setting when the spatial sampling is set to 3. The black grid lines represent the original FDTD grid, while the red lines represent the

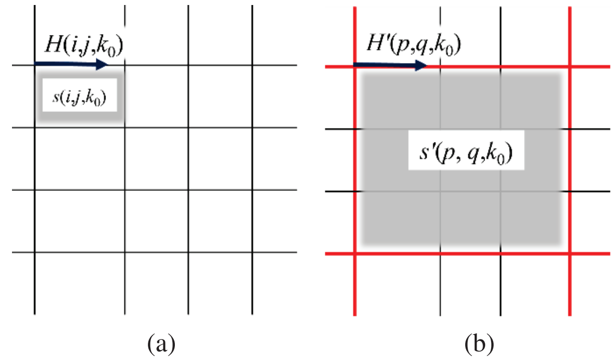

Fig. 1. Grid setting (a) without spatial sampling and (b) with spatial sampling set to 3.

sampling grid. Let $H_x(i,j,k_0)$ denote the magnetic field on the original grid, $H_x'(p,q,k_0)$ denote the magnetic field on the sampling grid, $s(i,j,k_0)$ denote the area of the original grid, $s\prime(p,q,k_0)$ denote the area of the sampling grid, M and N denotes the number of original grids in the x and y directions, and Ms and Ns denotes the number of sampling grids in the x and y directions, respectively. Then, we have:

$$\sum_{i=1,j=1}^{M,N} H_x(i,j,k_0)s(i,j,k_0) \simeq \sum_{p=1,q=1}^{Ms,Ns} H_x'(p,q,k_0)s'(p,q,k_0). \tag{10}$$

In equation (10), $H_x'(p,q,k_0)$ can be approximated using the average value method. If the number of intervals in the spatial grid is G, then the magnetic field components on the sampling grid can be approximated by the average value method as follows:

$$\bar{H}_x(p,q,k_0) = \frac{1}{G^2} \sum_{i=p,j=q}^{p+G-1,q+G-1} H_x(i,j,k_0). \tag{11}$$

By substituting equations (5), (6) and (7) into equation (4), the equation can be expressed as:

$$H_{x,k_0} = \sum_{i,j=1}^{M,N} \left\{ \begin{array}{l} Ac\frac{H_x^{n+1}(i,j,k_0+1)-H_x^{n+1}(i,j,k_0-1)}{2\Delta z} \\ +BH_x^{n+1}(i,j,k_0) \\ -A\frac{H_x^{n+2}(i,j,k_0)-H_x^{n}(i,j,k_0)}{2\Delta t} \end{array} \right\} \Delta_{ij}. \tag{12}$$

Substituting equation (11) into equation (12) gives:

$$H_{x,k_0} = \sum_{p,q=1}^{Ms,Ns} \left[\begin{array}{l} Ac\frac{\bar{H}_x^{n+1}(p,q,k_0+1)-\bar{H}_x^{n+1}(p,q,k_0-1)}{2\Delta z} \\ +B\bar{H}_x^{n+1}(p,q,k_0) \\ -A\frac{\bar{H}_x^{n+2}(p,q,k_0)-\bar{H}_x^{n}(p,q,k_0)}{2\Delta t} \\ \times \sum_{i=p,j=q}^{p+G-1,q+G-1} \Delta_{pq} \end{array} \right]. \tag{13}$$

Here, $Ms = INT((M\text{-}1)/G)$ and $Ns = INT((N\text{-}1)/G)$.

By comparing equations (12) and (13), the absolute error after sparsification of the spatial grid can be derived:

$$\delta_{x,k_0} = \sum_{i=p,j=q}^{p+G,q+G} \begin{bmatrix} Ac\frac{H_x^{n+1}(i,j,k_0-1)-\bar{H}_x^{n+1}(p,q,k_0-1)}{2\Delta z} \\ -Ac\frac{H_x^{n+1}(i,j,k_0-1)-\bar{H}_x^{n+1}(p,q,k_0-1)}{2\Delta z} \\ +\left(BH_x^{n+1}(i,j,k_0)-B\bar{H}_x^{n+1}(p,q,k_0)\right) \\ -A\frac{H_x^{n+2}(i,j,k_0)-\bar{H}_x^{n+2}(p,q,k_0)}{2\Delta t} \\ +A\frac{H_x^{n}(i,j,k_0)-\bar{H}_x^{n}(p,q,k_0)}{2\Delta t} \end{bmatrix} \times \Delta_{pq}. \tag{14}$$

From equation (14), it can be seen that δ_{x,k_0} is mainly influenced by the difference $H_x^n(i,j,k_0) - \overline{H}_x^n(p,q,k_0)$ and the product Δ_{pq}. Therefore, the error is likely to increase in two situations: first, where the field components vary sharply and, second, where the original FDTD grid is too coarse. Thus, in regions with significant field variation, such as at apertures, material boundaries and interfaces between different media, the grid discretization should be appropriately increased to mitigate the impact of spatial sparsity on the results.

B. Time sparse sampling method

In each time step of the current conventional algorithm, the near-field values are computed first by FDTD, then the magnetic field in the TDPO region is extrapolated using KSIR, and finally TDPO is used to calculate the far-field. The FDTD algorithm must comply with the Courant-Friedrichs-Lewy (CFL) condition [16] to guarantee the stability of the solution, which means that the time-step size of the FDTD algorithm is related to the minimum grid size in the three spatial directions. To reduce numerical dispersion caused by spatial discretization, the maximum grid size in the FDTD method is typically less than one-tenth of the shortest wavelength. When the object has fine structures, the minimum grid size may be only one-hundredth of the wavelength or even smaller. Therefore, the time step of the FDTD method is much smaller than that of the TDPO method. As the time step decreases, the number of time steps that need to be calculated increases, resulting in a greater computational load.

According to the time-domain sampling theorem, a band-limited signal $f(t)$ with a maximum frequency f_{max} can be uniquely represented by uniformly distributed samples, provided the sampling interval does not exceed $1/2f_{max}$. The time sparse sampling method optimizes FDTD by storing the field values on the extrapolation surface every N time steps. Subsequently, near-field extrapolation is performed using the Kirchhoff surface integral, and the far-field values for each time step are computed using the TDPO method. According to the Nyquist sampling theorem, the sampling interval only needs to satisfy $(N\text{-}1)\Delta t < 1/(2f_{max})$, which significantly reduces the number of iterations required for the extrapolation steps. Here Δt is the time-step length of FDTD and f_{max} denotes the maximum operating frequency.

III. NUMERICAL RESULTS

To illustrate the efficiency, accuracy and applicability of the proposed approach, we present two numerical cases. In the first case, a basic composite entity comprising both small-scale and large-scale structures relative to the wavelength is given and simulated. Various sets of sampling data are configured to assess the influence of the sampling number on result errors. A comparative analysis is conducted between the conventional FDTD/TDPO approach and the proposed FDTD/TDPO method, focusing on their efficiency and accuracy. In the second case, the applicability of the proposed approach to problems concerning a large parabolic antenna is demonstrated. Additionally, the findings are corroborated through validation using the commercial software CST.

A. Cube and plate

In the first example, we consider a PEC cube located at a distance of 10λ in front of a PEC plate. The metallic cube has a side length of 1λ, while the plate measures $100\lambda \times 100\lambda \times 1\lambda$. A modulated-Gaussian pulse plane wave with a frequency band 10$\sim$20 GHz is incident along the z-axis, with the electric field polarized parallel to x-axis. The result of the hybrid method is compared with that of FDTD to confirm the accuracy of the hybrid method. Figure 2 shows the transient far-field scattering response calculated by the conventional FDTD/TDPO hybrid method and the FDTD method.

It is evident that the two results are in good agreement. Due to the significant difference of four orders of magnitude in the field values between the FDTD region and TDPO region, the results are segmented by time intervals. Figure 3 (a) depicts the far-field for the time interval of 0-0.8 ns, representing the primary scattering

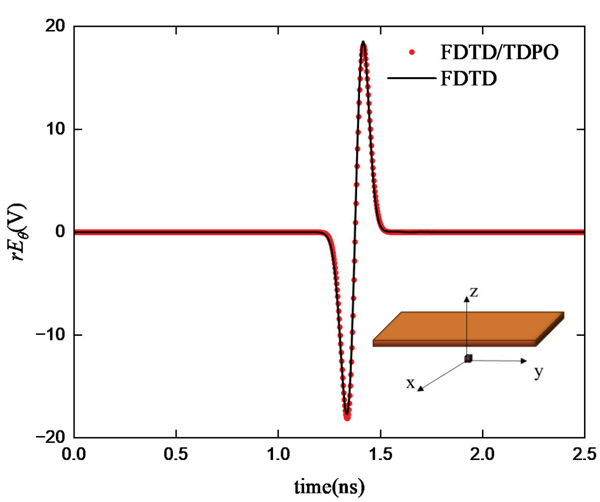

Fig. 2. Far-field in time domain.

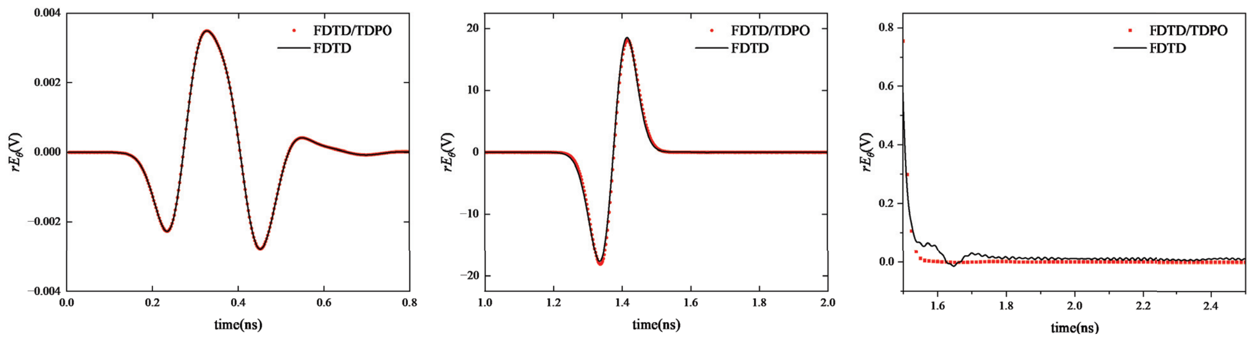

Fig. 3. Far-field for the time interval of (a) 0-0.8 ns, (b) 1-2 ns and (c) 1.5-2.5 ns.

from the small PEC cube. Figure 3 (b) illustrates the far-field for the time interval of 1-2 ns, representing the sum of the primary scattering from the plate and the coupled field between the plate and the cube. Figure 3 (c) presents the far-field values after 1.5 ns.

Overall, the backscattering fields of the combined target computed by two methods match well, with discrepancies emerging only after 1.5 ns. Such discrepancies are mainly attributed to the TDPO method only considering the induced currents on the plate surface, without considering the edge diffraction fields.

In the two algorithms, the FDTD algorithm took 16.23 hours while the FDTD/TDPO hybrid algorithm required 144.49 hours, indicating the need for optimization of the hybrid algorithm in terms of computation time. Therefore, we use spatial sparse sampling and time sparse sampling methods for optimization, and focus on analyzing the error in the coupling part of the results.

First, we fix the time sample at 5. Five sets of data with spatial sample of 1, 2, 4, 6 and 8 are selected for comparison over 500 time steps. Figure 4 shows the comparison of far-field obtained with different spatial samples, which are in good agreement. The relative errors of the far-field calculated with spatial sample of $N = 2$, 4, 6 and 8 compared to the case of no sampling interval (i.e., $N = 1$) are displayed in Fig. 5. The error is defined as a function of time by:

$$20\log_{10}(|E_\theta^1(t) - E_\theta^0(t)| \,/\, \max(|E_\theta^0(t)|)), \tag{15}$$

where $E_\theta^1(t)$ represents the electric field with spatial sample of N (N>1), and $E_\theta^0(t)$ represents the electric field with spatial sample of 1.

There are no relative error values in the earlier time segments because the algorithms for computing the primary scattering are the same, resulting in a relative error of 0. As can be seen in Fig. 4, the more sampling points there are, the smaller the error. However, excessive sampling leads to longer computation times, defeating the purpose of optimizing the algorithm.

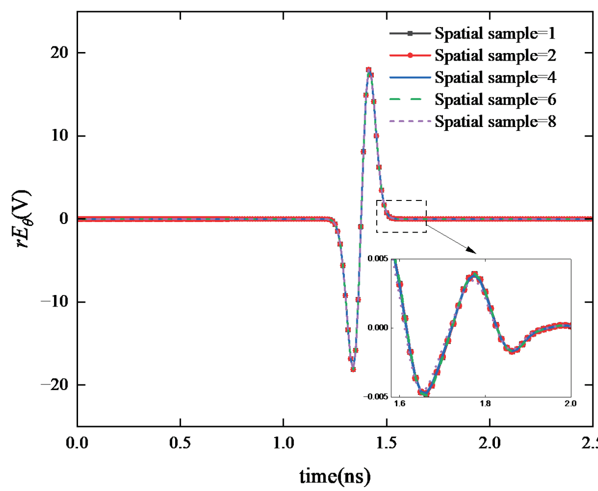

Fig. 4. Comparison of far-fields by different spatial samples.

Before 1.2 ns, there are no numerical errors in the earlier time segments because the algorithms for computing the primary scattering are the same, resulting in an infinitely small relative error. Taking a spatial sampling interval of 2 as an example, as shown in Fig. 3, a distinct time-domain waveform appears after 1.25 ns. Correspondingly, in Fig. 5, the relative error undergoes a rapid change between 1.25 ns and 1.4 ns, increasing to -128.05 dB, and then stabilizes between -172 dB and -113 dB. Figure 5 also shows that as the spatial sampling interval increases, the error slightly increases, though not significantly. Larger errors tend to occur when the electric field is near its peaks or troughs, leading to greater relative error. Conversely, when the electric field is near zero, the relative error is reduced. Therefore, the relative error fluctuates rather than remaining constant.

Table 1 presents the computation time and the maximum relative error corresponding to different spatial samples. As the spatial sample increases from 2 to 8, the maximum relative error increases from -112.21 dB

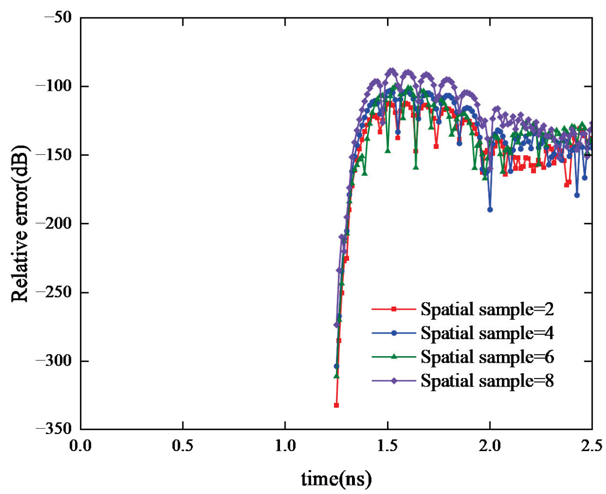

Fig. 5. Relative error of different spatial samples.

Table 1: Computation time and maximum relative error of different spatial samples

Spatial Sample	Computation Time (h)	Time Reduction	Maximum Relative Error (dB)
1	17.73		
2	5.34	1/3.32	-112.21
4	1.34	1/13.23	-102.86
6	0.39	1/45.46	-88.55
8	0.26	1/68.19	-85.69

to -85.69 dB, while the computation time decreases from 1064.03 min to 15.76 min. When the spatial sample is set to 10, the time is reduced to 1/67.51 of the original, indicating a substantial reduction in time. Although the increase in error with the larger spatial sample interval is not significant, the substantial reduction in time greatly enhances the computational capability of the hybrid algorithm.

Subsequently, we analyze the time sparse sampling. With spatial sample fixed at 4, five sets of data with time sample of 1, 2, 4, 8 and 16 are selected for comparison over 500 time steps. Figure 6 illustrates the far-field scattering results for different time samples, while Fig. 7 contrasts the relative errors corresponding to these time samples.

One can see that as the time sample increases, the sampling points become sparser, making it more likely to miss peaks or troughs in the field values, thus leading to larger errors. However, with the increase in the time sample, the maximum relative error fluctuates slightly, consistently remaining below -78 dB.

The time required is reduced to 1/21.63 of that when the time sample is 1, as shown in Table 2. Consequently,

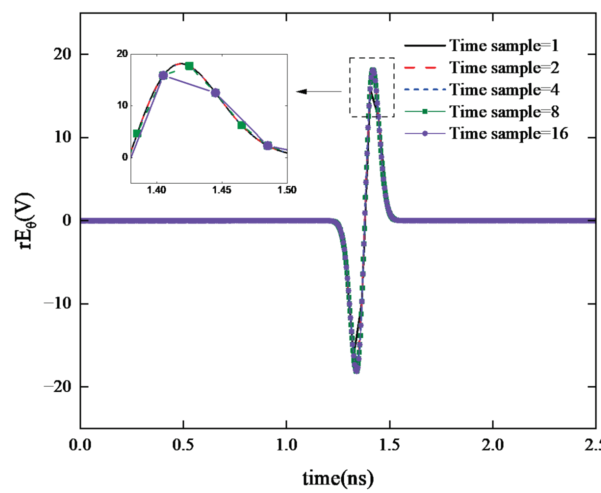

Fig. 6. Comparison of far-fields by different time samples.

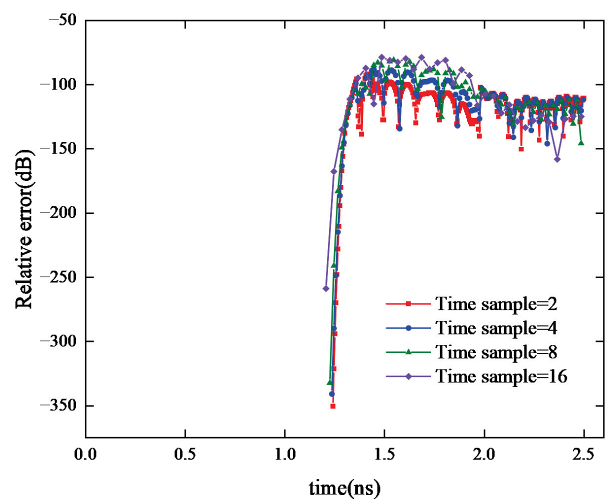

Fig. 7. Relative error of different time samples.

Table 2: Computation time and maximum relative error of different time samples

Time Sample	Computation Time (h)	Time Reduction	Maximum Relative Error (dB)
1	8.13		
2	3.12	1/2.61	-90.68
4	1.49	1/5.46	-87.87
8	0.73	1/11.14	-80.74
16	0.38	1/21.39	-78.60

although the increase in the time sample does not significantly increase the error, there is a significant reduction in time consumption, thereby notably enhancing the computational efficiency of the hybrid algorithm.

B. Parabolic antenna fed by horn

Here we consider an example of a composite target consisting of a parabolic antenna and a horn antenna, as depicted in Fig. 8.

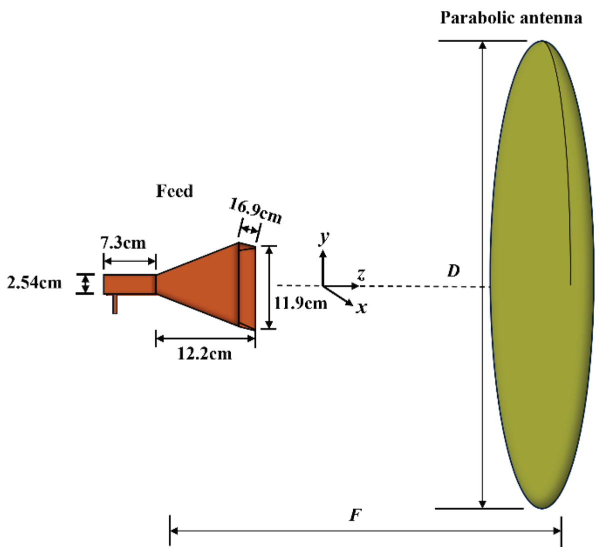

Fig. 8. Parabolic antenna fed by horn.

The horn antenna is placed as the feed source at the focus of the parabolic antenna. The operating frequency is $f = 6$ GHz, the aperture diameter of the parabolic antenna is $D = 100\lambda$, and the focal-to-diameter ratio is $F/D = 0.685$, where F denotes the focal length of the parabolic antenna. The waveguide length in the horn antenna is 7.3 cm, with a waveguide aperture size of 0.0508×0.0254 cm^2. The axial projection length of the horn is 12.2 cm and its aperture size is 16.9×11.9 cm^2. The horn antenna is excited by a coaxial feed with a Gaussian pulse signal.

The horn antenna in the FDTD computation domain is discretized using non-uniform hexahedral grids, comprising $71 \times 31 \times 75$ cells. The minimum grid sizes in the three directions are 0.4 mm, 0.8 mm and 0.3 mm, respectively. The time step is set to 8.24×10^{-13} s. The total number of grids on the extrapolation surface in the FDTD region is 26560. Within the TDPO computation domain, the parabolic antenna is partitioned into 2676 triangular patches. The FDTD/TDPO hybrid algorithm is optimized using both spatial and time sparse sampling methods.

Figure 9 illustrates the comparison of far-field electric field obtained with different spatial sampling when the time sampling is set to 20. Figure 10 compares the far-field electric field results obtained with different time sampling when the spatial sampling is set to 4. It is evident that the results of the proposed hybrid algorithm

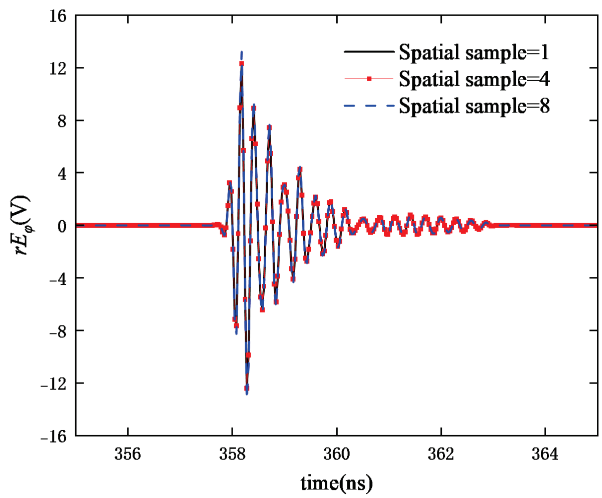

Fig. 9. Comparison of far-fields by different spatial samples.

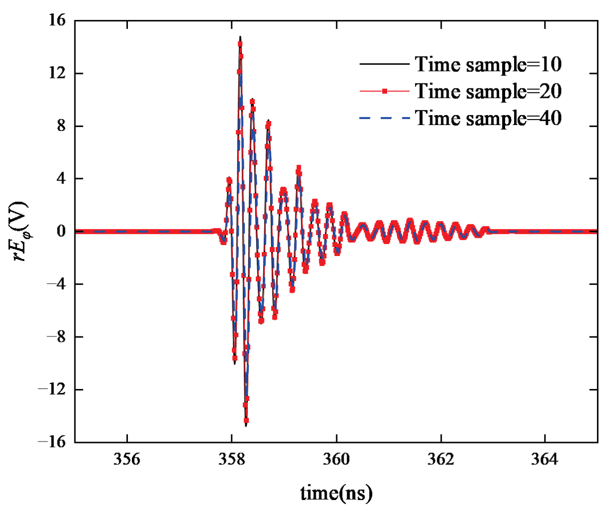

Fig. 10. Comparison of far-fields by different time samples.

align well with those of the original FDTD/TDPO hybrid algorithm.

The computation time and maximum relative error for different spatial samples and time samples are presented in Table 3. With an increase in spatial sampling, the maximum relative error remains relatively stable. When the time sample is fixed and the spatial sample is increased from 1 to 8, the computation time decreases from 29.01 hours to 2.46 hours, a reduction of 91.52%. Compared to the result at a spatial sampling of 1, the result at a spatial sampling of 4 exhibits a maximum relative error of -21.56 dB. When the spatial sample is fixed and the time sample is increased from 10 to 40, the computation time decreases from 9.83 hours to 3.20 hours,

Table 3: Computation time and maximum relative error of different spatial samples and time samples

Spatial Sample	Time Sample	Computation Time (h)	Reduction Rate	Maximum Relative Error (dB)
1	40	29.01		
4		3.20	88.97%	-39.37
8		2.46	91.52%	-21.56
4	10	9.83		
	20	5.08	48.45%	-18.31
	40	3.20	67.43%	-8.94

which is approximately 1/3.07 of the computation time with a time sample of 10. The maximum relative error is -8.94 dB in this case. This indicates that as the spatial and time sample increases, the increase in error is minimal, while there is a significant reduction in computation time, effectively enhancing the computational efficiency of the hybrid algorithm.

Figure 11 presents the corresponding results obtained from commercial software CST. Compared to the result obtained using the sparse sampling optimization method with a spatial sample of 4 and a time sample of 40, the two results are in good agreement. The CST software computed this example with a total grid count of 1.86×10^9, utilizing GPU acceleration, and the entire computation process took 35.8 hours. In contrast, the proposed hybrid algorithm generates 906315 cells in the FDTD computation region and 2616 triangular patches in the TDPO region, achieving a total computation time of 2.46 hours.

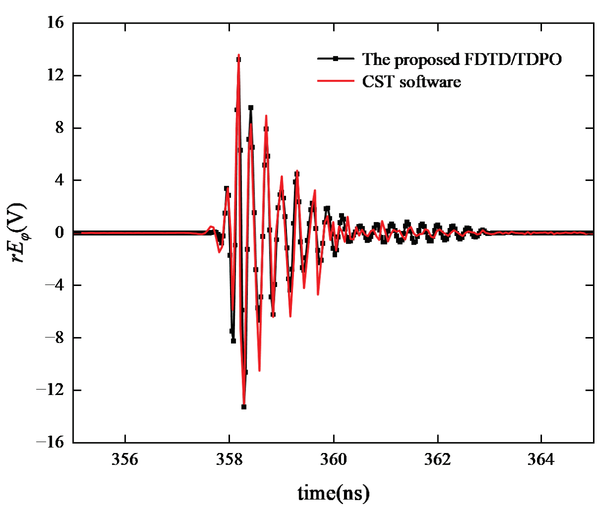

Fig. 11. Comparison of transient far-field computed by CST and the proposed FDTD/TDPO.

The method proposed in this paper does not consider the impact of hardware on computation speed and accuracy. Therefore, all methods in the paper were executed on the same computer configuration, detailed as follows: Windows 10 operating system, Intel(R) Xeon(R) 8360Y CPU @ 2.40 GHz 3.50 GHz processor and 1.0 TB RAM. If the size of the parabolic antenna continues to increase, the CST software would be unable to perform transient radiation simulation, whereas the proposed algorithm is not subject to such limitations.

IV. CONCLUSION

This paper presents an optimization algorithm based on the FDTD/TDPO hybrid method, which samples at intervals in the spatial and time domains. The proposed approach preserves the advantages of the hybrid algorithm by segmenting computation regions for composite objects computation, while addressing the issue of slow computation caused by excessive computation load. Numerical validation demonstrates that this optimization significantly enhances computational efficiency without appreciably compromising accuracy, thereby highlighting the reliability and efficiency of the algorithm.

ACKNOWLEDGMENT

This work was supported by the National Key Research and Development Program of China under No. 2020YFA0709800, the National Natural Science Foundations of China under No. 62122061 and the Shaanxi Natural Science Basic Research Project of Shaanxi Science and Technology Office under No. 2023-JC-QN-0673.

REFERENCES

[1] W. Chen, L. Wang, Z. Wu, M. Fang, Q. Deng, A. Wang, Z. Huang, X. Wu, L. Guo, and L. Yang, "Study on the electromagnetic scattering characteristics of high-speed target with non-uniform plasma via the FCC-FDTD method," *IEEE Trans. Antennas Propagat.*, vol. 70, no. 7, pp. 5744-5757, July 2022.

[2] A. G. Voronovich and V. U. Zavorotny, "The transition from weak to strong diffuse radar bistatic scattering from rough ocean surface," *IEEE Trans. Antennas Propagat.*, vol. 65, no. 11, pp. 6029-6034, Nov. 2017.

[3] B. Dong, J. Jia, Z. Li, G. Li, J. Shi, H. Wang, N. Chi, and J. Zhang, "Photonic-based flexible integrated sensing and communication with multiple targets detection capability for w-band fiber-wireless network," *IEEE Trans. Microwave Theory Techn.*, pp. 1-14, 2024.

[4] G.-Y. Zhu, W.-D. Li, W. E. I. Sha, H.-X. Zhou, and W. Hong, "A pre-splitting Green's function based hybrid fast algorithm for multiscale problems," *Applied Computational Electromagnetics Society (ACES) Journal*, pp. 652-666, Feb. 2024.

[5] Y. Liang and L. X. Guo, "A study of composite scattering characteristics of movable/rotatable targets and a rough sea surface using an efficient numerical algorithm," *IEEE Trans. Antennas Propagat.*, vol. 69, no. 7, pp. 4011-4019, July 2021.

[6] C. Ma, Y. Wen, J. Zhang, and D. Zhang, "A hybrid 3-D-ADI-TDPE/DGTD method for multiscale target echo simulation in large-scale complex environments," *IEEE Trans. Microwave Theory Techn.*, vol. 71, no. 3, pp. 997-1008, Mar. 2023.

[7] X. Wang, S.-X. Gong, J. Ma, and C.-F. Wang, "Efficient analysis of antennas mounted on large-scale complex platforms using hybrid AIM-PO technique," *IEEE Trans. Antennas Propagat.*, vol. 62, no. 3, pp. 1517-1523, Mar. 2014.

[8] H. Mai, J. Chen, and A. Zhang, "A hybrid algorithm based on FDTD and HIE-FDTD methods for simulating shielding enclosure," *IEEE Trans. Electromagn. Compat.*, vol. 60, no. 5, pp. 1393-1399, Oct. 2018.

[9] S. Zuo, Z. Lin, Z. Yue, D. Garcia Donoro, Y. Zhang, and X. Zhao, "An efficient parallel hybrid method of FEM-MLFMA for electromagnetic radiation and scattering analysis of separated objects," *Applied Computational Electromagnetics Society (ACES) Journal*, vol. 35, no. 10, pp. 1127-1136, Dec. 2020.

[10] K. S. Yee, "Numerical solution of initial boundary value problems involving maxwell's equations in isotropic media," *IEEE Trans. Antennas Propagat.*, vol. 14, no. 3, pp. 302-307, May 1966.

[11] E.-Y. Sun and W. V. T. Rusch, "Time-domain physical-optics," *IEEE Transactions on Antennas and Propagation*, vol. 42, no. 1, pp. 9-15, 1994.

[12] F. Le Bolzer, R. Gillard, J. Citerne, V. F. Hanna, and M. F. Wong, "An hybrid formulation combining FDTD and TDPO," in *IEEE Antennas and Propagation Society International Symposium. 1998 Digest. Antennas: Gateways to the Global Network. Held in conjunction with: USNC/URSI National Radio Science Meeting*, Atlanta, GA, pp. 952-955, 1998.

[13] L.-X. Yang, D.-B. Ge, and B. Wei, "FDTD/TDPO hybrid approach for analysis of the EM scattering of combinative objects," *PIER*, vol. 76, pp. 275-284, 2007.

[14] X. Zhu, J. Wang, Z. Chen, L. Cai, and T. Liang, "Hybrid PFDTD-PTDPO method for computing transient far-fields of single reflector," in *2012 International Conference on Microwave and Millimeter Wave Technology (ICMMT)*, Shenzhen, China, pp. 1-4, May 2012.

[15] O. M. Ramahi, "Near- and far-field calculations in FDTD simulations using Kirchhoff surface integral representation," *IEEE Transactions on Antennas and Propagation*, vol. 45, no. 5, pp. 753-759, 1997.

[16] A. Taflove and S. C. Hagness, *Computational Electromagnetics: The Finite-Difference Time-Domain Method*, 3rd ed. Boston, MA: Artech House, 2005.

Linxi Wang was born in Hubei, China, in 1993. She received the B.S. degree in engineering electronic science and technology from the Xi'an Liaotung University, Xi'an, China, in 2015 and the M.S. degree in microelectronics from the Xi'an Jiao University, Xi'an, China, in 2018. She is currently working toward the Ph.D. degree in electromagnetic field and microwave technology at the school of Information and Communications Engineering, Xi'an Liaotung University, Xi'an, China. Her current research interests include computational electromagnetics and antenna designs.

Juan Chen was born in Chongqing, China. She received the Ph.D. degree from Xi'an Jiaotong University, Xi'an, China, in 2008, in electromagnetic field and microwave technology. She is currently working in Xi'an Jiaotong University, Xi'an, China, as a professor. Her research interests include computational electromagnetics and microwave device design.

Miniaturized Polarization Conversion Metasurface for RCS Reduction

Xiwang Dai[1, 2], Ningqi Tang[1], Ze Li[1], Wenhao Hu[1], and Hui Hong[1]

[1]School of Electronic Information
Hangzhou Dianzi University, Hangzhou 310018, China
xwdai@hdu.edu.cn, 2669397247@qq.com, 1223406727@qq.com, 2274714528@qq.com, hongh@hdu.edu.cn

[2]State Key Laboratory of Millimeter Waves
Southeast University, Nanjing 210096, China

Abstract – In this study, a miniaturized polarization conversion metasurface (PCM) with a cell size of 6×6 mm is utilized to reduce the radar cross-section (RCS) of a circularly polarized antenna array. Each cell circuit of the PCM comprises a pair of folded L-shaped strips with a meander line, which are printed on the surface of the substrate. This configuration demonstrates a polarization rotation (PR) bandwidth of 112% and achieves a high polarization conversion ratio (PCR) of 90%. To confirm the efficacy of the RCS reduction, the PCM is integrated with a circularly polarized 2×2 dipole antenna array. The measured results of the array are in excellent agreement with the simulated data, indicating at least a 5 dB reduction in monostatic RCS for the proposed antenna array. Furthermore, the integration of the PCM does not degrade the radiation performance of the antenna array, confirming the PCM's suitability for RCS reduction without compromising antenna functionality.

Index Terms – Circularly polarized dipole antenna array, miniaturized, PCM, RCS.

I. INTRODUCTION

An antenna can not only radiate/receive electromagnetic waves, but also scatter electromagnetic waves as a special structure, which greatly increases the radar cross-section (RCS) of the antenna and seriously affects its application in safe communication. Developing an antenna that can achieve both ultra-wideband low RCS and wideband radiation is of great significance and necessity [1, 2].

Reflective polarization rotators have received considerable attention in the development of stealth platforms [3]. Linear-to-linear rotating polarization conversion metasurface (PCM) designs that use asymmetric elements can achieve a phase difference of 180°, making them suitable for stealth platforms [4–5].

Metasurface-based polarization rotators have the advantage of being compact and lightweight, making them highly suitable for antenna RCS reduction [6–9]. For example, a sawtooth polarization conversion metasurface operating in the terahertz (THz) band has been proposed [6]. A PCM positioned at an appropriate height above a coil can form a Fabry-Perot cavity to enhance gain [7]. An RCS reduction of circularly polarized antennas has been achieved using circular polarization conversion electromagnetic band-gap (CPC EBG) structures [8], while an improvement to the conventional L-shaped strip in a tapered strip design has expanded the polarization rotation bandwidth of PCM units to 117.2% [9]. Moreover, the antennas developed using this method often require multi-layer structures, whereby controlling the area of the metasurface can be difficult. Several methods are proposed for broadband RCS reduction, such as a dartboard-shaped layout [10], rotated phase coding phase [11], and two-layer stacked resonance absorber [12]. Based on the hybrid mechanism metasurface of the Panchartnam–Berry phase, a 2×2 array is proposed for 2∼13 GHz low RCS in [13]. However, these unit cells need complex multilayers or large size, which limit their application in antenna array.

A novel approach for reducing the RCS of a circular polarized dipole antenna, using a miniaturized PCM, has been presented in this paper. The meander lines are applied to the arms of L-shaped strip, which can greatly reduce the resonant frequency. Electromagnetic (EM) simulation and equivalent circuit are conducted for the performance and working mechanism of miniaturized cell. A 2×2 array with circularly polarization is integrated with PCM to validate the effect of RCS reduction.

II. THEORY OF THE PCM

A. Structure of PCM cell

The detailed parameters are given in Fig. 1. The substrate is F4B with a relative dielectric constant of $\varepsilon_r = 2.2$, $\tan\delta = 0.0009$, and a height of 4 mm. When the electromagnetic wave is incident on the cell, the folded part can provide a longer current path, thus realizing the miniaturization of the cell. We use a Floquet Port to simulate a periodic arrangement of the PCM cell. The overall

Submitted On: March 10, 2024
Accepted On: March 14, 2025
https://doi.org/10.13052/2024.ACES.J.400303

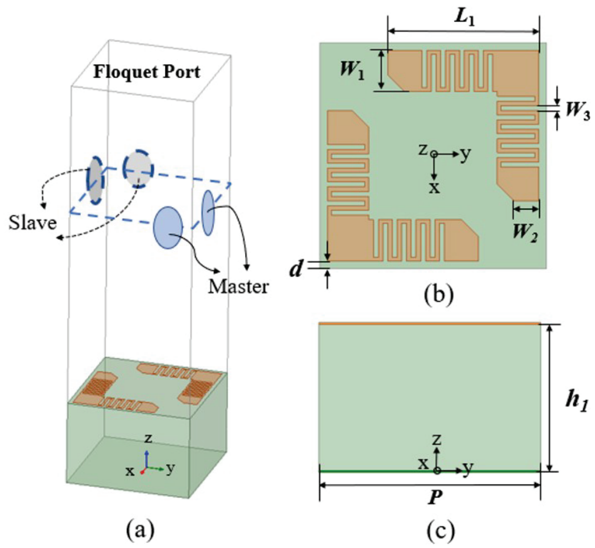

Fig. 1. Structure of the proposed PCM cell: (a) overall view, (b) top view and (c) side view.

structure was simulated and analyzed with the software of HFSS with the following optimized parameters: P=6, h_1 =4, L_1 =4, W_1 =1.1, $W_{2=}$0.44, W_3 =0.13, d=0.2, all units being in mm.

B. Design procedure

Polarization conversion ratio (PCR) is a key indicator to measure the ability of different polarization waves to be converted. It is defined as PCR=$|\Gamma_{xy}|^2/(|\Gamma_{xy}|^2+|\Gamma_{yy}|^2)$ to demonstrate the ability to convert when an y-polarized linear polarization (LP) incident wave to an x-polarized reflected wave. Here, $|\Gamma_{yy}|$ denotes the reflection coefficient of a y-polarized incident wave to a y-polarized reflected wave. Similarly, $|\Gamma_{xy}|$ denotes the reflection coefficient of a y-polarized incident wave to an x-polarized reflected wave.

The PCM cell iterative design from Model 1 to Model 4 shown in Fig. 2. A Floquet Port has been used to simulate a periodic arrangement of the models. The corresponding PCR values for each model, can be depicted from Fig. 3. Initially, Model 1 employs a L-shaped metallic strip with PCR greater than 0.9 at a narrow frequency band range of 20.1-20.9 GHz. Subsequently, another same strip is added and placed diagonally opposite the original shape. However, Model 2 exhibits a shift in the operating frequency towards lower frequencies and a resonant frequency in the PCR curve. Moreover, in the middle band, the PCR performance of Model 2 deteriorates. To address this problem, the interior of the patch is folded to create Model 3, which resonates in the middle frequency band. Although Model 3 enhances the PCR performance slightly at low and high frequencies, there is a band of poor results in the middle frequencies. Moreover, another resonant frequency occurs at 11.2 GHz. Finally, the number of times the patch is folded internally is optimized to achieve the best PCR performance for Model 4. In the entire broadband frequency range of 6.2-18.5 GHz, Model 4 exhibits excellent PCR performance, which is greater than 0.9. In particular, at four frequency points (6.6, 10.3, 16.3, and 17.7 GHz) the PCR assumes values close to 1.0, indicating that the proposed PCM achieves a phase of 90° rotation of polarization.

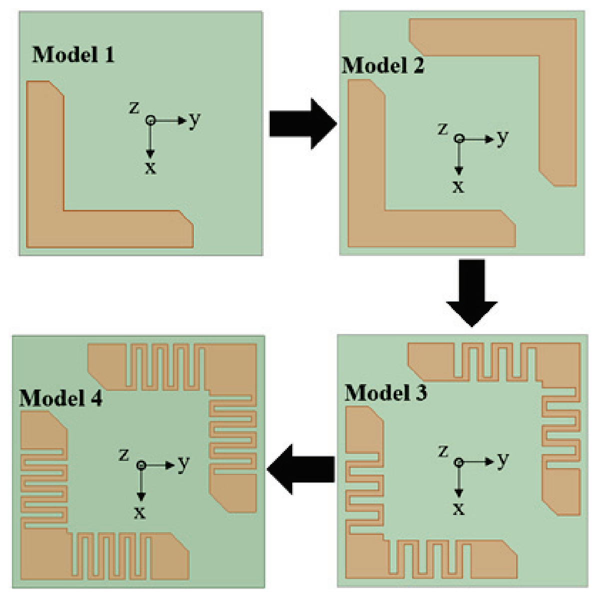

Fig. 2. Iterative design process of the PCM cell.

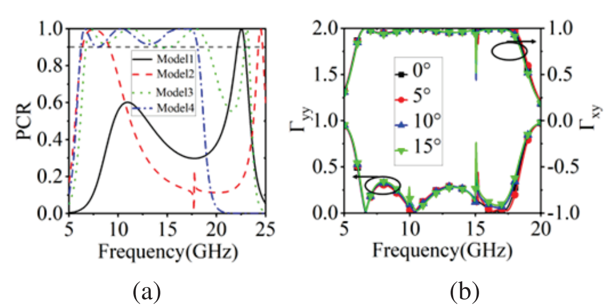

Fig. 3. Simulated performance of the PCM cell: (a) PCR of each model and (b) reflection coefficients of y-polarized incident wave.

Simulated magnitudes of the reflection coefficients $|\Gamma_{yy}|$ and $|\Gamma_{xy}|$ with y-polarized incident waves at different oblique angles are shown in Fig. 3 (b). $|\Gamma_{xy}|$ tends to deteriorate in specific frequency band as θ increases. The origins of the spikes are mainly caused by some self resonance generated by L-shaped strip with metal ground. When electromagnetic waves are obliquely incident on a cell, its folded lines no longer maintain their original inductance values; At the same time, the capacitance between the patch and the metal ground will also change. This leads to the appearance of spikes in the reflection coefficient.

C. Theoretical analysis

The L-shaped branch has two perpendicular arms that alter the polarization of the resonant electromagnetic waves on it. The anisotropy of the PCMs and the near-field variation caused by interference can be adjusted to control the polarization of the final reflected wave. Figure 4 (a) shows the electric field of an incident wave along the u-axis and v-axis directions, which can be expressed as:

$$\vec{E}^{i} = \hat{a}_u E_u^i e^{j\varphi_u} + \hat{a}_v E_v^i e^{j\varphi_v}. \tag{1}$$

The reflected wave can be expressed with reflection coefficients, where λ_u and λ_v are the reflection coefficients for the u and v axes:

$$\vec{E}_r^{i} = \hat{a}_u \lambda_u E_u^r e^{j\varphi_u} + \hat{a}_v \lambda_v E_v^r e^{j\varphi_v}. \tag{2}$$

Depending on those equations, the polarization of the incident wave will rotate by 90° when $\lambda_u = \lambda_v$ and the phase difference between the two reflected waves is $\Delta\varphi = 180°$. The reflection magnitude for the u and v axes are given in Fig. 4 (b).

To elucidate the underlying mechanism responsible for the polarization rotation (PR), the surface current distributions at the four resonant frequencies of the PCM cell are presented in Fig. 5. It is observed that the current intensity at both ends and in the middle of the two metal patches are relatively weak, whereas a strong current flows along both sides of the folding slit within the patch. Consequently, in this configuration, the folded structure can be conceptualized as a patch resonator, which establishes a current loop that induces magnetic resonance.

An equivalent circuit is constructed to explain the working mechanism of PCM, as shown in Fig. 6. The PCM is equivalent to two LC series circuits representing

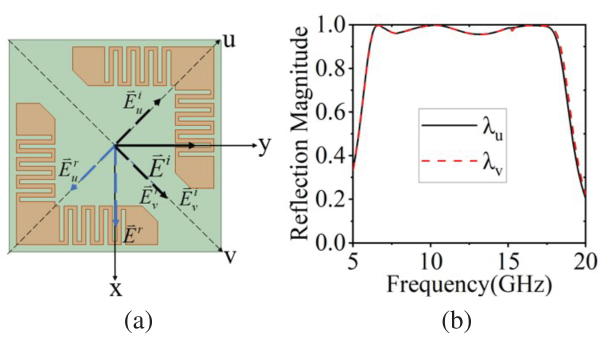

Fig. 4. PCM cell performance analysis under oblique polarization: (a) u- and v-field component and (b) reflection magnitude along u- and v-axis.

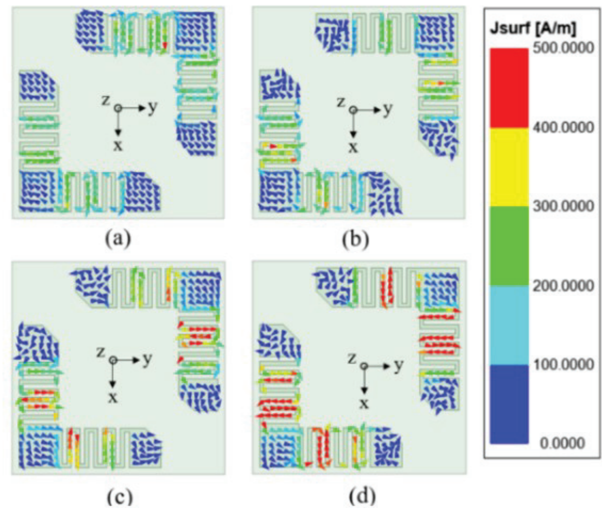

Fig. 5. Simulated surface current of the PCM unit at (a) 6.6 GHz, (b) 10.3 GHz, (c) 16.3 GHz, and (d) 17.7 GHz.

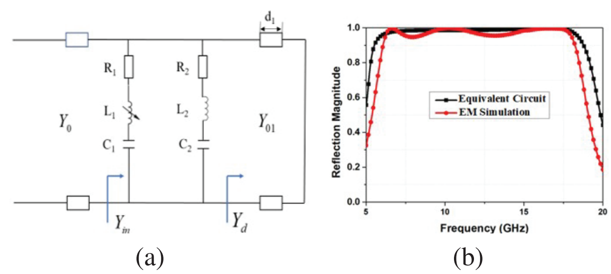

Fig. 6. Equivalent circuit of the proposed PCM: (a) circuit and (b) performance.

the metal patch and the coupling between the two metal patches. The resistance is introduced for the loss when the frequency of electromagnetic wave is not within the working frequency band . An adjustable inductor is used to represent the meander line of the L-shaped strip. The dielectric layer is represented by a transmission line with a length of d_1, and the reflector plate is represented by a short on the right. Y_0 represents the characteristic conductance of air and the reflection coefficient can be written as $\Gamma = (Y_0 - Y_{in})/(Y_0 + Y_{in})$, the conductances of two LC series circuits are labeled as Y_L, Y_{L2}, respectively. Then:

$$Y_{in} = Y_{L_1} + Y_{L_2} + Y_d, \tag{3}$$

$$Y_{L_1} = \frac{1}{R_1 + j\left(\omega L_1 - \frac{1}{\omega C_1}\right)}, \tag{4}$$

$$Y_{L_2} = \frac{1}{R_2 + j\left(\omega L_2 - \frac{1}{\omega C_2}\right)}, \tag{5}$$

$$Y_d = -jY_{01} d_1 \tan\beta. \tag{6}$$

The values of lumped elements in the equivalent circuit are given: $R_1 = 10\Omega$, $L_1 = 12.5$ nH, $C_1 = 0.076$

pF, R_2 =9Ω, L_2 = 1.02 nH, C_2 = 0.049 pF. With these parameters, the equivalent circuit is simulated with AWR Design Environment, and the corresponding results are added to Fig. 6 (b). The performance of equivalent circuits and electromagnetic simulation have good consistency throughout the entire frequency band.

III. CP DIPOLE ANTENNA ARRAY

A. Antenna element

The antenna element adopts the classic dipole with meander line arm to achieve compact size, as shown in Fig. 7. The dipole is placed above a PCM plane with 5×5 cells and supported by a F4B substrate with a height of 1 mm.

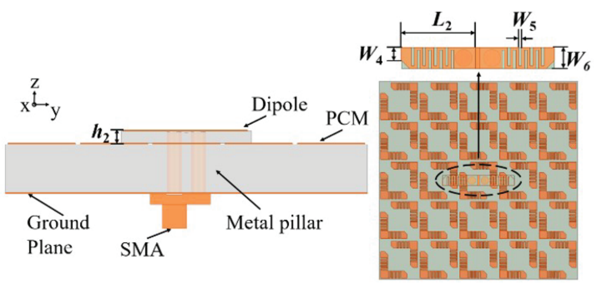

(a) (b)

Fig. 7. Structure of the antenna with PCM: (a) side view and (b) vertical view with the parameters of L_2 =5.3 mm, W_4 =0.9 mm, $W_{5=}$0.2 mm, W_6 =1.5 mm, h_2 =1 mm.

The performance of the antenna element is shown in Figs. 8 (a) and (b). The 3 dB axial ratio (AR) band covers 6.5 GHz to 7.5 GHz. The AR values within the impedance band of 6.87 to 7.35 GHz are all less than 3 dB. The antenna exhibits circular polarization characteristics throughout the band.

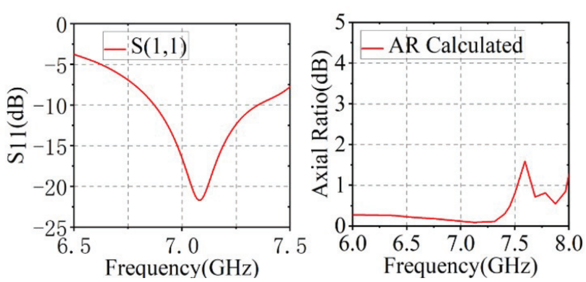

(a) (b)

Fig. 8. Simulated results: (a) reflection coefficient and (b) AR of dipole with PCM.

B. Antenna array

The four antenna units are sequentially rotated by 90° and arranged in a checkerboard configuration to form the array antenna. The reference array antenna, designated as Array 1, consists of four dipole cells that are rotated and combined as depicted in Fig. 9 (a). Each dipole is oriented in a manner that facilitates center-fed rotation, thereby enhancing circular polarization (CP) performance. The energy field from the port is evenly fed into the dipole antenna array through a one-to-four power divider as the feed network, which shares a common ground layer with the PCM plane.

The designed tessellated PCM is placed beneath the antenna to decrease its RCS. The final design structure, called Array 2, is shown in Fig. 9 (b). The structure comprises a dipole array, a substrate printed PCM coating, and a feed network. To verify the design structure, Arrays 1 and 2 were fabricated in Fig. 10 and the measured environment is shown in Fig. 11.

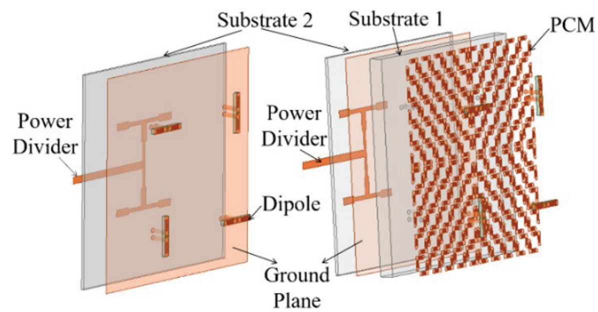

(a) (b)

Fig. 9. Exploded view of antenna array: (a) Array 1 without PCM and (b) Array 2 with PCM.

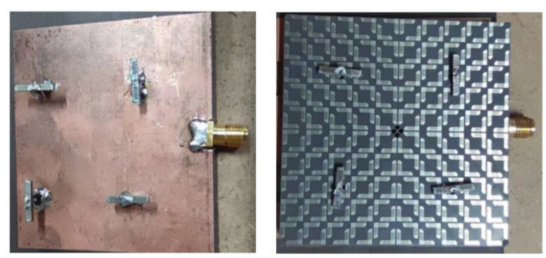

(a) (b)

Fig. 10. Photograph of antenna array: (a) Array 1 without PCM and (b) Array 2 with PCM.

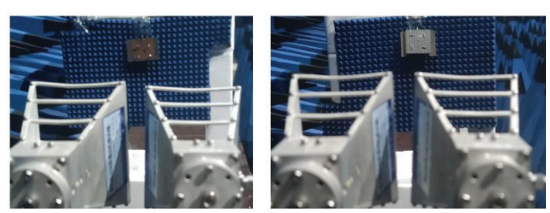

(a) (b)

Fig. 11. Measured environment of antenna array: (a) Array 1 without PCM and (b) Array 2 with PCM.

C. Simulation and measurement

To verify the performance of the proposed structure, Arrays 1 and 2 were fabricated, measured, and compared. A comparison of S11 of the simulated and measured arrays is provided in Fig. 12. It can be seen that the simulated working frequency bands of Array 1 extends from 6.85 to 7.02 GHz for $|S11| \leq$ -10 dB. The impedance bandwidth ranges from 6.82 to 7.12 GHz for Array 2. The bandwidth of the antenna is slightly broadened by addition of the PCM, due to the antenna being influenced by the surface electric field excited by the PCM. The measured bandwidth ranges from 6.86 to 7.12 GHz for Array 1 and 6.98 to 7.09 GHz for Array 2, respectively. The measured operating frequency was excursed by approximately 0.1 GHz towards the high frequencies while the trends remained constant.

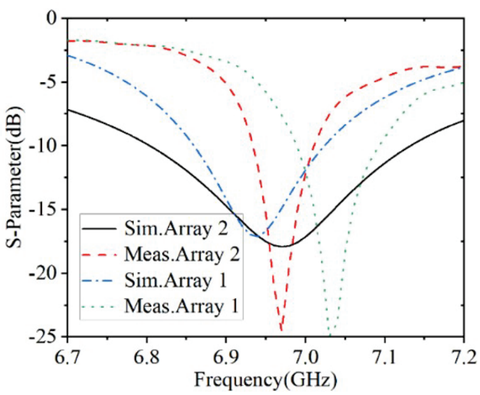

Fig. 12. Performance of Arrays 1 and 2.

Figure 13 shows the simulated and measured radiation patterns for Arrays 1 and 2 at 7.125 GHz. The simulated achieved gains are 11.356 dBi (Array 1) and 12.402 dBi (Array 2), respectively. Loading the PCM increases the gain of the ports by 1.0 dBi each. The measured actual gain is about 0.6 dBi less than the simulated gain in the XZ- and YZ-planes, respectively. This difference is mainly due to the loss of connector and manufacturing accuracy. The simulated and measured curves are in good agreement. Stable directional CP radiations with PCM coating are achieved. A high degree of isolation is achieved between the co-polarized and cross-polarized radiation on the aiming line.

Figure 14 shows the simulated and measured monostatic RCS reduction curves for Arrays 1 and 2 for x- and y-polarizations at normal incidence. The IncPWave Port of HFSS is used to simulate the general incident wave to obtain the simulation results of the metasurface. The simulated 5 dB RCS reduction scaling bandwidths for both polarizations are between 6.1 GHz and 20.7 GHz, which covers the operating band of the antenna. The measured 5 dB RCS reduction scaling bandwidths are from 6.1 GHz to 20.8 GHz and 6.2 GHz to 21.9 GHz (x-polarization) and 5.9 GHz to 20.7 GHz and 6.2 GHz to 22 GHz (y-polarization).

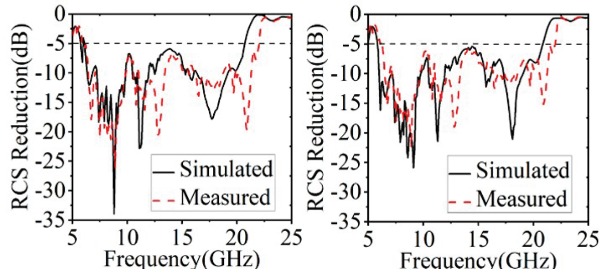

(a) (b)

Fig. 14. RCS reduction of the arrays: (a) x-polarization and (b) y-polarization.

The simulated 3D bistatic RCS of Arrays 1 and 2 at 8.0 GHz under normal incidence x-polarization wave are shown in Fig. 15. Given that the reflection amplitudes are equivalent, the phase difference between the mirror cells is 180° following the checkerboard arrangement, resulting in mutual cancellation that diminishes the scattered energy in the +z direction. Concurrently, the superpo-

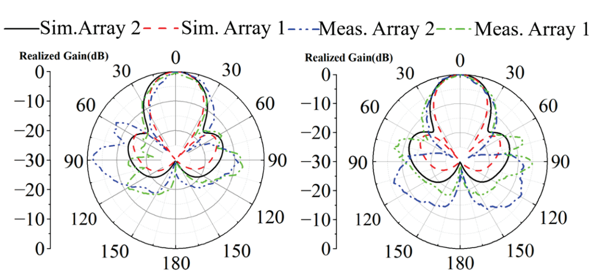

(a) (b)

Fig. 13. Simulated and measured radiation patterns: (a) XZ-plane and (b) YZ-plane at 7.125 GHz.

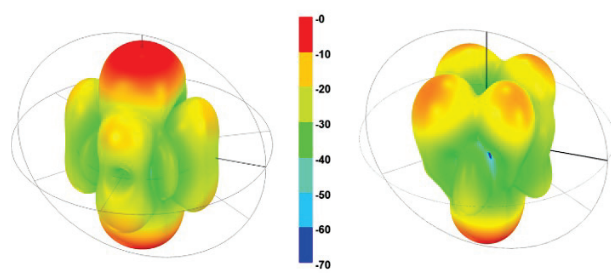

(a) (b)

Fig. 15. 3-D bistatic RCS of the array at 8 GHz under x-polarization incidence for (a) Array 1 and (b) Array 2.

Table 1: Comparison between other work and this work

Ref.	Electric Size ($\lambda_0\times\lambda_0$)	No. of PCM Unit	Impedance Matching BW (GHz)	Type of Reduction	Polarization	RCS Reduction BW (GHz)
[7]	1.41×1.41	4×4	9.5-11.6	In-band Out-of-band	Single LP	7.5-17.1 (78.0%)
[8]	0.90×0.90	4×4	4.8-7	In-band Out-of-band	CP	4.7-5.8 (21.0%)
[9]	1.76×1.76	7×7	6.06-6.75/ 6.28-6.47	Out-of-band	Dual LP	9.6-33.1(110.0%) 9.8-33.2(110.0%)
This work	**0.71×0.71**	**5×5**	**6.87-7.35**	**In-band Out-of-band**	**CP**	**6.1-20.7 (109.2%)**

sition of the reflected waves gives rise to four subdued scattering peaks.

A performance comparison between our work with other low-RCS antennas is listed in Table 1. As can be seen from the comparison, the model in reference [7] has ultra-wide impedance matching bandwidth, and its RCS reduction also reaches 78% bandwidth, but it is only applied in single-line polarization, and its electrical size is large. A miniaturized cell has been proposed and applied for RCS reduction [8]; however, its operating bandwidth is only 21%. A model with an RCS reduction bandwidth of up to 110% was proposed in [9], which demonstrated excellent working frequency band and dual line polarization operation, but the cell needs complex multilayers. The proposed antenna achieves a small size of $0.71\lambda_0\times0.71\lambda_0$ and the characteristics of miniaturization are obvious. Meanwhile, the RCS of this antenna is reduced in a broadband frequency range 6.1-20.7 GHz (109.2%) with 5 dB reduction and includes the working frequency band of the antenna.

IV. CONCLUSION

A low RCS, gain-enhanced, miniaturized CP array is presented in this paper. A folded ultra-wideband PCM is designed and applied as the coating of the array. The low-profile CP radiation is achieved through a tessellated PCM plane, which reduces the RCS of the array by 5 dB RCS in the range 6.1-20.7 GHz (109.2%). The PCM area used for the single antenna is only 30×30 mm ($0.71\lambda o\times0.71\lambda o$), a significant miniaturization feature. The performance of the array is investigated by simulation and testing.

ACKNOWLEDGMENT

This work is supported partly by "Pioneer" and "Leading Goose" R&D program of Zhejiang under contract of 2022C01119, partly by the National Natural Science Foundation of China under Contract of 62171169, partly by Project of State Key Laboratory of Millimeter Waves under contract of K202414.

REFERENCES

[1] T. Liu, X. Y. Cao, J. Gao, Q. Zheng, W. Li, and H. Yang, "RCS reduction of waveguide slot antenna with metamaterial absorber," *IEEE Trans. Antennas Propag.*, vol. 61, no. 3, pp. 1479-1484, Mar. 2013.

[2] Y. Q. Li, H. Zhang, Y. Q. Fu, and N.-C. Yuan, "RCS reduction of ridged waveguide slot antenna array using EBG radar absorbing material," *IEEE Antennas Wireless Propag. Lett.*, vol. 7, pp. 473-476, 2008.

[3] H. B. Wang, Y. J. Cheng, and Z. N. Chen, "Wideband and wide-angle single-layered-substrate linear-to-circular polarization metasurface converter," *IEEE Trans. Antenna Propag.*, vol. 68, no. 2, pp. 1186-1191, Feb. 2020.

[4] K. K. Chan, "Ultra-wide band variable linear polarization rotator with high cross-polarization discrimination for scanned beams," *IEEE International Symposium on Antennas and Propagation and USNC-URSI Radio Science Meeting (APS/URSI)*, Singapore, pp. 983-984, 2021.

[5] Meraj-E-Mustafa, R. Izhar, M. S. Wahidi, F. A. Tahir, and Q. H. Abbasi, "A broadband 90° polarization rotator metasurface," *International Conference on Microwave and Millimeter Wave Technology (ICMMT)*, Shanghai, China, pp. 1-2, 2019.

[6] Deepti, D. Gangwar, S. Singh, A. Sharma, and M. R. Tripathy, "Design of terahertz PCM and its application in polarisation conversion and RCS reduction," *IEEE Indian Conference on Antennas and Propagation (InCAP)*, Jaipur, Rajasthan, India, pp. 863-866, 2021.

[7] X. Liu, E. Wang, X. Geng, D. Yang, and Z. Yan, "Broadband RCS reduction for Fabry-Perot antenna with enhanced bandwidth using polarization conversion metasurface," *International Symposium on Antennas and Propagation (ISAP)*, Osaka, Japan, pp. 773-774, 2021.

[8] Q. Zheng, C. Guo, G. A. E. Vandenbosch, and J. Ding, "Low-profile circularly polarized array with gain enhancement and RCS reduction using polarization conversion EBG structures," *IEEE Trans. Antennas Propag.*, vol. 68, no. 3, pp. 2440-2445, Mar. 2020.

[9] J. Liu, J.-Y. Li, and Z. N. Chen, "Broadband polarization conversion metasurface for antenna RCS reduction," *IEEE Trans. Antenna Propag.*, vol. 70, no. 5, pp. 3834-3839, May 2022.

[10] W. Geng and Q. Guo, "Design of a dartboard metasurface for broadband RCS reduction," in *2023 IEEE 11th Asia-Pacific Conference on Antennas and Propagation (APCAP)*, Guangzhou, China, pp. 1-2, 2023.

[11] G.-Y. Deng, Y.-H. Zhang, H.-T. Gao, Y.-L. Shu, and G.-Q. Zhu, "A super diffuse broadband RCS reduction surface design based on rotated phase coding polarization conversion metasurfaces," *IEEE Transactions on Antennas and Propagation*, vol. 71, no. 9, pp. 7409-7417, Sep. 2023.

[12] D.-X. Song, S.-F. Wang, W.-J. Liao, and Y.-C. Hou, "Homogeneous two-layer structures for broadband and wide-angle RCS reduction," *IEEE Antennas and Wireless Propagation Letters*, vol. 22, no. 5, pp. 1074-1078, May 2023.

[13] L. Zhu, J. Sun, Z. Hao, X. Kuai, H. Zhang, and Q. Cao, "A broadband low-RCS antenna based on hybrid mechanism metasurface," *IEEE Antennas and Wireless Propagation Letters*, vol. 22, no. 5, pp. 975-979, May 2023.

Xiwang Dai was born in Caoxian, Shandong, China. He received the B.S. and M.S. degrees in electronic engineering from Xidian University, Xi'an, Shaanxi, China, in 2005 and 2008, respectively. Dai received the Ph.D. degree in electromagnetic fields and microwave technology from Xidian University in 2014. From March 2008 to August 2011, he worked at Guangdong Huisu Corporation as a manager of the antenna department. Presently, he is working at the Hangzhou Dianzi University, Hangzhou, China. His current research interests involve broadband antenna, RCS and metasurface.

Ningqi Tang was born in Yongzhou, Hunan, China. He received the B.S. degree in electronic engineering from Nanchang University, Nanchang, Jiangxi, China, in 2021. Presently, he is studying for the M.S. degree at Hangzhou Dianzi University, Hangzhou, China. His current research interests include broadband antenna and low-RCS antenna.

Ze Li was born in Wenzhou, Zhejiang, China. He received the B.S. degree in electronic engineering from Hangzhou Dianzi University Information Engineering College, Hangzhou, China, in 2023. Presently, he is studying for the M.S. degree at the Hangzhou Dianzi University, Hangzhou, China. His current research interests include transmitarray antenna and reflectarray antenna.

Wenhao Hu was born in Zoucheng, Shandong, China. He received the B.S. degree in Electronic Information Engineering from Shandong Technology and Business University, Yantai, Shandong, China, in 2022. Presently, he is studying for the M.S. degree at the Hangzhou Dianzi University, Hangzhou, China. His current research interests include MIMO antenna and array antenna decoupling.

Hui Hong received the Ph.D. degree from the College of Information Science and Electronic Engineering, Zhejiang University, Hangzhou, China, in 2007. He is currently a Full Professor at the School of Electronics and Information Engineering, Hangzhou Dianzi University, Hangzhou. His current research interests include brain-computer interface, microsystem integration and biological signal processing.

An Unknown Interference Suppression Scheme for Advanced Antenna Systems

L. T. Trang[1,2], N. V. Cuong[1], H. T. P. Thao[2], and T. V. Luyen[1]

[1]School of Electrical and Electronic Engineering
Hanoi University of Industry, Hanoi, Vietnam
tranglt@haui.edu.vn, cuongnv@haui.edu.vn, luyentv@haui.edu.vn

[2]Faculty of Electronics and Telecommunications
Electric Power University, Hanoi, Vietnam
thaohp@epu.edu.vn

***Abstract* –** An unknown interference suppression scheme for advanced antenna systems has been proposed to address critical challenges in enhancing wireless communication networks. This scheme focuses on improving beamforming capabilities and spectral efficiency while minimizing the impact of unknown interference. The ability to suppress unknown interference is achieved through a fitness function that does not rely on prior knowledge of interference characteristics. This function is designed based on the assumption that the desired signal is received through the main lobe, while interference predominantly resides in the sidelobes. By incorporating a constraint handling technique, specifically the static penalty method, the fitness function ensures that total output power is minimized only when interference power in the sidelobes is effectively reduced. Additionally, the optimization process is streamlined by reducing the number of optimization variables, focusing on uniform rectangular arrays with square element distributions. Metaheuristic algorithms, including the Binary Bat Algorithm, Binary Grey Wolf Optimization, and Binary Whale Optimization Algorithm, are applied to adaptively suppress unknown interference while reducing computational complexity. The proposed scheme significantly enhances advanced antenna systems performance by steering adaptive nulls toward unknown interference sources, ensuring robustness in dynamic wireless environments.

***Index Terms* –** Binary Grey Wolf Optimization, constraint handling techniques, static penalty method, uniform rectangular arrays, unknown interference suppression.

I. INTRODUCTION

Advanced antenna systems (AAS) are a key component of modern wireless communication networks, including 5th Generation (5G), beyond 5G, and emerging 6G technologies. These systems significantly enhance capacity, coverage, and energy efficiency. A key feature of AAS is their flexible beam control, enabled by technologies such as massive MIMO, beamforming, and adaptive antenna arrays [1]. These capabilities allow for more efficient spectrum utilization, higher throughput, and improved connectivity, all while minimizing interference. In the context of next-generation networks, AAS play a critical role in supporting ultra-reliable low-latency communications, massive machine-type communications, and enhanced mobile broadband, which are essential for deploying 5G, beyond 5G, and 6G [2].

One of the most important capabilities of AAS is their ability to precisely control beam patterns, enabling targeted signal transmission and reception. This capability enhances link quality, expands coverage, and supports higher user densities, especially in urban settings or industrial IoT applications. Additionally, AAS can dynamically adapt to changing network conditions, optimizing radiation patterns in real time to avoid interference and maximize system performance. However, as the number of antennas in these systems increases, so too does the number of optimization variables, complicating the optimization process and making it more time consuming. This presents a significant challenge, especially in real-time processing for 5G, beyond 5G, and 6G networks. Additionally, AAS continues to face substantial challenges in managing unknown interference from external sources.

In practical wireless communication environments, interference can arise from unintended sources such as co-channel transmissions, multipath effects, and external electronic devices. This interference is often unpredictable and lacks prior statistical or spatial information, making it “unknown interference”. This interference is often unpredictable in both direction and intensity,

Submitted On: December 4, 2024
Accepted On: February 27, 2025
https://doi.org/10.13052/2024.ACES.J.400304

leading to system degradation, reduced data rates, and increased latency. Traditional suppression methods assume prior knowledge of interference characteristics, limiting their effectiveness in real-world scenarios where unknown interference is common. As wireless environments grow more complex with the development of 5G, beyond 5G, and 6G, developing robust schemes for managing unknown interference is becoming increasingly critical [2, 3].

Interference suppression is a critical challenge in wireless communication, particularly in scenarios where interference characteristics are unknown. Various methods have been explored in the literature to address this issue. Known interference is typically addressed through methods like beamforming or adaptive filtering, both of which require prior knowledge of the interference source [4, 5]. For unknown interference, traditional techniques, such as blind source separation [6], have been widely used for signal extraction. Deep learning-based approaches have also gained significant attention for their ability to learn interference patterns directly from data, as discussed in [7, 8].

Recent advancements in interference suppression further extend these approaches. For instance, SlickScatter [9] introduces an interference-insensitive WiFi backscatter system that retrieves backscatter signals despite unknown ambient interference. Similarly, automatic modulation recognition techniques [10] leverage graph neural networks to classify unknown interference signals. Additionally, interference source positioning methods based on near-field scanning [11] provide effective localization of interference sources. In the context of hardware-based solutions, a 2-D MIMO receiver array [12] demonstrates autonomous spatial filtering to suppress unknown interference. Bayesian methods [13] have also been proposed to characterize unknown interference power in wireless networks, offering insights for rate adaptation. Furthermore, adaptive beamforming techniques [14] enhance robustness by iteratively placing radiation pattern nulls to suppress sidelobes and mitigate unexpected interference.

A promising scheme involves combining metaheuristic algorithms with constrained handling techniques (CHTs). Metaheuristic algorithms like Binary Bat Algorithm (BBA), Binary Grey Wolf Optimization (BGWO), and Whale Optimization Algorithm (BWOA) have shown promise in optimizing beamforming parameters, particularly in the presence of unknown interference. BBA, inspired by the echolocation behavior of bats, is known for its rapid exploration of the scheme space, offering quick convergence during early optimization stages [15, 16]. However, it can struggle to balance exploration and exploitation in more complex environments [17]. BWOA, which mimics the hunting strategies of humpback whales, excels in fine-tuning schemes and thoroughly exploring the search space, although it may take longer to fully converge [18]. BGWO, modeled after the social behavior of grey wolves during hunting, offers a balanced approach to exploration and exploitation, making it well-suited for complex, multi-dimensional optimization problems [19]. By leveraging the strengths of BBA, BGWO, and BWOA, combined with CHTs, a scheme can be achieved for beamforming, minimizing sidelobe levels (SLL), placing nulls in interference directions, and optimal resource allocation in the presence of both known and unknown interference [20].

This paper proposes a scheme for suppressing unknown interference in AAS without requiring prior knowledge of interference characteristics. The scheme achieves this by constructing a fitness function that minimizes total output power while ensuring that desired signals remain unaffected. This function is formulated using a constraint handling technique, specifically the static penalty method (SPM), which effectively suppresses interference residing in the sidelobes. To enhance computational efficiency, the scheme integrates metaheuristic algorithms with CHTs, optimizing interference suppression while minimizing the number of optimization variables in uniform rectangular arrays (URA). This reduces search time and complexity, making the approach particularly suitable for advanced communication networks, including 5G, beyond 5G, and emerging 6G technologies.

II. CONSTRAINED HANDLING TECHNIQUES AND CONSTRAINED OPTIMIZATION PROBLEMS

A. Constrained handling techniques

CHTs are a set of methods designed to address optimization problems where constraints must be satisfied while optimizing an objective function. CHTs play a critical role in ensuring that schemes meet predefined constraints, making them indispensable in solving constrained optimization problems. Their primary advantage lies in their ability to guide the optimization process towards feasible regions of the search space, avoiding schemes that violate the constraints. By balancing the search space exploration with the adherence to constraints, CHTs enhance the reliability and practicality of optimization outcomes, particularly in complex, multi-dimensional problem domains. The significance of CHTs is further amplified when dealing with constrained optimization problems, where schemes must not only maximize or minimize an objective function but also stay within the defined boundaries of the problem. These techniques are particularly useful in non-convex or discontinuous scheme spaces, where finding feasible schemes is challenging. CHTs encompass a range of approaches, from simple penalty methods, which impose costs for constraint violations, to more sophisticated techniques, like stochastic ranking and adaptive penalty methods, that dynamically adjust their behavior to meet the problem's constraints.

CHTs become even more crucial when applied to AAS due to the unique challenges these systems face. AAS requires precise control over beamforming patterns and interference mitigation while adhering to strict physical and operational constraints, such as maintaining the desired beam shape, minimizing SLLs, and steering nulls towards interference sources. These requirements naturally lead to constrained optimization problems where the goal is to optimize beamforming parameters without violating the system's constraints.

To address these challenges in AAS, four of the most commonly used CHTs in the literature are: (i) penalty methods, (ii) feasibility rules, (iii) the ε-constrained method, and (iv) stochastic ranking. Each of these techniques offers a unique way of handling constraints during the optimization process. Among these, objective function penalization stands out as the most traditional and widely employed approach. This method transforms a constrained problem into an unconstrained one by adding penalty terms to the objective function. The idea is to penalize schemes that violate constraints, making the optimization algorithm less likely to explore infeasible regions. Over time, various penalty-based methods have evolved, including static, dynamic, adaptive, and death penalty techniques, each tailored to handle different levels of problem complexity and optimization goals [21].

In summary, CHTs provide a powerful framework for solving the constrained optimization problems encountered in AAS, ensuring that both performance and constraint compliance are achieved. This makes them essential for the effective design and operation of advanced wireless communication networks, especially as these networks evolve into 5G, 5G beyond, and 6G systems.

B. Constrained optimization problems

A constrained optimization problem typically involves finding an optimal scheme to an objective function subject to a set of constraints. The general form of a constrained optimization problem can be expressed as [22]:

$$\begin{aligned} \text{minimize} \quad & f(\mathbf{x}): \\ & g_j(\mathbf{x}) \leq 0,\ j = 1,2,...,j \\ \text{subject to} \quad & h_k(\mathbf{x}) = 0,\ k = 1,2,...,K, \\ & x_i^l \leq x_i \leq x_i^u,\ i = 1,2,...,n \end{aligned} \tag{1}$$

where:

- $f(\mathbf{x})$: objective function concerning the vector variable $\mathbf{x}$
- $g_j(\mathbf{x})$: inequality constraints
- $h_k(\mathbf{x})$: equality constraints
- x_i^l, x_i^u represents the lower and upper limit values, respectively, of component x_i in $\mathbf{x}$.

In this article, SPM is applied, and then the constrained optimization problem (1) is transformed into an unconstrained optimization problem (2).

In the static penalty approach outlined by [23], the penalty coefficient escalates as the level of violation increases, as noted in [24]. Although the penalty functions remain unchanged, a static penalty function is proposed that adapts the static penalty parameter based on the severity of violations, as discussed in [25]. In the context of the static penalty function presented in [26], a constrained problem defined in (1) is converted into a non-constrained form:

$$Minimize\ \{f(\mathbf{x}) + \xi v(\mathbf{x})\}, \tag{2}$$

where $\xi v(\mathbf{x})$ presents a penalty term.

Inspired by the optimization in (2), the fitness function of the optimization in this study is defined as:

$$F(\mathbf{x}, \xi) = f(\mathbf{x}) + \xi v(\mathbf{x}). \tag{3}$$

In this context, each unmet constraint affects $\mathbf{x}$ by imposing a penalty equal. These penalties are aggregated and multiplied by ξ, the penalty parameter, which is then balanced against $f(\mathbf{x})$. Therefore, if the magnitude of the penalty term is minor compared to that of $f(\mathbf{x})$, it is highly likely that minimizing $F(\mathbf{x}, \xi)$ will not yield a feasible $\mathbf{x}$ for the original problem. Conversely, if ξ is sufficiently large, the penalty for any constraint violation will be substantial enough that minimizing the fitness function will lead to a feasible scheme.

Metaheuristic algorithms, such as BBA, BGWO, and BWOA, are particularly well-suited for solving complex constrained optimization problems. These algorithms efficiently explore the scheme space, making them potential candidates for optimizing AAS where multiple constraints need to be satisfied [22].

CHT transforms constrained optimization problems into single-objective optimization problems. By integrating penalty terms into the fitness function, metaheuristic algorithms can focus on optimizing a single criterion, such as interference suppression, while ensuring that the constraints are satisfied. This approach is particularly useful in AAS, where optimizing beamforming requires balancing multiple conflicting objectives.

III. PROBLEM FORMULATION

This paper examines URA, a type of uniform planar array of half-wavelength dipoles as shown in Fig. 1. The antenna array pattern can be represented as:

$$\begin{aligned} P(\theta,\phi) &= EF(\theta,\phi) AF(\theta,\phi) \\ &= EF(\theta,\phi) \sum_{m=0}^{M-1} \sum_{n=0}^{N-1} w_{m,n} e^{j\left(m\psi_z + n\psi_y\right)}, \end{aligned} \tag{4}$$

where:

- EF and AF are the element factor and the array factor of the dipole (θ,ϕ), respectively.

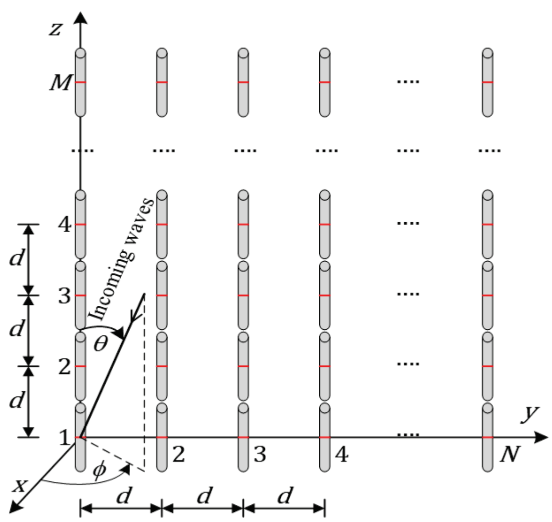

Fig. 1. Uniform rectangular array with $M \times N$elements.

- $EF(\theta,\phi) = \frac{\cos\left(\frac{\pi}{2}\cos(\theta)\right)}{\sin(\theta)}$,
- $\psi_z = \kappa d_z \cos(\theta); \psi_y = \kappa d_y \sin(\theta)\sin(\phi); \kappa = 2\pi/\lambda$;
- $w_{m,n} = a_{m,n} e^{j\delta_{m,n}}$ is the complex weight of the $(m,n)^{th}$ element, where $a_{m,n}$ and $\delta_{m,n}$ are the amplitude and the phase, respectively.

The main lobe can be steered towards the direction (θ_0,ϕ_0) by setting the phase shift of the $(m,n)^{th}$ antenna element as:

$$\delta_{m,n} = -\kappa\left(md_z\cos(\theta_0) + nd_y\sin(\theta_0)\sin(\phi_0)\right). \quad (5)$$

The array pattern for URAs can be expressed in the matrix form as:

$$P(\theta,\phi) = EF(\theta,\phi)\,\mathbf{s}(\theta,\phi)\,\mathbf{w}, \quad (6)$$

where:

- steering vector is expressed as:
$$\mathbf{s}(\theta,\phi) = \left[e^{j\left(m_0\psi_z + n_0\psi_y\right)}, \ldots, e^{j\left(m_{M-1}\psi_z + n_{N-1}\psi_y\right)}\right], \quad (7)$$
- optimal weight vector is expressed as:
$$\mathbf{w} = \left[w_{0,0}, \ldots, w_{M-1,N-1}\right]^T. \quad (8)$$

To achieve the desired array pattern with K nulls in the interference directions (θ_k,ϕ_k), the problem with respect to $\mathbf{w}$ can be formulated as (variable $\mathbf{w}$ corresponds to the variable $\mathbf{x}$ in section II):

$$\begin{aligned} \max_{w} \quad & P(\mathbf{w},\theta_0,\phi_0) \\ \text{s.t.} \quad & P(\mathbf{w},\theta_k,\phi_k) = 0 \qquad \forall k = 1,\ldots,K. \end{aligned} \quad (9)$$

IV. PROPOSED SCHEME

In this study, we propose an unknown interference suppression scheme in AAS, specifically for URAs. The scheme focuses on two main improvements. First, we reduce the number of optimization variables, which shortens the computational time, an important factor in optimizing the efficiency of AAS. Second, we apply CHT, specifically the SPM, to enforce constraints on beam pattern shaping and null placement in interference directions. This helps simplify the optimization process, thereby improving the overall performance of AAS.

Improvement 1: Minimize the number of variables that need to be optimized (consider the array containing elements distributed in a square). This improvement focuses on reducing the number of variables that need to be optimized, specifically in arrays with square element distributions. The goal is to simplify the optimization process, which is crucial for improving computational efficiency in AAS.

Algorithm 1: The algorithm determines the optimal weights while reducing the number of phase variables in the optimization search.

1: **Input:**

2: Number of antennas in z-axis M and y-axis N. The array contains elements arranged in a square configuration, so $M = N$

3: Binary schemes $\mathbf{s}_{\text{bin}}$ from metaheuristics algorithms

4: Resolution of phase shifters N_{bits}

5: **Operation:**

6: Determine the binary scheme of an individual in metaheuristic algorithms. The number of binary bits in the ith variable, $s_{\text{bin},i}$ with $i = 1,\ldots,M$, represents the number of phase shifts for an N_{bits} phase shifter

$$\mathbf{s}_{\text{bin}} = \left[s_{\text{bin},1},\ldots,s_{\text{bin},M}\right]^T. \quad (10)$$

7: Convert the binary scheme to a real number. In this paper, the number of binary bits in the variable $s_{\text{bin},i}$ is set to 1, and N_{bits} is set to 5:

$$\mathbf{s}_{\text{o}} = \left[s_1,\ldots,s_M\right]^T = \frac{\text{bin2dec}(\mathbf{s}_{\text{bin}})}{2^{N_{bits}} - 1}. \quad (11)$$

8: Determine the phase of elements on the z-axis and y-axis based on odd symmetry characteristics:

9: If M and N are even, then:

$$\begin{aligned}\boldsymbol{\delta}_y &= \left[s_1, \ldots, s_{M/2}, -s_{M/2}, \ldots, -s_1\right]^T \\ \boldsymbol{\delta}_z &= \left[s_{M/2+1}, \ldots, s_M, -s_M, \ldots, -s_{M/2+1}\right]^T\end{aligned}. \quad (12)$$

10: If M and N are odd, then:

$$\begin{aligned}\boldsymbol{\delta}_y &= \left[s_1, \ldots, s_{M/2}, 0, -s_{M/2}, \ldots, -s_1\right]^T \\ \boldsymbol{\delta}_z &= \left[s_{M/2+1}, \ldots, s_M, 0, -s_M, \ldots, -s_{M/2+1}\right]^T\end{aligned}. \quad (13)$$

11: Perform the outer sum operation to determine the phase for all elements in the URAs:

$$\boldsymbol{\delta}_{yz} = \mathrm{vec}\left(\boldsymbol{\delta}_y \oplus \boldsymbol{\delta}_z\right), \quad (14)$$

where:

- $\oplus$ the outer sum combines row and column positions to calculate the phase for each antenna in the URA.

12: The optimal phase based on the reference phase, for example, the phase of the weights when steering the main beam, is determined as:

$$\boldsymbol{\delta}_{\mathrm{o}} = \boldsymbol{\delta}_{yz} + \boldsymbol{\delta}_{\mathrm{ref}}. \quad (15)$$

13: Optimal weights when reducing the number of phase variables to be searched:

$$\begin{aligned}\mathbf{w}_{\mathrm{o}} &= \mathbf{a}_{\mathrm{ref}} \odot e^{j\boldsymbol{\delta}_{\mathrm{ref}}} \odot e^{j\boldsymbol{\delta}_{yz}} \\ &= \mathbf{w}_{\mathrm{ref}} \odot e^{j\boldsymbol{\delta}_{yz}} = \mathbf{a}_{\mathrm{ref}} \odot e^{j\delta_{\mathrm{o}}}\end{aligned}, \quad (16)$$

where:

- $\mathbf{w}_{\mathrm{o}}$ is optimal weight
- $\mathbf{a}_{\mathrm{ref}}$ is the array response vector corresponding to a specific reference direction. It represents the antenna array's response to a signal arriving from that direction.
- $\odot$ is the Hadamard product.

14: **Output:**

15: Optimal weight coefficients: $\mathbf{w}_{\mathrm{o}}$.

Improvement 2: Using CHT, specifically the SPM, to construct the fitness function in the optimization process.

If the main lobe is steered toward (ϕ_0, θ_0), most of the high-magnitude sidelobes occur at $(\phi = [-180^\circ : 180^\circ], \theta = \theta_0)$ and $(\phi = \phi_0, \theta = [0^\circ : 180^\circ])$. Nulls can be positioned freely in 3D space, but interferences that occur in high-power sidelobes are the most problematic. Therefore, this paper assumes that interferences arise at $(\phi = [-90^\circ : 90^\circ], \theta = \theta_0)$.

Therefore, the term $f(\mathbf{w})$ utilized for maintaining the desired main lobe is represented as:

$$f(\mathbf{w}) = \sum_{\phi=\phi_0-\phi_{\mathrm{FNBW}}/2}^{\phi_0+\phi_{\mathrm{FNBW}}/2} \left|P_{\mathrm{o}}(\mathbf{w}, \theta_0, \phi) - P_{\mathrm{ref}}(\mathbf{w}, \theta_0, \phi)\right|^2$$

$$+ \sum_{\theta=\theta_0-\theta_{\mathrm{FNBW}}/2}^{\theta_0+\theta_{\mathrm{FNBW}}/2} \left|P_{\mathrm{o}}(\mathbf{w}, \theta, \phi_0) - P_{\mathrm{ref}}(\mathbf{w}, \theta, \phi_0)\right|^2, \quad (17)$$

where:

- $P_{\mathrm{ref}}(\mathbf{w}, \theta_0, \phi)$ and $P_{\mathrm{o}}(\mathbf{w}, \theta_0, \phi)$ correspond to the reference pattern and the optimized patterns using metaheuristic algorithms, respectively.
- θ_{FNBW} and ϕ_{FNBW} correspond to the elevation and azimuth angles at the first null beamwidth (FNBW).

Generally, both the desired signal and interference sources reach the receiving arrays simultaneously. The desired signal is assumed to enter through the main lobe, whereas interference is distributed across the sidelobes. To effectively suppress unknown interference without requiring prior knowledge, we design the fitness function based on total output power minimization. This function incorporates a CHT, specifically the SPM, which ensures that only interference power is minimized while maintaining the main lobe for the desired signal. The term $v(\mathbf{w})$ is formulated to impose nulls in interference directions by leveraging the total received power across all antenna elements. Since the interference resides in the sidelobes, the algorithm adaptively adjusts weights to minimize interference impact while preserving signal integrity. This enables robust suppression of unknown interference, making the scheme effective even in scenarios with unpredictable interference sources.

The term $v(\mathbf{w})$, used to impose nulls in the directions of interference, is defined by the total output power of all received signals including both the desired signal and interference. The output power is computed by summing the product of signal weights and the magnitude of the array pattern in the directions of the desired $(\theta_0, \phi_0)$and interfering signals [27]:

$$v(\mathbf{w}) = \frac{1}{\sum|\mathbf{w}|} \sum_{k=1}^{K} \left|sig_k P_{\mathrm{o}}(\mathbf{w}, \theta_k, \phi_k)\right|^2, \quad (18)$$

where:

- sig_k: signal strength,
- $P_{\mathrm{o}}(\mathbf{w}, \theta_k, \phi_k)$ is the pattern for k^{th} signal,
- K is the total number of incoming signals.

Thus, the fitness function for addressing the unconstrained problem can be expressed as:

$$F(\mathbf{w}, \xi) = \frac{f(\mathbf{w})}{\xi} + v(\mathbf{w}). \quad (19)$$

The optimization algorithm used to illustrate the proposed scheme is based on the BGWO algorithm. The flowchart of the proposed scheme to improve unknown interference suppression in AAS, particularly for URAs, is shown in Fig. 2. This scheme combines two key improvements: minimizing optimization variables to reduce computational complexity and integrating CHT, specifically SPM, to improve interference rejection. The stopping criteria for the BGWO algorithm are defined by reaching the maximum number of iterations.

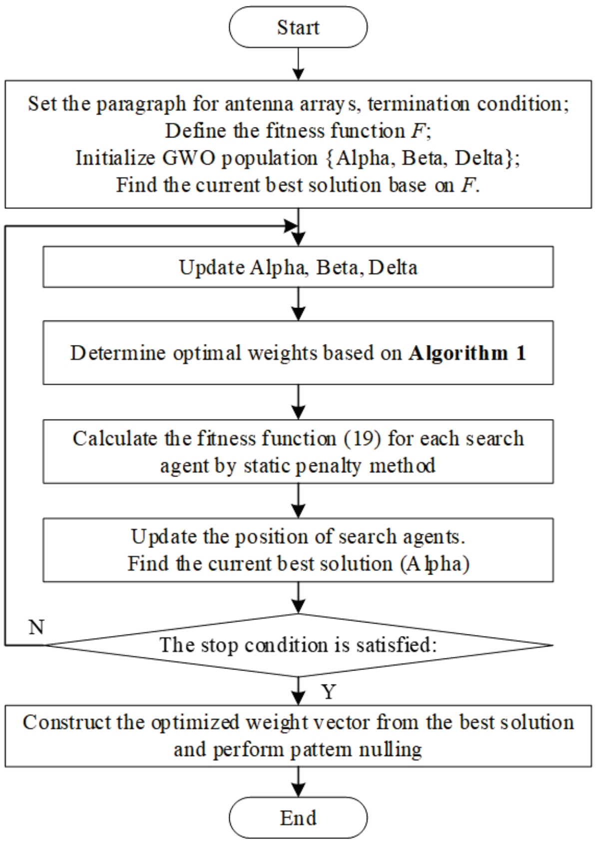

Fig. 2. Flowchart of the proposed scheme to improve unknown interference suppression.

Below is a description of how to improve unknown interference suppression in AAS, particularly for URAs.

Initialize:

- The initial setup involves defining input data such as the number of array elements, the population size, the penalty factor, assumed direction of arrival of interferences, stopping condition (or maximum number of iterations), and the radiation pattern of the array elements.
- Define the objective function $f(\mathbf{w})$ from (17) and the term $v(\mathbf{w})$, used to impose nulls in the directions of interference, from (18), in which the array pattern is computed according to (4).
- Mapping solutions (sets of weights) to locations of wolves in the population during the optimization process.

Find the weight vector with reduced phase variables:

After updating the positions of the Alpha, Beta, and Delta wolves, Algorithm 1 is implemented as described in Improvement 1.

Calculate fitness function by CHTs:

The fitness function, utilizing the SPM, is detailed in Improvement 2.

Find the best solution based on BGWO:

The beamformer iteratively computes and explores the current optimal solution using the BGWO. The process persists until the termination criterion is satisfied. Subsequently, the final optimal solution is acquired.

Construct of array element weights:

The beamformer establishes the corresponding weights for each URAs element based on the optimized solution. Pattern nulling is performed using these weights.

V. NUMERICAL RESULTS AND DISCUSSION

To assess the effectiveness of the proposed unknown interference suppression scheme, three metaheuristic algorithms were employed: BBA, BGWO, and BWOA. Among these, BGWO was selected as the primary optimization algorithm due to its well-balanced exploration and exploitation capabilities in complex search spaces. The simulations were conducted on three distinct scenarios to evaluate the unknown interference suppression performance of the proposed scheme for AAS.

The parameter setup for the simulations is as follows. The population size is set to 50, with a maximum of 30 iterations. The URA has dimensions of $M = N = 11$, with SLL constraint of -25 dB. The angle step size is 0.5 degrees. Additionally, the number of phase bits for optimization is set to 5, and the penalty factor is 10. The signal-to-interference ratio of the k-th interference is -30 dB. The results across all scenarios represent the average values of 100 independent simulations. These simulation results are detailed in the following sections, where each scenario is discussed along with the corresponding parameters and findings.

A. Effect of penalty parameter

In this scenario, we evaluate the impact of the penalty parameter on the performance of unknown interference suppression. The objective is to assess how different penalty values affect the suppression of interference at the desired angle $\theta = 25°$, while also considering related factors such as null depth level (NDL) and SLL. Simulation results with the BGWO algorithm show:

Figure 3: The plot illustrates the NDL at 25° as a function of the penalty parameter ξ for four signal-to-interference ratios (SIR): 0 dB, -10 dB, -20 dB,

and -30 dB using the BGWO algorithm. At 0 dB SIR, the NDL stabilizes around -20 dB when the penalty ξ reaches approximately $1e4$, indicating consistent nulling performance with minimal sensitivity to the penalty parameter. In contrast, at -10 dB SIR, the NDL initially remains high but drops significantly as the penalty increases, reaching approximately -35 dB when the penalty ξ reaches approximately $1e5$, suggesting enhanced nulling depth with increasing penalty values. For -20 dB SIR, the NDL follows a similar trend but starts at a lower level, quickly decreasing to around -45 dB when the penalty ξ reaches approximately $1e2$, demonstrating that higher penalties significantly improve nulling performance under moderate interference. At the most challenging SIR level of -30 dB, the NDL begins near 0 dB and declines steeply as the penalty parameter rises, reaching about -50 dB when the penalty ξ reaches approximately $1e1$. These results indicate that increasing the penalty parameter enhances the interference suppression capability of the system, especially under severe interference conditions, with progressively deeper nulls observed at lower SIR levels. Penalty plays a crucial role in optimizing the trade-off between exploration and exploitation, resulting in better interference suppression, particularly under high interference conditions.

Figure 4: The graph illustrates the relationship between the maximum SLL and the penalty ξ for different SIR levels (0 dB, -10 dB, -20 dB, -30 dB) using the BGWO algorithm. For $SIR = 0$ dB, SLL initially increases but stabilizes around -19 dB when the penalty ξ reaches approximately $1e4$. For $SIR = -10$ dB and -20 dB, SLL also initially rises but stabilizes near -20 dB, respectively, when the penalty ξ is around $1e3$. For $SIR = -30$ dB, SLL remains constant at -20 dB when the penalty ξ is around $1e1$. These results show that the BGWO algorithm maintains stable control over the SLL as penalty ξ increases, but there is no significant improvement in reducing SLL as SIR decreases. SLL tends to decrease as the penalty ξ increases under high interference conditions, but it reaches a stable value after a certain threshold. This suggests that an optimal penalty ξ value is needed to balance between interference suppression and SLL control.

While ξ has a noticeable positive effect on reducing NDL and improving interference suppression, its effect on SLL is more stable. The SLL only slightly changes with increasing ξ and does not decrease much after reaching its threshold. Therefore, increasing ξ tends to improve interference suppression without significantly impacting SLL. The results show a clear correlation between penalty values and interference suppression performance. Therefore, to achieve a balanced trade-off, a penalty value of 10 will be selected for the remaining scenarios.

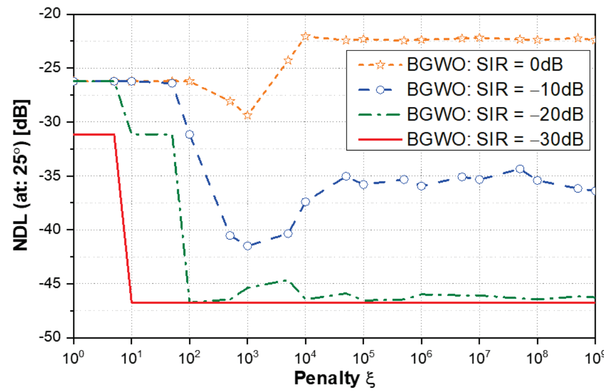

Fig. 3. NDL at 25° with different ξ values.

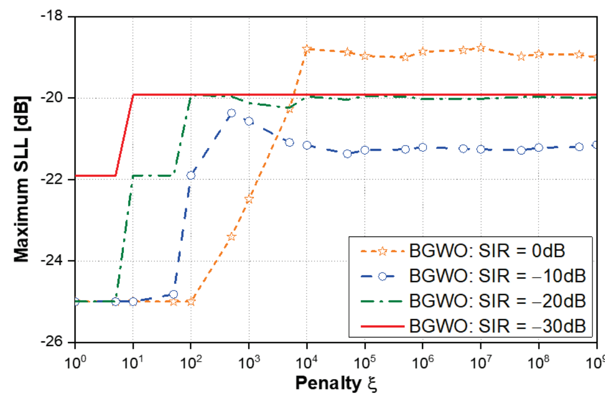

Fig. 4. Maximum SLL with different ξ values.

B. Convergence characteristics

In this scenario, we evaluate the convergence speed of the BGWO algorithm and compare it with other binary metaheuristic algorithms by adaptively imposing nulls when an interference emerges at $\theta = 25°$. The three figures below provide insights into the performance of the algorithms in suppressing unknown interference.

Figure 5: The convergence characteristics of the fitness function over iterations for various population sizes using the BGWO algorithm reveal distinct patterns. With a population size of 10, the algorithm begins at a high initial fitness value, followed by a rapid decline and gradual convergence around iteration 20. Increasing the population size to 30 results in faster convergence, with stability achieved by iteration 10, while a population of 50 follows a similar pattern, stabilizing shortly after iteration 10. For a population size of 100, convergence occurs slightly more slowly, yet it reaches the same fitness level by iteration 5, as seen in larger populations.

The fitness value's rapid decline with iteration count highlights the BGWO algorithm's ability to converge swiftly towards an optimal scheme. Larger populations, specifically sizes 50 and 100, exhibit greater stability during convergence, with minimal oscillation after reaching a plateau. In contrast, smaller populations such as 10 converge more gradually and show pronounced oscillation in the early iterations, although they ultimately attain comparable fitness levels to larger populations.

Beyond iteration 5, all population sizes converge to similar fitness values, indicating that increasing the population size beyond a certain threshold yields limited gains in solution quality. However, larger population sizes contribute to faster and more stable early convergence, underscoring their advantage in initial stabilization.

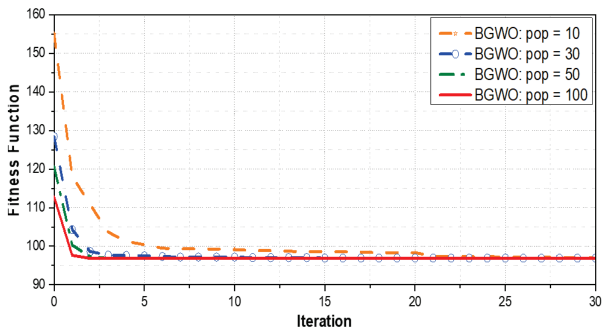

Fig. 5. Convergence of fitness function with different population sizes using BGWO.

Figure 6: Based on the provided graph, we can observe a comparison between the BBA, BWOA, and BGWO algorithms in terms of the convergence of the fitness function over iterations.

- **BBA:** Starts with a higher fitness value compared to the other two algorithms but decreases quickly in the first few iterations and gradually converges to a stable state around iteration 10.
- **BWOA:** Exhibits a faster initial decline than BBA and reaches a stable state around iteration 10.
- **BGWO:** Similar to BWOA, BGWO drops rapidly and reaches stability fairly early, around iteration 5. BGWO seems to converge faster and achieves the lowest fitness value among all the algorithms.

All algorithms show a sharp decline in fitness values during the initial iterations, but BGWO demonstrates the fastest and most stable convergence compared to BBA and BWOA. After around iteration 5 – 10, all algorithms reach similar convergence levels; however, BGWO shows an advantage in terms of both speed and early stability. This suggests that BGWO could be the

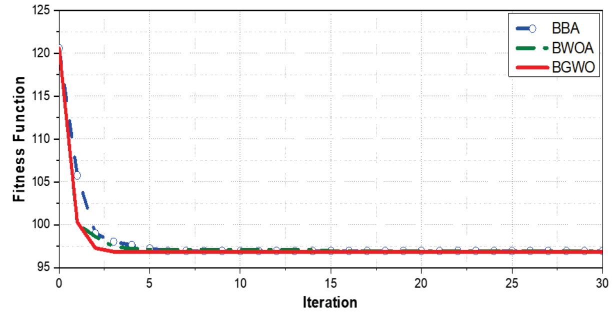

Fig. 6. Comparison of SPM fitness functions based on three different optimization algorithms.

more efficient algorithm for optimizing the fitness function with fewer iterations compared to BBA and BWOA.

Figure 7: The graph compares the convergence of the fitness function between two versions of the BGWO algorithm: with and without optimal variable number minimization.

- **BGWO with optimal variable number minimization:** convergence speed is faster, with the fitness function rapidly decreasing from the first iterations and reaching a stable value after approximately 3 iterations. The fitness function converges to a lower and more stable level compared to the method without variable number minimization.
- **BGWO without optimal variable number minimization:** convergence speed is slower, requiring more iterations to achieve a lower fitness value. It takes more than 10 iterations to approach convergence, and the decrease in the fitness function is more gradual compared to the method with variable number minimization.

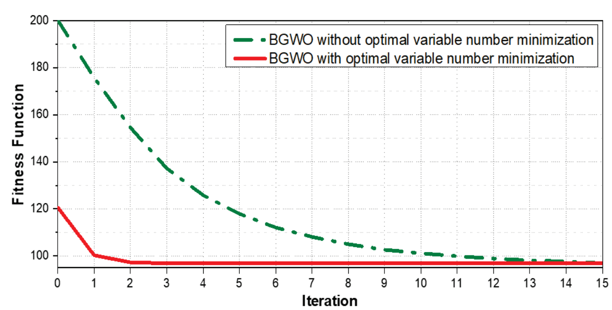

Fig. 7. Comparison of fitness function of SPM based on BGWO with and without optimal variable number minimization.

The comparison shows that the BGWO method with optimal variable number minimization demonstrates better performance in terms of convergence speed and optimal scheme quality. This indicates that reducing the number of variables during optimization can enhance the algorithm's performance, achieving better results in a shorter time.

C. Adaptive null-steering capability

This scenario illustrates the beamformer's adaptive null-steering capability through the use of BBA, BWOA, and BGWO optimization algorithms based on the SPM. The population size is configured to 50, and the maximum iteration limit is set to 3. Figure 8 illustrates the optimized radiation patterns, assuming an interference emerges within a broad null from $\phi = 30°$ to $41°$, while steering the main lobe towards $\theta = 90°$ and $\phi = 5°$. The optimized patterns generated by BBA, BWOA, and BGWO based on SPM retain most of the characteristics of the Chebyshev pattern, including a half-power beamwidth of 6.4° and SLL of -25 dB, except for the maximum SLL of -19.3 dB and a wide null range from 30° to 41°. NDL reaches a minimum of approximately -33 dB for the BGWO, BBA, and BWOA patterns. The CDF (cumulative distribution function) plot of SLL between the Chebyshev -25 dB method and BGWO in Fig. 9 highlights these results, with the BGWO curve showing lower SLL values compared to the Chebyshev method for most SLL values. This indicates that BGWO reduces the SLL comparable to the Chebyshev -25 dB method in certain scenarios. From Fig. 9, it can be seen that the BGWO method not only optimizes the SLL but also reduces the interference levels to deeper negative values.

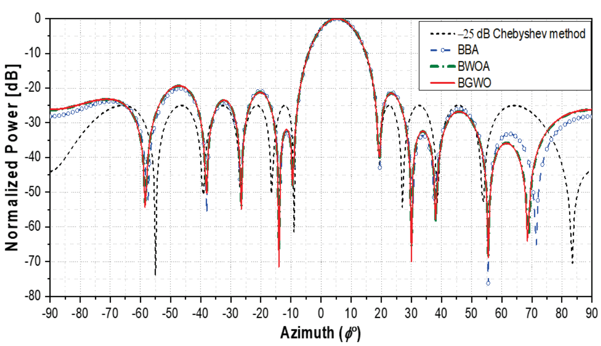

Fig. 8. Adapted patterns with a broad null when steering the main lobe.

To further evaluate the impact of SLL constraint on beamforming performance, we generated optimized radiation patterns with different SLL constraints, as shown in Fig. 10. The results demonstrate that when the SLL constraint is set to -25 dB, the proposed method effectively suppresses unknown interference while maintaining a narrow half-power beamwidth. When the constraint is further reduced to -30 dB, -32 dB, and -34 dB, suppression capability remains effective but the half-power beamwidth increases accordingly. This trade-off

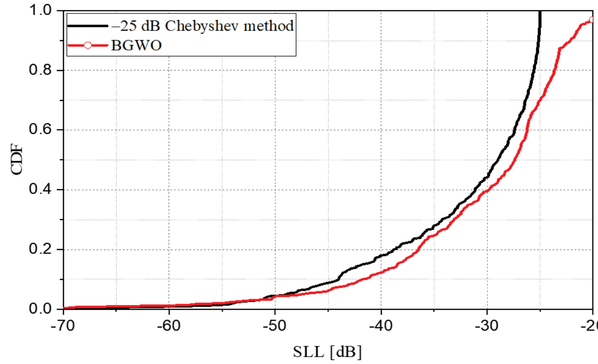

Fig. 9. CDFs of SLLs for cases of BGWO with SPM and a broad null from $\phi = 30°$ to $41°$.

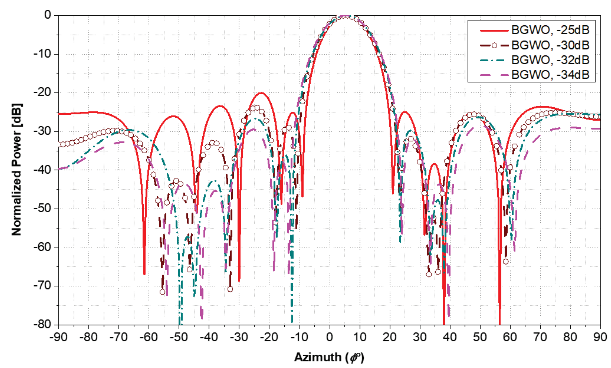

Fig. 10. Optimized radiation patterns with different SLL constraints (-25 dB, -30 dB, -32 dB, and -34 dB).

occurs because a deeper SLL constraint forces the optimization process to limit sidelobes more strictly, which in turn affects main lobe shaping. Additionally, due to the structural properties of Algorithm 1, the phase matrix in the optimization process exhibits odd symmetry, leading to a slight increase in SLL at the symmetric direction of the interference source. However, this effect is minimal and does not degrade the interference suppression capability of the proposed method.

Table 1 presents convergence times for the three algorithms BGWO, BWOA, and BBA, measured over 1000 Monte Carlo runs on MATLAB Online using an Intel(R) Xeon(R) CPU @ 2.20 GHz. Results show that

Table 1: Convergence time ($F(\mathbf{w}, \xi) \leq 220$) and maximum iterations for BGWO, BWOA, and BBA algorithms

Time (s) to Achieve	**BGWO**	**BWOA**	**BBA**
$F(\mathbf{w}, \xi) \leq 220$	0.0191	0.0127	0.0159
Maximum number of iterations is reached	0.0642	0.0570	0.0558

BWOA has the fastest convergence time to the target value $F(\mathbf{w},\xi) \leq 220$, achieving it in 0.0127 seconds, followed by BBA at 0.0159 seconds, and BGWO at 0.0191 seconds. Despite BGWO being slightly slower in this instance, its convergence to the scheme is still efficient. When the maximum number of iterations is reached, BGWO takes the longest at 0.0642 seconds, while BWOA and BBA perform similarly, taking 0.0570 seconds and 0.0558 seconds, respectively. This highlights the trade-off between speed and performance consistency across different algorithms.

VI. CONCLUSION

This paper has proposed a scheme to address unknown interference suppression in AAS. First, we reduce the complexity by minimizing the number of optimization variables, significantly shortening computational time, which is an essential factor for efficient AAS deployment. Second, we integrate a CHT, specifically the SPM, with metaheuristic algorithms, including the BBA, BGWO, and BWOA, to improve interference suppression in URAs. The effectiveness of the scheme is validated through simulations, demonstrating strong convergence and the ability to suppress interference in sidelobe regions without prior knowledge of interference direction. These results underscore the scheme's potential for unknown interference management in AAS. Future research should explore alternative CHT methods, additional array configurations, and control over multiple main lobes, as well as addressing interference in the main lobe region. Expanding this approach to broader challenges within AAS could further enhance its practical applications.

REFERENCES

[1] H. Asplund, J. Karlsson, F. Kronestedt, E. Larsson, D. Astely, P. von Butovitsch, T. Chapman, M. Frenne, F. Ghasemzadeh, M. Hagström, B. Hogan, and G. Jöngren, *Advanced Antenna Systems for 5G Network Deployments: Bridging the Gap Between Theory and Practice*. Cambridge, MA: Academic Press, 2020.

[2] N. Trabelsi, L. C. Fourati, and C. S. Chen, "Interference management in 5G and beyond networks: A comprehensive survey," *Computer Networks*, vol. 239, 2024.

[3] C. A. Balanis, *Antenna Theory: Analysis and Design*, 4th ed. Oxford: John Wiley and Sons, 2016.

[4] L. T. Trang, N. V. Cuong, and T. V. Luyen, "Interference suppression approaches utilizing phase-only control and metaheuristic algorithms: A comparative study," *Lecture Notes of the Institute for Computer Sciences, Social Informatics and Telecommunications Engineering*, vol. 558, 2024.

[5] T. V. Luyen and N. V. Cuong, "An adaptive beamformer utilizing Binary Bat Algorithm for antenna array pattern nulling," *Journal of Science and Technology, Hanoi University of Industry*, vol. 57, pp. 52-57, 2021.

[6] J. Yin, Z. Liu, Y. Jin, D. Peng, and J. Kang, "Blind source separation and identification for speech signals," in 2017 *International Conference on Sensing, Diagnostics, Prognostics, and Control (SDPC)*, Shanghai, China, pp. 398-402, 2017.

[7] T. Oyedare, V. K. Shah, D. J. Jakubisin, and J. H. Reed, "Interference suppression using deep learning: Current approaches and open challenges," *IEEE Access*, vol. 10, pp. 66238-66266, 2022.

[8] D. Chen, Y. Zhuang, J. Huai, X. Sun, X. Yang, and M. Awais Javed, "Coexistence and interference mitigation for WPANs and WLANs from traditional approaches to deep learning: A review," *IEEE Sensors J.,* vol. 21, no. 22, pp. 25561-25589, 2021.

[9] S. Wang, F. Han, Y. Yan, Y. Ding, P. Yang, and X.-Y. Li, "SlickScatter: Retrieve WiFi backscatter signal from unknown interference," in *2024 IEEE/ACM 32nd International Symposium on Quality of Service (IWQoS)*, pp. 1-10, 2024.

[10] Q. Zhang, H. Ji, L. Li, and Z. Zhu, "Automatic modulation recognition of unknown interference signals based on graph model," *IEEE Wireless Communications Letters*, vol. 13, no. 9, pp. 2317-2321, 2024.

[11] Z. Xu, T. Song, and X. Wei, "Unknown interference source positioning based on near-field scanning," in *2021 IEEE MTT-S International Wireless Symposium (IWS)*, pp. 1-3, 2021.

[12] T.-Y. Huang, B. Lin, A. Ahmed, M.-Y. Huang, and H. Wang, "A 23-37-GHz autonomous 2-D MIMO receiver array with rapid full-FoV spatial filtering for unknown interference suppression," *IEEE Transactions on Microwave Theory and Techniques*, vol. 71, no. 11, pp. 4841-4854, 2023.

[13] M. Zaher, E. Björnson, and M. Petrova, "A Bayesian approach to characterize unknown interference power in wireless networks," *IEEE Wireless Communications Letters*, vol. 12, no. 8, pp. 1374-1378, 2023.

[14] I. P. Gravas, Z. D. Zaharis, T. V. Yioultsis, P. I. Lazaridis, and T. D. Xenos, "Adaptive beamforming with sidelobe suppression by placing extra radiation pattern nulls," *IEEE Transactions on Antennas and Propagation*, vol. 67, no. 6, pp. 3853-3862, 2019.

[15] T. V. Luyen, H. M. Kha, N. V. Tuyen, and T. V. B. Giang, "An efficient ULA pattern nulling approach in the presence of unknown interference," *Journal of Electromagnetic Waves and Applications*, vol. 35, no. 1, pp. 1-18, 2021.

[16] T. Luyen and C. Nguyen, "An effective beamformer for interference suppression without knowing the direction," *International Journal of Electrical and Computer Engineering (IJECE)*, vol. 13, no. 1, pp. 601-610, 2023.

[17] S. Mirjalili, S. M. Mirjalili, and X. S. Yang, "Binary Bat Algorithm," *Neural Computing and Applications*, vol. 25, no. 3-4, pp. 663-681, 2014.

[18] A. G. Hussien, A. E. Hassanien, E. H. Houssein, S. Bhattacharyya, and M. Amin, "S-shaped binary Whale Optimization Algorithm for feature selection," *Advances in Intelligent Systems and Computing*, vol. 727, 2019.

[19] E. Emary, H. M. Zawbaa, and A. E. Hassanien, "Binary Grey Wolf Optimization approaches for feature selection," *Neurocomputing*, vol. 172, pp. 371-381, 2016.

[20] A. Sharma, "Antenna array pattern synthesis using metaheuristic algorithms: A review," *IETE Technical Review*, pp. 1-26, Mar. 2022.

[21] N. D. Lagaros, M. Kournoutos, N. Ath. Kallioras, and A. N. Nordas, "Constraint handling techniques for metaheuristics: A state-of-the-art review and new variants," *Optim. Eng.,* vol. 24, pp. 2251-2298, 2023.

[22] X.-S. Yang, *Nature Inspired Optimization Algorithms*. Amsterdam: Elsevier, 2014.

[23] I. Rahimi, A. H. Gandomi, F. Chen, and E. Mezura-Montes, "A review on constraint handling techniques for population-based algorithms: From single-objective to multi-objective optimization," *Arch. Computat. Methods Eng.,* vol. 30, pp. 2181-2209, 2023.

[24] A. R. Jordehi, "A review on constraint handling strategies in particle swarm optimization," *Neural Comput. & Applic.,* vol. 26, pp. 1265-1275, 2015.

[25] Ö. Yeniay, "Penalty function methods for constrained optimization with genetic algorithms," *Math. Comput. Appl.*, vol. 10, no. 1, pp. 45-56, 2005.

[26] H. M. Kha, T. V. Luyen, and N. V. Cuong, "An efficient beamformer for interference suppression using rectangular antenna arrays," *J. Commun.,* vol. 18, no. 2, pp. 116-122, 2023.

[27] F. B. Gross, *Smart Antennas with MATLAB*, 2nd ed. New York, NY: McGraw-Hill Education Press, pp. 387-391, 2015.

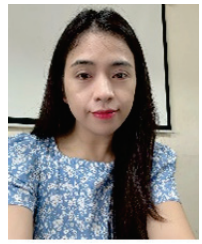

Le Thi Trang obtained both the B.E. degree and the M.S. degree from the Institute of Military Technology in 2007 and 2011, respectively. Her research interests primarily focus on beamformers, smart antennas, nature-inspired optimization algorithms, and constraint handling techniques.

Nguyen Van Cuong received the Engineer's and master's degrees from Hanoi University of Industry, in 2020 and 2022, respectively. His research interests include emerging wireless communication technologies, metaheuristics algorithms, deep learning, and convex optimization.

Hoang Thi Phuong Thao was born in Vietnam in 1981. She received the Diploma of Engineer (2004), Master of Science (2007), and Ph.D. degree (2019) in Electronics and Telecommunications from Hanoi University of Science and Technology, Vietnam. Her research interests are designing antenna, localization systems, and wireless communication technology.

Tong Van Luyen received the B.S. and M.S. degrees from the Hanoi University of Science and Technology, in 2002 and 2004, respectively, and Ph.D. degree from VNU University of Engineering and Technology in 2019. His research interests are in beamforming and beam steering for antenna arrays, smart antennas, optimum array processing, nature-inspired optimization algorithms, and artificial intelligence.

Design and Analysis of a Novel Vivaldi Antenna With Improved Gain for Fan Motion Detection in Smart Homes Using IR-UWB Radar

Ho-Gyun Yu[1] and Sun-Woong Kim[2*]

[1]Department of Information and Communication Engineering
Chosun University, Gwangju, Republic of Korea
1030ghrbs@naver.com

[2]Center for Advanced Meta-Materials
Daejeon 34103, Republic of Korea
*Corresponding author: woongskim1@naver.com

***Abstract* –** The proposed antenna is an ultra-wideband Vivaldi antenna optimized for impulse-radio ultra-wideband (IR-UWB) radar applications in smart home environments. Designed to detect indoor object motion, including fan movement, the antenna demonstrates enhanced directivity by integrating five semicircular slots and a polygonal structure in the radiating element. Fabricated on a TRF-45 substrate (dielectric constant of 4.5, loss tangent of 0.0035, thickness of 1.62 mm), the antenna exhibits an impedance bandwidth of approximately 2.28 GHz and achieves a maximum gain of 9.59 dBi at 8.5 GHz. The proposed design advances indoor motion detection capabilities for smart home applications by providing a compact, high-gain, and wideband antenna solution.

***Index Terms* –** Impulse-radio ultra-wideband radar, smart home, Vivaldi antenna.

I. INTRODUCTION

By 2024, the number of single-person households in South Korea will exceed 10 million, and account for 41.8% of all households. This significant demographic shift has raised critical concerns about safety and energy efficiency. The ability to detect indoor emergencies and manage energy efficiently is becoming increasingly important for single-person households [1].

Smart home systems are able to control household appliances in real time and recognize human movement to quickly identify emergency situations. These systems increase the safety of single-person households and contribute to efficient energy use [2–4].

In smart home systems, accurate differentiation between people and objects is essential. This maximizes energy savings and prevents unnecessary energy consumption. The ability to differentiate between people and appliances such as fans contributes to the efficient operation of smart home systems [5].

Impulse-radio ultra-wideband (IR-UWB) radar uses ultra-wideband signals to detect subtle movements of both people and objects with high precision. This capability makes the UWB radar a promising technology for smart home systems and offers numerous potential applications [6–7].

In this paper, we propose an antenna with wide bandwidth, high gain, and high directivity, optimized for smart home applications. While typical UWB antennas have a bandwidth of 100-130%, the antenna presented in this study is specifically designed to maximize performance in selected frequency bands required through a practical IR-UWB radar system [8–9]. The IR-UWB radar module used in this research, IU-D-M-0.0 from Grit Custom IC, was experimentally tested in combination with the proposed antenna to validate its applicability in smart home environments. The module operates in key frequency bands of 7.7, 8.0, and 8.4 GHz, all of which are covered by the proposed antenna's 6.25-8.53 GHz bandwidth [10]. Through this design, our study provides optimized performance for object detection in smart home applications and distinguishes itself from conventional UWB antennas.

Furthermore, this study holds unique value as it presents an object detection technology realized through an antenna design that achieves superior performance within selected frequency bands for smart home applications. The proposed antenna enables effective motion detection with its wide bandwidth and high gain, outperforming typical UWB antennas, and demonstrates potential to enhance energy management and safety in smart home systems. Our tailored antenna design addresses potential frequency range challenges in smart home environments. Through experimental validation, we establish its practical applicability in smart home scenarios, with

Submitted On: October 1, 2024
Accepted On: February 21, 2025
https://doi.org/10.13052/2024.ACES.J.400305

contributions toward improved accuracy and efficiency in object detection for future smart home systems.

Accordingly, in this paper the design and structure of the proposed antenna is discussed in section II and the measurement results to validate its performance are presented in section III. Finally, section IV describes the application of the antenna in an IR-UWB radar system to evaluate its potential for smart home applications. The objective of this study was to demonstrate that the proposed antenna can contribute to efficient and reliable motion detection in smart home systems.

II. ANTENNA DESIGN

A. Antenna geometry

The geometry of the proposed Vivaldi antenna for the IR-UWB radar is shown in Fig. 1. Vivaldi antennas radiate radio waves in the z-axis direction through a slot that tapers into a triangular structure. These radiating elements are located on the top layer. To supply the radiating element of the antenna with a radio wave signal, an input source was also fed through a microstrip line located on the bottom layer.

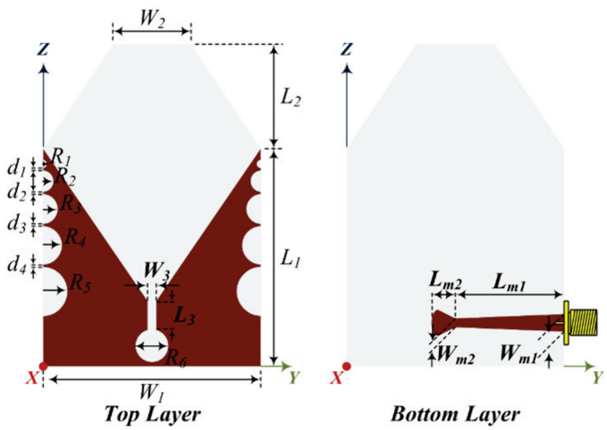

Fig. 1. Geometry of the proposed Vivaldi antenna for IR-UWB radar.

To increase the gain, five semicircular slots and a polygon structure were added to the radiating element on the top layer and aperture of the edge. The proposed Vivaldi antenna was fabricated on a TRF-45 substrate with a dielectric constant of 4.5, loss tangent of 0.0035, and thickness of 1.62 mm. The design parameters of the proposed antenna follow.

The fundamental gain of the proposed antenna is determined by design parameters L_1 and W_1, and the radiating element slot of the antenna tapers linearly to a triangular structure from W_1 to W_3. However, to achieve a higher antenna gain, five semicircular slots with different radii (R_1-R_5) and polygonal structures (L_2 and W_2) are designed. Finally, the design parameters for the microstrip line are L_m, W_{m1}, and W_m. The proposed Vivaldi antenna was designed using HFSS, and the design parameters are as follows: L_1=50 mm, W_1=50 mm, L_2=21.65 mm, W_2=22.70 mm, L_3=8.4 mm, W_3=1.5 mm, R_1=1 mm, R_2=2 mm, R_3=3 mm, R_4=4 mm, R_5=5 mm, R_6=3 mm, d_1=1 mm, d_2 =1 mm, d_3 =1 mm, d_4 =1 mm, L_{m1}=25.5 mm, W_{m1}=3 mm, L_{m2}=3 mm, and W_{m2}=1 mm.

B. Antenna analysis

To explain the design process of the proposed Vivaldi antenna, it was designed using three main design methods. The designs are shown in Fig. 2. The proposed antenna was designed using a conventional Vivaldi antenna, as shown in Fig. 2 (a). A conventional Vivaldi antenna is characterized by end-fire radiation, which concentrates radio waves and signals in one direction. However, depending on the application, it may be necessary to further improve the directivity and gain of the antenna to concentrate the signal in a specific direction. To improve the directivity and gain of the antenna, five semicircular slots and a polygon structure were added to the conventional Vivaldi antenna, as shown in Figs. 2 (b) and (c).

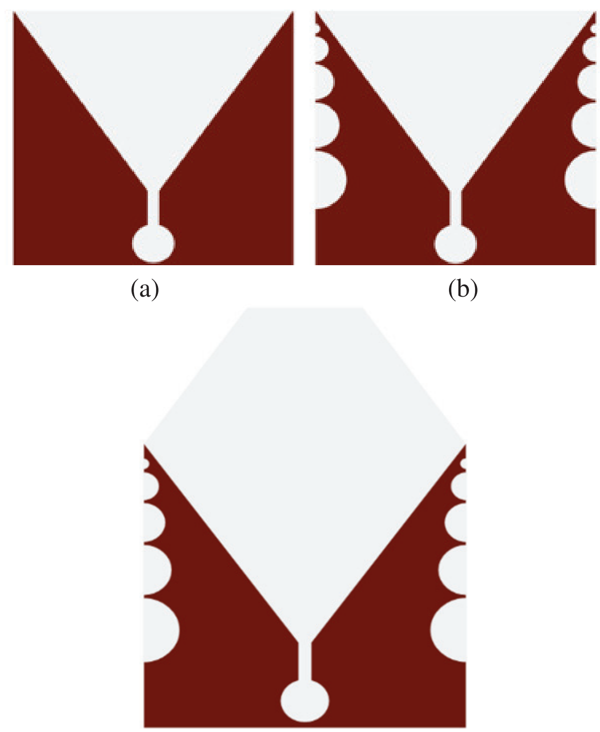

Fig. 2. Schematic design of the proposed Vivaldi antenna: (a) conventional Vivaldi antenna, (b) Vivaldi antenna with five circular slots, and (c) final design of proposed Vivaldi antenna.

For the design of the proposed Vivaldi antenna, simulations were conducted with the results presented in

Fig. 3. As shown in Fig. 3 (a), the VSWR characteristics for each design were compared. The conventional Vivaldi antenna achieved a bandwidth of 2.27 GHz in the 6.28-8.55 GHz range with VSWR<2, while the Vivaldi antenna with five circular slots showed an improved bandwidth of 2.43 GHz within the 6.19-8.61 GHz range.

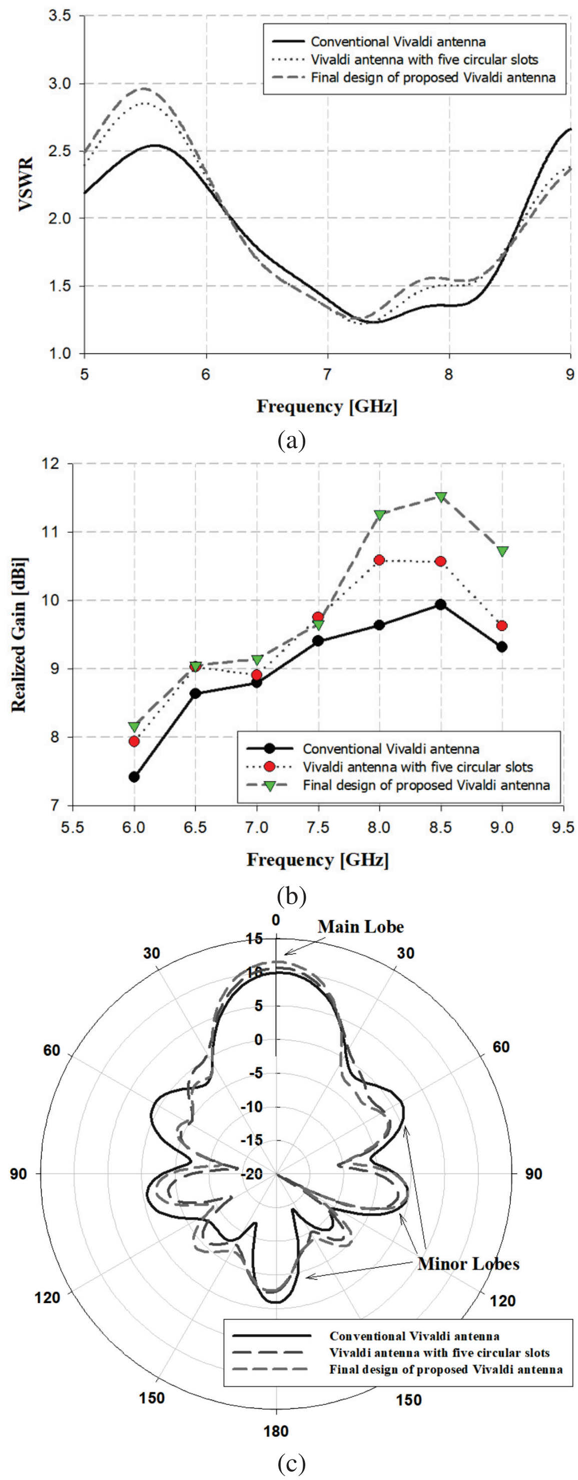

Fig. 3. Simulation results of three configurations for the Vivaldi antenna: (a) VSWR, (b) realized gain, and (c) radiation pattern in the 8.5 GHz band.

The final design of the proposed Vivaldi antenna achieved the widest bandwidth, covering 2.46 GHz in the 6.20-8.66 GHz range, demonstrating enhanced performance over previous designs. As shown in Fig. 3 (b), the realized gain simulation results indicate that the final design of the Vivaldi antenna improves gain across the bandwidth. The conventional Vivaldi antenna achieved a maximum gain of 9.94 dBi at 8.5 GHz, while the Vivaldi antenna with five circular slots reached 10.67 dBi at 8.85 GHz. The final design of the proposed antenna recorded the highest gain of 11.53 dBi at 8.85 GHz. Figure 3 (c) illustrates the radiation pattern for the 8.5 GHz band, showing that the radiation characteristics of the proposed antenna are enhanced, primarily in the main lobe.

The enhancement of the main lobe in the proposed antenna can be attributed to the addition of five circular slots and polygonal structures, which contribute to optimizing the antenna's directivity. These structural modifications adjust the current distribution on the radiating surface, increasing the gain of the main lobe while reducing the size of the side lobes, thereby improving the overall directivity. In other words, the circular slots and polygonal structures focus the radiated energy into the main lobe and suppress unnecessary side lobes, resulting in a more defined radiation pattern. The final design of the proposed Vivaldi antenna was suppressed to below 0 dBi in the minor lobes, except for the main lobe, and the main lobe was improved by more than 10 dBi. The simulation results for the three design methods are listed in Table 1.

Table 1: Comparison of the simulation results for the design methods

Frequency (GHz)	**Simulation Results of the Realized Gain (dBi)**		
	Conventional Vivaldi Antenna	Vivaldi Antenna with Five Circular Slots	Proposed Vivaldi Antenna
6	7.42	7.94	8.17
6.5	8.64	9.03	9.05
7	8.80	8.91	9.15
7.5	9.41	9.76	9.66
8	9.64	10.59	11.27
8.5	9.94	10.57	11.53
9	9.32	9.63	10.74

The proposed Vivaldi antenna shows an improved realized gain across the entire frequency range compared to the conventional Vivaldi antenna and the Vivaldi antenna with five circular slots. Notably, it achieves a maximum gain of 11.27 dBi at 8 GHz and 11.53 dBi at 8.5 GHz, demonstrating superior radiation characteristics overall.

To explain the radiation mechanism of the proposed Vivaldi antenna, a surface-current simulation was performed for the E-field, as shown in Fig. 4.

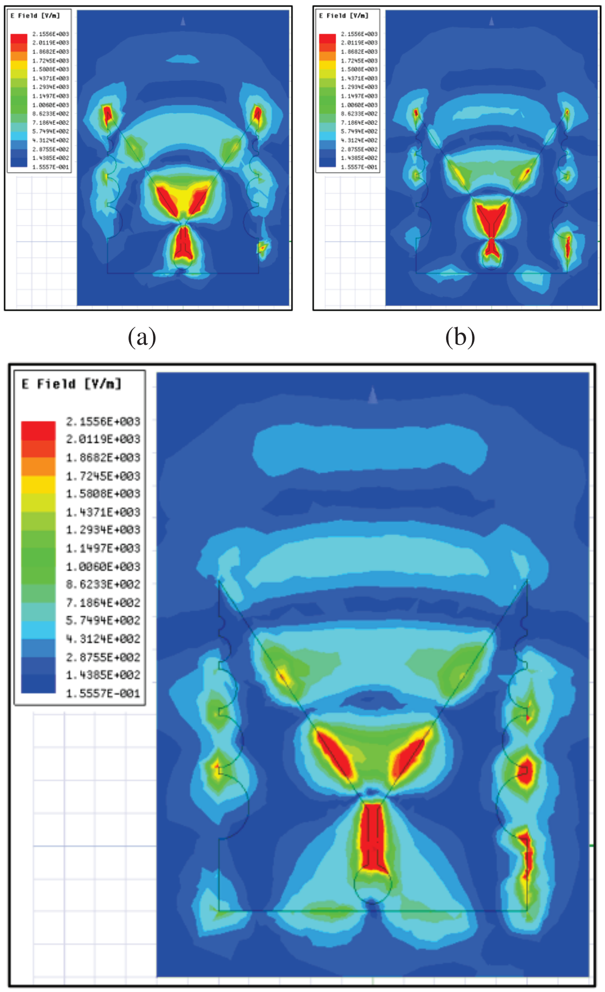

(a) (b)

(c)

Fig. 4. Simulation analysis of the surface current distribution for the proposed Vivaldi antenna: (a) 6.5 GHz, (b) 7.5 GHz, and (c) 8.5 GHz.

As shown in Fig. 4, the Vivaldi antenna exhibits a current distribution along the length of its tapered slot. This current extends to the termination of the slot, leading to the emission of radiation along the z-axis. At different frequencies, this current induces the generation of wavelengths resulting in the directional radiation properties observed at the open end of the antenna. These radiated waves were directed with precision to the intended transmission orientation within the planned radar system.

III. RESULTS AND DISCUSSION OF THE ANTENNA

A. Experimental environment

The proposed Vivaldi antenna was fabricated to verify the design, and the measurement results were obtained using a variety of instruments. A photograph of the fabricated Vivaldi antenna is shown in Fig. 5.

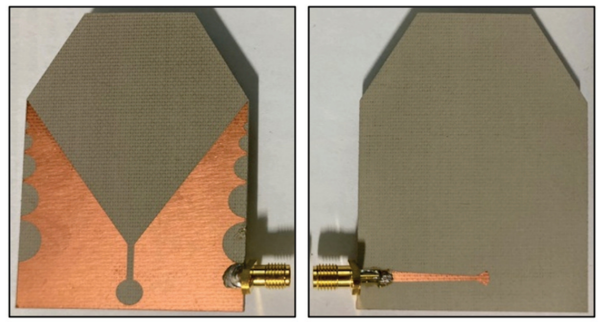

(a) (b)

Fig. 5. Photograph of the fabricated Vivaldi antenna: (a) top layer and (b) bottom layer.

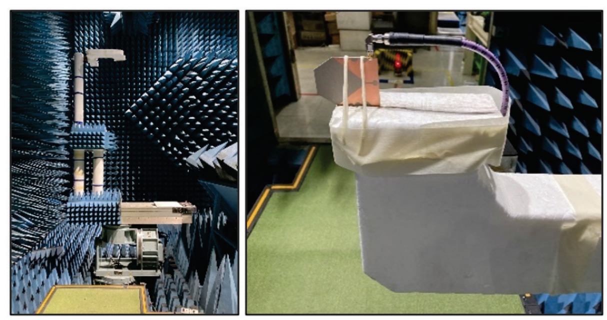

(a) (b)

Fig. 6. Measurement configuration: (a) experimental environment-1 and (b) experimental environment-2.

The gain and radiation pattern of the fabricated Vivaldi antenna were measured using a large antenna measurement system. The measurement results within the proposed bandwidth were obtained with a Tx antenna in a far-field anechoic chamber. The experimental environment is shown in Fig. 6.

B. Measurement results

To obtain the VSWR results, the fabricated Vivaldi antenna was measured using a vector network analyzer (E8361A, Agilent Co.). The VSWR results for the fabricated Vivaldi antenna are shown in Fig. 7.

As shown in Fig. 7, the simulated VSWR result of the fabricated Vivaldi antenna was satisfied by VSWR$<$2 at 6.25-8.53 GHz, resulting in an impedance

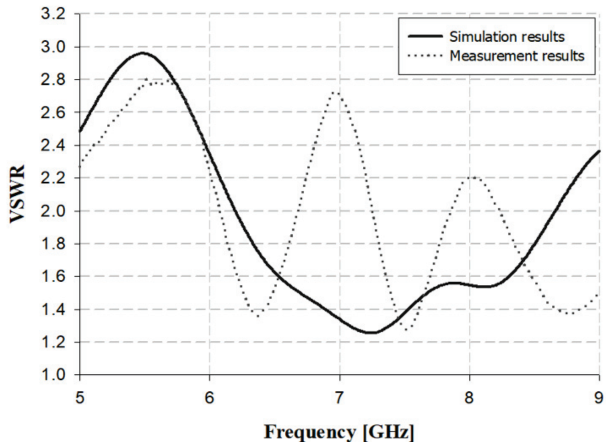

Fig. 7. VSWR results of the fabricated Vivaldi antenna.

bandwidth of 2.28 GHz. In contrast, the measurement results showed some discrepancies from the simulation results. The measurement results were included in the impedance bandwidth of the simulation, but the 7 GHz and 8 GHz bands were somewhat suppressed. However, this should not be a major problem in the proposed application. This will be demonstrated in the next section.

The simulation and measurement results for the 2D radiation pattern were analyzed in the E-plane (YZ plane) and H-plane (XZ plane), as shown in Figs. 8 and 9.

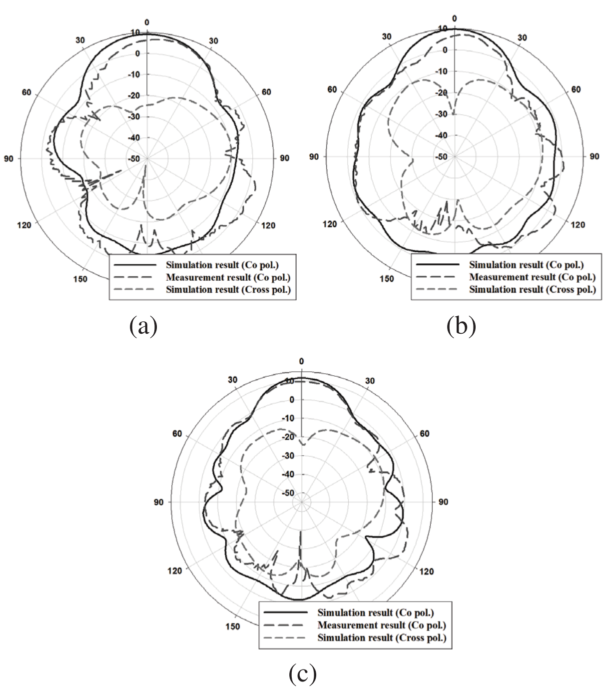

Fig. 8. 2D radiation pattern results for the E-plane (YZ-plane) of the fabricated Vivaldi antenna: (a) 6.5 GHz, (b) 7.5 GHz, and (c) 8.5 GHz.

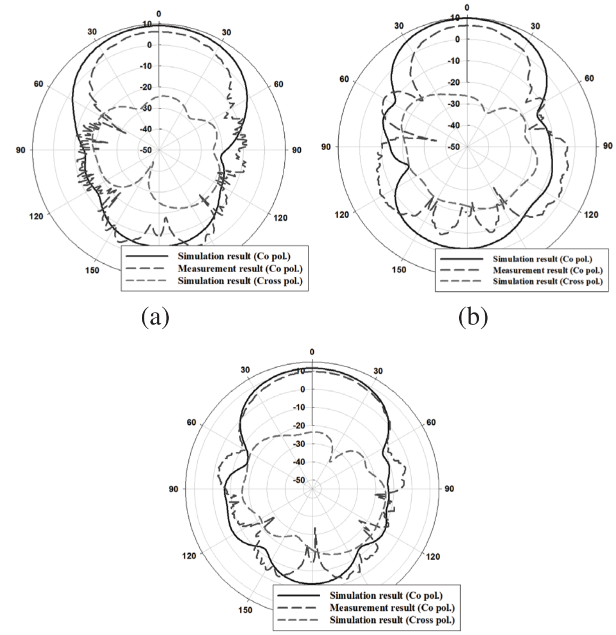

Fig. 9. 2D radiation pattern results for the H-plane (XZ-plane) of the fabricated Vivaldi antenna: (a) 6.5 GHz, (b) 7.5 GHz, and (c) 8.5 GHz.

As shown in Figs. 8 and 9, the 2D radiation patterns of the fabricated Vivaldi antenna were analyzed for the directional radiation pattern, in which the waves were concentrated in both the E- and H-planes in the Z direction. The 3 dB beamwidth (HPBW: half power beam width) of the simulation and measurement results for the E-plane are 45° and 38° at 6.5 GHz, 35° and 41° at 7.5 GHz, and 30° and 34° at 8.5 GHz. For the simulation and measurement results, the H-plane is 74° and 58° at 6.5 GHz, 60° and 45° at 7.5 GHz, and 59° and 60° at 8.5 GHz. In addition, the simulation and measurement results for the maximum gain are 9.05 dBi and 7.07 dBi at 6.5 GHz, 9.66 dBi and 7.24 dBi at 7.5 GHz, and 11.53 dBi and 9.59 dBi at 8.5 GHz. Furthermore, the simulated cross-polarized radiation pattern showed attenuated radiation characteristics in both the E- and H-planes compared to the main radiation direction, which complements the directional characteristics and contributes to enhancing the antenna's performance.

A noticeable difference is observed between the simulation and measurement results, which can be attributed to a few factors. First, as the antenna was fabricated using an etching process, minor inaccuracies may have arisen during fabrication. The etching process could have caused a dimensional variation of a few millimeters, potentially affecting the measurement results. Second, there may be unaccounted losses between the antenna and the measurement cable. Despite this noticeable discrepancy, the proposed antenna's practicality was verified by successfully integrating it with an actual IR-UWB radar system.

In this study, existing studies were compared with the proposed antenna to analyze its performance.

Table 2: Performance comparison between existing wideband antenna designs and the proposed antenna

Ref.	Antenna Type	Frequency Range (GHz)	Gain (dBi)	Application
[11]	Vivaldi	4.00-8.00	8.3	Through-wall radar
[12]	Bowtie	0.34-0.77	9.2	Ground penetrating radar
[13]	Vivaldi	0.47-1.00	2.57	UHF DVB-T/T2
[14]	Patch	7.1-7.9	8.4	IR-UWB radar
[15]	Vivaldi	660-15	15	Concealed object detection
[16]	Bowtie	0.31-0.93	9.3	Ground penetrating radar
[17]	Vivaldi	2.42-11.52	8.61	Medical imaging
Proposed Antenna	Vivaldi	6.25-8.53	9.59	Smart home system

Table 2 presents a performance comparison of different types of wideband antennas, including bowtie, patch, and Vivaldi antennas. These antennas are widely used in different fields because of their high gain and wide bandwidth. The proposed Vivaldi antenna operates in the frequency range of 6.25-8.53 GHz with a gain of 9.59 dBi, demonstrating its potential for smart home system applications.

IV. EXPERIMENTAL STUDY AND RESULTS

A. Setup and configuration of the radar

As shown in Fig. 10, a test setup was established to verify the performance of the fabricated antenna. The radar module used for the fan motion detection experiment was an IU-D-M-0.0 from GRIT Customs IC Inc. In this experiment, the radar module consists of a transmitter and a receiver. The transmitted UWB signal is reflected off the rotating fan blades and received by the receiver. The radar records amplitude variations in the reflected signal over time, frame by frame, to analyze changes in the signal caused by the rotation of the fan blades. This allows the radar system to detect the motion of the fan blades, and the measured data is used to determine the positional variations and rotation cycle of the fan.

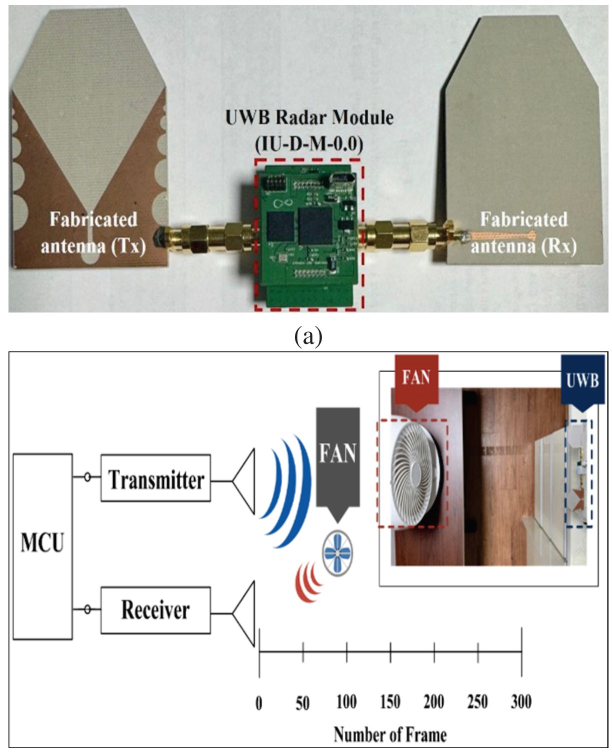

Fig. 10. Testing setup for the fan motion detection experiment: (a) radar configuration and (b) fan motion detection setup.

The specifications of the IU-D-M-0.0 radar module, summarized in Table 3, were selected to optimize the detection of fan motion within the experimental setup [10]. These specifications enabled precise measurement

Table 3: Specification for the experiment

Parameter	Min	Typical	Max	Unit
Frequency range	7.7	8.0	8.4	GHz
Bandwidth		1.7	1.9	GHz
EIRP	-45.7	-44.0	-43.1	dBm/MHz
	-17.9	-16.0	-14.7	dBm/50 MHz
Equivalent sampling rate		20.48		Gbps
Detection range	0.1		15	m

and analysis of fan motion and ensured accurate performance evaluation of the fabricated antenna.

B. Signal processing and experimental results

As shown in Fig. 11, two important filters were applied to process the UWB radar data: clutter reduction and high-frequency noise reduction. These filters are critical for improving fan motion detection by suppressing clutter signals and emphasizing the relevant motion signals.

Fig. 11. Block diagram of UWB radar signal processing.

In this study, the received signal r_i consists of three components: the clutter signal $r_{c,i}$, the target signal $r_{t,i}$, and noise r_n, as represented by the equation:

$$r_i = r_{c,i} + r_{t,i} + r_n. \tag{1}$$

The clutter reduction step is designed to remove the static background noise $r_{c,i}$ (clutter) from the radar signal, which typically originates from stationary objects in the environment. This is done using a difference filter that calculates the difference between the current and previous signal samples. This approach emphasizes dynamic changes in the signal while suppressing static components such as clutter. The filter can be expressed in the z-domain as follows:

$$H(z) = \frac{1 - z^{-1}}{1 - \lambda z^{-1}}, \tag{2}$$

where λ is a filter coefficient that controls the rate of clutter attenuation. The numerator $1 - z^{-1}$ represents a high-pass characteristic that filters out low-frequency components associated with static clutter, while the denominator $1 - \lambda z^{-1}$ introduces an exponential moving average to smooth the signal [18–19]. After clutter reduction, the radar signal enters the high-frequency noise reduction phase, where a low-pass filter is applied to suppress high-frequency noise and preserve the low-frequency components associated with the fan's movement. In the final stage of target visualization, the processed radar signals are converted into graphical representations to clearly depict the detected motion of the fan. Figure 12 illustrates the three stages of signal processing.

In Fig. 12, the first result (a) shows the raw data in which the clutter signals dominate. After clutter reduction, the result (b) shows a cleaner signal with reduced noise. Finally, result (c) demonstrates the high-frequency noise-reduction phase, in which the signal is smoothed and only the essential motion signals are retained. Figure 13 illustrates the detection of the movement of the fan.

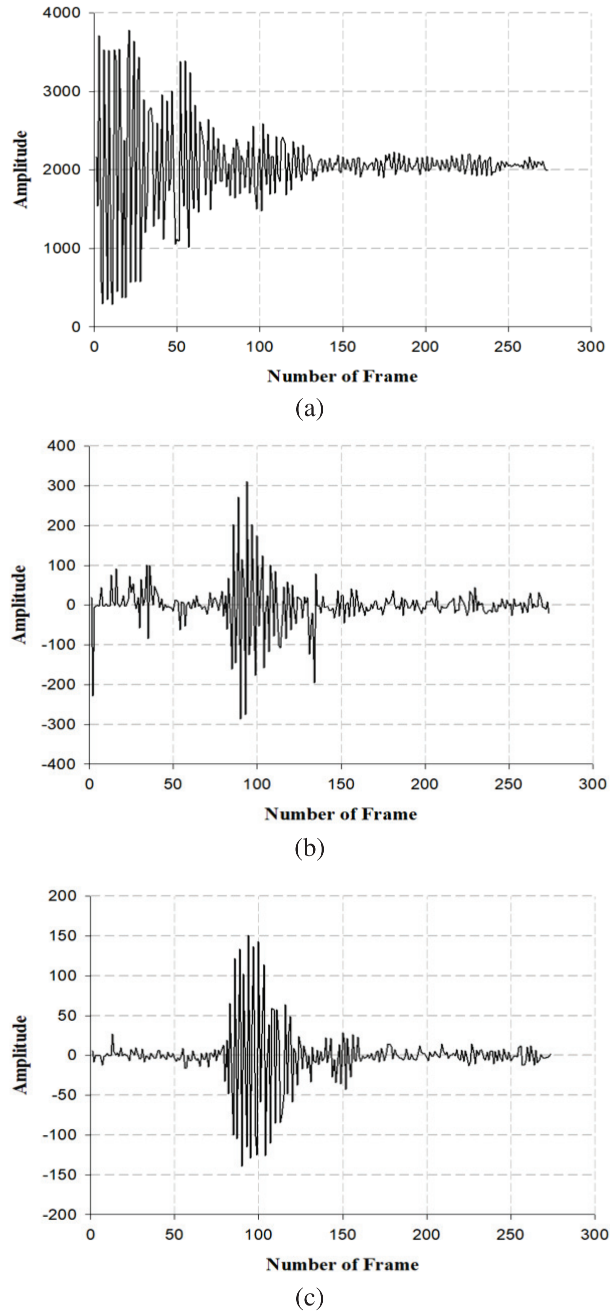

Fig. 12. Results of signal processing: (a) raw radar data, (b) data after clutter reduction, and (c) data after high-frequency noise reduction.

As shown in Fig. 13, a periodic movement of the fan at a certain distance was detected using the time and distance axis. This result shows that the radar system successfully detected the movement of the fan.

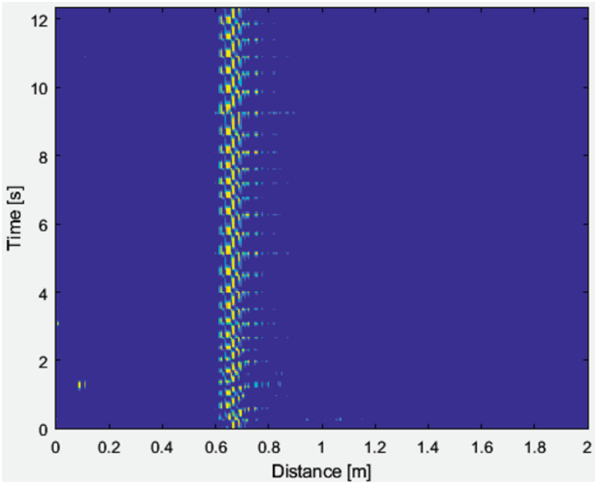

Fig. 13. Detection of the movement of the fan.

V. CONCLUSION

In this study, a high-gain antenna capable of detecting indoor motion for smart home systems was proposed to meet the growing need for safety and energy efficient management in single-person households. The proposed antenna is characterized by a wide impedance bandwidth of 2.28 GHz in the frequency range of 6.25 to 8.53 GHz, a high gain of 9.59 dBi in the 8.5 GHz band, and excellent directivity characteristics. Based on these performance characteristics, the antenna was integrated into an IR-UWB radar module and successfully validated through experiments to detect the motion of objects, such as fans, in an indoor environment.

The contribution of this research lies in the successful demonstration of the applicability of the proposed antenna for precise motion detection and energy management in smart home systems. The wide bandwidth and high gain of the antenna provide the basis for improving the accuracy of motion detection in various applications and emphasize its importance as a component in future smart home configurations.

However, limitations of this study include the need for further miniaturization of the antenna and challenges in measuring fan rotation due to the low frame rate of the radar. Future research should focus on the development of low-profile antennas with improved resolution for IoT-based indoor occupancy detection and smart home systems. In addition, further experiments are needed on fan movement, human positioning, and biometric data measurement. These efforts pave the way for the integration of AI-based intelligent radar technologies and further expand the potential of the proposed system.

REFERENCES

[1] The Dong-A Ilbo, *Single-person households reach 10 million in Korea* [Online]. Available: https://www.donga.com/en/article/all/20240410/4871941/1#:~:text=10%2C%202024%2007%3A48.,all%20household%20types%20at%2041.8%2510April2024.

[2] A. Sanchez-Comas, K. Synnes, and J. Hallberg, “Hardware for recognition of human activities: A review of smart home and AAL related technologies,” *Sensors*, vol. 20, no. 15, pp. 1-26, July 2020.

[3] D. Bouchabou, S. M. Nguyen, C. Lohr, B. LeDuc, and I. Kanellos, “A survey of human activity recognition in smart homes based on IoT sensors algorithms: Taxonomies, challenges, and opportunities with deep learning,” *Sensors*, vol. 21, no. 18, pp. 1-28, Sep. 2021.

[4] G. Bhavanasi, L. Werthen-Brabants, T. Dhaene, and I. Couckuyt, “Patient activity recognition using radar sensors and machine learning,” *Neural Computing and Applications*, vol. 34, pp. 16033-16048, May 2022.

[5] M. Diyan, B. N. Silva, and K. Han, “A multi-objective approach for optimal energy management in smart home using the reinforcement learning,” *Sensors*, vol. 20, no. 12, pp. 1-20, June 2020.

[6] S. Klavestad, G. Assres, S. Fagernes, and T.-M. Gronli, ”Monitoring activities of daily living using UWB radar technology: A contactless approach,” *IoT*, vol. 1, no. 2, pp. 320-336, Oct. 2020.

[7] S. Singh, Q. Liang, D. Chen, and L. Sheng, ”Sense through wall human detection using UWB radar,” *EURASIP Journal on Wireless Communications and Networking*, vol. 2011, no. 20, pp. 1-11, June 2011.

[8] V. Portosi, A. M. Loconsole, A. Campana, F. Anelli, and F. Prudenzano, “A novel L-shaped metalens for ultra-wide band (UWB) antenna gain improvement,” *Applied Sciences*, vol. 13, no. 08, pp. 1-15, Apr. 2023.

[9] J. Ghimire and D. Y. Choi, “Ultra-wide band double-slot podal and antipodal Vivaldi antennas feed by compact out-of-phase power divider slot for fluid properties determination,” *Sensors*, vol. 22, no. 12, pp. 1-19, June 2022.

[10] *GRIT Custom Integrated-Chip* [Online]. Available: http://www.gritcic.com/ 12 Sep. 2024.

[11] J. Zhang, H. Lan, M. Li, and Y. Yang, “A handheld nano through-wall radar locating with the gain-enhanced Vivaldi antenna,” *IEEE Sensors Journal*, vol. 20, no. 05, pp. 4420-4429, Dec. 2019.

[12] Y. Li and J. Chen, “Design of miniaturized high gain bow-tie antenna,” *IEEE Transactions on Antennas and Propagation*, vol. 70, no. 01, pp. 738-743, Jan. 2022.

[13] N-R. Kwon, S-H. Ahn, and W-S. Lee, “Wideband printed antipodal Vivaldi antenna using straight

slots for UHF DVB-T/T2 applications," *Applied Computational Electromagnetics Society (ACES) Journal*, vol. 37, no. 06, pp. 726-732, June 2022.

[14] V-T. Nguyen and J-Y. Chung, "Design of a planar antenna array with wide bandwidth and narrow beamwidth for IR-UWB radar applications," *Applied Sciences*, vol. 12, no. 17, pp. 1-9, Aug. 2022.

[15] A. O. Asok, G. Nath S. J., and S. Dey, "Concealed object detection with microwave imaging using Vivaldi antennas utilizing novel time-domain beamforming algorithm," *IEEE Access*, vol. 10, pp. 116987-117000, Nov. 2022.

[16] S. Pi, T. Wang, and J. Lin, "Directional and high-gain ultra-wideband bow-tie antenna for ground-penetrating radar applications," *Remote Sensing*, vol. 15, no. 14, pp. 1-17, July 2023.

[17] S. Saleh, T. Saeidi, and N. Timmons, "Simple compact UWB Vivaldi antenna arrays for breast cancer detection," *Telecom*, vol. 05, no. 02, pp. 312-332, Apr. 2024.

[18] A. Lazaro, A. Girbau, and R. Villarino, "Techniques for clutter suppression in the presence of body movements during the detection of respiratory activity through UWB radars," *Sensors*, vol. 14, no. 02, pp. 2595-2618, Feb. 2014.

[19] S. Ahmed, D. Wang, J. Park, and S.-H. Cho, "UWB-gestures, a public dataset of dynamic hand gestures acquired using impulse radar sensors," *Scientific Data*, vol. 102, no. 08, pp. 1-9, Apr. 2021.

Ho-Gyun Yu received his M.S. degree and completed his Ph.D. coursework from the Department of Information and Communication Engineering at Chosun University, Gwangju, South Korea, in 2019 and 2023, respectively. He is currently a Researcher at the Mechatronics Research Institute in Gwangju. His research interests include UWB antennas, UWB radar, and AI.

Sun-Woong Kim received his M.S. and Ph.D. degrees from the Department of Information and Communication Engineering at Chosun University, Gwangju, South Korea, in 2014 and 2018, respectively. He is currently a Researcher at the Center for Advanced Meta-Materials. His research interests include antennas, UWB antennas, IR-UWB radar, and metasurface antennas.

Low SAR-UWB Rectangular Microstrip Magnetic Monopole Antenna for S-Band and Biomedical Applications

Chemseddine Zebiri[1], Samira Mekki[1], Djamel Sayad[2], Issa Elfergani[3,4], Mohamed Lamine Bouknia[1], Rami Zegadi[1], Atul Varshney[5], and Jonathan Rodriguez[3]

[1]Laboratoire d'Electronique de Puissance et Commande Industrielle (LEPCI)
Department of Electronics, University of Ferhat Abbas, Setif 1, 19000 Setif, Algeria
czebiri@univ-setif.dz, samira.mekki@univ-setif.dz, ml.bouknia@univ-setif.dz, ramizegadi@univ-setif.dz

[2]Laboratoire d'Electronique de Skikda (LRES)
Department of Electrical Engineering, University of 20 Aout 1955-Skikda, 21000, Skikda, Algeria
d.sayad@univ-skikda.dz

[3]Instituto de Telecomunicações
Campus Universitário de Santiago 3810-193 Aveiro, Portugal
i.t.e.elfergani@av.it.pt, jonathan@av.it.pt

[4]Faculty of Engineering and Informatics
University of Bradford, Bradford, UK

[5]Electronics and Communication Engineering Department
FET, Gurukul Kangri (Deemed to be) University, Uttarakhand, India
atulgkvright@gmail.com

***Abstract* –** The development of low specific absorption rate (SAR) antennas is crucial for safety and efficiency in wireless communication and biomedical applications. This study introduces a low SAR ultra-wideband (UWB) rectangular microstrip monopole antenna with an extended ground plane. The design operates effectively in free space and on a human body phantom. It achieves a reflection coefficient of -42.59 dB at 2.48 GHz and covers the S-band from 2.31 GHz to 4.12 GHz with a peak gain of 5.09 dBi in free space. The antenna maintains consistent performances when placed on a human phantom. With reverse and front patch faces, its gain improves to 5.53 dBi and 5.80 dBi, respectively. Experimental validation of the fabricated prototype shows excellent agreement with simulations conducted using high-frequency structure simulators (HFSS) and advanced design systems (ADS). Additionally, lumped-element equivalent circuits are used to analyze impedance behavior in both environments, confirming the antenna's robust design.

***Index Terms* –** Biomedical, human phantom model, ISM band, low SAR, RLC-equivalent circuit, S-band, UWB monopole antenna.

I. INTRODUCTION

Recently, in advanced biomedical applications, planar microstrip antennas have gained significant importance. The planar microstrip antennas are widely used for human in-body (ingestible antennas), on-body (implantable antennas) and off-body (textile or wearable antennas) wireless communication devices. They enable physiological information monitoring and disease diagnosis and provide treatment for patients through wireless telemetry [1]. Moreover, ongoing research on implantable medical devices, such as endoscopy [2], neural recording [3] and blood glucose monitoring [4], has further propelled the importance of planar antennas in biomedical applications. Wearable wireless communication systems, such as body area networks (BANs), are constantly in need of lightweight, compact, flexible, low-profile and durable designs ensuring comfort and ease of use for the wearer [5]. Ultra-wideband (UWB) monopole microstrip antennas play a vital role in meeting system requirements and the linked budget necessities of BAN devices [5–6], medical telemetry applications [7], microwave imaging systems [8] and others [9–12].

Since the human body is a lossy platform for electromagnetic (EM) wave propagation, the efficiency and insensitivity of the antenna to the proximity effect of the

Submitted On: August 8, 2024
Accepted On: February 18, 2025
https://doi.org/10.13052/2024.ACES.J.400306

human body must be maximized to ensure its reliability and effectiveness [13].

In general, the radiation efficiency of an omnidirectional antenna decreases dramatically when placed close to the human body. To minimize the impact on the human body and reduce the body's exposure to electromagnetic radiation, an antenna with a unidirectional radiation pattern is a good choice. It should be insensitive to the proximity effect and should have the least amount of radiation towards the human body [14]. Special design considerations are necessary to meet the requirements of minimizing potential harm to human tissue, particularly by maintaining a minimum specific absorption rate (SAR) of radiation [15]. Many antennas for 2.4 GHz ISM band and biomedical applications have been reported in the literature [5, 6, 16–20]. Most of these antennas exhibit a narrow bandwidth characteristic as well as complex designs. Elshaekh et al. [21] present a design for implantable biomedical devices featuring two distinct integrated antennas on a single chip. The design objective is to handle different tasks: a sensing multi-band meander line antenna for data communication and a wideband dipole antenna for RF energy harvesting. The challenges of signal loss due to human tissue and enhancing device functionality are addressed. Both antennas are fabricated using UMC180nm CMOS technology on a 0.55 mm^2 chip. This antenna system offers high data rates and reduced radiation exposure compared to traditional imaging techniques. This separation simplifies circuit design and improves efficiency by avoiding interference between functions.

Some research works have explored wearable antennas for medical monitoring, revealing ongoing challenges in their design. This area has experienced a notable surge in interest recently. Innovations include a button-shaped wearable antenna and an L-shaped PIFA developed for e-health applications [22]. Additionally, in [23], a UWB-printed antenna tailored for monitoring cardiac activity is addressed.

The rising costs of healthcare for aged population and limited access to medical services highlight the need for telemedicine and ongoing remote patient monitoring. Traditional methods for measuring respiration, using ECG and other wearable devices, tend to be expensive and intrusive, potentially altering natural breathing patterns and leading to inaccurate readings. These devices often restrict patient movement with wired connections and are limited in their ability to provide continuous, long-term monitoring, especially for chronic conditions like stroke. In contrast, non-contact RF radar sensors offer a cost-effective, comfortable and low-power alternative for healthcare applications. These sensors, which detect small physiological movements like respiration and heartbeat through Doppler shifts, have been in use since the 1970s. Beyond their medical applications, radar systems are also employed for search and rescue, security and indoor fall detection. Recently, radar technology has been adapted for precise respiration measurement in cancer radiotherapy. Mpanda et al. [24] developed a low-cost, compact Doppler-based system at 2.4 GHz for non-contact vital signs monitoring. This continuous-wave radar system was compared with traditional contact-based devices to evaluate its performance. The study focused on heart rate and respiration signals, revealing that a dipole array antenna outperforms both a 2×1 patch array antenna and Yagi-Uda antennas. Due to its advantageous characteristics, including lightweight, compact design and cost-effectiveness, the dipole array antenna emerges as a superior choice for integrating into medical devices for vital signs monitoring. Varshney et al. [25, 26] fabricated and tested modified circular patch antennas at 2.45 GHz with wide bandwidth and good gain. However, they exhibit big size issues in the ISM band. In biomedical and ISM band applications, compact size is highly desirable and challenging.

Neebha et al. [27] designed a compact C-shaped narrow band antenna using artificial transmission line theory and extracted the RLC electrical equivalent circuit using the transmission line method at 2.4 GHz. The proposed antenna achieves a 77.55% fractional bandwidth from 2.33 GHz to 2.52 GHz with a gain value of 2.1 dBi. Varshney et al. [28] designed a 2×2 MIMO antenna for the 5G n78 band and extracted the electrical equivalent circuit using the antenna structure.

Research Gap: The antenna compact size results in a narrow bandwidth at 2.45 GHz when a full ground is used. However, as the ground length decreases, the -10dB bandwidth becomes wider [25, 26]. Achieving high gain with wide bandwidth is always challenging. The miniaturization of the antenna size at lower frequencies presents an additional challenge. Furthermore, to control the SAR value within the government-specified limits is another emerging challenge.

A. Research objectives

The following are the objectives of the proposed research.

Design of a miniaturized UWB antenna with a gain higher than 5dBi and low SAR for biomedical applications.

Analysis of the design performances in free space as well as on the human body in reverse and front face study cases.

A further aim of this study is to extract the antenna RLC electrical equivalent circuits in free space and on-body configurations (with reverse and front face cases) and compare their results to validate the antenna performance.

B. Contribution and novelty

This work presents a wideband antenna with a peak gain higher than 5 dBi. Additionally, the electrical RLC equivalent circuit is extracted using advanced design system (ADS) software for three configurations: the antenna is considered in free space, placed on the human body with antenna patch side on the skin (reverse face) and placed on the human body with the antenna ground side on the skin (front face). The low SAR values in each case have been evaluated, they fall under government-specified limits.

Details of the antenna design, using high-frequency structure simulator (HFSS), are described, and simulated results, such as reflection coefficient in free space and on the human body, and specific SAR are presented, measured and analyzed.

II. ANTENNA CONFIGURATION

The proposed antenna is a microstrip monopole antenna with an extended ground plane printed on an FR-4 substrate with a thickness of h = 1.58 mm, a relative dielectric permittivity of $\varepsilon_r = 4.4$ and a loss tangent of 0.002. A trapezoidal-shaped microstrip feed line is used to excite the antenna for better impedance matching. The rectangular radiating patch has dimensions of 34×28 mm^2. The antenna is optimized to meet the ISM band requirements at 2.48 GHz. The optimized design dimensional parameters are illustrated in Fig. 1 and displayed in Table 1.

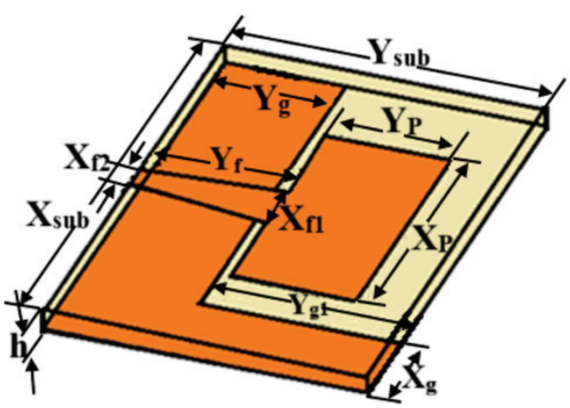

Fig. 1. Proposed antenna with trapezoidal-feed and extended L-shaped ground plane.

Table 1: Dimensions of the proposed patch antenna

Parameter	Value (mm)	Parameter	Value (mm)	Parameter	Value (mm)
Y_P	11	X_{sub}	34	X_{f2}	2
X_P	18	Y_{sub}	28	Y_f	12.54
Y_f	12.54	Y_g	10.5	Y_{g1}	17.5
X_{f1}	4	X_g	6	h	1.58

A. Parametric study

The proposed antenna is first designed as an edge fed monopole rectangular patch antenna as shown in Fig. 2 (a). The ground plane is then extended in an L-shaped form (Fig. 2 (b)) and finally, the feed line is made trapezoidal (a total tapering of 2 mm from antenna port to antenna edge) as illustrated in Fig. 2 (c). The reflection coefficients (S_{11}) of all the antenna design steps are presented in Fig. 3.

It can be noticed, from S_{11} comparisons, that the L-shaped extended ground plane improves the reflection coefficient below -10 dB and tunes the antenna at 2.48 GHz. The trapezoidal feed line excellently improves the

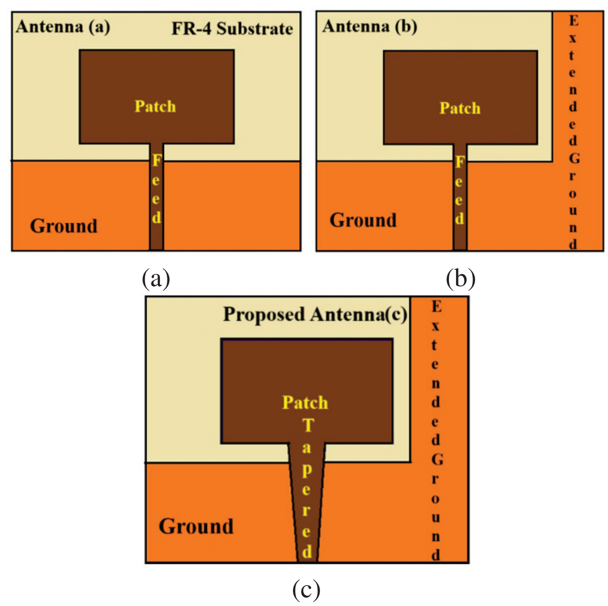

Fig. 2. Step-by-step antenna design development.

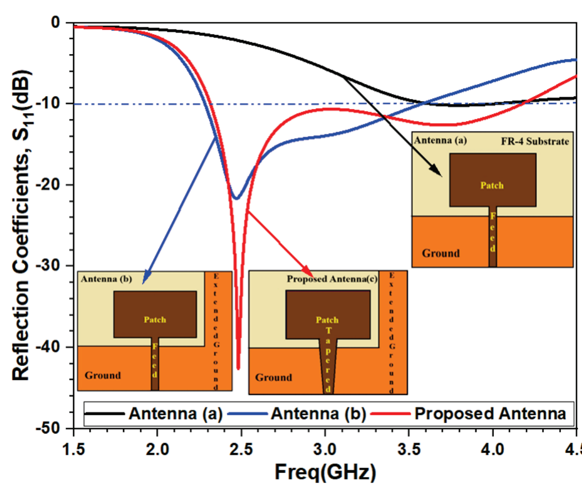

Fig. 3. Reflection coefficient (S_{11}) of antenna design development (step-by-step).

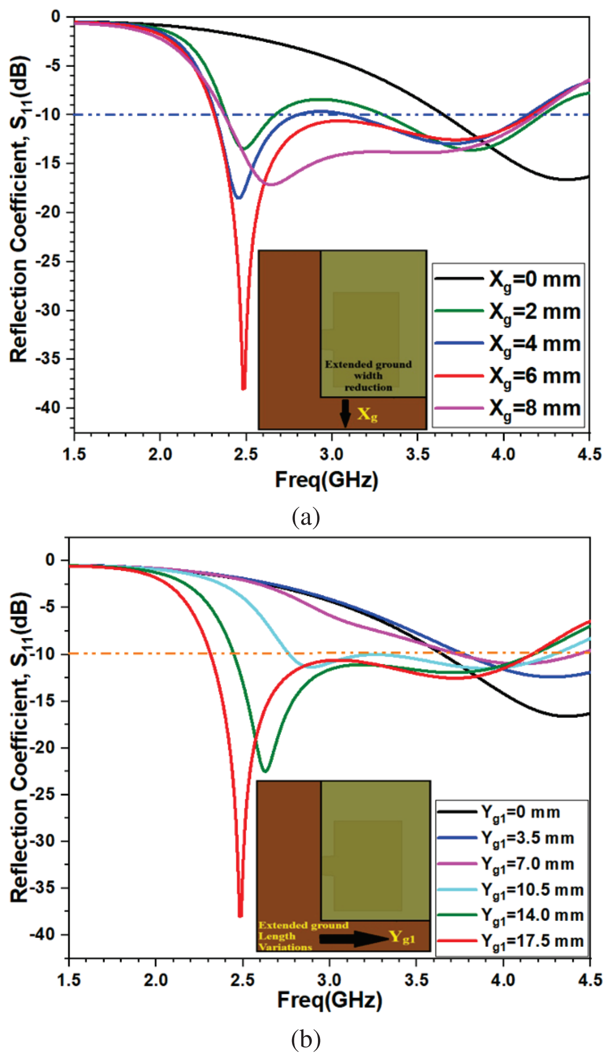

Fig. 4. Effect of the ground geometrical parameters on S_{11} (a) width X_g and (b) length Y_{g1}.

impedance matching and reduces the reflection coefficients well below -10 dB at resonance frequency 2.48 GHz.

The extended ground plane width (X_g) and length (Y_{g1}) variation effects are shown in Fig. 4 (a,b). X_g is changed in a step size of 2 mm and Y_{g1} is varied in a step size of 3.5 mm. The extended ground's width helps to improve impedance matching while its length helps to tune the resonance frequency close to the desired frequency 2.5 GHz. The effect of X_g and Y_{g1} on the reflection coefficient are represented in Fig. 4.

B. Human tissue model properties

The proposed antenna, with the desired resonance frequency at the ISM band (2.4-2.4835 GHz), is now imbedded on a 50×50 mm human tissue for test. It consists of three different layers: skin, fat and muscle. The thicknesses and dielectric properties of the human tissue for the proposed antenna are given in Table 2 [29, 30]. The antenna size is very convenient for the human tissue with antenna resonance. In this research, the antenna is placed on the body in two ways: the antenna ground is in contact with the body (Case 1: reverse Face1) and the antenna patch is in contact with the body (Case 2: front Face2) as shown in Fig. 5.

Table 2: Human tissue layers and their thicknesses [29, 30]

Human Tissue	Thickness (mm)	Conductivity σ (S/m)	Relative Permittivity (ε_r)
Skin	4	1.46	38
Fat	4	0.10	5.28
Muscle	8	1.73	52.7

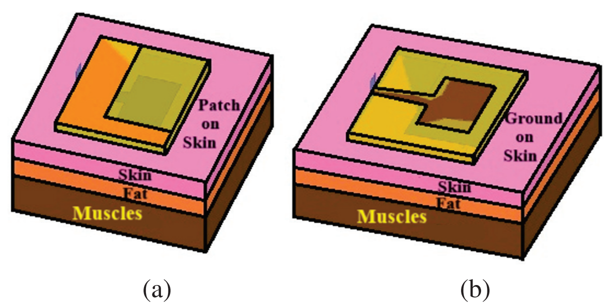

Fig. 5. Antenna placement on the human body phantom model: (a) Case 1 and (b) Case 2.

III. ANTENNA SIMULATION RESULTS AND VALIDATION

The proposed antenna is initially designed and simulated in free space. Subsequently it is evaluated on the body in Case 1 and Case 2 configurations. The S_{11} in the free space case shows an ultra-wide bandwidth of 73% fractional bandwidth ranging from 2.30 GHz to 4.125 GHz covering the full ISM band and resonating at around 2.5 GHz (Fig. 6). It can be noticed that human tissue significantly impacts the antennas behavior, altering the S_{11} peaks and bandwidth. Case 1 most affects the frequency response of the antenna which shifts the frequency band backward resulting in a wider bandwidth. The antenna response is slightly affected in Case 2 configuration with a better impedance matching at higher frequencies. Additionally, in both cases, the antenna preserves its UWB characteristic. The S_{11} plots drop below -10 dB and their corresponding bandwidths become slightly wider compared to the free-space case.

The effect of electromagnetic exposure on the human body has been studied in terms of SAR at 2.4

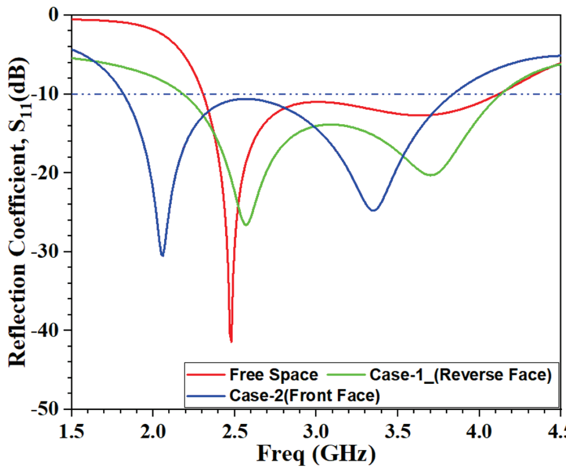

Fig. 6. Reflection coefficients (S_{11}) of the proposed antenna.

GHz. Corresponding results are presented in Fig. 7. It can be observed that the maximum SAR value in both cases is very low. It is well below the FCC/IC limit of 1.6 W/kg (1 g) and the EU limit of 2.0 W/kg (10 g) across the active bandwidth [31].

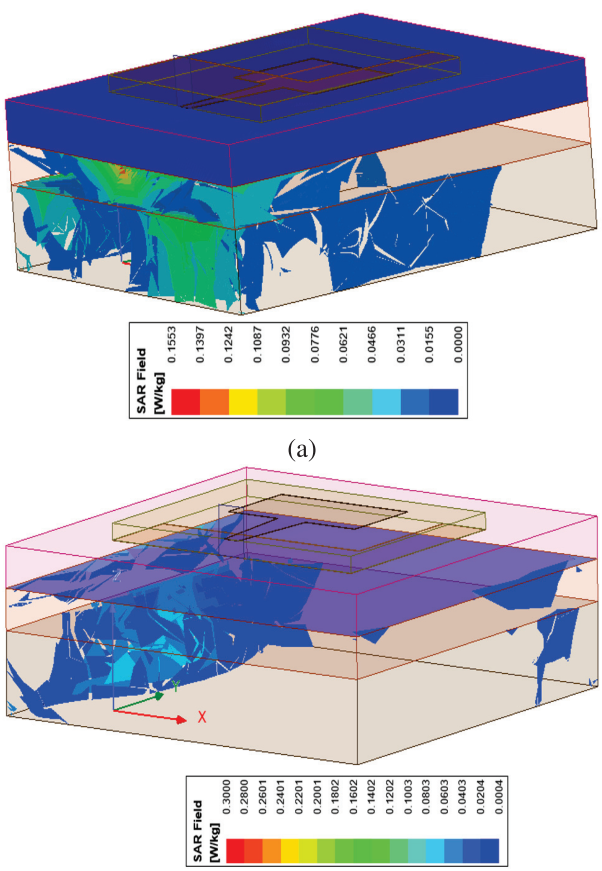

Fig. 7. Antenna 1g SAR at 2.4 GHz (a) Case 1 and (b) Case 2.

The proposed antenna gains in free space and on-body have been evaluated and compared in Fig. 8 (a). It can be observed that the gain of the antenna is improved when it is placed on the body. The peak gain achieved by the antenna in all three cases are higher than 5 dBi. The highest value of the peak gain 5.80 dBi is achieved when the antenna patch touches the body (reverse face). The radiation efficiency, gain and directivity of the proposed antenna simulated in free space and on-body (Cases 1 and 2) are presented in Fig. 8. According to these results, the antenna exhibits the same gain value [Fig. 8 (a)], however, its efficiency decreases by 50% when placed near the human body [Fig. 8 (b)]. Since omnidirectional antennas radiate energy uniformly in every direction of a plane, lower directivity results since power is spread

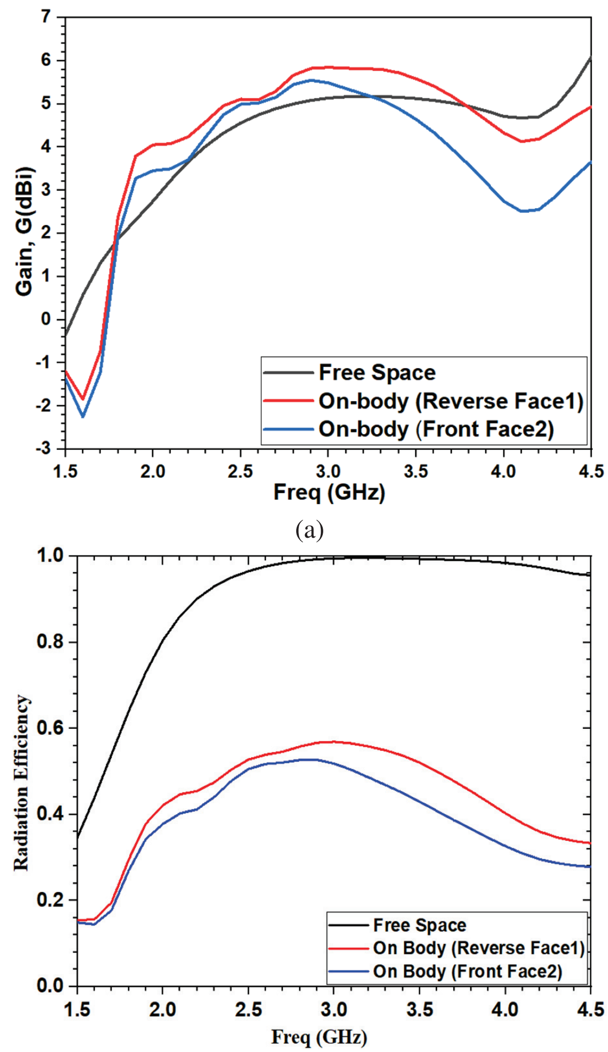

Fig. 8. *Continued.*

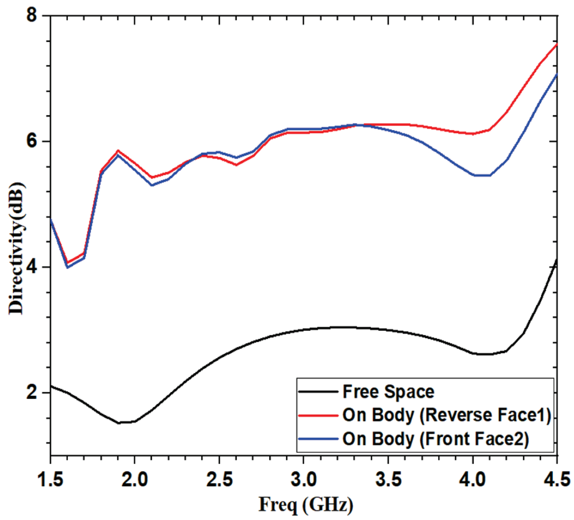

(c)

Fig. 8. Proposed antenna performance parameters: (a) gain, (b) radiation efficiency and (c) directivity.

over a big area. While single-plane antennas can concentrate energy into narrower beams, higher directivity has been achieved by the power that is radiated in one

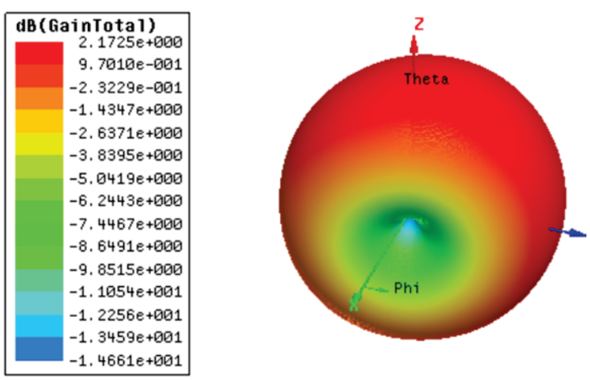

(a)

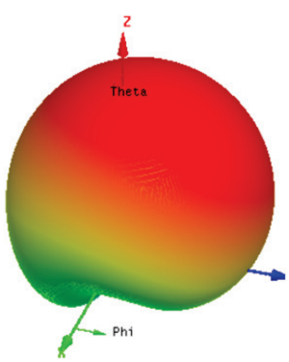

(b)

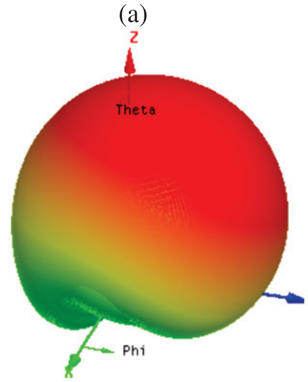

(c)

Fig. 9. Gain 3D plot of the proposed antenna: (a) free space, on-body (b) Case 1 and (c) Case 2.

direction rather than spreading in all directions. The radiation resistance of a half-wavelength dipole is $R = 73\ \Omega$, and the maximum directivity is 1.64. For a quarter-wavelength monopole, the radiation resistance is $73/2\ \Omega$ [32]. As a result, the directivity is multiplied by two as shown in Fig. 8 (c).

The antenna 3D gain plot in free space at 2.45 GHz is depicted in Fig. 9 (a). In free space, the antenna exhibits an omnidirectional radiation pattern. However, when the antenna is placed on the human body, the body acts as a reflector. This alters the radiation pattern of the antenna. Considering all the factors mentioned, it becomes evident that the radiation pattern, as illustrated in Figs. 9 (b-c), improves antenna directivity and is the primary factor responsible for affecting radiation efficiency.

According to the surface current distributions shown in Fig. 10 and the E- and H-field distributions presented

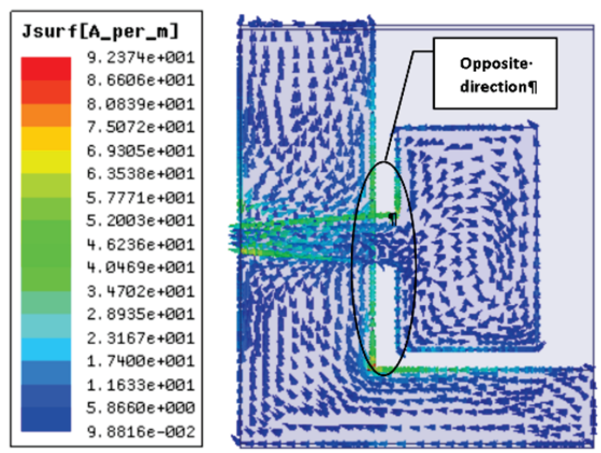

(a)

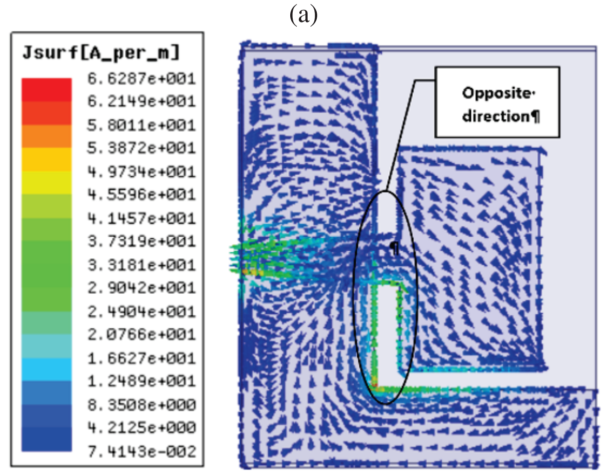

(b)

Fig. 10. Surface current density distribution of the proposed antenna at 2.4 GHz: (a) front Face1 (b) reverse Face2.

in Fig. 11, the proposed antenna can be qualified as a magnetic dipole. A magnetic dipole antenna is characterized by two parallel wires of equal lengths, fed with alternating current in opposite phases [33]. By examining Fig. 11 (a), it is evident that the normal component of the electric field is significantly weaker compared to the tangential component H-field depicted in Fig. 11 (b). This disparity in field strengths helps to explain the resulting low SAR. Additionally, it is important to note that biological tissues possess a high dielectric constant, which acts as a reflector. Consequently, the normal components of the E-field are reflected in free space, as illustrated in Fig. 11 (a).

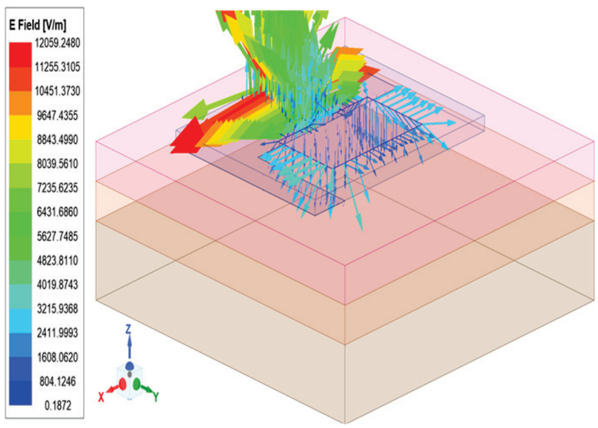

(a)

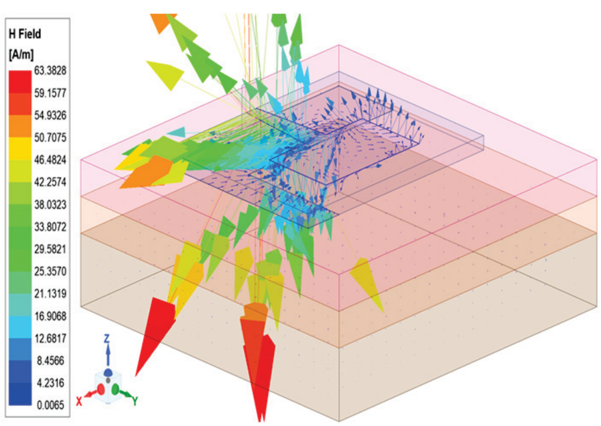

(b)

Fig. 11. Field distribution of the proposed antenna at 2.4 GHz: (a) E-field and (b) H-field.

A prototype antenna (Fig. 12) is fabricated and measured to validate the simulation results. The reflection coefficient (S_{11}) in free space and on the human body, for both cases, is measured at 2.4 GHz. The simulated and measured reflection coefficient of the proposed antenna

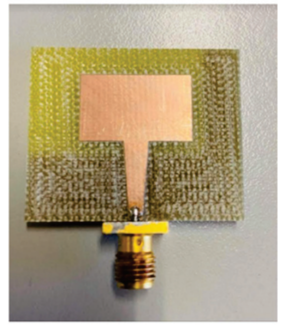

(a)

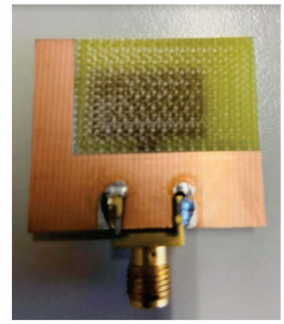

(b)

(c)

Fig. 12. Prototype of the proposed antenna: (a) top face, (b) bottom face and (c) on-body (Case 2).

in free space and on the body are illustrated in Fig. 13. The simulated and measured results are found to agree well within the operating band.

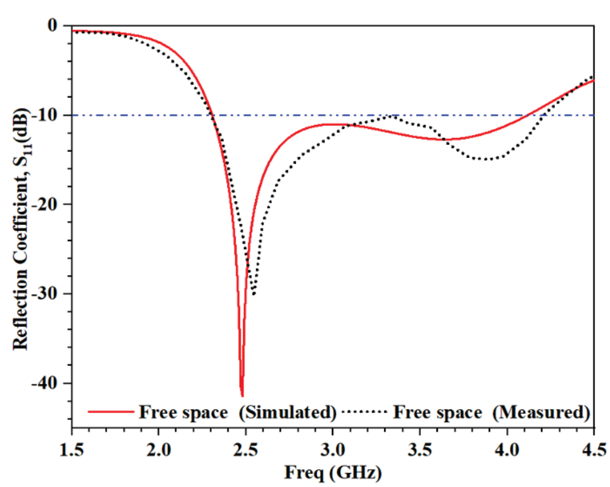

(a)

Fig. 13. *Continued.*

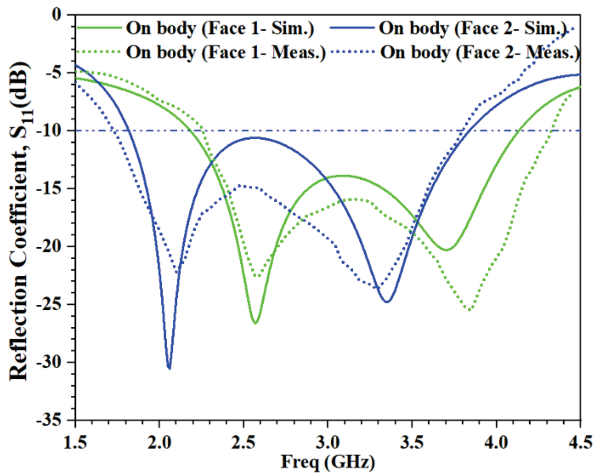

(b)

Fig. 13. Simulated and measured S_{11} in (a) free space and (b) on-body (Case 1 and Case 2).

IV. EQUIVALENT CIRCUIT ANALYSIS

The RLC resonator model is commonly used to model microwave sensors and radiating antennas [34, 35]. Various studies have developed equivalent circuits for resonant antenna structures, such as Chu's [36] dipole antenna circuit. To avoid the complexity of calculating the total electric energy in the capacitances of the equivalent circuit, Chu approximates it using a simple series RLC circuit. The values of these components are determined by equating the resistance, reactance and the derivative of reactance with those of the series RLC circuit [36]. Recent research works have also focused on antenna design using electrical circuits. They often compare commercial software results with electrical models through S-parameters [34].

In the field of antenna design, a radiating structure is represented by an RLC electrical equivalent circuit model (ECM). To accurately characterize the radiator's behavior, the circuit elements (R, L and C) must be precisely derived. Many studies [35] propose lumped equivalent circuit models based on S-parameter amplitudes; however, these models often fail to provide precise RLC values, leading to an incomplete understanding of the radiator's behavior within the operating band.

This study differs by deriving the RLC components from complex-valued impedance parameters obtained through ADS simulations, validated against HFSS results. This approach enables better differentiation between resonant modes, such as radiating, non-radiating and adaptation modes. The proposed antenna's RLC equivalent circuit is modeled as a parallel combination of impedances [28, 34, 35], with circuit models for free space and on-body scenarios (Case 1 and Case 2) shown in Figs. 14 and 15.

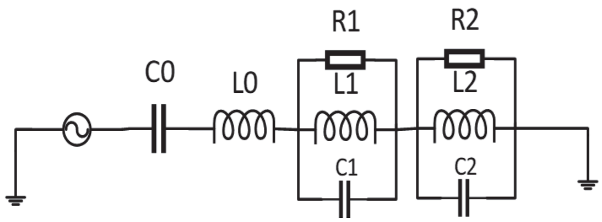

Fig. 14. Equivalent circuit model of the proposed UWB antenna in free space.

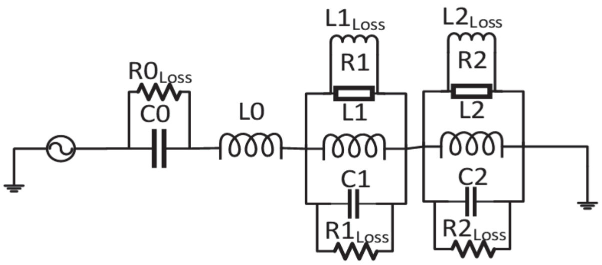

Fig. 15. Antenna equivalent circuit model on the human body (Case 1 and Case 2).

Furthermore, it is commonly accepted in the literature that UWB applications can be modeled such that each resonant mode is represented by a parallel RLC component [37, 38]. This modeling strategy captures the interactions of multiple adjacent resonant circuits within UWB antennas, effectively characterizing their input impedance characteristics. Since our work involves UWB applications with two distinct resonant modes, we represent these modes using two parallel blocks of RLC components. Understanding how equivalent circuit models adapt to different environments, such as off- and on-body, is key to analyzing antenna behavior.

A. In free space

The antenna's equivalent circuit features two parallel RLC blocks R1, L1, C1 and R2, L2, C2, starting with capacitors C_0 and inductance L0. The antenna's physical dimensions and geometry as well as its operating frequency determine these inductances. The circuit model includes resistors that account for losses due to radiation and material imperfections and capacitors that represent the antenna's ability to store electric energy. This parallel configuration allows for multiple resonant modes within the antenna.

B. On human body Case 1

Where the antenna is in direct contact with the human body, the equivalent circuit model effectively captures this direct interaction with the lossy medium. The configuration comprises two parallel RLC blocks R1, L1, C1 and R2, L2, C2, with capacitors C0 in parallel with a shunt resistor $R0_{Loss}$ Lossand inductance L0.

In this model, resistors R1 and R2 are positioned in parallel with their respective lossless inductances $L1_{Loss}$ and $L2_{Loss}$.

C. On human body Case 2

While the same configuration applies on human body Case 2, where the antenna is not in direct contact with the body, the values of these components will be fine-tuned based on performance metrics such as input impedance and return loss under varying conditions. This adjustment is crucial for optimizing the antenna's performance when coupled to the human body, ensuring effective energy transfer while minimizing losses due to tissue absorption. The equivalent circuit model provides a more accurate representation of antenna behavior when placed on or near the human body. By incorporating these parallel blocks, it allows for an analysis of how different resonant modes interact and how both the antenna's characteristics and its environment influence them. The inclusion of lossless inductances and shunt resistors simulates energy dissipation in a lossy medium while maintaining an accurate depiction of critical resonant frequencies necessary for effective operation in UWB applications.

When the antenna is placed on the human body (lossy medium), the equivalent circuit remains almost the same compared to the equivalent circuit in free space. Inductances L0, L1 and L2 remain the same as in free space, and when the human body is a lossy medium, the resistors R1 and R2 can be represented by lossless inductances $L1_{Loss}$ and $L2_{Loss}$, respectively, and the capacitors C0, C1 and C2 can be represented by shunt resistors R0Loss, R1Loss and R2Loss, as shown in Fig. 15 for on-body placement Case 1 and Case 2.

Table 3: Element values of the equivalent circuit model in free space, on-body (Case 1) and on-body (Case 2)

Components	Free Space	On-body (Case 1)	On-body (Case 2)
R1 (Ω)	75	49	74
L1 (nH)	0.746	0.973	1.304
C1 (pF)	6.449	6.129	4.020
R2 (Ω)	82	42	68
L2 (nH)	1.084	0.760	1.334
C2 (pF)	2.182	3.161	1.918
L0 (nH)	1.985	1.902	2.758
C0 (pF)	2.397	2.023	1.590
$L1_{Loss}$ (nH)	– – – –	1808	30000
$L2_{Loss}$ (nH)	– – – –	20.677	20.507
$R1_{Loss}$ (kΩ)	– – – –	1.500	37.257
$R2_{Loss}$ (kΩ)	– – – –	5	2.908
$R0_{Loss}$ (kΩ)	– – – –	5	2.228

The input impedance and reflection coefficients of the proposed antenna in free space using HFSS and equivalent circuit models using ADS are compared in Fig. 16, in Fig. 17 for Case 1 and in Fig. 18 for Case 2. Excellent agreement between the circuit model and the EM model have been achieved. The optimized elements values are shown to be very close to each other and are listed in Table 3.

Table 4 summarizes the obtained results compared with the literature at 2.4-2.5 GHz ISM band. It is clear that the proposed design shows interesting performances in terms of reduced size and low reflection, its innovative and simple structure and practical feasibility places it among the most competitive antennas.

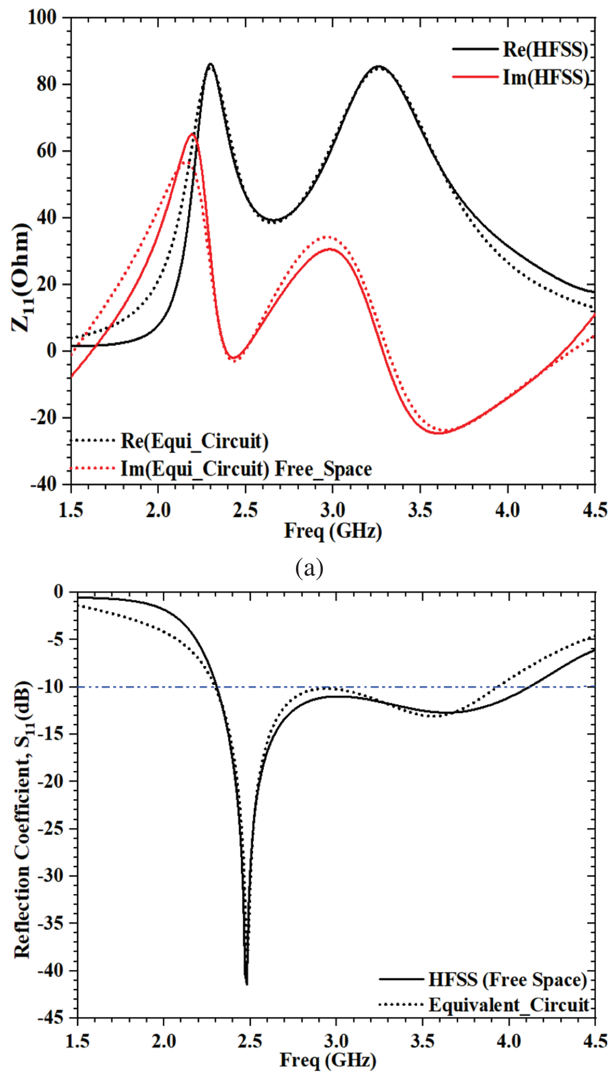

Fig. 16. Simulated results compared to EM model in free space: (a) input impedance and (b) S_{11}.

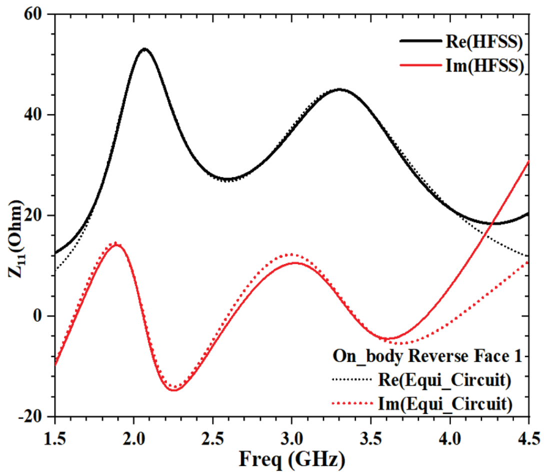

(a)

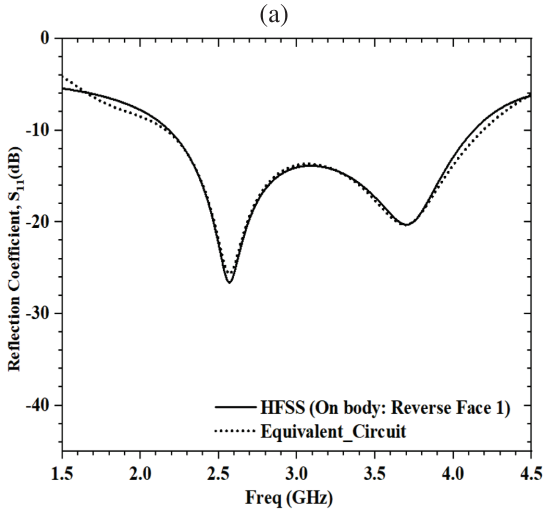

(b)

Fig. 17. Simulated results compared to EM model of the proposed antenna on-body (Case 1): (a) input impedance and (b) S11.

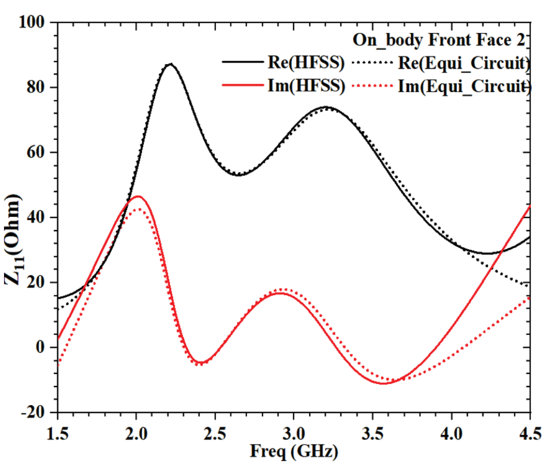

(a)

Fig. 18. *Continued.*

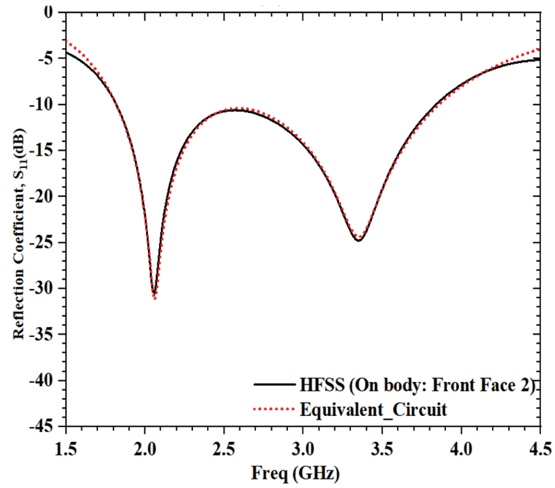

(b)

Fig. 18. Simulated results compared to EM model of the proposed antenna on-body (Case 2): (a) input impedance and (b) S11.

Table 4: Comparative analysis of proposed and reference antennas

Ref	**Size (mm^2)**	**Resonating Frequency f_r (GHz)**	**S_{11} (dB)**	**Gain (dBi)**
[5]	50×16	2.45	−14.2	1.98 On-body
[6]	62×43	2.45	−23	3.01 Off-body 2.11 On-body
[16]	60×60	2.4	−25.90	4.66 Off-body
[17]	50.33×32	2.4	−22	Not Given
[18]	35×40	2.4	−31	Not Given
[19]	55×60	2.45	−29.73	7.04 Off-body
[20]	41.5×29	2.45	−36.66	Not Given
This work	28×34	2.48	−42.59	5.80 On-body

V. CONCLUSION

This paper presents a low SAR miniaturized microstrip UWB monopole antenna operating at 2.48 GHz for ISM band biomedical applications. The proposed antenna is fabricated and good agreement is realized between simulation and measurement results. To facilitate analysis and optimization, an RLC electrical equivalent circuit model of the antenna is developed and fine-tuned using ADS software. The proposed antenna holds significant potential for enabling safe and efficient wireless communication with the human body. Its compatibility with UWB and ISM band applications, combined with its excellent performance characteristics, make it a promising solution for future on-body communication systems.

ACKNOWLEDGMENT

This publication has received funding from the European Union's Horizon 2020 research and innovation program under grant agreement H2020-MSCA-RISE-2018-eBorder-872878. This publication has received funding from the European Union's Horizon Europe research and innovation program under grant agreement HE-MSCA-SE-6G-TERAFIT- 101131501. This work is also funded by the FCT/MEC through national funds and when applicable co-financed by the ERDF, under the PT2020 Partnership Agreement under the UID/EEA/50008/2020 and UIDP/50008/2020 project. This work was supported in part by the DGRSDT (Direction Générale de la Recherche Scientifique et du Development Technologique), MESRS (Ministry of Higher Education and Scientific Research), Algeria.

REFERENCES

[1] S. Ahmad, B. Manzoor, M. M. Shair, S. Khan, A. Akram, A. Ghaffar, A. J. Abdullah Al-Gburi, E. M. Ali, F. Arpanaei, and M. Alibakhshikenari, "Novel implantable antenna with miniaturized footprint size for wideband biomedical telemetry applications," *Frequenz,* vol. 77, no. 5-6, pp. 293-301, 2023.

[2] S. M. A. Shah, M. Zada, J. Nasir, O. Owais, A. Iqbal, and H. Yoo, "Miniaturized four-port MIMO implantable antenna for high-data-rate wireless-capsule-endoscopy applications," *IEEE Transactions on Antennas and Propagation*, vol. 71, no. 4, pp. 3123-3133, 2023.

[3] A. Sharma, E. Kampianakis, and M. S. Reynolds, "A dual-band HF and UHF antenna system for implanted neural recording and stimulation devices," *IEEE Antennas Wireless Propag. Lett.*, vol. 16, pp. 493-496, 2017.

[4] D. Hecht, I. Ullmann, D. Oppelt, T. Pfahler, N. Amer, and M. Vossiek, "Millimeter-wave imaging and near-field spectroscopy for burn wound assessment," *Frequenz,* vol. 76, no. 11-12, pp. 661-667, 2022.

[5] I. Gil and R. Fernández-García, "Wearable PIFA antenna implemented on jean substrate for wireless body area network," *Journal of Electromagnetic Waves and Applications*, vol. 31, no. 11-12, pp. 1194-1204, 2017.

[6] S. M. Ali, V. Jeoti, T. Saeidi, and W. P. Wen, "Design of compact microstrip patch antenna for WBAN applications at ISM 2.4 GHz," *Indonesian Journal of Electrical Engineering and Computer Science*, vol. 5, no. 3, pp. 1509-1516, 2019.

[7] R. Bala, R. Singh, A. Marwaha, and S. Marwaha, "Wearable graphene based curved patch antenna for medical telemetry applications," *Applied Computational Electromagnetics Society* (*ACES*) *Journal,* pp. 543-550, 2016.

[8] N. Ojaroudi, M. Ojaroudi, N. Ghadimi, and M. Mehranpour, "UWB square monopole antenna with omni-directional radiation patterns for use in circular cylindrical microwave imaging systems," *Applied Computational Electromagnetics Society* (*ACES*) *Journal*, pp. 123-129, 2013.

[9] D. Sayad, C. Zebiri, H. Obeidat, I. Elfergani, A. Amroun, A. Palandoken, M. L. Bouknia, R. Zegadi, and J. Rodriguez, "New elliptical miniaturized antenna using concentric open rings for UWB applications," *Progress In Electromagnetics Research C*, vol. 134, pp. 79-91, 2023.

[10] A. Amroun, C. Zebiri, D. Sayad, I. Elfergani, A. Desai, M. L. Bouknia, R. Zegadi, and J. Rodriguez, "Miniaturized six-ring elliptical monopole-based MIMO antenna for ultrawideband applications," *International Journal of Communication Systems*, vol. 36, no. 14, p. e5557, 2023.

[11] C. Bensid, M. L. Bouknia, D. Sayad, I. Elfergani, H. Bendjedi, R. Zegadi, J. Rodriguez, A. Varshney, and C. Zebiri "Novel pentagonal-shaped monopole antenna with a CSRR metamaterial loaded defected ground for UWB applications," *Progress in Electromagnetics Research C*, p. 139, 2023.

[12] Y. Tighilt, C. Bensid, D. Sayad, S. Mekki, R. Zegadi, M. L. Bouknia, I. Elfergani, P. Singh, J. Rodriguez, and C. Zebiri, "Low-profile UWB-MIMO antenna system with enhanced isolation using parasitic elements and metamaterial integration," *Electronics*, vol. 12, no. 23, p. 4852, 2023.

[13] F. Benmahmoud, P. Lemaitre-Auger, and S. Tedjini, "Wearable folded planar dipole antenna: Design and assessment for on-body wireless communication devices," *IEEE Antennas and Propagation Magazine*, vol. 65, no. 1, pp. 27-39, 2023.

[14] T. S. See and Z. N. Chen, "Experimental characterization of UWB antennas for on-body communications," *IEEE Transactions on Antennas and Propagation*, vol. 57, no. 4, pp. 866-874, 2009.

[15] A. Lak, Z. Adelpour, H. Oraizi, and N. Parhizgar, "Design and SAR assessment of three compact 5G antenna arrays," *Scientific Reports*, vol. 11, no. 1, p. 21265, 2021.

[16] G. Demirbas and A. K. A. R. Ekrem, "Design and interpretation of microstrip patch antenna operating

at 2.4 GHz for wireless WI-FI application," *Avrupa Bilim ve Teknoloji Dergisi*, vol. 34, pp. 672-675, 2022.

[17] M. Salim and A. Pourziad, "A novel reconfigurable spiral-shaped monopole antenna for biomedica applications," *Progress in Electromagnetics Research Letters*, vol. 57, pp. 79-84, 2015.

[18] X. Guo, Y. Hang, Z. Xie, C. Wu, L. Gao, and C. Liu, "Flexible and wearable 2.45 GHz CPW-fed antenna using inkjet-printing of silver nanoparticles on pet substrate," *Microwave and Optical Technology Letters*, vol. 59, no. 1, pp. 204-208, 2017.

[19] M. S. Islam, M. I. Ibrahimy, S. M. A. Motakabber, A. Z. Hossain, and S. K. Azam, "Microstrip patch antenna with defected ground structure for biomedical application," *Bulletin of Electrical Engineering and Informatics*, vol. 8, no. 2, pp. 586-595, 2019.

[20] S. Sukhija and R. K. Sarin, "Design and performance of two-sleeve low profile antenna for biomedical applications," *Journal of Electrical Systems and Information Technology*, vol. 4, no. 1, pp. 49-61, 2017.

[21] D. Elshaekh, S. Kayed, and H. Shawkey, "Single-chip two antennas for MM-Wave self-powering and implantable biomedical devices," *Applied Computational Electromagnetics Society* (*ACES*) *Journal,* vol. 36, no. 7, pp. 885-893, 2021.

[22] W. Huang and A. A. Kishk, "Compact antenna designs for wearable and medical portable systems," *Applied Computational Electromagnetics Society* (*ACES*) *Journal,* vol. 26, no. 4, Apr. 2011.

[23] E. Pittella, P. Bernardi, M. Cavagnaro, S. Pisa, and E. Piuzzi, "Design of UWB antennas to monitor cardiac activity," *Applied Computational Electromagnetics Society* (*ACES*) *Journal,* vol. 26, no. 4, pp. 267-274, Apr. 2011.

[24] R. S. Mpanda, L. Qi, Q. Liang, L. Xu, J. Shi, and L. Zhao, "Design and evaluation of typical antennas for monitoring vital signs," *Applied Computational Electromagnetics Society* (*ACES*) *Journal*, pp. 497-505, 2019.

[25] A. Varshney, V. Sharma, T. M. Neebha, and N. P. Kumari, "Notch-band eliminator wideband CSRR loaded monopole fractal antenna for ISM and PCS communications," *World Journal of Engineering*, vol. 21, no. 4, pp. 821-834, 2024.

[26] A. Varshney, T. M. Neebha, V. Sharma, and A. D. Andrushia, "Low-cost L-band to Ku-band frequency reconfigurable BAR64-02V controlled antenna for satellite, military, and radar applications," *IETE Journal of Research*, vol. 70, no. 6, pp. 1-14, 2024.

[27] T. M. Neebha, A. D. Andrushia, P. M. Bruntha, A. Varshney, R. Manjith, and S. Dhanasekar, "On the design of miniaturized C-shaped antenna based on artificial transmission line loading technique," *Journal of Electromagnetic Waves and Applications*, vol. 37, no. 6, pp. 814-826, 2023.

[28] A. Varshney, V. Sharma, and A. K. Sharma, "RLC-equivalent circuit-based stub loaded 2x2 MIMO antenna for wireless applications," *Microwave Review*, vol. 29, no. 1, pp. 44-54, 2023.

[29] Z. Duan, Y. X. Guo, R. F. Xue, M. Je, and D. L. Kwong, "Differentially fed dual-band implantable antenna for biomedical applications," *IEEE Transactions on Antennas and Propagation,* vol. 60, no. 12, pp. 5587-5595, 2012.

[30] S. Gabriel, R. W. Lau, and C. Gabriel, "The dielectric properties of biological tissues: III. Parametric models for the dielectric spectrum of tissues," *Physics in Medicine & Biology*, vol. 41, no. 11, p. 2271, 1996.

[31] J. C. Lin, "RF health safety limits and recommendations [Health Matters]," *IEEE Microwave Magazine*, vol. 24, no. 6, pp. 18-77, 2023.

[32] J. L. Volakis, *Antenna Engineering Handbook*. New York: McGraw-Hill Education, 2007.

[33] J. R. James, P. S. Hall, and C. Wood, "Microstrip antenna: Theory and design," *IET*, vol. 12, 1986.

[34] S. Mekki, R. Zegadi, S. Mosbah, D. Sayad, I. Elfergani, M. L. Bouknia, J. Rodriguez, A. Desai, M. Palandoken, and C. Zebiri, "Equivalent circuit of a planar microwave liquid sensor based on metamaterial complementary split ring resonator," *Frequenz*, vol. 78, no. 1-2, pp. 37-45, 2024.

[35] S. Mekki, A. Varshney, D. Sayad, I. Elfergani, H. Bendjedi, M. L. Bouknia, R. Zegadi, J. Rodriguez, M. Palandoken, K. Karaçuha, and C. Zebiri, "Design and investigation of orthogonal hybrid dual-mode single-CDR-based MIMO antenna with high self-isolation at 5.8 GHz," *IEEE Access*, vol. 12, pp. 187234-187254, 2024.

[36] L. J. Chu, "Physical limitations of omni-directional antennas," *J. Appl. Phys.*, vol. 19, p. 1163, 1948.

[37] Y. Wang, J. Li, and L. X. Ran, "An equivalent circuit modeling method for ultra-wideband antennas," *Progress in Electromagnetics Research*, vol. 82, pp. 433-445, 2008.

[38] P. Prabhu, M. Subramani, and K.S. Kwak, "Analysis of integrated UWB MIMO and CR antenna system using transmission line model with functional verification," *Scientific Reports*, vol. 12, no. 1, p. 14128, 2022.

Chemseddine Zebiri received an Engineering degree in Electronics from the University of Constantine, Algeria, in 2001, and a Magister degree from the University of Ferhat Abbas, Algeria, in 2003. He joined the Department of Electronics, University of Ferhat Abbas, Sétif, Algeria, as a senior lecturer in 2006, where he is currently a professor at the same department and Director of the Power Electronics and Industrial Control Laboratory (LEPCI). He received his Ph.D. degree in electronics from the University of Constantine in 2011. Zebiri has published 160 journals and refereed conference papers. His current research interests are dielectric resonator antennas, MIMO antennas, mmWave antennas, magnetic materials, microwave sensors, and complex material components in the microwave and optical domains. Zebiri is the Guest editor/special issue of *Electronics* “Recent Advances in Antenna Design for 5G Heterogeneous Networks volume II” (ISSN 2079-9292), and Guest Editor/special issue of *CMES - Computer Modeling in Engineering and Sciences* “Green IoE for Smart 5G and Beyond (5GB) Applications.” He reviews several good-ranked journals such as the *International Journal of Microwave and Wireless Technologies* and *Wireless Communications and Mobile Computing*. He has been on the technical program committee of a large number of international conferences.

Samira Mekki received her master’s degree in telecommunications systems in 2018 from Akli Mohand Oulhadj University of Bouira, Algeria. Currently, she is a Ph.D. student in telecommunication systems at Ferhat Abbas University-Setif, Department of Electronics. Her research interests are in the simulation and fabrication of antennas, MIMO antennas and equivalent circuits.

Djamel Sayad received a Ph.D. degree in electronics from the University of Skikda, Algeria, in 2017. He is currently a Lecturer with the Department of Electrical Engineering, University of Skikda. He has several journals and conference articles publications covering a wide area in the design of antennas using metamaterial and dielectric antennas. His current research interests include electromagnetics complex media and microwave propagation and antennas.

Mohamed Lamine Bouknia received his master’s degree from the University of Ferhat Abbas, Algeria, in 2017 and his Ph.D. degree in telecommunication systems from the University of SETIF, Algeria, in 2022. He is currently a Lecturer with the Electronics Department, University of FERHAT Abbas, SETIF. He has several journals conference articles and publications treating the complex medium the antenna features and the design of antennas. His current research interests include electromagnetics complex media and microwave propagation and antennas.

Rami Zegadi obtained his bachelor’s degree in Electronics from the University of Ferhat Abbas, Sétif 1, Algeria, in 2015, and his master’s degree from the University of Ferhat Abbas, Algeria, in 2017. He received his Ph.D. degree from the University of Farhat Abbas, Setif 1, Algeria, in 2021. His dissertation was devoted to the study of light propagation in silicon-based nanostructured waveguides. Since 2021, he has been in the electronics department as a lecturer at the University of Farhat Abbas, Setif 1. He is interested in photonic integrated circuits for optical communication, antennas, and sensing applications.

Issa Elfergani (Senior Member, IEEE) received M.Sc. and Ph.D. degrees in electrical and electronic engineering from the University of Bradford, UK, in 2008 and 2013, respectively. Since 2013, he has been working as a Postdoctoral Researcher then as an Investigator Junior at the Mobile Systems Group, Instituto de Telecomunicações, Aveiro, Portugal. In 2014, he received the prestigious FCT Fellowship for his postdoctoral research. The evaluation of the first triennium of this scholarship was given an excellent rating by the evaluators. He is currently a Senior Researcher with the Instituto de Telecomunicações, working with European research- funded projects while leading technical activities in antenna design for ENIAC ARTEMOS (2011-2014), EUREKA BENEFIC (2014-2017), CORTIF (2014-2017), GREEN-T (2011-2014), VALUE (2016-2016), THINGS2DO (2014-2018), H2020-ITN-SECRET (2017-2020), POSITION-II (2018-2021), and Moore4Medical (2019-2023), some of the projects have been successfully concluded and some still ongoing. He is also working on (5GWAR) Novel 5G Millimetre-Wave Array Antennas for Future Mobile Handset Applications as a principal investigator. He is also an Honorary Visiting Research Fellow with the Faculty of Engineering and Informatics, University of Bradford, UK. He has around 160 high-impact publications in international conferences, journal papers, and books/book chapters with a Google Scholar H-index of 21. He is a member of IET. He is the Guest Editor/Special Issue of “Electronics Recent Technical Developments in Energy Efficient 5G Mobile Cells” and Special Issue on *Recent Advances in Engineering Systems Journal* (ASTESJ), a Guest Editor/Special Issue of *Electronics* “Recent Advances in Antenna Design for 5G Heterogeneous Networks,” and a Guest Editor/Special Issue of *Electronics* “Unable RF Front-End Circuits for 5G and Beyond: Design, Challenges and Applications.”

Atul Varshney received his Ph.D. at the Department of Electronics and Communication Engineering, Gurukula Kangri (Deemed to be University), Haridwar, India, in 2023, M.Tech. degree in microwaves from Madhav Institute of Engineering and Technology and Science, Gwalior, India in 2008, and B.Tech. degree in electronics and communication engineering from UPTU, Lucknow, India, in 2005. His research interests include the fabrication and design of microstrip to waveguide transitions, ring resonators, microwave filters, all types of antenna design, metamaterial and fractal structures, RLC electrical equivalent circuits generation of any microwave 2D/3D components, filters, frequency and pattern reconfigurable antennas. He is an RF microwave and antenna researcher and published nine patents, more than 75 research articles in SCI and Scopus-indexed journals, conferences, and three national and international books in this particular area.

Jonathan Rodriguez (Senior Member, IEEE) received the master's and Ph.D. degrees in electronic and electrical engineering from the University of Surrey, UK, in 1998 and 2004, respectively. In 2005, he became a Researcher at the Instituto de Telecomunicações, Portugal. In 2017, he was appointed as a Professor of mobile communications at the University of South Wales, UK. He has served as a Project Coordinator for major international research projects, including Eureka LOOP, FP7 C2POWER, and H2020-SECRET, whilst serving as a Technical Manager for FP7 COGEU and FP7 SALUS. He is the author of more than 500 scientific works, including 11 book editorials. He is a fellow of the IET (FIET) and a Senior Fellow of the Higher Education Academy (SFHEA). His professional affiliations include Chartered Engineer (C.Eng.).

Uncertainty Quantification of Transmission Efficiency in EV-WPT System Based on Gaussian Process Regression

T. H. Wang, K. F. Zhao, H. W. Duan, Q. Y. Yu, L. L. Xu, and S. S. Guan

College of Instrumentation & Electrical Engineering
Jilin University, Changchun 130026, China
wangtianhao@jlu.edu.cn, zhaokf23@mails.jlu.edu.cn, duanhw24@mails.jlu.edu.cn,
qyyu20@mails.jlu.edu.cn, xull21@mails.jlu.edu.cn, guanshanshan@jlu.edu.cn

Abstract – The power transfer efficiency of electric vehicle wireless power transmission (EV-WPT) systems is susceptible to differences in the processing of coils and circuit components as well as the driver's operating level. In order to quantify the uncertainty and save the computational cost, this paper adopts the Gaussian process regression (GPR) agent model to obtain predicted confidence intervals and transmission efficiency probability density function and calculates the response surface based on the agent model, and finally analyzes the degree of the influence of each variable on transmission efficiency by using the Morris one-at-a-time (MOAT) method. The computational time cost of the GPR agent-based model uncertainty quantification method obtained through simulation experiments is 9 hours and 21 minutes, which improves the computational time by 94.5% compared to the Monte Carlo (MC) method. The prediction error of the predicted values of the GPR agent model is only 1.0294% of the measured values, and its variance error is only 3.5587% of the measured values, so that the GPR agent model is able to realize uncertainty quantification (UQ) accurately and efficiently. Results show that the offset between the coupling mechanism and the diameter of the transmitting coil cross-section are the main factors affecting transmission efficiency.

Index Terms – Gaussian process regression, power transmission efficiency, uncertainty quantification, vehicle engineering, wireless power transfer.

I. INTRODUCTION

As the problems of social environmental pollution, energy crisis and global warming become more and more prominent, the development and utilization of clean energy has become an inevitable trend of today's social development [1-3]. At the same time, with the advancement of related technologies in the field of new energy electric vehicles (EVs), EVs have gained more and more attention and recognition from automobile manufacturers and consumers [4, 5]. Compared with fuel vehicles, EVs can effectively reduce pollutant emissions, carbon emissions and consumption of non-renewable resources, and can realize high energy conversion efficiency [6, 7]. However, the rapid development of EVs still faces many problems, such as long charging and queuing waiting times, bulky batteries and insufficient effective range. In addition, the rapid development of the EV industry has put forward urgent requirements for improving EV charging technology and accelerating the construction of charging facilities [8].

EV charging methods can be mainly categorized into cable charging and wireless charging. With the rapid development of the new energy electric vehicle industry, its charging method has improved on the traditional cable charging method [9]. Wireless power transfer (WPT) technology is the core development direction of the intelligent transportation field, and safe and reliable WPT technology is a key step to promote all kinds of intelligent mobile devices to realize the interconnection of everything [10]. When using wired charging to charge vehicles, a person needs to manually connect the charging gun to the EV charging port. The exposed charging gun can develop problems caused by repeated plugging and unplugging, and is difficult to use in open air in wet environments such as rain and snow [11]. Since charging requires manual operation, it is generally installed in dedicated charging locations, such as garages and parking lots, and cannot realize flexible charging. Unlike the wired charging method, wireless charging technology charges through non-physical contact, which is conducive to improving the reliability, flexibility, automation and intelligence of the system [12]. WPT technology removes the mechanical interface, improves safety, achieves charging in operation and overcomes drawbacks of the traditional cable charging method. The technology is gradually maturing [13], and is expected to become typical of EV charging technology in the future [14]. Unlike the wired charging method, wireless charging is carried out through non-physical contact, thus avoiding interaction between human and

Submitted On: November 8, 2024
Accepted On: March 18, 2025
https://doi.org/10.13052/2024.ACES.J.400307

charging equipment, improving the reliability and safety of the system, and completely eliminating the need for manual operation, which is more conducive to the realization of the intelligence and automation of the EV charging process [15].

However, for the performance index of wireless power transmission efficiency, due to the complexity of the design and control of the transmission system and the differences in the actual operation techniques, the relevant factors in the design of the coil structure, transmission distance, coupling mechanism offset and compensation topology parameters directly or indirectly affect the transmission efficiency of the system [16]. Considering the uncertainty of the above relevant factors as input parameters inevitably leads to uncertainty in the transmission efficiency of electric vehicle wireless power transmission (EV-WPT) systems, so accurately quantifying the magnitude of uncertainty in the transmission efficiency of EV-WPT systems is beneficial to the design of engineering structures and decision-making.

Parameter uncertainty quantification (UQ) methods include statistical and non-statistical methods, of which the statistical methods are dominated by the Monte Carlo (MC) method and its improvements, which usually require a large number of calculations to achieve good accuracy. When the complexity and computational cost of the test system are high, MC and its improved methods are not applicable and are usually only used to verify the accuracy of other UQ methods [17, 18]. The non-statistical type of method obtains an approximate alternative model by learning the real model, and the subsequent calculation of UQ does not need to call the original real model, which greatly reduces the computational cost. When computational accuracy is controlled within a reasonable range, it can usually replace the MC method for UQ analysis, and has been widely researched and applied [19–22]. Rossi et al. [21] combined the theory of the generalized chaotic polynomials approach (gPCE) with the radiative near-field in the device-to-equipment, and constructed a UQ framework for the power transfer efficiency of WPT systems, which proved to be more flexible and efficient than the on-the-fly configuration method based on a single gPCE and the direct MC analysis [23]. The mapping solution process of the PCE agent model brings the problem of "dimensionality catastrophe". With the development of artificial intelligence, machine learning has been gradually applied to the field of WPT electromagnetic compatibility. Trinchero et al. [22] investigated the least-squares support vector machine (LS-SVM) regression and its optimization form to quantify the uncertainty of WPT transmission efficiency and proved that LS-SVM regression based on kernel technology can better solve the high-dimensional spatial nonlinear UQ problem [24], but the selection of hyperparameters lacks a priori knowledge and is not rigorous [25] and there is no strict mathematical basis for obtaining them. Other scholars have applied the Kriging agent model [25, 26] and deep learning [27–29] to the simplified WPT system UQ and optimization, and its uncertainty quantification ability remains to be verified for the structurally complex WPT simulation model. Gaussian process regression (GPR) based on Gaussian stochastic process, kernel technique and Bayesian inference theory is a nonparametric probabilistic model that can quantify the prediction uncertainty and is not restricted by a specific functional form, and the hyper-parameters follow a strict mathematical derivation, with a strong ability to simulate complex models [30].

In this paper, based on the effect of transceiver coil mutual inductance on transmission efficiency, we propose to adopt GPR as the UQ framework for EV-WPT transmission efficiency with the following contributions:

(1) The UQ framework of the GPR agent model proposed in this paper can quantify the uncertainty of the power transfer efficiency of EV-WPT systems with a solution accuracy that is approximately consistent with the MC method and a 94.5% computational speedup.

(2) In this paper, based on the GPR proxy model, the Morris one-at-a-time (MOAT) algorithm is used to filter the importance of uncertainty input variables to provide a new idea for sensitivity analysis.

(3) The MOAT mean and standard deviation are solved based on the GPR agent model, which proves that the offset between the transmitting and receiving coils and the diameter of the transmitting coil cross-section are the main factors affecting the transmission efficiency, and this conclusion can be used to guide the optimal design of the EV-WPT system in future work, so that it can be realized with an optimal structure for the building of the WPT system based on the degree of influence of the uncertainty factors.

The main contents of this paper are as follows. Section II describes the working principle and simulation model parameters of the EV-WPT system. Section III describes the implementation process of the quantitative agent model for efficiency uncertainty of EV-WPT system and its UQ based on GPR implementation, and the MOAT screening method based on GPR implementation. Section IV describes the simulation experiment validation session of this paper to realize the efficiency UQ assessment and influencing factors screening of EV-WPT system. Section V summarizes the work in this paper.

II. NUMERICAL SIMULATION MODEL OF EV-WPT SYSTEM

In this paper, a simulation model of a magnetically coupled resonant EV-WPT system is established based on the principle of magnetic coupling resonance, which utilizes the space alternating magnetic field to transfer energy. The EV's comprehensive model and its square magnetic coupling mechanism are depicted in Fig. 1.

Drawing inspiration from a majority of family car models available in the market, the design features a body size of 4500×2000×1500 mm, primarily constructed from aluminum, with other non-electromagnetic materials being disregarded. The magnetic coupling mechanism houses the energy transmission coil group on its inner side. The outer contour of this mechanism measures 600×600 mm, while the inner contour is sized at 300×300 mm. The vertical distance between the transmitting and receiving coils, denoted as z, ranges from 100 mm to 150 mm. Each side of the coil features 11 turns of copper wire, with a conductor cross-sectional diameter of d_{wire} being 2 mm. To enhance coupling coefficient and minimize magnetic field leakage, thereby improving transmission efficiency, the coil group is encased by a ferrite layer, which mirrors the outer contour of the energy transfer coil and is 10 mm thick.

Offsets of the coupling mechanism along the horizontal x and y axes are represented by Δx and Δy, respectively. Given that WPT coils typically exhibit low coupling coefficients, the S-S and P-S topological structures are more appropriate for efficient WPT systems [17]. In this paper, we employ an S-S type compensation circuit, as illustrated in Fig. 2.

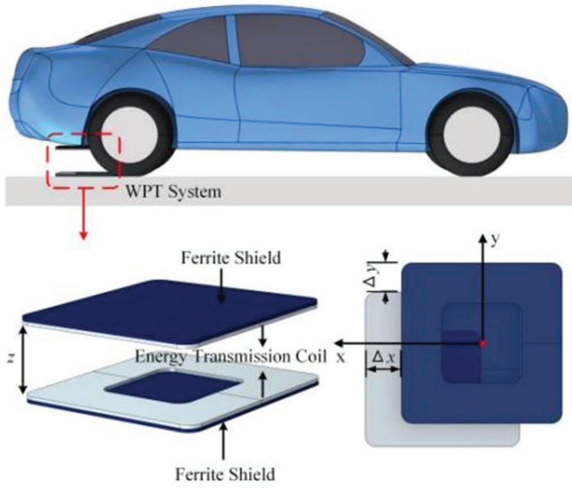

Fig. 1. Wireless charging of electric vehicles and the magnetic coupling mechanism.

I_S is the AC current source, R_T is the equivalent resistance of the loop at the transmitter end, R_R is the equivalent resistance of the loop at the receiver end, R_L is the load resistance, such that R_Z=R_R+R_L, C_T and C_R are the compensating capacitance at the transmitter end and the receiver end, respectively, L_T and L_R are the equivalent inductance of the transmitter coil and the receiver coil, respectively, and M is the mutual inductance between the two coils.

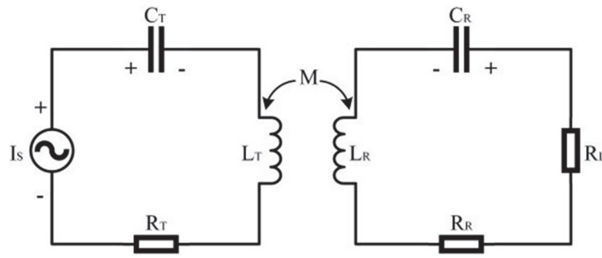

Fig. 2. EV-WPT system S-S compensation circuit.

When L_T=L_R=L and C_T=C_R=C, the resonant angular frequency $\omega = \frac{1}{\sqrt{LC}}$, the power is transmitted in the system with an efficiency of:

$$\eta = \frac{R_L}{R_R + R_L} \frac{\omega^2 M^2}{\omega^2 M^2 + R_T\left(R_R + R_L\right)}. \tag{1}$$

In practice, the uncertainty in coil dimensions, circuit element parameters, the dislocation of the transmitting and receiving coil packs due to the differences in the level of coil and circuit element processing and manufacturing, and the level of driver operation affects the mutual inductance and mutual coupling coefficients, which inevitably results in uncertainty in the transmission efficiency of the EV-WPT system. Therefore, the usual deterministic studies are not representative and it is necessary to carry out a UQ study of the transmission efficiency of EV-WPT systems in the form of statistical characterization and to analyze the extent to which a wide range of parameters affect the transmission efficiency of WPT systems. In this paper, we focus on the UQ of the transmission efficiency of the coupling mechanism of EV-WPT systems with uncertainties in the offset, physical dimensions and component parameters. In the next section, a UQ framework for the transmission efficiency of EV-WPT systems is developed based on GPR machine learning.

III. UNCERTAINTY QUANTIFICATION OF TRANSMISSION EFFICIENCY BASED ON GPR MACHINE LEARNING

A. GPR transmission efficiency agent model

Agent modeling machine learning is widely used for its simple uncertainty quantification principle. GPR has excellent solving ability for nonlinear problems due to its excellent global and local prediction performance. GPR is a nonparametric model characterized by high flexibility and scalability, and is a parameter-free stochastic process regression based on Gaussian distribution, which gives probabilistic approximate prediction of the quantity of interest and computes the input parameter space at each predicted variance at the sample point. In this paper, we use GPR to train the WPT system input parameters d-dimensional column vectors $\boldsymbol{x}_{n\times d}$ with transmission efficiency $\boldsymbol{\eta}_{n\times 1}$ to build a GPR agent model, which gives the predicted mean and variance of the transmission efficiency.

First, based on the function space perspective, the Gaussian process can be expressed as:

$$f(\boldsymbol{x}) \sim GP(m(\boldsymbol{x}), k_\theta(\boldsymbol{x},\boldsymbol{x}')), \tag{2}$$

where θ denotes the hyperparameter of the covariance function, and $m(\boldsymbol{x})$ and $k_\theta(\boldsymbol{x},\boldsymbol{x}')$ are the mean and covariance functions of the stochastic process $f(x)$, respectively.

The GPR training process is shown in Fig. 3 [30]. The learning problem for GPR is:

$$\boldsymbol{\eta}=f(\boldsymbol{x})+\boldsymbol{\varepsilon}. \tag{3}$$

ε is the estimation noise of the GPR and ε~N(0, ${\sigma_n}^2$), f is regarded as a latent function, and $f_1, f_2, \ldots, f_n$ satisfy the joint Gaussian distribution.

To simplify the computation, let the prior form of η constructed from n training sample points ($x_{n\times d}$, $\eta_{n\times 1}$) be η~N(0, K_{ff}+${\sigma_n}^2$I), and let the function constructed from m test sample points be f^*, then the joint prior distribution of η and f^* is:

$$\begin{bmatrix}\eta\\ f^*\end{bmatrix} \sim N\left(\mathbf{0}, \begin{bmatrix}\mathbf{K_{ff}}+{\sigma_n}^2\mathbf{I} & \mathbf{K}_{\mathbf{ff}^*}^{\mathrm{T}}\\ \mathrm{K}_{\mathrm{ff}^*} & \mathrm{K}_{**}\end{bmatrix}\right), \tag{4}$$

where K_{ff}, K_{**}, K_{ff^*} are shorthand for training samples, test samples and covariance matrix between training and test samples, respectively. The specific expression is:

$$Kff = K(X,X) = \begin{bmatrix} k(x1,x1) & k(x1,x2) & \cdots & k(x1,xn)\\ k(x2,x1) & k(x2,x2) & \cdots & k(x2,xn)\\ \vdots & \vdots & \ddots & \vdots\\ k(xn,x1) & k(xn,x2) & \cdots & k(xn,xn)\end{bmatrix}, \tag{5}$$

$$Kff* = K(X^*,X) = \begin{bmatrix} k(x*^{(1)},x1) & k(x*^{(1)},x2) & \cdots & k(x*^{(1)},xn)\\ k(x*^{(2)},x1) & k(x*^{(2)},x2) & \cdots & k(x*^{(2)},xn)\\ \vdots & \vdots & \ddots & \vdots\\ k(x*^{(m)},x1) & k(x*^{(m)},x2) & \cdots & k(x*^{(m)},xn)\end{bmatrix}, \tag{6}$$

$$K_{**} = K(X^*,X^*) = \begin{bmatrix} k(x*^{(1)},x*^{(1)}) & k(x*^{(1)},x*^{(2)}) & \cdots & k(x*^{(1)},x*^{(m)})\\ k(x*^{(2)},x*^{(1)}) & k(x*^{(2)},x*^{(2)}) & \cdots & k(x*^{(2)},x*^{(m)})\\ \vdots & \vdots & \ddots & \vdots\\ k(x*^{(m)},x*^{(1)}) & k(x*^{(m)},x*^{(2)}) & \cdots & k(x*^{(m)},x*^{(m)})\end{bmatrix}. \tag{7}$$

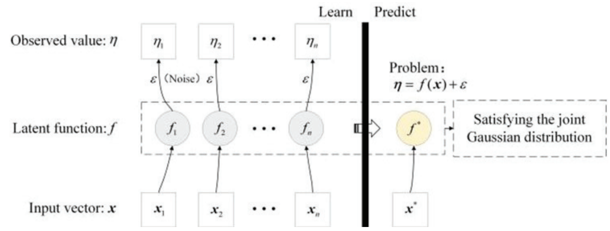

Fig. 3. GPR prediction process for transmission efficiency.

According to Bayesian theory, the mean $\overline{f^*}$ and variance ${\sigma_*}^2$ of the predictive distribution can be derived as:

$$\overline{\boldsymbol{f}^*} = \boldsymbol{K}_{ff^*}\left(\boldsymbol{K}_{ff}+\sigma_n^2\mathbf{I}\right)^{-1}\boldsymbol{\eta}, \tag{8}$$

$$\sigma_*^2 = \boldsymbol{K}_{**} - \boldsymbol{K}_{\boldsymbol{ff}^*}\left(\boldsymbol{K}_{\boldsymbol{ff}}+\sigma_n^2\mathbf{I}\right)^{-1}\boldsymbol{K}_{\boldsymbol{ff}^*}^{\mathrm{T}} \tag{9}$$

where $\overline{\boldsymbol{f}^*}$ gives a probabilistic approximation of the predicted value of the transmission efficiency and it usually ensures that the model achieves a small decision loss. ${\sigma_*}^2$ gives the uncertainty of the prediction and it can be used to quantify the credibility of the predicted results.

The kernel function approach allows the model not to care about the specific form of the mapping function (group) and not to worry about the “dimensionality catastrophe” and other issues, which not only greatly facilitates the computation, but also improves the model’s learning and prediction effect to a greater extent, because the kernel function approach allows the model to measure the data in the higher or even infinite dimensional feature space similarity, and the Bayesian theoretical framework ensures that its learning and prediction are reasonable in high-dimensional or even infinite-dimensional space. The kernel function method is based on the fact that when the kernel function satisfies the Mercer condition, the low-dimensional points are mapped to the high-dimensional feature space by vector inner product, which effectively avoids the “dimensionality catastrophe” and the trouble of overfitting. Commonly utilized kernel functions include:

- Squared kernel (SE covariance):

$$k_{SE}(\boldsymbol{x},\boldsymbol{x}') = {\sigma_f}^2 \exp\left(-\frac{1}{2l^2}\left\|\boldsymbol{x}-\boldsymbol{x}'\right\|^2\right). \tag{10}$$

- Matérn 3/2 core:

$$k_{v=\frac{3}{2}}\left(\boldsymbol{x},\boldsymbol{x}'\right) = \sigma_f^2\left(1+\frac{\sqrt{3\left\|\boldsymbol{x}-\boldsymbol{x}'\right\|^2}}{\boldsymbol{l}}\right) \exp\left(-\frac{\sqrt{3\left\|\boldsymbol{x}-\boldsymbol{x}'\right\|^2}}{\boldsymbol{l}}\right). \tag{11}$$

In this paper, the Matérn 3/2 kernel is applied for regression analysis according to the need of solving accuracy.

GPR, as a nonparametric Bayesian method, has a variety of parameters with noise that can be varied in the kernel function of GPR, which are collectively known as hyperparameters and have an impact on the model effect. By adjusting the parameters of the kernel function, the fit of the model to the data and the predictive performance can be changed. In GPR, it is often assumed that the observed data contain a certain amount of noise. The hyperparameters of the noise term represent the variance of this noise, which reflects the uncertainty of the observed data. By adjusting the hyperparameters of the noise term, the degree of model fit to the data and the uncertainty of prediction can be balanced. When adjusting the hyperparameters, it is necessary to balance the degree of fit of the model with its ability to generalize. A model that is too complex may lead to overfitting, while a model that is too simple may not adequately capture the characteristics of the data. The log-likelihood function is the logarithm of the probability density function of the observed data for a given model parameter, and the optimal hyperparameter values can be found by maximizing this function. The optimization algorithm is based on gradient descent, and the optimal hyperparameters are obtained by finding the maximum value of the log-edge likelihood function (12) for the training samples:

$$\begin{aligned}\log p(\boldsymbol{\eta} \mid \boldsymbol{x}) = &-\frac{1}{2}\boldsymbol{\eta}^{\mathrm{T}}\left(\boldsymbol{K}_{ff}+\boldsymbol{\sigma}_n^2\boldsymbol{I}\right)^{-1}\boldsymbol{\eta} \\ &-\frac{1}{2}\log\left|\boldsymbol{K}_{ff}+\boldsymbol{\sigma}_n^2\boldsymbol{I}\right|-\frac{n}{2}\log 2\pi. \end{aligned} \quad (12)$$

B. GPR transmission efficiency UQ framework

In this paper, based on the above theoretical foundation, we perform EV-WPT system transmission efficiency uncertainty quantification based on GPR machine learning, which is mainly divided into three stages, as shown in Fig. 4.

Phase 1: Preparation of training data

Uncertainty input parameters follow specific distributions and, in conjunction with the practical situation, it is assumed that the spatial location uncertainty input parameters follow a uniform distribution. The coil structure, size and element uncertainty input parameters follow a normal distribution, given the mean, variance and fluctuation range of each parameter. Latin hypercube sampling is used to prepare the training data ($x_{n\times d}$, $\eta_{n\times 1}$) to model the transmission efficiency GPR agent.

Phase 2: Constructing GPR agent model

Select equation (8) as the covariance function for GPR training and obtain the optimal set of hyperparameters.

Phase 3: Uncertainty quantification of transmission efficiency of EV-WPT system

Calculate the probability density function of the predicted value of transmission efficiency and its mean and variance. Based on the UQ results, gain insight into the effect of uncertainty inputs on the power transfer efficiency of the EV-WPT system.

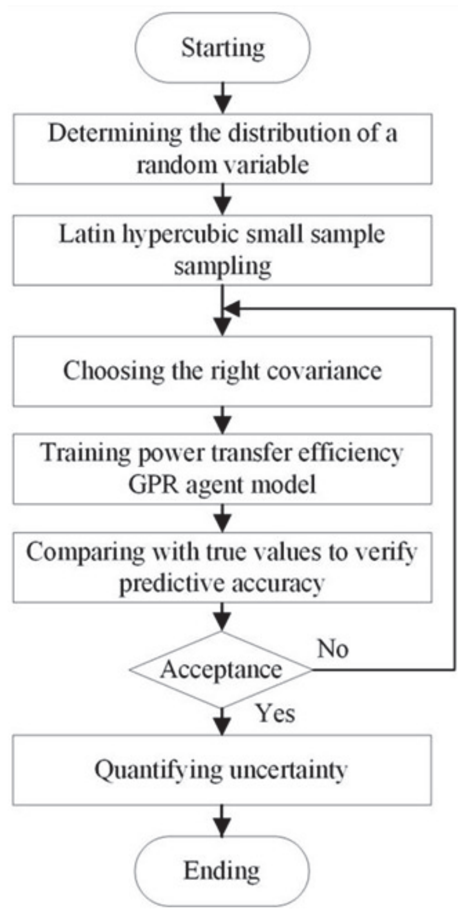

Fig. 4. UQ flow chart of EV-WPT system transmission efficiency.

IV. MOAT screening of uncertainty input variables

The MOAT algorithm is a lightweight global screening method that provides a qualitative measure of the importance of each input parameter [24]. The method is purely sample-based and requires relatively little computational effort from the model. MOAT becomes an ideal method when the number of input parameters is too large for computationally expensive uncertainty quantification studies.

MOAT first uses Morris sampling to obtain p trajectories and generates l levels for each dimension θ_i (i=1,...,d) of the d-dimensional variable to generate l levels. Then the sampled data points are $\theta_{i,j}$ (j=1,...,p), and the level of influence of the i input variable can be calculated as:

$$P_{i,j} = \frac{f\left(\theta_{1,j}, \theta_{2,j}, \ldots, \theta_{i,j} \pm \Delta, \ldots, \theta_{d,j}\right)}{\Delta}$$

$$-\frac{f\left(\theta_{1,j},\theta_{2,j},\ldots,\theta_{i,j}\pm\Delta,\ldots,\theta_{d,j}\right)}{\Delta}.$$

$$\Delta=\frac{l}{2(l-1)}=\frac{1}{2}+\frac{1}{2(l-1)} \tag{13}$$

The expression for mean value of MOAT for the i input, based on the basic effect of the p replicates, is:

$$\mu_i=\frac{1}{p}\sum_{j=1}^{p}|Pi,j|. \tag{14}$$

The expression for standard deviation of MOAT for the i input is:

$$\sigma i=\sqrt{\frac{1}{p}\sum_{j=1}^{p}(Pi,j-\mu i)^2}. \tag{15}$$

The MOAT method calculates the MOAT mean and standard deviation for each input parameter and displays them in a MOAT scatter plot. The ordering of the MOAT mean and standard deviation gives the relative importance of the input parameter. The higher the former means that the parameter significantly affects the amount of attention; the higher the latter means that the parameter either has a strong interaction with other parameters, a non-linear effect, or both. In this paper, based on the results of MOAT calculations, we filter out the variables that have a strong influence on the WPT efficiency of EVs, so as to find the most important influencing factors.

V. SIMULATION ANALYSIS

Based on the WPT system model in section I, it can be seen that EV-WPT transmission efficiency is subject to strong uncertainties due to the coupling mechanism offset, coil structure and circuit component parameter uncertainties. For the prior condition of spatial location distribution, in practical applications, the likelihood of distance offsets is the same for all possibilities, which conforms to a uniform distribution in engineering. For the coil parameters in the processing of the error, all kinds of enterprises in the development of test standards commonly used normal distribution to ensure its scientific and objective, so this paper also selected Gaussian distribution.

According to the actual situation, 10 random variables and their distribution intervals that have an impact on the transmission efficiency are considered in this paper, as shown in Table 1, where Δx is the horizontal offset of the WPT system, Δy is the vertical offset, z is the coil spacing, $d_{\text{wire-T}}$ is the transmitting coil cross-sectional diameter, $d_{\text{wire-R}}$ is the receiving coil cross-sectional diameter, I_S is the excitation current of the current source, R_T is the transmitting coil self-resistance, R_Z is the load resistance, C_T is the transmitting-side compensation capacitance and C_R is the receiving-side compensation capacitance. The above 10 uncertainty factors are unavoidable errors in the WPT system itself or in the driver's operation, mapped to the uncertainty effects considered in this paper.

Table 1: Parameter distribution of random variables

Input	Distribution	Unit
Δx	U (-0.1,0.1)	m
Δy	U (-0.1,0.1)	m
z	U (0.15,0.2)	m
$d_{\text{wire-T}}$	N (2e-3,1e-4)	m
$d_{\text{wire-R}}$	N (2e-3,1e-4)	m
I_S	N (100,5)	A
R_T	N (0.2,0.01)	Ω
R_Z	N (10,0.5)	Ω
C_T	N (120,6)	nF
C_R	N (130,6.5)	nF

According to the parameter distributions of random variables in Table 1, 500 training samples are collected using the Latin Hypercube Sampling (LHS) method to establish the GPR agent model, and 10,000 MC experiments are conducted based on the agent model. Meanwhile, 10,000 MC experiments of the real model are conducted to verify the accuracy of the GPR method based on experience and UQ stability. The simulation model takes about 1 minute to extract each sample point, and the computation time is given for a computer with a 6-core/12-thread processor (Intel Core i5-10400, 2.90 GHz) and 16 GB RAM running Windows. The GPR model predictions were compared with the true values, as shown in Fig. 5, and the relevant statistical parameters measuring the predictive power were calculated, as shown in Table 2. The results show that the GPR agent model is trained with high accuracy and can be used as a basis for sample prediction for uncertainty quantification.

Establishing the response surface based on the above GPR agent model can save computational cost and achieve good accuracy. The response surface of EV-WPT system transmission efficiency based on GPR agent model is shown in Fig. 6.

Based on the above experimental basis and the EV-WPT model proposed in section II, this paper quantifies the uncertainty of the transmission efficiency of the EV-WPT system around GPR and MC, as shown in Fig. 7 and Table 3.

Establishing the response surface based on the above GPR agent model can greatly save computational cost and achieve good accuracy.

Table 2: Statistical parameters related to prediction

Method	Mean Absolute Percentage Error	Root Mean Squared Error	Coefficient of Determination
GPR	0.0005	0.0006	0.9989

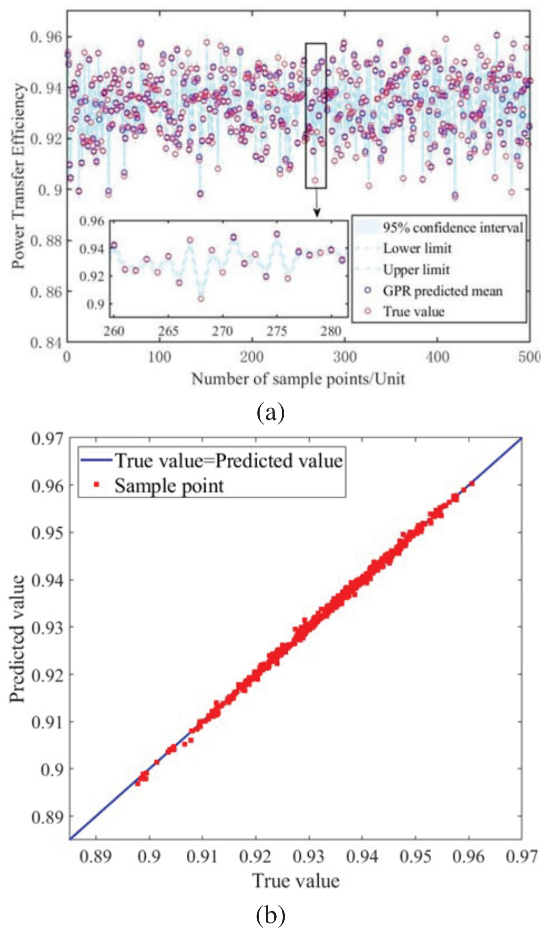

Fig. 5. GPR training process and prediction accuracy: (a) uncertainty in GPR projection and (b) comparison of predicted and true values of GPR transmission efficiency.

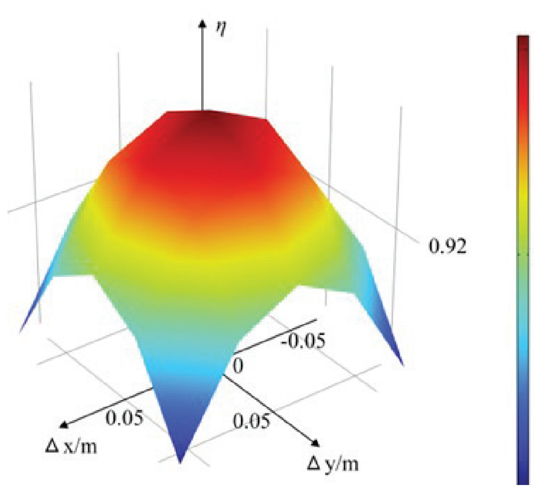

Fig. 6. Response surface of transmission efficiency based on GPR agent model.

From the above calculation results, it is obvious that the UQ accuracy of the established GPR agent model is basically the same as that of the MC method, but its computational time cost is reduced by 94.5% compared with the MC method, which greatly reduces the computational cost. In addition, it can be observed from Fig. 7 and Table 3 that, under the influence of uncertainty factors, the efficiency of the WPT system has large ups and downs with large transformation intervals, which is attributed to the fact that the coupling effect between the two coils becomes weaker under the influence of uncertainty factors, and the efficiency of the energy transfer subsequently becomes lower. In addition, in the presence of positional deviation, the leakage of electromagnetic field is also one of the potential dangers. Thus, in order to design a rational WPT system, it is necessary to screen out the influential variables so as to make a targeted strategy.

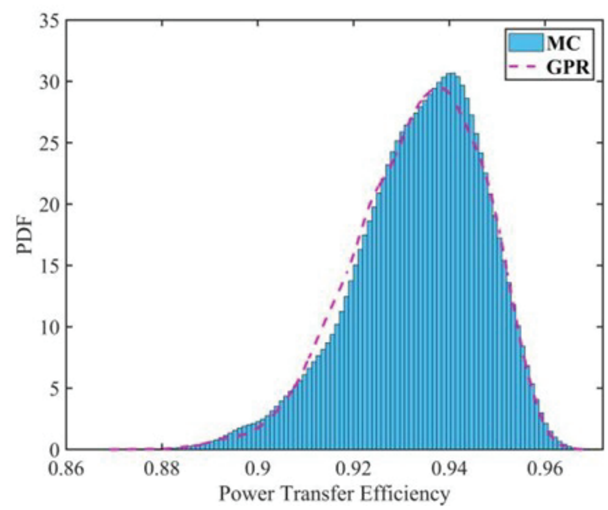

Fig. 7. Contrast of probability density function.

Table 3: Comparison of MC and GPR model with uncertainty inputs

	Mean	Variance	Relevant Error		Elapsed Time
MC	0.9229	0.0281	**Mean**	**Variance**	7 days and 2 hours
GPR	0.9195	0.0291	0.3684%	3.5587%	9 hours and 21 minutes

To qualitatively assess the significance of the 10 input parameters and identify those exerting a more substantial influence on transmission efficiency, this study employs the MOAT approach to address the GPR agent model. The outcomes are illustrated in Fig. 8.

From the results, it can be seen that the variables that have the greatest impact on the transmission efficiency are the horizontal offset Δx, Δy, coil spacing z, and the

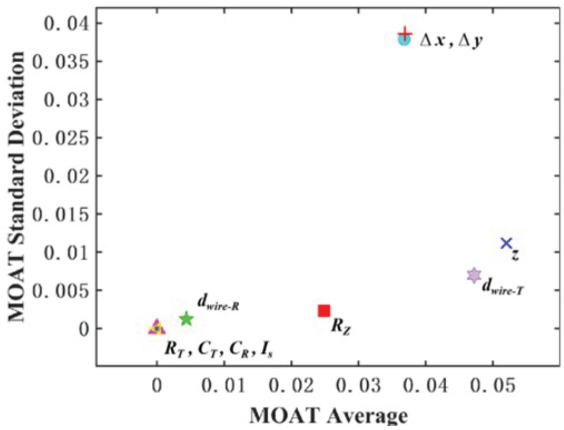

Fig. 8. MOAT mean and standard deviation of the related variables.

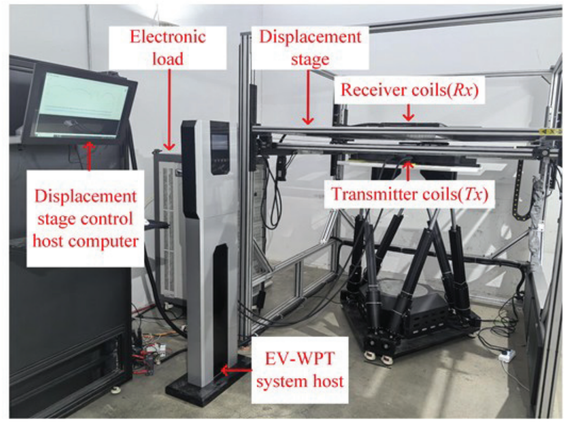

Fig. 9. Experimental setup.

cross-section diameter of the transmitting coil $d_{\text{wire-T}}$. The standard deviation of their MOAT and the mean are significantly higher than those of the other factors, which is consistent with the performance of the WPT efficiency in actual use [24] and, therefore, these factors should be emphasized in the design of the actual WPT system. In addition, the receiver side resistance R_Z and the receiver side coil cross-section diameter $d_{\text{wire-R}}$ also have an impact on transmission efficiency, while other input variables have less impact on the uncertainty of the transmission efficiency.

The above results indicate that in order to make the transmission efficiency as high as possible, in addition to accurately designing the geometrical structure parameters of the WPT system as well as the parameters of the compensation circuits, attention should be focused on the offset between the transmitting and receiving coils. Based on the conclusions obtained from the above results, in the practical design method, the above types of uncertainty factors with obvious effects should be considered in the optimization design of WPT and, since uncertainty factors cannot be avoided, they should be considered as the background of the design, so as to achieve the system to maintain high efficiency under the influence of uncertainty factors.

In order to verify the calculation accuracy of the above GPR-based EV-WPT system transmission efficiency proxy model, an experimental platform based on an EV-WPT system with an operating frequency of 85 kHz and a power of 11 kW is constructed to carry out an experimental validation of the GPR system transmission efficiency proxy model in this paper. The experimental platform is shown in Fig. 9. Among them, the displacement stage is able to realize the position offset on the three-dimensional space of the EV-WPT system and control its displacement through the computer terminal. In the uncertainty quantification verification experiment, this paper adopts the discrete step form to realize the value of uncertainty factors and, according to the limiting range of uncertainty factors in Table 1, the probability density function (PDF) distribution of transmission efficiency of the experimentally verified EV-WPT system is shown in Fig. 10.

Figure 10 shows that the uncertainty quantization results of the GPR-based EV-WPT system transmission efficiency proxy model proposed in this paper are basically consistent with the experimental results, indicating that the GPR proxy model in this paper is accurate. Therefore, the UQ method of the GPR-based EV-WPT system transmission efficiency proxy model proposed in this paper has significant practical applications and provides theoretical guidance for the optimization and design of practical EV-WPT systems.

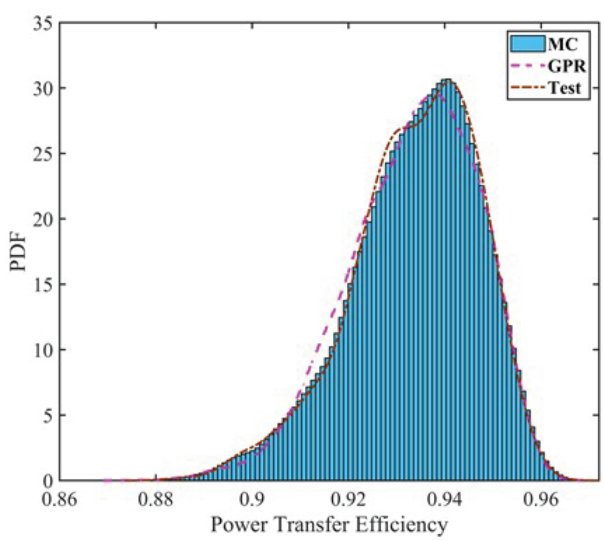

Fig. 10. Contrast of probability density function.

VI. CONCLUSION

In this paper, the GPR machine learning method is used to build and establish the transmission efficiency agent model of an EV-WPT system. Based on the GPR agent model, it realizes solving the response surface of the transmission efficiency and quantifying the uncertainty of the transmission efficiency, so as to realize the efficiency assessment under the uncertainty background. Finally, the uncertainty input parameters affecting the transmission efficiency are screened by MOAT to quantify the degree of influence of different parameters and, finally, the effectiveness of the GPR agent model in this paper is verified by experiment, so as to provide theoretical guidance on the optimization aspect of the system efficiency of the WPT system.

ACKNOWLEDGMENT

This research is partially funded by the Jilin Scientific and Technological Development Program under Grant 20240101117JC, Grant 20230201122GX, and the Key Laboratory for Comprehensive Energy Saving of Cold Regions Architecture of Education, Jilin Jianzhu University under Grant JLJZHDKF202203.

REFERENCES

[1] A. Triviño, J. M. González-González, and J. A. Aguado, “Wireless power transfer technologies applied to electric vehicles: A review,” *Energies*, vol. 14, pp. 1-21, Mar. 2021.

[2] B. Wang, X. Kestelyn, E. Kharazian, and A. Grolet, ”Application of normal form theory to power systems: A proof of concept of a novel structure-preserving approach,” in *2024 IEEE Power & Energy Society General Meeting (PESGM)*, Seattle, WA, USA, pp. 1-5, 2024.

[3] E. Hasani, F. Torabi, and A. Salavati-Zadeh, “Electrochemical simulation of lithium-ion batteries: A novel computational approach for optimizing performance,” *Hydrogen, Fuel Cell & Energy Storage*, vol. 11, no. 4, pp. 215-224, Nov. 2024.

[4] L. Chaoqun, W. Xiaokang, W. Bin, and G. Yan, ”Research on influence of the electric vehicle on life safety during the wireless charging process,” in *2018 IEEE 2nd International Electrical and Energy Conference (CIEEC)*, Beijing, China, pp. 507-512, Nov. 2018.

[5] A. Ahmad, M. S. Alam, and R. Chabaa, “A comprehensive review of wireless charging technologies for electric vehicles,” *IEEE Trans. Transp. Electrif.*, vol. 4, no. 1, pp. 38-63, Mar. 2018.

[6] A. Shafiee, H. R. Moghadam, M. Merikhipour, and J. Lin, “Analyzing post-pandemic remote work accessibility for equity through machine learning analysis,” in *International Conference on Transportation and Development 2024: Transportation Planning, Operations, and Transit (ICTD)*, Atlanta, GA, USA, pp. 453-462, 2024.

[7] D. Patil, M. K. McDonough, J. M. Miller, B. Fahimi, and P. T. Balsara, “Wireless power transfer for vehicular applications: Overview and challenges,” *IEEE Trans. Transp. Electrif.*, vol. 4, no. 1, pp. 3-37, Mar. 2018.

[8] S. Sheikhahmadi, M. Moezzi, and H. Ghafoorifard, “A low phase noise class-C oscillator with improved resonator and robust start-up,” *IEEE Transactions on Circuits and Systems II: Express Briefs*, vol. 68, no. 1, pp. 92-96, Jan. 2021.

[9] M. Ghorbani Eftekhar, Z. Ouyang, M. A. E. Andersen, P. B. Andersen, L. A. de S. Ribeiro, and E. Schaltz, “Efficiency study of vertical distance variations in wireless power transfer for E-mobility,” *IEEE Trans. Magn.*, vol. 52, no. 7, pp. 1-4, July 2016.

[10] K. Sheida, M. Nobari, B. Baigzadehnoe, and H. Bevrani, “An artificial bee colony based PID controller for depth control of an autonomous underwater vehicle,” in *2022 8th International Conference on Control, Instrumentation and Automation (ICCIA)*, Tehran, Islamic Republic of Iran, pp. 1-6, 2022.

[11] H. Kim, C. Song, D.-H. Kim, D.Y. Jung, I.-M. Kim, and Y.-I. Kim, “Coil design and measurements of automotive magnetic resonant wireless charging system for high-efficiency and low magnetic field leakage,” *IEEE Trans. Microwave Theory Tech.*, vol. 64, no. 2, pp. 383-400, Feb. 2016.

[12] R. Narayanamoorthi, “Modeling of capacitive resonant wireless power and data transfer to deep biomedical implants,” *IEEE Trans. Compon. Packag. Manuf. Technol.*, vol. 9, no. 7, pp. 1253-1263, July 2019.

[13] X. Shang, L. Xu, Q. Yu, L. Bo, G. Lv, Y. Chi, and T. Wang, “Uncertainty quantification and optimal design of EV-WPT system efficiency based on adaptive Gaussian process regression,” *Applied Computational Electromagnetics Society (ACES) Journal*, vol. 38, no. 12, pp. 929-940, Dec. 2023.

[14] A. Madanimohammadi, M. Abbasian, M. Delshad, and H. Saghafi, “Electromagnetic and thermal analysis of a 6/4 induction switched reluctance machine for electric vehicle application,” *Applied Computational Electromagnetics Society (ACES) Journal*, vol. 38, no. 05, pp. 361-370, May 2023.

[15] H. Ni, H. Jiang, X. Li, Q. Jia, and X. Wang, “Simulation analysis of electromagnetic environment effect and shielding effectiveness for VPX chassis under plane wave radiation,” *Applied Computational Electromagnetics Society (ACES) Journal*, vol. 38, no. 11, pp. 875-885, Nov. 2023.

[16] P. Manfredi, "A stochastic active learning strategy for Gaussian process models with application to the uncertainty quantification of signal integrity," in *2023 IEEE Electrical Design of Advanced Packaging and Systems (EDAPS)*, Rose-Hill, Mauritius, pp. 1-3, Mar. 2023.

[17] G. S. Fishman, *Monte Carlo: Concepts, Algorithms, and Applications*. New York: Springer, 1995.

[18] T. Tan, T. Jiang, Y. Wu, Y. Zhu, and Y. Chi, "Safety assessment of gender-specific human electromagnetic exposure with aortic valve stents for EV-WPT," *Applied Computational Electromagnetics Society (ACES) Journal*, vol. 39, no. 08, pp. 742-753, Aug. 2024.

[19] T. Wang, Q. Yu, B. Li, G. Lv, Y. Wu, and S. Guan, "Uncertainty quantification of human electromagnetic exposure from electric vehicle wireless power transfer system," *IEEE Trans. Intell. Transp. Syst.*, vol. 24, no. 8, pp. 8886-8896, Aug. 2023.

[20] A. Shah, Y. Cho, and H. Yoo, "Safety evaluation of medical implants in the human body for a wireless power transfer system in an electric vehicle," *IEEE Trans. Electromagn. Compat.*, vol. 63, no. 3, pp. 681-691, June 2021.

[21] M. Rossi, G. Stockman, H. Rogier, and D. V. Ginste, "Stochastic analysis of the efficiency of a wireless power transfer system subject to antenna variability and position uncertainties," *IEEE Sens. J.,* vol. 16, no. 7, pp. 1-15, 2016.

[22] R. Trinchero, M. Larbi, H. M. Torun, F. G. Canavero, and M. Swaminathan, "Machine learning and uncertainty quantification for surrogate models of integrated devices with a large number of parameters," *IEEE Access*, vol. 7, pp. 4056-4066, 2019.

[23] P. Yao, P. Lionel, B. Mohamed, and L.-B. Yann, "Uncertainty quantification in the design of wireless power transfer systems," *Open Physics*, vol. 18, no. 1, pp. 391-396, 2020.

[24] T. Wang, Y. Wu, B. Li, Q. Yu, L. Xu, and S. Guan, "Design of electric vehicle's wireless power transfer system based on deep learning combined with multi-objective optimization," *IEEE Trans. Compon. Packag. Manuf. Technol.*, vol. 12, no. 12, pp. 1983-1994, Dec. 2022.

[25] T. Shimamoto, I. Laakso, and A. Hirata. "In-situ electric field in human body model in different postures for wireless power transfer system in an electrical vehicle," *Phys. Med. Biol.*, vol. 60, no. 1, pp. 163-173, Jan. 2015.

[26] S. Jeong, J. Jung, K. A. Kim, and J. Kim, "Analytical investigation of optimal wireless power transfer topology for electric vehicles," in *2015 IEEE PELS Workshop on Emerging Technologies: Wireless Power (2015 WoW)*, Daejeon, South Korea, pp. 1-5, 2015.

[27] T. Hofmann, B. Schölkopf, and A. J. Smola, "Kernel methods in machine learning," *The Annals of Statistics, Institute of Mathematical Statistics*, vol. 36, no. 3, pp. 1171-1220, 2008.

[28] Q. Yu, J. Lin, X. Ma, B. Li, L. Xu, and T. Wang, "Efficiency optimization of wireless power transfer system for electric vehicle based on improved marine predators algorithm," *IEEE Trans. Intell. Transp. Syst.*, vol. 24, no. 7, pp. 7847-7858, July 2023.

[29] Q. Zhu, M. Su, Y. Sun, W. Tang, and A. P. Hu, "Field orientation based on current amplitude and phase angle control for wireless power transfer," *IEEE Trans. Ind. Electron.*, vol. 65, no. 6, pp. 4758-4770, June 2018.

[30] X. Wan, J. Cai, S. Luo, Z. Tian, L. Zhang, and X. Xia, "Gaussian process for the machine learning-based smart fire detection system," in *2022 IEEE 6th Information Technology and Mechatronics Engineering Conference (ITOEC*), Chongqing, China, pp. 100-104, 2022.

Tianhao Wang received the B.S. degree in electrical engineering and the Ph.D. degree in vehicle engineering from Jilin University, Changchun, Jilin, China, in 2010 and 2016, respectively. From 2016 to 2019, he was a Post-Doctoral Researcher at the Department of Science and Technology of Instrument, Jilin University, where he is currently an Associate Professor with the College of Instrumentation and Electrical Engineering. His research interests include the uncertainty quantification of wireless power transfer of EVs and human electromagnetic exposure safety.

Kaifeng Zhao received the B.S. degree in electrical engineering and automation from the College of Instrumentation and Electrical Engineering, Jilin University, Changchun, Jilin, China, in 2023, where he is currently pursuing the M.S. degree in electrical engineering. His research interests include human electromagnetic safety protection and electromagnetic compatibility of EVs.

Hongwei Duan received the B.S. degree in electrical engineering and automation from the College of Electrical Engineering, Northeast Electric Power University, Jilin, China, in 2024. He's currently working on his M.S. degree at Jilin University, Jilin, China. Since 2024, he has worked on the operation and the application of micro-grid systems.

Quanyi Yu received the B.S. and the M.S. degrees from the College of Communication Engineering, Jilin University, Changchun, Jilin, China, in 2016 and 2020, respectively, where he is pursuing the Ph.D. degree. His research interests include uncertainty quantification and electromagnetic compatibility of EVs.

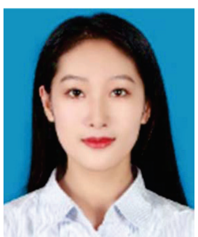

Linlin Xu received the B.S. degree and M.S. degree in electrical engineering and automation from the College of Instrumentation and Electrical Engineering, Jilin University, Changchun, Jilin, China, in 2020 and 2024, respectively. Her research interests include electromagnetic safety.

Shanshan Guan received the B.S. degree in precision instruments and machinery and the Ph.D. degree in measurement technology and instruments from Jilin University, Changchun, Jilin, China, in 2008 and 2012, respectively. In 2019, she was a Visiting Scholar at the Southern University of Science and Technology, Shenzhen, China. She is currently an Associate Professor with the College of Instrumentation and Electrical Engineering, Jilin University. Her research interests include forward modeling and inverse algorithms of EM fields, and the development of electromagnetic instruments.

Advanced Perspectives on Metamaterial Integration in Wireless Power Transfer: A Review

Muhammad Sukriyllah Yusri[1], Mohamad Harris Misran[1*], Tan Kim Geok[2*], Sharul Kamal Abdul Rahim[3], Norbayah Yusop[1], Maizatul Alice Meor Said[1], and Azahari Salleh[1]

[1]Centre for Telecommunication Research and Innovation
Fakulti Teknologi dan Kejuruteraan Elektronik dan Komputer, Universiti Teknikal Malaysia Melaka, Hang Tuah Jaya 76100, Durian Tunggal, Melaka, Malaysia
M022120002@student.utem.edu.my, harris@utem.edu.my*, norbayah@utem.edu.my, maizatul@utem.edu.my, azahari@utem.edu.my

[2]Faculty of Engineering and Technology
Multimedia University, Melaka 75440, Malaysia
kgtan@mmu.edu.my*

[3]Wireless Communication Centre
Universiti Teknologi Malaysia, Skudai 81310, Johor, Malaysia
sharulkamal@utm.my

Abstract **–** The field of wireless power transfer (WPT) has recently seen much innovation and improvement and, as a result, there is an ever-increasing need for high power transfer efficiency (PTE) of the WPT systems, as well as enhanced transmission distance for end users. However, some of the currently available WPT systems have a restricted PTE and transfer distance because they use an inductive coupling technique. With this method, the PTE suffers a significant drop as the distance between the transmitter and receiver coils grows. Alternately, magnetic resonance coupling (MRC) is employed as a mid-range WPT solution. For this method, metamaterials (MTMs) are used to increase efficiency by inserting them between the transmitter (Tx) and receiver (Rx) coils. MTMs are artificially manufactured materials that demonstrate unusual electromagnetic properties. These traits include evanescent wave amplification and negative refractive characteristics, both of which have the potential to be employed for the improvement of PTE. This paper offers an in-depth summary of recent research and development in MTM-based WPT systems. In this overview, we examine previously reported MTM-based WPT systems across a range of characteristics, including configuration, operating frequency, size, and PTE. A comparative of the various MTM-based WPT systems is also provided in this paper. PTEs for these systems were also presented against their normalized transfer distances. This study was conducted with the intention of providing a resource for academics studying WPT systems and their practical implementations. This analysis exposes the developments occurring in MTM-based WPT systems.

Index Terms **–** Inductive power transfer, metamaterials (MTMs), power transfer efficiency (PTE), wireless power transfer (WPT).

I. INTRODUCTION

In today's environment, electronic devices like mobile phones and laptops need wireless power transmission in order to be charged wirelessly. This not only offers protection against interruptions in the power supply but also enables the devices to charge themselves without the need for a conducting line. Wireless electricity is a method that involves the transmission of electrical energy by means of an electromagnetic field between a transmitter and a receiver. It's possible that we'll have access to this kind of technology in the not-too-distant future. Because of this, there is no longer a need for using batteries to power portable gadgets. Radio receivers are necessary for the operation of the system, and the device in question has to be positioned such that it is within range of the transmitter. Electromagnetic connection between the two coils causes the energy to be transferred [1]. The primary operating basis for such systems is the notion of resonant objects efficiently resonating energy while non-resonant things do not.

The history of wireless power transfer (WPT) may be traced back to the latter half of the 19th century and the early part of the 20th century, when various

Submitted On: January 2, 2024
Accepted On: January 14, 2025
https://doi.org/10.13052/2024.ACES.J.400308

kinds of wireless energy transfer were initially developed and tested by scientists and engineers. Nikola Tesla is frequently cited as the individual who came up with the concept of WPT for the first time. In the early 1890s, he demonstrated the transmission of high frequency alternating current over short distances without the need of wires. The magnetic resonance approach was yet another early type of WPT. It was initially conceived of by Alexander Popov in the latter half of the 19th century. One of the resonant circuits in this approach acts as the energy generator, while the other acts as the energy receiver. This method includes the transmission of energy between two resonant circuits as shown in Fig. 1 [2].

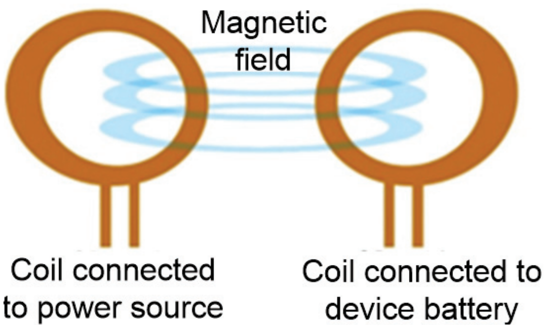

Fig. 1. A simple method of wireless power transfer [2].

In the early part of the 20th century, when inductive charging devices for batteries were being developed, the first commercial uses of WPT were put into practice. These systems move energy from a power source, such as a wall-mounted charging station, to a receiver coil in a battery-powered device, such as a toothbrush or shaver, by use of magnetic induction. Other examples of power sources are solar panels and wind turbines.

The WPT method may be broken down into two different subfields, known as near-field and far-field WPT. WPT systems that have a transfer distance that is shorter than their operational wavelength are said to have a near-field configuration. Magnetic resonance coupling (MRC) and inductive coupling WPT are the two technologies most widely used and correlate most closely to this categorization. Nevertheless, while MRC-based WPT can transfer power across a moderate range (cm to m), extending the transfer distance has the consequence of reducing the magnetic coupling between the transmitter (Tx) and receiver (Rx) coils. Hence, the MRC-based WPT system's transfer distance is limited, and power transfer efficiency (PTE) falls [3]. Radioactive wireless power transfer is a long-range application, better known as far-field energy transfer [4]. In terms of far-field WPT, the microwave energy transfer technique known as radiative WPT falls under this category. Figure 2 shows the different areas of electromagnetic field in wireless power transfer [5]. The radiative WPT process involves power that is emitted from a transmitter antenna and then travels a great distance via the air as it radiates outward. This electromagnetic (EM) wave may be picked up by a rectenna, a combination of a rectifier and an antenna, and converted into direct current (DC) power. PTE is relatively low since radio waves travel in air in an omnidirectional manner, therefore losses occur during long-distance propagation. Moreover, there are challenges in designing a rectenna, such as overcoming challenges in the design of the feeding network to realize impactful beamforming for high PTE, minimizing mutual coupling among both antenna arrays that degrades rectenna performance, and mitigating high losses associated with array feeding networks.

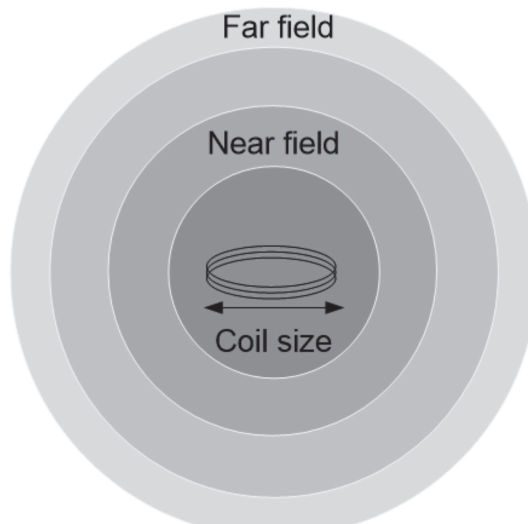

Fig. 2. Areas of the electromagnetic field [5].

WPT has received increased attention as a result of the development of new technologies and applications. Some examples of these developments include wireless charging for mobile phones, electric cars, and medical equipment. As the distance between the transmitter and receiver increase in the wireless power transfer system, the transmission efficiency drops. Transmission efficiency may be improved, and the effective power transfer distance can be extended by increasing coil quality factor and magnetic coupling for both the transmitter and receiver coils [6]. Since near-field energy transfer depends on the coupling of the magnetic fields between the two coils, which accounts for its small range, it is additionally categorized as electromagnetic induction. The near-field energy transfer field shrinks exponentially. Power may be transferred over relatively short distances with a high transfer efficiency using near field transmission techniques, commonly referred to as non-radiative methods [7]. It consists of magneto-dynamic coupling, resonant capacitive coupling, resonant inductive coupling, and capacitive power transfer [8]. Additionally, far-field energy transfer is categorized as electromagnetic radiation. Long-range applications benefit from it the most. However, because of the power losses, it is less effective in comparison. It uses microwaves and lasers to convey power [9].

William C. Brown's presentation of his capacitive methods study in 1961 was a seminal moment in the field's history. In the study, a systematic approach to transferring power at the microwave level was given. The intrinsic benefit of being able to traverse greater distances may have contributed to the selection of a frequency that is so low as to be practically insignificant. On the other hand, the approach was restricted in that it could only transmit electricity at a low level and had a reduced degree of efficiency. The accompanying misalignment of power transmitter and receiver devices was one of the additional challenges that had to be overcome at this time. This misalignment further contributed to an unpredictable power transfer, which decreased the efficiency of the process.

II. WPT USING INDUCTIVE TECHNIQUES

The utilization of inductive coupling for WPT has garnered considerable attention in contemporary discourse, particularly within domains such as electric vehicle charging, biomedical implants, and consumer electronics [10, 11]. The foundational principle involves the transference of power between two coils, intricately linked through inductive means. In this dynamic, an alternating current within the primary coil engenders a corresponding alternating magnetic field, thereby inducing a current in the secondary coil [12, 13]. The efficiency and efficacy of power delivery are contingent upon a nuanced interplay of factors, including the coupling coefficient, quality factors, operating frequency, coil geometry, and compensation networks [14, 15].

Empirical evidence underscores the pivotal role of resonant compensation networks in optimizing efficiency, yielding a load-independent voltage gain [11, 16]. Prevailing series-series and series-parallel topologies, notably applied in electric vehicle systems, have demonstrated efficiencies reaching 90% [17]. Furthermore, strategies such as achieving zero voltage switching through methodologies like phase shift control contribute substantively to loss mitigation [18]. The scope of inductive coupling extends to wireless battery charging, exemplified by the work of Ragab et al. [19], who devised a photovoltaic charging interface employing inductive coupling and regulating power to the battery through phase control.

Efficiency within the field of magnetic coupling is contingent upon critical parameters. Mutual inductance between coils, dictated by their relative orientation, emerges as a direct determinant of power transfer efficiency [13]. Research findings presented by Shevchenko et al. [20] assert that single-layer coils may manifest superior efficiency in contrast to their double-layer counterparts. Moreover, losses are incurred due to parasitic coupling between non-corresponding coils in multiple input multiple output systems [21]. The ongoing scholarly endeavor is dedicated to optimizing both coupling and compensation mechanisms, thereby augmenting the commercial viability of mid-range inductive WPT. Figure 3 shows a schematic diagram of inductive WPT [22].

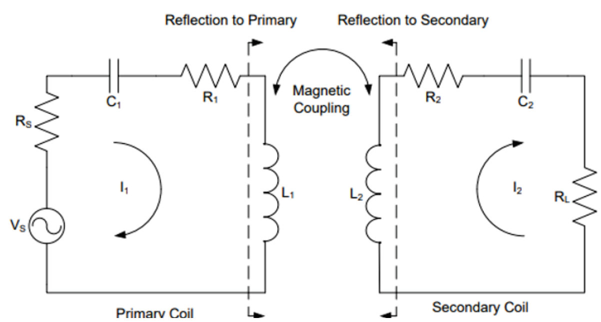

Fig. 3. Schematic diagram of inductive WPT [22].

Continuous advancements in magnetic materials, coil structures, and compensation techniques are playing a pivotal role in augmenting the capabilities of inductive WPT systems. A study conducted by Yamada et al. [23] has yielded analytical expressions for mutual inductance in coils featuring ferrite cores, utilizing image theory. The results exhibit a robust alignment with numerical outcomes, facilitating simplified modeling and design considerations. Notably, the field of vehicle charging remains a focal point, with Aziz et al. [24] conducting a comprehensive review of inductive charging developments, encompassing innovations like movable power tracks and methodologies for foreign object detection. These innovations collectively contribute to enabling safe high-power operation.

The significance of compensation networks is underscored in ensuring efficiency across variable coupling and load conditions. In a comparative experimental study by Rehman et al. [25], series-series and series-parallel topologies were assessed, revealing that the latter demonstrated superior efficiency, particularly with larger transmitter coils. Diep et al. [26] further contributed to this discourse by designing an electric vehicle system employing series-series compensation, achieving an impressive average efficiency of 89.5%, even during dynamic charging scenarios. The landscape of converter architectures has also evolved, as evidenced by the introduction of a novel transformerless multilevel inverter for inductive power transfer by Lee et al. [27], realizing an 84% converter efficiency from input to load.

In the field of multiple-device WPT, Vo et al. [28] developed a technique that enables independent control of load voltages by dynamically tuning the transmitter array. Addressing orientation sensitivity challenges, Roberts et al. [29] delved into conformal resonant magnetic coupling, achieving a notable 60% efficiency over a 100 MHz link through the use of compact high-Q resonators. Compatibility strides, exemplified by Wandinger et al. [30], extended the efficiency of inductive transfer through saltwater, opening up novel applications such as underwater charging. Persistent endeavors in modeling resonant conditions [31], optimizing coil structures [32], estimating system parameters [33], and integrating power management solutions [34] collectively lay a robust foundation for the ongoing innovation in mid-range inductive WPT.

Inductive energy transfer results in the production of dipole fields that are aligned longitudinally. As the transmitter and receiver move apart, these fields become weaker. Therefore, the distance that separates the two coils is one of the parameters that influences the efficiency of the power transfer. As a result, the efficiency increases in proportion to the distance between the receiver and the transmitter [34, 35].

III. METHODS TO ENHANCE EFFICIENCY OF POWER TRANSFER

Many investigations have been carried out with the goal of increasing the distance between the coils without effecting efficiency of power transmission.

A. Type of antenna

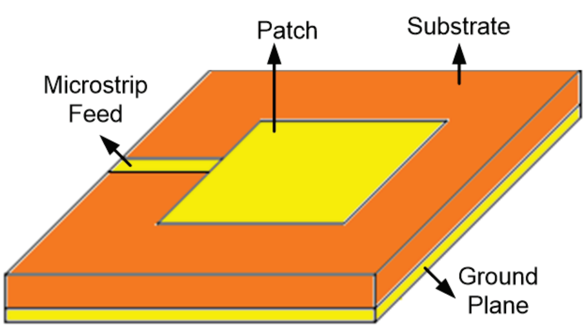

Fig. 4. Microstrip patch antenna [36].

As shown in Fig. 4, the antenna radiates from the patch's width and not its length; the effectiveness of the antenna's radiation is dependent on the patch's width [36]. Because of this, the length of the patch has no bearing on the antenna's ability to radiate (W). When the value of W is low, the amount of radiation emitted is low, and when the value of W is high, the amount of radiation emitted is high [37]. The antenna's bandwidth is influenced both by the substrate thickness (h) of the dielectric materials and by the value of the parameter W. A greater bandwidth is indicated by a bigger W number. The value of W is one of the factors that determines the gain of the antenna. This value also depends on a number of other characteristics. The greater the value of W, the greater the gain that the antenna provides. The operation of the antenna is determined mostly by the relative permittivity (r) value of the substrate material and, as a result, the h material may be determined.

Research on spiral antennas has been going on for several decades, and these antennas have recently emerged as top contenders for use in applications that need circularly polarized broadband antennas [38]. Spirals can have a single arm or many arms, and they have been implemented both in the form of microstrips and in the form of slots as shown in Fig. 5.

Fig. 5. Example of a microstrip circular spiral coil antenna and square spiral antenna [38].

Mirrors serve as the conceptual foundation for this form of microstrip configuration's use of the radiation principle [38]. The ratio of the front to the rear of the signal grows as the frequency of the signal rises, allowing for the possibility of one-sided radiation.

At a certain frequency, which is determined by the structural properties of the spiral, the direction of the highest radiation will begin to sway in the opposite direction. As frequency continues to increase, the direction of the deflection shifts to both sides of the axis that is perpendicular to the surface of the antenna. Within the dielectric, the height of the slab is stipulated to be around a fourth of the wavelength at the antenna's center frequency [38]. This height is determined by the antenna.

Therefore, height tends to be equal to one-half of the wavelength at the relevant frequencies when considering the higher frequency bands [38]. When it reaches the spiral plane, the phase of the original signal is exactly the opposite of that of the wave that was reflected by the ground plane. This is because of the phase of the wave that was reflected by the ground plane. Following the superposition of the signals, there is a reduction in the amount of radiation at the broadside, and the main lobe begins to separate.

These antennas have the capacity to resonate in frequencies considerably lower than those that conventional multiband antennas are capable of and, at the same time, they have a very compact size [38]. The extended length of the current route through the conductor area as a result of the spiral shape of this conductor is the critical factor in achieving this level of performance.

B. Multiple coils

By coupling together many coils and transferring their energy to one another, it is possible to create a WPT system that is effective across a considerable distance [39]. In [40], multiple coils, also known as repeater coils or relay resonators, are utilized to supply energy for the load. These multiple coils are arranged in the shape of a domino [40, 41].

Fig. 6. Experimental setup for multiple coils [39].

Figure 6 shows the experimental setup for multiple coils where the second coil placed at the center is the repeater. The practicability of the system is severely compromised as a result of the presence of a great number of relay coils between the transmitter and the receiver [42]. In addition to this, the efficiency of the system plummets as the relay coils move further away from their intended location.

C. Resonant coupling

Since Kim [43] published their findings, the use of resonant coupling technology has become more significant in the field of wireless power transmission.

In order to create effective methods of wireless power transfer based on Fig. 7, Kim relied on the ideas developed by Nikola Tesla. Interestingly, Kim demonstrated that electricity could be transmitted across lengths of two meters with an efficiency of just 20%. Despite the fact that this efficiency was somewhat poor, the transmitted power could reach up to a notional value of 50 W at a radio frequency that covered a range of 9.4 MHz. The enhanced influence of radiation as well as the complexity connected with manufacture both served as limitations on the endeavor.

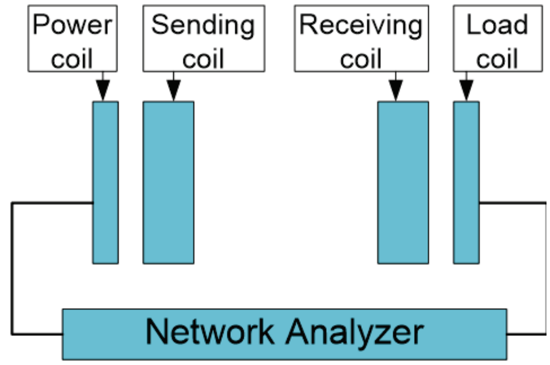

Fig. 7. Schematic diagram of resonant coupling [43].

D. High Q-factor

Under the assumption that there is only a weak coupling between particles, power transfer efficiency may be written as stated in [44]. It is plain to observe that the use of high-Q coils is capable of bringing about significant progress in terms of power transfer efficiency.

In [45], the authors suggest a self-resonant structure that is built on a foil layer and has a Q-factor of 1183, as shown in Fig. 8. This structure obtained a power transfer efficiency of 94% at a relatively wide transfer distance in comparison to the solid or Lize wire. In [46], coils with quality factors ranging from 15 to 1000 were used to obtain a PTE of 10% when the transmission distance was about nine times greater than the radius of the coils. However, a high Q-factor will result in significant voltage pressures being placed on the transfer coils. This is because the reactive current or voltage that the coils are expected to handle should be Q-times the actual power current or voltage that is being carried by the coils.

In addition to this, having a high frequency would result in a narrow band, which in turn would need a precise control technique. Both [47] and [48] have underlined how important it is to have a high Q-factor when building a coil with a high efficiency. This may be accomplished by raising the inductance of the coil while simultaneously lowering its resistance value. The multilayer coil that was suggested in [49, 50] includes a number of concentric coils whose cross-sectional area grows with the number of coils in the stack [51]. The number of coils in the stack has an effect that causes the internal resistance to decrease [52]. In addition to this, inductance will grow while the diameter of the coil will stay the same, which will contribute to a high efficiency tiny coil design that is appropriate for wireless power transfer operation [51].

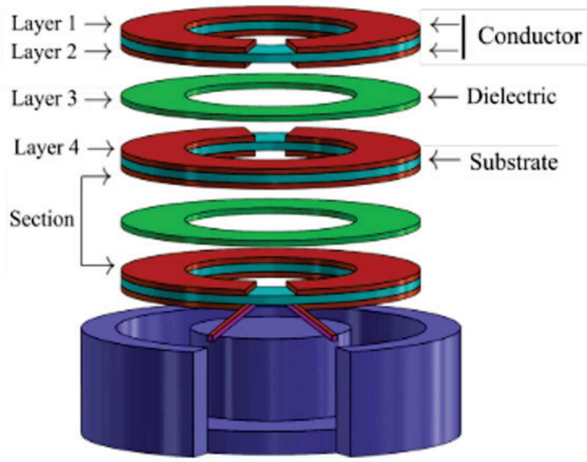

Fig. 8. A self-resonant structure [45].

The ground-breaking research conducted by Zhu and colleagues [53] in 2008 prepared the way for a new technological advance in the area of wireless power transfer. The researchers used the idea of back emf to the receiving coil in their investigation. This idea helped boost the transmission distance and the conveyed power even at a moderate range of radio frequencies. The benefit of electricity being transported over or past barriers was one of the most significant developments made possible by this approach. Despite the fact that this significant milestone has already been reached in the field of signal transmission, wireless power transmission is lagging behind in this area. The generation of eddy currents in the magnetic field that was being transmitted was the consequence of employing back emf, and this restriction was brought about by the presence of metallic objects. The effectiveness of the systems in urban or urbanized areas was greatly hindered as a result of this.

References [49, 53] demonstrate Brooks coil designs. Optimized performance is achieved by a standardized number of stacked layers and a multilayer coil orientation with a square cross-sectional area. As the maximum number of stacked layers varies with coil size, this is done in accordance with those parameters. This kind of design makes it possible to get the maximum possible inductance value with a wire that has a finite length [49].

In spite of Brooks coil and multilayer coil design, the use of a magnetic core for the WPT coil design proved ineffective due to core saturation [49] and a detrimental influence [51] on wireless devices in the nearby area. As a result of this, [49, 51] have shown that the use of an air core, which is efficient and does not influence inductance with an increase in current, is warranted. As a result, careful attention must be given to the frequency of operation in conjunction with the number of stack layers, and the application of core in coil design is of the utmost importance.

Furthermore, the efficiency and reliability of WPT systems are significantly influenced by capacitor stability. The efficient transmission of energy is dependent on a continuous state of resonance between the transmitter and receiver coils, which is facilitated by capacitors in resonant circuits [54]. Nevertheless, capacitor instability can result from factors such as temperature fluctuations, dielectric degradation, and ageing, which can result in changes in resonance frequency and a decrease in efficiency over time [55]. Applications that necessitate consistent power levels for extended periods are particularly susceptible to this instability. The enhanced resilience to temperature fluctuations and reduced dielectric losses of advanced materials, such as polymer and ceramic capacitors, have been investigated, rendering them suitable for WPT systems in high-temperature or long-duration environments. Recent research indicates that the utilization of these stable capacitors can improve the durability of the system, thereby assuring a more sustained PTE by reducing the frequency detuning that is frequently caused by capacitor instability [56].

E. Metamaterials for WPT systems

The word ”meta” in metamaterials (MTMs) comes from the Greek meaning “beyond” MTMs are defined as man-made materials that exhibit unusual an-d exotic properties that cannot be quickly identified in naturally occurring materials, allowing them to overcome limitations associated with using conventional materials in microwave and optical systems [5, 57]. Veselago presented the first theoretical analysis of MTMs in 1968. He postulated the wave particle duality of materials with simultaneously negative electric permittivity and magnetic permeability, which are characteristics of MTMs. This inquiry was the first of its kind.

Materials can be divided into four zones based on the polarity of permittivity and permeability since these two parameters indicate the electromagnetic properties of materials [58]. Permittivity and permeability are two factors that reflect the electromagnetic characteristics of materials, making this possible. The materials are classified as double-positive (DPS) materials, which are the typical materials, since their permittivity and permeability polarities are both positive at the same time, as shown in Fig. 9.

The materials are considered to be epsilon-negative (ENG) if their permittivity values are below zero and their permeability values are above zero ($\varepsilon<0$, $\mu>0$). The materials are considered to be mu-negative (MNG) when their permittivity is positive, but their permeability is negative ($\varepsilon>0$, $\mu<0$). In particular, when it is designed to have both of these characteristics be negative, the

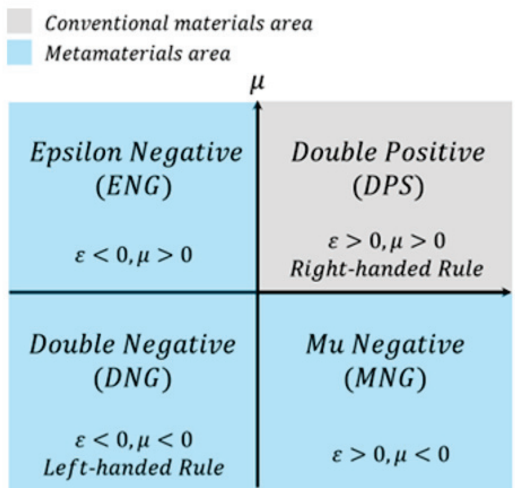

Fig. 9. Types of metamaterials based on permeability (μ) and permittivity (ε) values [58].

material in question is referred to as a double-negative material (DNG) and, in general, MTMs are recognized to be the material of choice. When ENG and MNG materials display such peculiar traits at frequencies where typical materials do not, they can also be classified as MTMs. This is the case when the materials display MTMs characteristic.

Electromagnetic waves can travel through a medium if the values of both its permittivity and its permeability are in a state that is either positive or negative at the same time. The right-handed rule is followed by the electric, magnetic, and wave vectors in typical (DPS) media. The Poynting vector, on the other hand, is parallel to the wave vector, indicating that energy is lost together with the wave's movement. The electric, magnetic, and wave vectors all follow the left-handed rule when it comes to MTMs (DNG) media. Energy flow is also anti-parallel to the source's phase propagation direction since the Poynting vector has the opposite direction of wave propagation [59]. Because of this, MTMs are also sometimes referred to as left-handed materials [60] or backward-wave media [34].

In addition to this, the negative permittivity and permeability values of the DNG materials cause the electromagnetic wave that is travelling through the medium to have a negative refractive index. The electromagnetic phenomena known as the refractive index takes place between two different kinds of materials. Snell's law, which describes the connection between the incidence angle and the consequent refracted angle of EM wave transmission at the interface of two materials, is adhered to by both the DPS and DNG materials. This law indicates that DPS and DNG materials behave in the same manner.

MTMs are notable for a number of key qualities, one of which is evanescent wave amplification. This is in addition to the negative refraction property. Rong [35] published their findings on evanescent wave amplification features in 2000.

As was noted earlier, near-field WPT systems have attracted a significant amount of attention due to the fact that they may be utilized in a variety of settings. However, because they rely on inductive coupling as their primary method of power transmission, the vast majority of today's WPT systems have limitations when it comes to the efficiency of power transfer and the distance it can cover. MRC-based WPT is an alternative that might be considered. When Tx and Rx coils are tuned to resonate at the same frequency [61], the MRC-based WPT system may be constructed and put into operation.

An investigation was done employing a system with two coils [62]. However, the two-coil system's transfer efficiency rapidly decreased as the transmission distance increased. Additionally, transfer efficiency was strongly impacted by changes in load, and transfer distance that could be practically accomplished with the two-coil WPT system was restricted. Several alternative methods, such as a three-coil system [49], a four-coil system [63], adaptive methodology [64], frequency adaptive matching technique [65], coupling optimization approach [66], and multi-resonator relay approach [67], have been researched in order to enhance transfer efficiency and distance.

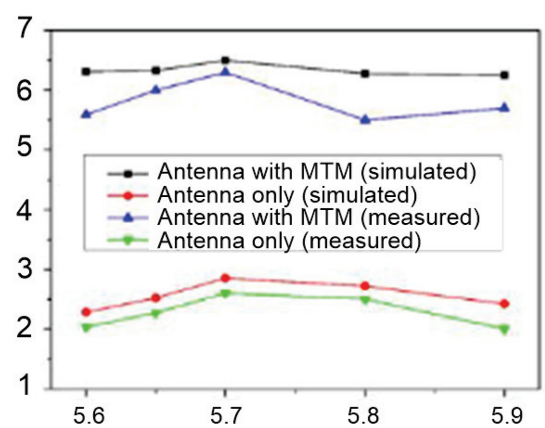

Fig. 10. Comparison of gain at 5.7 GHz [69].

Because regular materials do not possess the EM characteristics that metamaterials have, the difficulties outlined previously can be overcome by employing metamaterials [68]. It enhances transfer efficiency and distance by manipulating the electromagnetic waves that are generated by a microwave device [69]. It has been shown that placing a metamaterial over a patch antenna can lower the surface waves, leading to an increase in both the gain and the bandwidth of the antenna [68–70] as shown in Fig. 10. If the antenna is able to fulfil the requirements of the conventional resonance cavity, then the reflected wave will be able to go through the metamaterial unit cell with the same phase. In turn, the antenna's gain will improve as a result of this.

Alternately, [71] explored the use of the MTM slab in the MRC-based WPT system a few years ago, which resulted in a significant improvement in the transfer efficiency of the WPT. The MTM slab, which included a near-field WPT system based on MRC, has since been the subject of intensive study employing a wide range of methodologies. Often, one or more MTM slabs are placed between the transmitter and receiver coils. This helps to concentrate the magnetic field on the receiver coil, which in turn results in a large improvement in PTE. In addition to this widely used design, there have been reports of a wide variety of alternative structures.

MTM slabs are integrated into WPT systems in a variety of different ways to achieve high PTE. This is accomplished by making use of the one-of-a-kind qualities of MTMs, which include negative refraction and evanescent wave amplification. The magnetic field that is produced by a Tx coil in a WPT system, such as the one shown in Fig. 11, displays its flux lines in a symmetrical pattern around the coil. If the Rx coil is placed in the area where the flux lines from the Tx coil reach then, according to Faraday's law, the magnetic flux that is crosslinked inside the Rx coil will cause current flows in the Rx coil, resulting in the wireless transmission of power. There is a problem caused by the fact that the magnetic flux created by the Tx coil is not entirely caught by the Rx coil, which results in a low PTE and leakage.

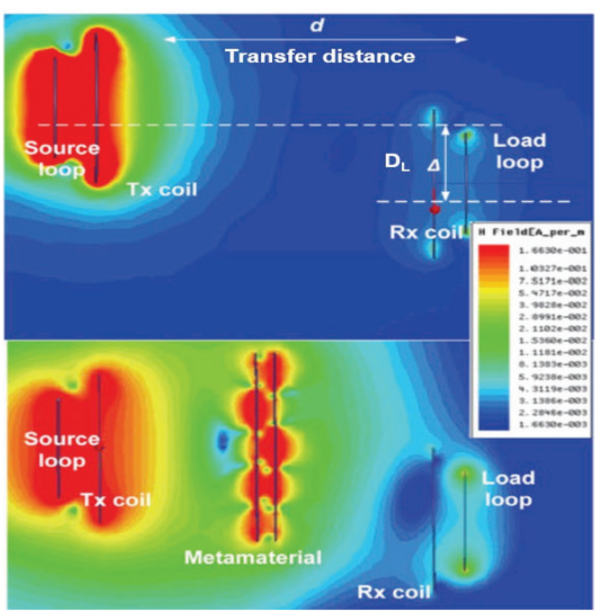

Fig. 11. WPT magnetic field distribution [71].

A conceptual schematic representing the MTM-based WPT's underlying idea can be seen in Fig. 12 (a). Figure 12 (b) illustrates what happens when an MTM slab is placed between Tx and Rx, due to the fact that the MTM slab has a negative refraction index. Since it can concentrate the magnetic field lines directly on the Rx, it can boost power transmission efficiency. Using this idea of MTM-based WPT MTMs, a variety of structures have been examined. These architectures have varying dimensions, and the MTM slabs are located in a variety of different places.

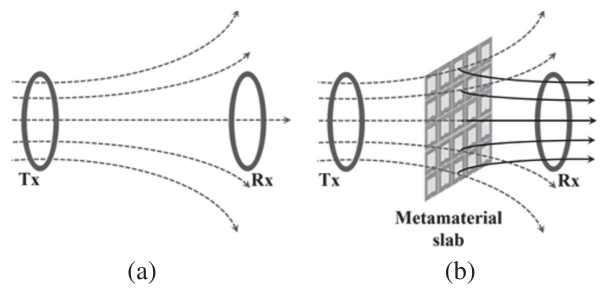

Fig. 12. Concept MTM based on WPT.

The effectiveness of MTM structures in WPT applications is significantly influenced by their design and geometry. Liu [72] conducted a study that highlighted the significance of the geometry and structure of the MTM unit in WPT systems. The study introduced a practical model for MTMs. Research showed that the efficacy of the system is significantly impacted by the resonance frequency and quality factor of MTMs, which are determined by their geometric configuration. The study highlighted the importance of precise MTM design for optimal functionality by providing a circuit-based model to predict the performance of MTM-enhanced WPT systems.

Lee [73] conducted an additional study that concentrated on the optimization of low-frequency magnetic MTMs to improve the efficiency of WPT. The research emphasized the critical role of the shape and arrangement of MTM units in attaining the desired magnetic properties, which in turn enhances PTE. The experimental results presented in the study demonstrated a substantial increase in PTE as a result of the implementation of optimized MTM designs, thereby validating the theoretical models that were proposed.

In addition, Li [74] conducted a thorough examination of MTM-based WPT systems, which included a discussion of the efficacy of the systems and the various MTM configurations. The review emphasized that certain MTM geometries, including Swiss roll structures and split-ring resonators, are effective in enhancing PTE and focusing magnetic fields. The authors emphasized the necessity of meticulous MTM design to address the challenges associated with efficiency and alignment in WPT systems.

IV. THE DIFFICULTIES OF MTMS ON WPT SYSTEMS

Integrating MTMs into WPT systems has the potential to greatly boost both the PTE and transmit distance of such systems. The reason for this is that MTMs have properties that contribute to the enhancement, specifically negative refraction and evanescent wave amplification. The introduction of MTMs will unquestionably speed up the development of WPT systems. However, research into the applications of MTM-based WPT systems is still in its preliminary stages. As a result, a number of viewpoints and difficulties associated with MTM-based WPT systems are reviewed here with a view towards future advancement.

Prior to any other consideration, the insertion loss of the MTM slab needs to be minimized as much as possible since PTE is one of the most important merit factors of the WPT system. Despite the inserted MTM slab making the PTE of the WPT systems better, it will invariably suffer from insertion losses in WPT systems that are used in the real world. Chabalko [75] measured Tx and Rx insertion losses with and without MTM slabs and a single-turn resonator. They showed that the PTE of the WPT system may be significantly increased by using a single turn resonator, much more so than by employing an MTM slab, under certain conditions. The insertion loss of the MTM slab is much larger than that of the single turn resonator due to the MTM's complex construction and the MTM's non-optimized raw material choices. The previously reported phenomena may be traced back to this root cause.

A superconductor-based MTM slab with minimal conductor loss was shown by Wang [76]. It has been demonstrated that the reduced loss qualities of the superconductor, when combined with the properties of MTMs, may significantly increase the PTE of WPT systems in an efficient manner. Furthermore, it has been hypothesized that such cumbersome structures aren't necessary to create the negative refraction effect [77]. This is an interesting development. Because a thick substrate might cause an increase in the amount of substrate loss, it is best to utilize an MTM slab with a smaller thickness in order to reduce the amount of insertion loss caused by the MTM slab. Because the MTM slab's insertion loss has a direct impact on the PTE of the WPT systems, it should be one of the design priorities to minimize it. This is because reducing it has the potential to provide significant improvements to the PTE of the WPT systems, which is why it should be investigated further. When it comes to the final applications, there are other losses that might have an impact on the PTE. Power supplies, amplifiers, resonators, rectifiers, DC-DC converters, loads, and other parts comprise the MRC-based WPT systems as a whole. The end-to-end PTE is significantly impacted by the losses that occur in each step as well as the unpredictability of changes to the parameters (weight, transfer distance, orientation) that occur in WPT environments. Hence, it is vital to enhance the efficiency of each phase in the procedure in MTM-based WPT systems, and the entire WPT system must be able to respond to a broad range of WPT circumstances.

Despite the fact that MTMs, because of their one-of-a-kind features, are able to boost the PTE of WPT systems, the development of MTM-based WPT systems for real-world use remains in its infancy. Although WPT system development is being aggressively pursued in a wide range of industries and uses, including the recharging of handheld electronic gadgets, it is clear that this technology has applications in transportation apparatuses or vehicles that run on electricity [78, 79] and medical device replacements [50, 80, 81]. The development of workable MTM-based WPT systems requires substantial investment of time and resources. Most of the observed MTM slabs have a bulky and thick build, which restricts the applications for which these slabs may be used. It is possible that it would not be viable to do so if the additional hefty MTM slab were to be put in the route of the power transmission. The WPT systems' reduced usefulness and adaptability would make them even less appealing than the more traditional wire charging methods. The following is an outline of the several potential solutions to these problems. To begin, the MTM slab has the potential to be included into the WPT systems. In the near future, research has to be done to determine how best to optimize the location of the MTM slab when it is embedded using this strategy. Second, it can involve incorporating the MTM into intermediary items in a way that does not disrupt the consumers' experience. In the future, in preparation for real-world deployments, it will be necessary to do more research on MTM-based WPT systems that make use of embedded methods.

Alternatively, one might take into account the current trend of MTM devices. Recent research [82] has focused on active MTMs that may adapt their characteristics in accordance with the information received from the environment. Conventional MTMs, also known as passive MTMs, contain characteristics that are fixed after the device has been manufactured, which restricts the uses of MTM devices. Because they used passive MTMs, the majority of earlier research found that once the MTMs had been constructed, their characteristics could not be altered in any way. Additionally, the MTM

Table 1: Different techniques to enhance WPT system

Ref.	Type of Antenna	Size of Antenna	Metamaterial Shape	Frequency	Distance	Transfer Efficiency
[63]	Single-turn square coils	100×100 mm	2-sided spiral square coil - 5 turns	6.78 MHz	40 cm	24%
[69]	Hexagonal patch	35×25 mm	Hexagon	5.7-10.3 GHz	17.53 mm	90.63%
[70]	Microstrip slot	-	Rectangular Sierpinski fractal	1.38 GHz	-	34%
[73]	Spiral coils	R=50 mm	YBCO spiral-coil structure - 13 turns	58.8 MHz	20 cm	13.58%
[83]	Circular coils	-	2-sided square helical coil - 10 turns	1 MHz	100 mm	9%
[87]	Loop coil antenna	R=20 cm	2-sided square spiral - 3 turns	24 MHz	50 cm	47%
[88]	Loop coil antenna	Tx=4.5 cm Rx=2 cm	2-layer square spiral - 13 turns	4 MHz	10 cm	22%
[89]	Spiral coils	15×15 cm	Hybrid metamaterial slab design - 14.5 turns	6.78 MHz	20 cm	47%
[90]	Spiral coil	R=15 cm	Honeycomb hexagon-shaped spiral copper - 9 turns	6.4 MHz	20 cm	51%
[91]	Square coil	13×13 cm	1-sided spiral coil - 5 turns	13.56 MHz	30 cm	36.4%
[92]	Square coil	D=10 cm	Square spiral coil copper - 11 turns	13.56 MHz	30 cm	13.4%
[93]	Circular coil	D=40 cm	Circular spiral coil - 3 turns	6.5 MHz	100 cm	15.1% (1-sided), 34.4% (2-sided)
[94]	Circular coil	D=500 mm	1-sided square spiral coil - 3 turns	2.8 MHz	160 cm	18.58%
[95]	Square coil	13×13 cm	1-sided square spiral - 5 turns	13.56 MHz	30 cm	41.7%
[96]	Circular coil	R=20 cm	1-sided meander line	27.4 MHz	20 cm	10.7%

slab's operating frequency will remain constant for the same reason. Several studies in the field of MTM-based WPT systems have focused on active MTMs [83]. An active MTM has been developed by Ranaweera [82] as a method for dynamically field localizing WPT systems. Using this technique, electricity may be sent selectively and under control directly to the desired area (hot zone). Using defect cavities with tunable resonant frequencies that are created on MTM unit cells, it is possible to realize the hot zone. It is possible to increase both PTE and safety by bringing about upgraded fields on the desired region. However, due to the fact that they have been using non-resonant loops for both the Tx and Rx coils, the transmission distance has been restricted.

In addition, there has been no extensive research carried out on transfer distance, which is one of the key characteristics that determine the effectiveness of WPT systems. There is a need for greater investigation into active MTM-based WPT systems, despite the fact that they have proven the active MTM's value in the field of WPT.

In particular, research that has been done on the active MTMs' capacity to exhibit negative refraction might be one of the options. With the ability to manipulate the MTM slab's negative refraction, the WPT's magnetic fields may be redirected depending on their location. If the Rx coil is not lined with the Tx coil, for example, the active MTM slab's negative refraction index can be adjusted to re-direct the electric flux to the Rx.

The receiving efficiency in WPT systems is influenced not only by distance but also by the angle at which the receiving coil is positioned relative to the transmitter. Misalignment in the angle affects magnetic coupling, as angular deviation reduces the effective magnetic flux linkage between coils. This misalignment can significantly decrease transfer efficiency, especially in near-field applications like wearable devices and consumer electronics [84]. Prior research highlights that angular deviations lead to reduced magnetic coupling, causing a notable drop in PTE. Because of this, the MTM slab is able to correct the alignment issue. Addressing these angle-related losses, recent studies have explored implementation of MTMs strategically within WPT systems to improve PTE despite angular misalignments. Placing MTM slabs at specific points in the system can enhance electromagnetic wave control, allowing the magnetic field to be effectively redirected and, thus, mitigating efficiency losses due to angular displacement [85]. If the MTM unit cells' negative refraction property can be altered, it would be possible to obtain a higher degree of flexibility in MTM-based WPT systems, which will lead to a wider range of applications for these systems. It is anticipated that the active MTMs would open up new possibilities for the implementation of MTM-based WPT systems in a variety of settings, including misaligned circumstances and asymmetric WPT environments, among other potential scenarios [86]. These placements can improve PTE by broadening angular tolerance, a significant step forward for stable and efficient WPT across diverse applications.

Table 1 shows a summarization of various techniques for transfer efficiency enhancement. This review aims to provide a quick reference for people engaged in WPT research and shed light on the evolving nature of MTM-based WPT system technologies. Additionally, the prospects and difficulties associated with MTM-based WPT systems have been explored in relation to the development of the technology in general as well as the applications that make use of it.

ACKNOWLEDGMENT

The authors would like to acknowledge the Ministry of Higher Education, Centre for Research and Innovation Management (CRIM) and Universiti Teknikal Malaysia Melaka for supporting this project through FRGS grant numbering FRGS/1/2021/TK0/UTEM/02/52. The authors also would like to extend their sincere gratitude to Multimedia University (MMU) for providing the essential resources and support required to complete this study. Special thanks are due to the Telekom Malaysia Research Grant, project code MMUE220012, for its support, which has been instrumental in facilitating this research.

REFERENCES

[1] S. K. Singh, T. S. Hasarmani, and R. M. Holmukhe, "Wireless transmission of electrical power: Overview of recent research & development," *International Journal of Computer and Electrical Engineering*, vol. 4, no. 2, pp. 207-211, 2012.

[2] *Qi and Magsafe* [Online]. Available: appleinsider.com/articles/21/01/01/qi-and-magsafe—everything-an-iphone-user-needs-to-know-about-wireless-charging

[3] A. Kurs, R. Moffatt, and M. Soljačić, "Simultaneous mid-range power transfer to multiple devices," *Appl. Phys. Lett.*, vol. 96, no. 4, pp. 2009-2011, 2010.

[4] E. Baghdadi and J. Van Mierlo, "Study of wireless power transfer for electric vehicles," in *Proceedings of the 2018 19th IEEE Mediterranean Electrotechnical Conference (MELECON)*, Marrakesh, Morocco, pp. 1-6, 2018.

[5] G. Yılmaz and C. Dehollain, *Wireless Power Transfer*, 4th ed. Amsterdam: Elsevier, 2017.

[6] S. Maslovski, S. Tretyakov, and P. Alitalo, "Near-field enhancement and imaging in double planar polariton-resonant structures," *J. Appl. Phys.*, vol. 96, no. 3, pp. 1293-1300, 2004.

[7] Z. Chen, B. Guo, Y. Yang, and C. Cheng, "Metamaterials-based enhanced energy harvesting: A review," *Phys. B Condens. Matter*, vol. 438, pp. 1-8, 2014.

[8] K. Sun, S. V. Georgakopoulos, and M. P. Nikdast, "An overview of metamaterials and their achievements in wireless power transfer," *Journal of Materials Chemistry C*, vol. 6, no. 12, pp. 2925-2943, 2018.

[9] B. Wang, W. Yerazunis, and K. H. Teo, "Wireless power transfer: Metamaterials and array of coupled resonators," *Proc. IEEE*, vol. 101, no. 6, pp. 1359-1368, 2013.

[10] C. Yee Yong and K. Fen Chen, "Wireless power transfer technology using resonant technique," *IOP Conf. Ser. Earth Environ. Sci.,* vol. 268, no. 1, 2019.

[11] D. Stepins, J. Zakis, P. Padmanaban, and D. Deveshkumar Shah, "Suppression of radiated emissions from inductive-resonant wireless power transfer systems by using spread-spectrum technique," *Electron.*, vol. 11, no. 5, 2022.

[12] B. Esmaeili Jamakani, A. Mosallanejad, E. Afjei, and A. Lahooti Eshkevari, "Investigation of triple quadrature pad for wireless power transfer system of electric vehicles," *IET Electr. Syst. Transp.*, vol. 11, no. 1, pp. 58-68, 2021.

[13] I. Alhamrouni, M. Iskandar, M. Salem, L. J. Awalin, A. Jusoh, and T. Sutikno, "Application of inductive coupling for wireless power transfer," *Int. J. Power Electron. Drive Syst.*, vol. 11, no. 3, pp. 1109-1116, 2020.

[14] K. N. Mude, S. S. Williamson, and S. K. Panda, "Comprehensive review and analysis of two-element resonant compensation topologies for wireless inductive power transfer systems," *Chinese Journal of Electrical Engineering*, vol. 5, no. 2, pp. 14-31, 2019.

[15] O. D. Oyeleke, S. Thomas, P. Nzerem, and G. Koyunlu, "Design and construction of a prototype wireless power transfer device," *Int. J. Eng. Manuf.*, vol. 9, no. 2, pp. 16-30, 2019.

[16] M. Carbajal-Retana, J. Hernández-González, and J. R. Rangel-Magdaleno, "Interleaved buck converter for inductive wireless power transfer in DC-DC converters," *Electronics*, vol. 9, no. 6, pp. 1-15, 2020.

[17] A. Mahesh, B. Chokkalingam, and L. Mihet-Popa, "Inductive wireless power transfer charging for electric vehicles-A review," *IEEE Access*, vol. 9, pp. 137667-137713, 2021.

[18] P. H. Chen, C. Li, Z. Dong, and M. Priestley, "Inductive power transfer battery charger with IR-based closed-loop control," *Energies*, vol. 15, no. 21, 2022.

[19] A. Ragab, M. I. Marei, M. Mokhtar, and A. Abdelsattar, "Design and performance evaluation of a PV interface system based on inductive power transfer," *Int. J. Power Electron. Drive Syst.*, vol. 12, no. 1, pp. 364-373, 2021.

[20] V. Shevchenko, M. Khomenko, I. Kondratenko, O. Husev, and B. Pakhaliuk, "Experimental comparison of designed inductance coils for wireless power transfer," *Electr. Control Commun. Eng.*, vol. 16, no. 2, pp. 102-109, 2020.

[21] Electrice, "Actualităţi şi perspective în domeniul maşinilor electrice," *Actualităţi şi Perspective în Domeniul Maşinilor Electrice*, pp. 66-75, 2005.

[22] M. H. Misran, M. A. M. Said, M. A. Othman, R. A. Manap, S. Suhaimi, and N. I. Hassan, "A systematic optimization procedure of antenna miniaturization for efficient wireless energy transfer," *International Journal of Electrical and Computer Engineering (IJECE)*, vol. 9, no. 4, pp. 3159-3166, Aug. 2019.

[23] Y. Yamada, T. Imura, and Y. Hori, "Theorizing a simple ferrite cored coil using image coils in wireless power transfer," *IEEE Access*, vol. 11, pp. 8065-8072, 2023.

[24] A. F. Abdul Aziz, M. F. Romlie, and Z. Baharudin, "Review of inductively coupled power transfer for electric vehicle charging," *IET Power Electron.*, vol. 12, no. 14, 2019.

[25] M. Rehman, P. Nallagownden, and Z. Baharudin, "Efficiency investigation of SS and SP compensation topologies for wireless power transfer," *Int. J. Power Electron. Drive Syst.*, vol. 10, no. 4, pp. 2157-2164, 2019.

[26] N. T. Diep, N. K. Trung, and T. T. Minh, "Wireless power transfer system design for electric vehicle dynamic charging application," *Int. J. Power Electron. Drive Syst.*, vol. 11, no. 3, pp. 1468-1480, 2020.

[27] J. Lee, M. Y. Kim, and S. H. Lee, "Novel transformerless multilevel inductive power transfer system," *IEEE Access*, vol. 10, pp. 55565-55573, 2022.

[28] Q. T. Vo, Q. T. Duong, and M. Okada, "Load-independent voltage control for multiple-receiver inductive power transfer systems," *IEEE Access*, vol. 7, pp. 139450-139461, 2019.

[29] D. M. Roberts, A. P. Clements, R. McDonald, J. S. Bobowski, and T. Johnson, "Mid-range wireless power transfer at 100 MHz using magnetically coupled loop-gap resonators," *IEEE Trans. Microw. Theory Tech.*, vol. 69, no. 7, pp. 3510-3527, 2021.

[30] J. N. Wandinger, D. M. Roberts, J. S. Bobowski, and T. Johnson, "Inductive power transfer through saltwater," in *2021 13th Int. Conf. Electromagn. Wave Interact. with Water Moist Subst. ISEMA*, vol. 2, no. 4, 2021.

[31] C. Y. Liu, G. Bin Wang, C. C. Wu, E. Y. Chang, S. Cheng, and W. H. Chieng, "Derivation of the resonance mechanism for wireless power transfer using class-e amplifier," *Energies*, vol. 14, no. 3, 2021.

[32] B. A. Rayan, U. Subramaniam, and S. Balamurugan, "Wireless power transfer in electric vehicles: A review on compensation topologies, coil structures, and safety aspects," *Energies*, vol. 16, no. 7, 2023.

[33] Z. Despotovic, D. Reljic, V. Vasic, and D. Oros, "Steady-state multiple parameters estimation of the inductive power transfer system," *IEEE Access*, vol. 10, pp. 46878-46894, 2022.

[34] H. Sadeghi Gougheri and M. Kiani, "An inductive voltage-/current-mode integrated power management with seamless mode transition and energy recycling," *IEEE Journal of Solid-State Circuits*, vol. 54, no. 3, pp. 874-884, Mar. 2019.

[35] C. Rong, W. Li, Z. Zhou, C. Zhu, and Z. Deng, "A critical review of metamaterial in wireless power transfer system," *IET Power Electronics*, vol. 14, no. 9, pp. 1541-1559, 2021.

[36] R. Jyosthna, R. A. Sunny, A. A. Jugale, and M. R. Ahmed, "Microstrip patch antenna design for space applications," in *Proceedings of the 2020 International Conference on Communication and Signal Processing (ICCSP)*, Chennai, India, pp. 406-410, 2020.

[37] M. H. Misran, M. A. M. Said, M. A. Othman, R. Abd Manap, S. Suhaimi, and N. I. Hassan, "DGS based CP antenna for 5G communication with harmonic," *International Journal of Integrated Engineering*, vol. 16, no. 1, pp. 301-311, 2024.

[38] D. Ahn and S. Hong, "A study on magnetic field repeater in wireless power transfer," *IEEE Trans. Ind. Electron.*, vol. 60, no. 1, pp. 360-371, 2013.

[39] M. Liu, M. Fu, Y. Wang, and C. Ma, "Battery cell equalization via megahertz multiple-receiver wireless power transfer," *IEEE Trans. Power Electron.*, vol. 33, no. 5, pp. 4135-4144, 2018.

[40] Z. Dong, S. Liu, X. Li, Z. Xu, and L. Yang, "A novel long-distance wireless power transfer system with constant current output based on domino-resonator," *IEEE J. Emerg. Sel. Top. Power Electron.*, vol. 9, no. 2, pp. 2343-2355, 2021.

[41] W. X. Zhong, C. K. Lee, and S. Y. R. Hui, "Wireless power domino-resonator systems with noncoaxial axes and circular structures," *IEEE Trans. Power Electron.*, vol. 27, no. 11, pp. 4750-4762, 2012.

[42] C. Cheng, Z. Zhou, W. Li, C. Zhu, and Z. Deng, "A multi-load wireless power transfer system with series-parallel-series compensation," *IEEE Transactions on Power Electronics,* vol. 34, no. 8, pp. 7126-7130, 2019.

[43] Y. H. Kim, S. Y. Kang, S. Cheon, M. L. Lee, J. M. Lee, and T. Zyung, "Optimization of wireless power transmission through resonant coupling," in *SPEEDAM 2010 Int. Symp. Power Electron. Electr. Drives, Autom. Motion*, pp. 1069-1073, 2010.

[44] Q. Ke, W. Luo, G. Yan, and K. Yang, "Analytical model and optimized design of power transmitting coil for inductively coupled endoscope robot," *IEEE Trans. Biomed. Eng.*, vol. 63, no. 4, pp. 694-706, 2016.

[45] A. L. F. Stein, P. A. Kyaw, and C. R. Sullivan, "Wireless power transfer utilizing a high-Q self-resonant structure," *IEEE Trans. Power Electron.*, vol. 34, no. 7, pp. 6722-6735, 2019.

[46] J. O. Mur-Miranda, J. H. Lang, K. A. Gilhousen, and J. P. Florance, "Wireless power transfer using weakly coupled magnetostatic resonators," in *Proceedings of the 2010 IEEE Energy Conversion Congress and Exposition (ECCE)*, pp. 4179-4186, 2010.

[47] J. H. Park, B. C. Park, J. H. Lee, Y. H. Ryu, E. S. Park, and S. W. Kwon, "Optimum frequency of high Q-factor resonator for magnetic resonance coupling," in *Proceedings of the 41st European Microwave Conference (EuMC)*, pp. 61-63, 2011.

[48] Y. Kawamura and M. Shoyama, "Wireless power transmission using LC cancellation," in *2013 IEEE ECCE Asia Downunder 5th IEEE Annu. Int. Energy Convers. Congr. Exhib. IEEE ECCE Asia 2013*, pp. 1041-1045, 2013.

[49] K. Tashiro, H. Wakiwaka, S. I. Inoue, and Y. Uchiyama, "Energy harvesting of magnetic power-line noise," *IEEE Trans. Magn.*, vol. 47, no. 10, pp. 4441-4444, 2011.

[50] B. H. Soong, Y. L. Sum, W. Liu, and S. Ramachandran, "Characterizing wire wound inductor coils for optimized wireless power transfer," in *IEEE/ASME Int. Conf. Adv. Intell. Mechatronics (AIM)*, pp. 469-474, 2009.

[51] M. Takato, T. Yamada, T. Nishikawa, and K. Saito, "Multilayer ceramic coil for wireless power transfer system by photo resist film process," in *Proceedings of the 2014 International Conference on Electronics Packaging (ICEP)*, pp. 326-331, 2014.

[52] N. S. Artan, R. C. Patel, C. Ning, and H. J. Chao, "High-efficiency wireless power delivery for medical implants using hybrid coils," in *Proc. Annu. Int. Conf. IEEE Eng. Med. Biol. Soc. (EMBS)*, no. 3, pp. 1683-1686, 2012.

[53] C. Zhu, K. Liu, C. Yu, R. Ma, and H. Cheng, "Simulation and experimental analysis on wireless energy transfer based on magnetic resonances," in *2008 IEEE Veh. Power Propuls. Conf. (VPPC) 2008*, pp. 18-21, 2008.

[54] S. A. Chowdhury, S. Kim, S. Kim, J. Moon, I. Cho, and D. Ahn, "Automatic tuning resonant capacitor to fix the bidirectional detuning with ZVS in wireless power transfer," *IEEE Transactions on Industrial Electronics*, vol. 71, no. 6, pp. 5683-5692, June 2024.

[55] G. Giovannetti and D. De Marchi, "Capacitors quality effect in magnetic resonance radiofrequency coils," *J. Med. Biol. Eng.*, vol. 37, pp. 639-643, 2017.

[56] M. I. A. Abdel Maksoud, R. A. Fahim, A. E. Shalan, M. A. Abd Elkodous, M. A. Olojede, M. M. Allam, and H. O. M. Ibrahim, "Advanced materials and technologies for supercapacitors used in energy conversion and storage: A review," *Environmental Chemistry Letters*, vol. 19, pp. 375-439, 2021.

[57] A. Boardman, "Pioneers in metamaterials: John Pendry and Victor Veselago," *Journal of Optics*, vol. 13, no. 2, p. 020401, 2010.

[58] K. Sun, J. Wang, Y. Ma, Z. Wu, and Y. Zhang, "Random copper/yttrium iron garnet composites with tunable negative electromagnetic parameters prepared by in situ synthesis," *RSC Advances*, vol. 5, no. 75, pp. 61155-61160, 2015.

[59] N. Engheta and R. W. Ziolkowski, "A positive future for double-negative metamaterials," *IEEE Trans. Microw. Theory Tech.*, vol. 53, no. 4 II, pp. 1535-1555, 2005.

[60] J. Shin, A. Akyurtlu, M. Deshpande, and R. W. Ziolkowski, "Comments on 'design, fabrication, and testing of double negative metamaterials'," *IEEE Trans. Antennas Propag.*, vol. 53, no. 2, pp. 891-892, 2005.

[61] S. White, "The transmission of electrical energy without wires as a means for furthering peace," *Electrical World and Engineer*, Mar. 5, 1904.

[62] A. A. Eteng, S. K. A. Rahim, C. Y. Leow, S. Jayaprakasam, and B. W. Chew, "Low-power near-field magnetic wireless energy transfer links: A review of architectures and design approaches," *Renew. Sustain. Energy Rev*., vol. 77, pp. 486-505, Apr. 2017.

[63] W. Li, P. Wang, C. Yao, Y. Zhang, and H. Tang, "Experimental investigation of 1D, 2D, and 3D metamaterials for efficiency enhancement in a 6.78MHz wireless power transfer system," in *2016 IEEE Wirel. Power Transf. Conf. (WPTC) 2016*, pp. 19-22, 2016.

[64] M. S. Yusri, M. H. Misran, N. Yusop, M. A. M. Said, M. A. Othman, and S. Suhaimi, "Transfer efficiency enhancement on wireless power transfer using metamaterial," in *2023 International Conference on Information Technology (ICIT),* Amman, Jordan, pp. 724-729, 2023.

[65] J. Park, Y. Tak, Y. Kim, Y. Kim, and S. Nam, "Investigation of adaptive matching methods for near-field wireless power transfer," *IEEE Trans. Antennas Propag*., vol. 59, no. 5, pp. 1769-1773, 2011.

[66] T. C. Beh, M. Kato, T. Imura, S. Oh, and Y. Hori, "Automated impedance matching system for robust wireless power transfer via magnetic resonance coupling," *IEEE Trans. Ind. Electron*., vol. 60, no. 9, pp. 3689-3698, 2013.

[67] F. Zhang, S. A. Hackworth, W. Fu, C. Li, Z. Mao, and M. Sun, "Relay effect of wireless power transfer using strongly coupled magnetic resonances," *IEEE Trans. Magn*., vol. 47, no. 5, pp. 1478-1481, 2011.

[68] A. K. Singh, M. P. Abegaonkar, and S. K. Koul, "High-gain and high-aperture-efficiency cavity resonator antenna using metamaterial superstrate," *IEEE Antennas Wirel. Propag. Lett*., vol. 16, pp. 2388-2391, 2017.

[69] N. Rajak, N. Chattoraj, and R. Mark, "Metamaterial cell inspired high gain multiband antenna for wireless applications," *AEU Int. J. Electron. Commun*., vol. 109, pp. 23-30, 2019.

[70] G. Varamini, A. Keshtkar, N. Daryasafar, and M. Naser-Moghadasi, "Microstrip Sierpinski fractal carpet for slot antenna with metamaterial loads for dual-band wireless application," *AEU Int. J. Electron. Commun*., vol. 84, pp. 93-99, Oct. 2018.

[71] B. Wang, T. Nishino, and K. H. Teo, "Wireless power transmission efficiency enhancement with metamaterials," in *2010 IEEE Int. Conf. Wirel. Inf. Technol. Syst. (ICWITS 2010)*, no. 1, pp. 2-5, 2010.

[72] J. Liu, Z. Gong, S. Yang, H. Sun, and J. Zhou, "Practical model for metamaterials in wireless power transfer systems," *Appl. Sci.*, vol. 10, p. 8506, 2020.

[73] W. Lee and Y.-K. Yoon, "Wireless power transfer systems using metamaterials: A review," *IEEE Access*, vol. 8, pp. 147930-147947, 2020.

[74] W. Li, F. Yu, X. Rong, and H. Qin, "Optimization of low-frequency magnetic metamaterials for efficiency improvement in magnetically coupled resonant wireless power transfer systems," *IEEE Access*, vol. 10, pp. 125445-125457, 2022.

[75] M. J. Chabalko, J. Besnoff, and D. S. Ricketts, "Magnetic field enhancement in wireless power with metamaterials and magnetic resonant couplers," *IEEE Antennas Wirel. Propag. Lett*., vol. 15, pp. 452-455, 2016.

[76] X. Wang, Y. Wang, Y. Hu, Y. He, and Z. Yan, "Analysis of wireless power transfer using superconducting metamaterials," *IEEE Trans. Appl. Supercond*., vol. 29, no. 2, 2019.

[77] D. R. Smith, D. Schurig, J. J. Mock, P. Kolinko, and P. Rye, "Partial focusing of radiation by a slab of indefinite media," *Appl. Phys. Lett*., vol. 84, no. 13, pp. 2244-2246, 2004.

[78] K. A. Cota, P. A. Gray, M. Pathmanathan, and P. W. Lehn, "An approach for selecting compensation capacitances in resonance-based EV wireless power transfer systems with switched capacitors," *IEEE Trans. Transp. Electrif*., vol. 5, no. 4, pp. 1004-1014, 2019.

[79] Y. Liu, U. K. Madawala, R. Mai, and Z. He, "Zero-phase-angle controlled bidirectional wireless EV charging systems for large coil misalignments," *IEEE Trans. Power Electron*., vol. 35, no. 5, pp. 5343-5353, 2020.

[80] K. Zhang, C. Liu, Z. H. Jiang, Y. Zhang, X. Liu, H. Guo, and X. Yang, "Near-field wireless power transfer to deep-tissue implants for biomedical applications," *IEEE Transactions on Antennas and Propagation*, vol. 68, no. 2, pp. 1098-1106, 2020.

[81] M. Song, K. Baryshnikova, A. Markvart, P. Belov, E. Nenasheva, C. Simovski, and P. Kapitanova, "Smart table based on a metasurface for wireless power transfer," *Physical Review Applied*, vol. 11, no. 5, p. 054046, 2019.

[82] A. L. A. K. Ranaweera, T. S. Pham, H. N. Bui, V. Ngo, and J. W. Lee, "An active metasurface for field-localizing wireless power transfer using dynamically reconfigurable cavities," *Sci. Rep*., vol. 9, no. 1, pp. 1-12, 2019.

[83] M. A. Badwey, N. H. Abbasy, and G. M. Eldallal, "An efficient design of LC-compensated hybrid wireless power transfer system for electric vehicle

charging applications," *Alexandria Eng. J.*, vol. 61, no. 8, pp. 6565-6580, 2022.

[84] S. Wang, C. Jiang, X. Tao, F. Chen, C. Rong, C. Lu, Y. Zeng, X. Liu, R. Liu, B. Wei, and M. Liu, "Enhancing the stability of medium range and misalignment wireless power transfer system by negative magnetic metamaterials," *Materials*, vol. 13, 2020.

[85] J. Wang, R. Chen, C. Cai, J. Zhang, and C. Wang, "An onboard magnetic integration-based WPT system for UAV misalignment-tolerant charging with constant current output," *IEEE Transactions on Transportation Electrification*, vol. 9, pp. 1973-1984, 2023.

[86] Z. Yuan, Q. Yang, X. Zhang, R. Wang, X. Ma, C. Cai, P. Zhang, and H. Lin, "A power-enhancing complementary coupling integration strategy for misalignment-tolerant WPT systems," *IEEE Transactions on Power Electronics*, vol. 38, pp. 14689-14701, 2023.

[87] B. Wang, K. H. Teo, T. Nishino, W. Yerazunis, J. Barnwell, and J. Zhang, "Experiments on wireless power transfer with metamaterials," *Appl. Phys. Lett.*, vol. 98, no. 25, pp. 1-4, 2011.

[88] Y. Z. Cheng, J. Jin, W. L. Li, J. F. Chen, B. Wang, and R. Z. Gong, "Indefinite-permeability metamaterial lens with finite size for miniaturized wireless power transfer system," *AEU Int. J. Electron. Commun.*, vol. 70, no. 9, pp. 1282-1287, 2016.

[89] Y. Cho, S. Lee, J. Lee, and J. Lee, "Hybrid metamaterial with zero and negative permeability to enhance efficiency in wireless power transfer system," in *Proceedings of the 2016 IEEE Wireless Power Transfer Conference (WPTC)*, Aveiro, Portugal, pp. 1-3, 2016.

[90] W. Xin, C. C. Mi, F. He, M. Jiang, and D. Hua, "Investigation of negative permeability metamaterials for wireless power transfer," *AIP Adv.*, vol. 7, no. 11, 2017.

[91] J. Chen and H. Tan, "Metamaterial for wireless power transfer system at 13.56 MHz with coil misalignment," in *Proc. 2017 7th IEEE Int. Symp. Microwave, Antenna, Propagation, EMC Technol. (MAPE 2017)*, pp. 313-317, 2017.

[92] C. Lu, X. Huang, C. Rong, Z. Hu, J. Chen, X. Tao, S. Wang, B. Wei, and M. Liu, "Shielding the magnetic field of wireless power transfer system using zero-permeability metamaterial," *The Journal of Engineering*, vol. 2019, no. 16, pp. 1812-1815, 2019.

[93] A. L. A. K. Ranaweera, T. P. Duong, and J. W. Lee, "Experimental investigation of compact metamaterial for high efficiency mid-range wireless power transfer applications," *J. Appl. Phys.*, vol. 116, no. 4, 2014.

[94] C. Rong, X. Tao, C. Lu, Z. Hu, X. Huang, Y. Zeng, and M. Liu, "Analysis and optimized design of metamaterials for mid-range wireless power transfer using a Class-E RF power amplifier," *Appl. Sci.*, vol. 9, no. 1, p. 26, 2018.

[95] J. Chen, X. Liu, Y. Zhao, and Y. Sun, "Metamaterial-based high-efficiency wireless power transfer system at 13.56 MHz for low power applications," *Progress in Electromagnetics Research B*, vol. 72, pp. 17-30, 2017.

[96] T. Shaw, A. Roy, and D. Mitra, "Efficiency enhancement of wireless power transfer system using MNZ metamaterials," *Prog. Electromagn. Res. C*, vol. 68, pp. 11-19, Aug. 2016.

Muhammad Sukriyllah Yusri graduated from Universiti Malaysia Terengganu where he received his B.Sc. Applied Science majoring in Physics Electronic and Instrumentation. He currently is pursuing the M.Sc. degree in Electronic Engineering from Universiti Teknikal Malaysia Melaka. His current research interests focus on enhancing the inductive wireless power transfer using metamaterial. He is also interested in electronic circuit design, embedded systems, and wireless communication technologies.

Mohamad Harris Misran was born in Johor, Malaysia. He obtained his degree in B.Eng. in Electronics Engineering (Telecommunication) from University of Surrey, UK, in 2006 and M.Eng. in Engineering (Telecommunication) in 2008 from University of Wollongong, Australia. He is Ph.D. holder in Electrical Engineering from Universiti Teknologi Malaysia (UTM), Johor, Malaysia. Currently he is working with UTeM Melaka since 2006 and focusing on RF and microwave circuits, devices and also wireless power transfer.

Tan Kim Geok received the B.E., M.E., and PhD. degrees in electrical engineering from University of Technology Malaysia, in 1995, 1997, and 2000, respectively. He was Senior RD engineer in EPCOS Singapore in 2000. In 2001-2003, he joined DoCoMo Euro-Labs in Munich, Germany. He is currently a member of the academic staff at Multimedia University. His research interests include radio propagation for outdoor and indoor, RFID, multi-user detection technique for multicarrier technologies, and A-GPS.

Norbayah Yusop received the B.Sc. degree in telecommunication electronics from the Universiti Teknikal Malaysia Melaka (UTeM), the M.Sc. degree in telecommunication and information engineering from the Universiti Teknologi Mara (UiTM) and the Ph.D. degree in space science from the Universiti Kebangsaan Malaysia (UKM). She was attached to the Fakulti Kejuruteraan Elektronik dan Kejuruteraan Komputer (FKEKK) as a tutor in 2009. She completed her Ph.D. studies in 2019. Her research interests include lightning physic, microwave propagation and telecommunication engineering.

Maizatul Alice Meor Said received the B.Eng. in Electronics Engineering (Telecommunication) from University of Surrey, UK, in 2006. She obtained M.Eng. in Master of Engineering (Telecommunication) in 2009 from University of Wollongong, Australia. Currently, she is a Ph.D. holder at the Universiti Teknikal Malaysia Melaka (UTeM), Melaka, Malaysia. Her research areas include RF energy harvesting, resonators, amplifiers and antennas and microwave sensors.

Azahari Salleh received both first and master's degree from Universiti Teknologi Malaysia, in Electrical Electronic Engineering 2003 and 2008. He joined UTeM in 2005 and currently pursuing Ph.D. in microwave imaging. His research interest on microwave device and imaging system design.

Sharul Kamal Abdul Rahim received his first degree from University of Tennessee, USA, majoring in Electrical Engineering, graduating in 1996, M.Sc. in Engineering (Communication Engineering) from Universiti Teknologi Malaysia (UTM) in 2001, and Ph.D. in Wireless Communication System from University of Birmingham, UK, in 2007. Currently, he is an Associate Professor at Wireless Communication Centre, Faculty of Electrical Engineering, UTM. His research interest is smart antenna communication systems.

Inversion Method of Lightning Current Distribution on a Surface Conductor Represented by Thin Lines

Zemin Duan[1], Chen Tong[1], Yeyuan Huang[2,3,4], Xinping Li[5], Shanliang Qiu[2,3,4], Xiaoliang Si[2,3,4], Yan Wei[1], and Yao Ling[1]

[1]School of Electrical Engineering and Automation
Hefei University of Technology, Hefei 230009, China
duanzemin@yeah.net, 2018110388@mail.hfut.edu.cn, 2020170474@mail.hfut.edu.cn, 862060425@qq.com

[2]National Key Laboratory of Electromagnetic Information Control and Effects
Hefei 230031, China
yeyuan_huang@outlook.com, wobenshanliang1983@163.com, sixiaoliang1985@126.com

[3]Key Laboratory of Strong Electromagnetic Environment Protection Technology
Hefei 230031, China

[4]Key Laboratory of Aircraft Lightning Protection of Anhui Province
Hefei 230031, China

[5]School of Mathematics
Hunan Institute of Science and Technology, Yueyang 414006, China
xpli@hnist.edu.cn

Abstract **–** Electromagnetic simulation and pre-analysis of electromagnetic compatibility for lightning effects are important. It is difficult to estimate the surface current of surface structures represented by thin lines. In this study, we simplified the partial element equivalent circuit (PEEC) equation and deduced an equation for the magnetic field based on the thin-line representation method. An inversion method was used to determine the surface current in a frequency-domain PEEC. Parallel computing technology was used to improve the inversion efficiency. Additionally, the capacitive and inductive characteristics of the elements of Darney's circuit method were developed for PEEC. The results were compared with calculations using the finite integration technique. The application of the thin-line representation method was broadened, and its efficiency has been improved.

Index Terms **–** Lightning current distribution, magnetic field distribution, partial element equivalent circuit, thin-line representation method.

I. INTRODUCTION

As the complexity and intensity of the electromagnetic environment increase, electromagnetic simulation and pre-analysis [1–5] become more important, especially in the analysis of structural surface current distributions and magnetic field distributions [6, 7–13]. The distribution of the lightning surface current and magnetic field is important, particularly for lightning protection.

Among electromagnetic simulation methods, the thin-line representation method [14–16], proposed in 1986, is well known for its high efficiency. In recent years, it has attracted the attention of scholars because it can rapidly perform sensitivity analyses [17–20]. The thin-line representation has been applied for solving electromagnetic problems under the framework of the classical circuit [21, 22] and partial element equivalent circuit (PEEC) [23]. The framework of the classical circuit described in the previous study, also called Darney's circuit method, has been extended for electromagnetic compatibility and electromagnetic interference (EMC/EMI) [24]. The PEEC framework described above is called the one-dimensional (1D)-PEEC.

Thin-line representation is likely to become an important preparatory step for future electromagnetic simulations [25]. It is mainly used to solve difficulties related to structures composed of lines such as high-voltage transmission towers and grounding grids [26–28]. Li analyzed the shielding effect of modern buildings with wire mesh structures in a lightning environment [29]. Ye et al. proposed an efficient full-wave PEEC equation for thin-line structures in a lossy ground for transient lightning analysis [27]. Prost et al.

Submitted On: December 4, 2024
Accepted On: March 6, 2025
https://doi.org/10.13052/2024.ACES.J.400309

conducted thin-line modeling of A320 landing gear [30]. However, these studies only considered the application of the thin-line representation when the structure was a thin wire rather than surface structures.

For surface structures, the structure is represented by parallel lines, or only the cross-section is analyzed [25]. Several studies have considered the application of the thin-line representation for surface structures. Lv used thin-line representation to analyze the scattering of an aircraft [31]. Torchio used a method based on PEEC to analyze fast voltage transient and toroidal coils in a JT-60SA fusion reactor [23, 32]. This study showed that the thin-line representation could simulate full-wave electromagnetic processes using appropriate solution methods. However, there are few studies on current distribution in lightning environments.

Regarding the lightning current distribution of surface structures, Parmantier et al. analyzed the cable response in a lightning environment under a simplified two-dimensional (2D) cross-section [25]. In these studies, the current was restricted to the flow perpendicular to the cross-section [21, 22]. Although they simulated the proximity effect of the lightning current, the study of the lightning current distribution involves far more than that.

The difficulty in inverting the surface current distribution of a surface structure lies in determining the height of the magnetic field strength, which is associated with the surface current. In the finite-difference time-domain (FDTD), the surface current can be calculated using the magnetic field near the conductor [33]. Unlike the FDTD, free space is not meshed regardless of Darney's circuit method or 1D-PEEC. Therefore, the surface current cannot be calculated directly using a magnetic field.

In this study, PEEC equations were simplified by analyzing the difference in the PEEC in a situation where the surface structure is represented by thin lines. The influences of simplification and delay on the results were also analyzed. An inversion method for the surface current distribution was proposed by calculating the average value of the magnetic field strength of all surface elements. In addition, parallel computing was used to improve the efficiency of the method. Finally, the capacitance-inductance duality characteristics in classical circuit theory were extended to PEEC.

II. PEEC METHOD

The PEEC method is an integration method that introduces the concept of partial elements and performs circuit interpretation on the electric field integral equation (EFIE) through the resistance, partial inductance, and potential coefficient [23]. Thus, the resulting equivalent circuit is studied by the Tableau analysis method or by means of Spice-like circuit solvers in both time and frequency domains [23]. It is a full-wave method based on EFIE and is widely used in EMC/EMI and other research fields.

The application of the 1D-PEEC to aircraft lightning effects differs from that of thin-wire structures such as high-voltage towers, grounding grids, and down conductors. This difference is analyzed below. If the conductors are thin-wire structures, the thin-wire representation is very simple, as shown in Figs. 1 (a) and (b). When the computational domain contains soil, the half-space of the soil [27] and air must be considered.

For surface structures such as landing gear and aircraft fuselages, the structure is simplified, or only the cross-section is discretized, as shown in Figs. 1 (e) and (f) [25, 30].

This paper focusses on current distribution inversion, in which surface structures are represented by thin wires, when lightning strikes an aircraft. Unlike the soil medium that exists in a ground lightning strike environment, only one air medium exists when an aircraft is struck by lightning. When the aircraft is discretized using

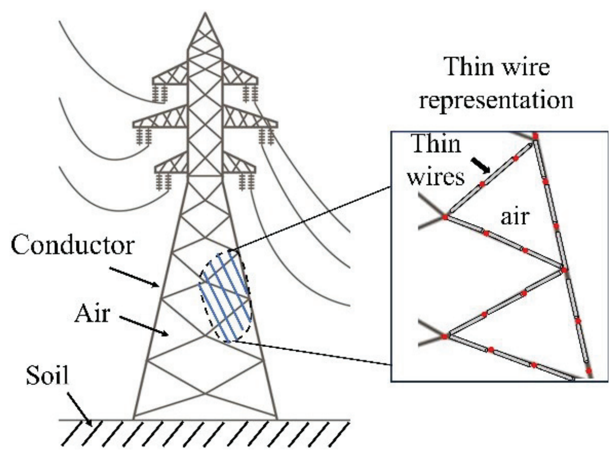

(a)

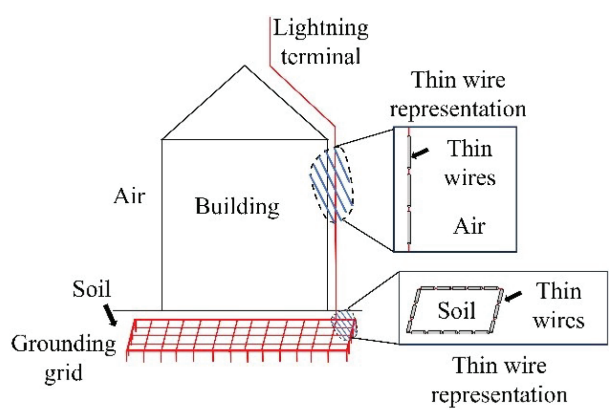

(b)

Fig. 1. *Continued.*

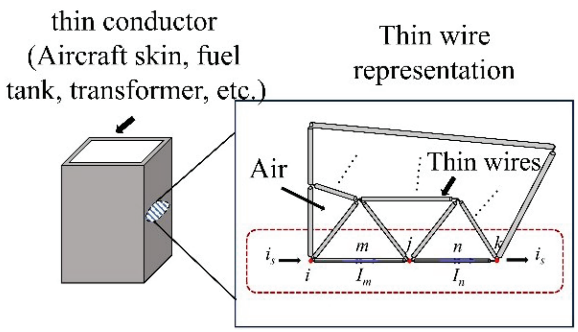

(c)

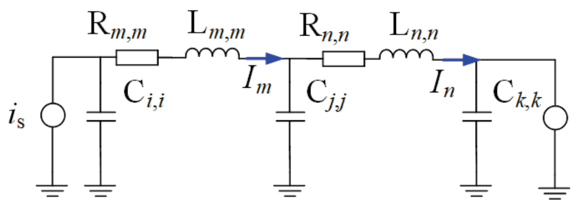

(d)

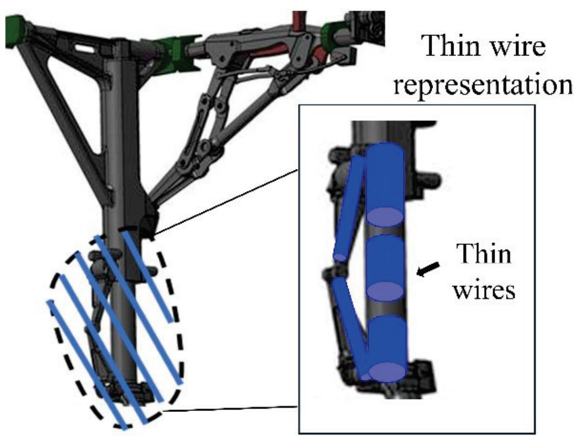

(e)

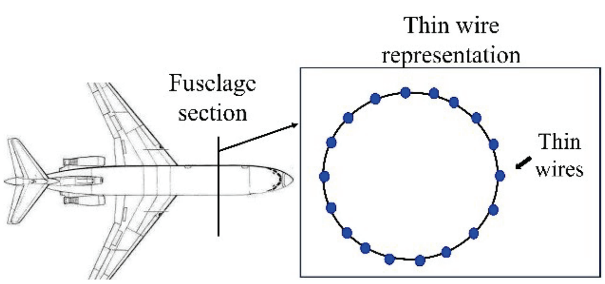

(f)

Fig. 1. Power PEEC of the thin-wire model. (a) Thin-line representation process of a high-voltage tower [27, 35], (b) thin-wire representation process of a grounding grid [35], (c) structures modeled as thin lines, (d) equivalent circuit diagram of some nodes and sticks, (e) thin-wire representation process of landing gear [30], and (f) thin-wire representation process of aircraft fuselage cross-section [25].

triangular surface elements, the edges of the triangle are extracted as line segments, as shown in Fig. 1 (c). The equivalent circuit model can be obtained according to the PEEC, as shown in Fig. 1 (d).

In Fig. 1 (c), the red dots represent the potential (capacitance) matrix node, which correspond to the potential matrix element $C_{i,i}$, and the blue crosses represent the inductance (current) matrix node, which corresponds to the resistance matrix element $R_{m,m}$ and inductance matrix element $L_{m,m}$ of the sticks, where the subscripts *i, j,* and *k* represent the *i*th, *j*th, and *k*th points, respectively, and *m* and *n* represent the *m*th and *n*th sticks, respectively. i_s represents the injected current of the node.

According to Fig. 1 (d), the PEEC equation can be expressed as:

$$\begin{bmatrix} \mathbf{A}^T & \mathbf{R}+j\omega\mathbf{L} \\ j\omega\mathbf{P}^{-1}+\mathbf{Y}_L & -\mathbf{A} \end{bmatrix} \begin{bmatrix} \mathbf{V} \\ \mathbf{I} \end{bmatrix} = \begin{bmatrix} -\mathbf{Vs} \\ \mathbf{Is} \end{bmatrix}, \tag{1}$$

where **A** is the correlation matrix that represents the relationship between the line sticks and the nodes. The resistance matrix, **R**, is a $l\times l$ diagonal matrix (where l is the number of the sides of the objects, inductive elements). The matrix of inductances, **L**, is a $l\times l$ matrix where l is the number of the inductive elements (sides) that discretize the objects and ω is the angular frequency. The matrix of coefficients of potential, **P**, is an $n\times n$ matrix, where n is the number of nodes (capacitive elements) that are the endpoints of the inductive elements (from the standpoint of the electrical equivalent circuit). $\mathbf{Y}_L$ is the admittance matrix, **V** is the node voltage, **I** is the current of the sticks, $\mathbf{V}_s$ is the external voltage excitation, and $\mathbf{I}_s$ is the external current excitation. Because **P** is nonsparse to avoid its inversion matrix, the above equation can be rewritten as:

$$\begin{bmatrix} \mathbf{A}^T & \mathbf{R}+j\omega\mathbf{L} \\ j\omega\mathbf{1}+\mathbf{P}\mathbf{Y}_L & -\mathbf{PA} \end{bmatrix} \begin{bmatrix} \mathbf{V} \\ \mathbf{I} \end{bmatrix} = \begin{bmatrix} -\mathbf{Vs} \\ \mathbf{PIs} \end{bmatrix}. \tag{2}$$

The voltages and currents at the grid nodes can be solved by inverting the matrix. To calculate the matrix in equation (2), this study used the Gauss-Legendre quadrature formula [23].

III. SIMPLIFICATION OF PEEC AND THE INVERSION METHOD OF SURFACE CURRENT DISTRIBUTION

A. Simplification of PEEC

In PEEC for surface structures, using a finite number of sticks to represent the conductors may introduce a capacitance that does not exist. To avoid introducing a capacitor, the current flowing through it can be ignored. The PEEC equations can be simplified as:

$$\begin{bmatrix} \mathbf{R}+j\omega\mathbf{L} & \mathbf{A}^T \\ \mathbf{A} & \mathbf{0} \end{bmatrix} \begin{bmatrix} \mathbf{I} \\ \mathbf{V} \end{bmatrix} = \begin{bmatrix} -\mathbf{Vs} \\ -\mathbf{Is} \end{bmatrix}. \tag{3}$$

To analyze the influence of simplification, the results of considering and not considering the capacitor are compared in parts A and B of section IV by sweeping the frequency and injecting the time-domain lightning current, respectively.

Because lightning current is typically expressed as a function of time I(t), fast Fourier transformation (FFT) is required to obtain I(ω); thus, the current in the frequency domain can be obtained via equation (3). The current in the thin wire $\vec{I_i}$ in the time-domain can be obtained by performing an inverse FFT (IFFT) on the results. The errors caused by the FFT and IFFT are also analyzed in part C of section IV.

B. Magnetic field calculation method

According to Maxwell's equations, the magnetic field and vector magnetic potential satisfy the following relationship:

$$\vec{B} = \nabla \times \vec{A}. \tag{4}$$

Thin-line currents can then be used to calculate the vector magnetic potential. The magnetic field intensity at observation point P is generated by all the line currents passing through the following:

$$\mathbf{H} = \frac{\nabla \times \mathbf{A}}{\mu_0} = \frac{1}{4\pi}\sum_{i=1}^{l} \nabla \times \int_{l_i} \frac{\vec{I_i}}{\left|\vec{r_p'} - \vec{r_i'}\right|} dl_i$$
$$= \frac{1}{4\pi}\sum_{i=1}^{l} \int_{l_i} \frac{\vec{I_i} \times \mathbf{r}'}{r'^3} dl_i \tag{5}$$

where l_i represents the length of the ith line, $\vec{I_i}$ represents the current vector on the ith line, and $\left|\vec{r_p'} - \vec{r_i'}\right|$ represents the distance between the observation point and differential element. To distinguish it from r, r' is used to represent the distance between P and the integration position point.

C. Inversion method of the surface current distribution

After obtaining $\mathbf{H}$, $\mathbf{J}_s$ can be expressed according to the continuity conditions at the interfaces:

$$\mathbf{J}_s = e_n \times (\mathbf{H}_2 - \mathbf{H}_1). \tag{6}$$

The surface current density can then be derived from the magnetic field using equation (6). In FDTD or FEM, surface currents are often calculated by interpolating adjacent grids [36]. In the 1D PEEC, only the conductor is meshed, whereas free space is not (as shown in Fig. 1). In this case, the positions of $\mathbf{H}_1$ and $\mathbf{H}_2$ cannot be determined and, as a result, $\mathbf{J}_s$ cannot be estimated using equation (6). The key to estimating $\mathbf{J}_s$ lies in determining the height of the magnetic field calculation.

To determine the height, ignoring the influence of other strong magnetic field sources, for a current-carrying conductor, the closer the magnetic field observation point is to the current-carrying conductor, the stronger the magnetic field strength.

Based on the assumptions above, the magnetic field at the height at which the maximum magnetic field occurs can be used to estimate $\mathbf{J}_s$. However, when the structure is represented by thin wires, the surface element is filled with an air medium, and all thin-line currents generate a magnetic field. Therefore, it may be difficult to determine the height of the peak value of the magnetic field.

The magnetic field strength of all the surface elements is determined by taking the radius of the thin wire as the step size. The height of the magnetic field calculation point is then defined as k times the radius of the conductor, as shown in Fig. 2.

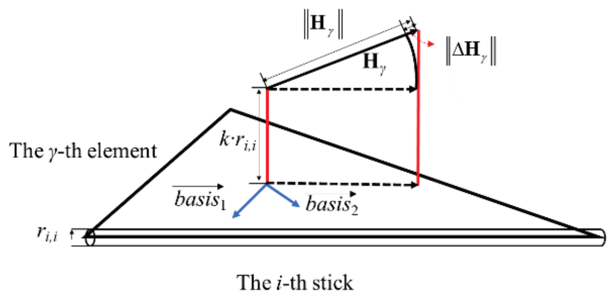

Fig. 2. Inversion method of the surface current distribution.

The average value of the magnetic field strength of all surface elements is defined as:

$$j_a(k) = \frac{\sum_{\gamma=1}^{N_{\text{element}}} \|\mathbf{H}_\gamma\|}{N_{\text{element}}}. \tag{7}$$

In equation (7), $\mathbf{H}_\gamma$ is the magnetic field strength at a height $k{\cdot}r_{i,i}$ from the γ-th element. When $j_a(k)$ is largest, k is defined as k_{max}.

Because the normal vector of $\mathbf{H}_\gamma$ is caused by the thin-line representation and $k_{max}{\cdot}r_{i,i}$ height, the magnitude of the magnetic field at k_{max} is used to estimate the surface current:

$$J_\gamma = \|\mathbf{H}_\gamma(k_{\max})\|. \tag{8}$$

In equation (8), the modulus of the magnetic field strength is used to calculate the surface current, rather than the tangential component. Therefore, it is necessary to analyze the differences caused by the orthogonal decomposition.

To analyze the difference, a unit orthogonal basis, $\overrightarrow{basis_1}$ and $\overrightarrow{basis_2}$, on the face element can be determined by the vertices of the face element. The direction of the face element is defined as:

$$\vec{n_\gamma} = \overrightarrow{basis_1} \times \overrightarrow{basis_2}. \tag{9}$$

$\|\Delta\mathbf{H}_\gamma\|$ represents the difference between the magnetic field modulus and the tangential component:

$$\|\Delta\mathbf{H}_\gamma\| = \|\mathbf{H}_\gamma\| - \left\|\mathbf{H}_\gamma \bullet \overrightarrow{basis_1} \cdot \overrightarrow{basis_1} + \mathbf{H}_\gamma \bullet \overrightarrow{basis_2} \cdot \overrightarrow{basis_2}\right\|. \tag{10}$$

The subtrahend in equation (10) represents the magnitude of the tangential component of $\mathbf{H}_\gamma$. Thus, the average error caused by the orthogonal decomposition can be expressed as:

$$Error_{OD} = \frac{\sum_{\gamma=1}^{N_{\text{element}}} \left\| \Delta \mathbf{H}_\gamma \right\|}{N_{\text{element}}}. \tag{11}$$

IV. RESULTS AND DISCUSSION

A. Analysis of the influence of P and delay on the results by sweeping frequency

We first analyzed the impact of the potential matrix and delay on the results from a frequency-domain perspective. Then, we analyzed the efficiency and accuracy of different simulation settings under lightning current excitation and compared them with the finite integration technique (FIT).

In the frequency-domain analysis, currents of different frequencies were injected into an aluminum plate with dimensions of 500×250×2 mm. The current inflow and outflow points are shown in Fig. 3 with an injected current value (I_{inject}) of 1 A. The structure was automatically divided into triangular surface elements using commercial software, and the vertex coordinates of the surface elements were extracted to form a thin-wire model constructed using triangular vertices. The number of nodes N was 689.

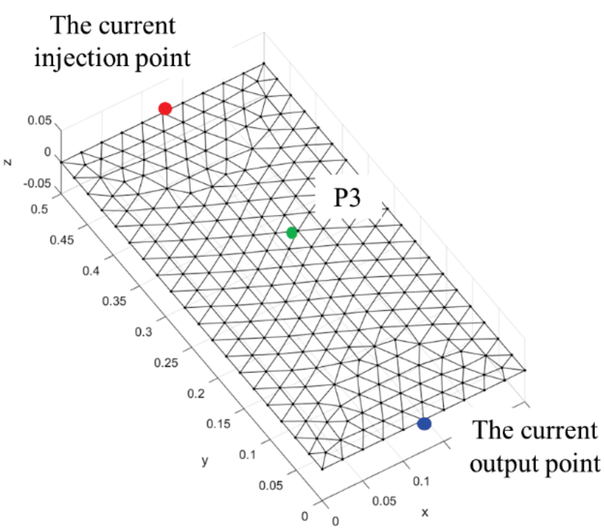

Fig. 3. Current outflow and inflow points after flat plate meshing.

As described in part A of section III, the PEEC is simplified by ignoring the capacitance (**P**). It is necessary to analyze the effect of **P** on the results. If the capacitance was considered, equation (2) was used. Otherwise, without considering capacitance, equation (3) was used for the solution.

Delay is another factor that influences the results, particularly for large structures. To consider the delay, internal elements **P** and **L** in equations (2) and (3) must be modified as follows:

$$\begin{aligned} P_d &= P \cdot e^{-j \cdot d \cdot 2\pi f \cdot \sqrt{\varepsilon_0 \mu_0}} \\ L_d &= L \cdot e^{-j \cdot d \cdot 2\pi f \cdot \sqrt{\varepsilon_0 \mu_0}} \cdot \end{aligned} \tag{12}$$

In the above equations, P and L are the matrix elements when the delay is not considered, and P_d and L_d are the matrix elements when the delay is considered. d in equation (12) is the distance between nodes, f is the frequency of the injected current, and μ_0 and ε_0 are the magnetic permeability and dielectric constant in vacuum, respectively. For the specific codes, refer to [36].

The effect of delay on the results was related to the relative size. The relative size is defined as follows:

$$S = \frac{l_w}{l_p} = \frac{c}{f \cdot l_p}, \tag{13}$$

where S is the relative size, l_w is the wavelength, l_p is the physical scale, c is the speed of wave propagation, and f is the frequency.

Results for different frequencies were compared with those obtained with and without considering **P** and the time delay, as shown in Fig. 4. The percentage error in Fig. 4 can be expressed as:

$$error = \frac{\sqrt{\sum_{j=1}^{N} \left(\widehat{i_j} - i_j \right)^2}}{I_{inject}} \%. \tag{14}$$

In equation (14), I_{inject} is the injected current, which was set to 1 in the situation. N is the total number of current nodes, which was 689. i_j is the current of the j-th node when considering capacitance and delay. When

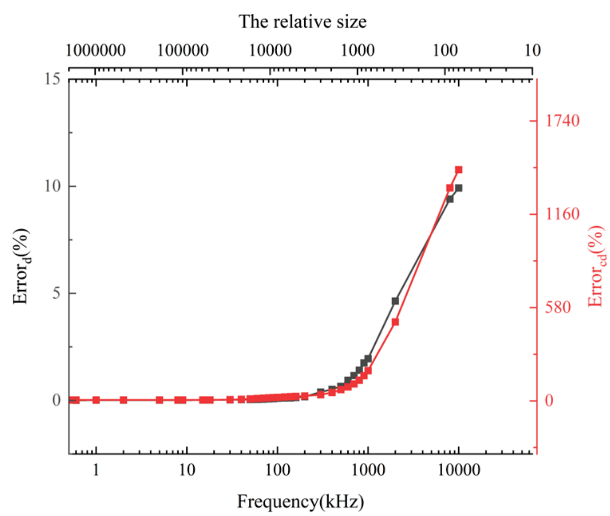

Fig. 4. Error at different frequencies. Error$_d$ and Error$_{cd}$ calculated by equation (14) represent the differences caused by not considering delay and not considering capacitance and delay, respectively.

calculating the error caused by ignoring delay, $\widehat{i_j}$ is the j-th node current when delay is ignored and capacitance is considered. When calculating the error caused by ignoring capacitance and delay, $\widehat{i_j}$ is the node current without considering capacitance and delay.

As shown in Fig. 4, with an increase in the frequency, the error caused by the delay was relatively small at 1 MHz (S>600, within 2%). It exhibited a rapidly increasing trend after exceeding 1 MHz (S<600). However, the error was still small, only 9.9% at 10 MHz (S=60), compared to the results obtained when ignoring **P**. This is because the aluminum plate analyzed in this study was small.

Ignoring **P** caused a large difference in the calculation results. The error reached 22% at 100 kHz (S=6000).

B. Analysis of the influence of P and delay on the results by injecting lightning current component A

The lightning current component A in SAE-ARP-5412 with a duration of 300 μs was sampled at 1 MHz and replaced with the swept frequency current described above. The equation for the lightning current component A is defined as:

$$I(t) = I_0 \left(e^{-\alpha t} - e^{-\beta t}\right)\left(1 - e^{-\gamma t}\right)^2. \qquad (15)$$

In equation (15), I_0=218810, α=11354, β=647265, and γ=5423540. Subsequently, the signal transformed by the FFT was set to inject the current. In Fig. 5 (a), the waveform of lightning current component A is represented by the red curve. Its frequency component is shown in Fig. 5 (b). As shown in Fig. 5 (a), the coordinates of the observation point position P3 were (0.125, 0.250, 0.050) [unit: m].

As shown in Fig. 5 (b), in terms of the frequency components of the lightning current component A, most of the frequency components were within 10 kHz. Therefore, errors caused by **P** may still be extremely small.

As shown in Fig. 5 (a), the results when the potential matrix was considered were higher than those when the potential matrix was not considered. The error between the two values was within 18%. Moreover, as the waveform slowed down, the error caused by **P** gradually decreased, which was caused by ω in PEEC (see equation (1)). If ω is small, $j\omega P^{-1}$ is small and $j\omega P^{-1} + Y_L$ can be set to 0. Then, equations (1) and (3) are equivalent.

From the frequency perspective, the trailing edge of the lightning current waveform corresponded to the low-frequency region, and the error in the low-frequency region was relatively low, as shown in Fig. 4.

In any case, the error at the peak moment in the time domain was considerably lower than that shown in Fig. 4 because the lightning current component A had greater energy at low frequencies.

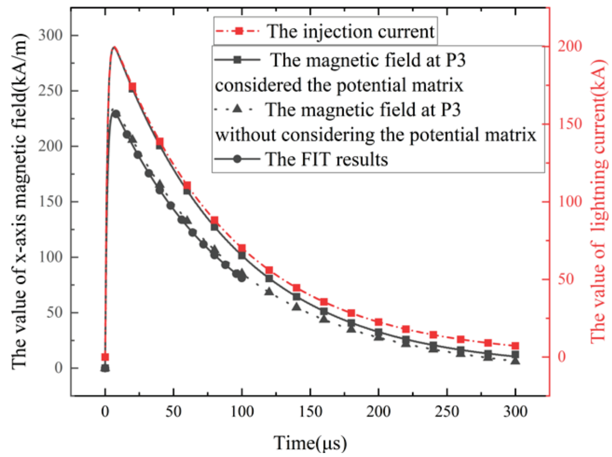

(a)

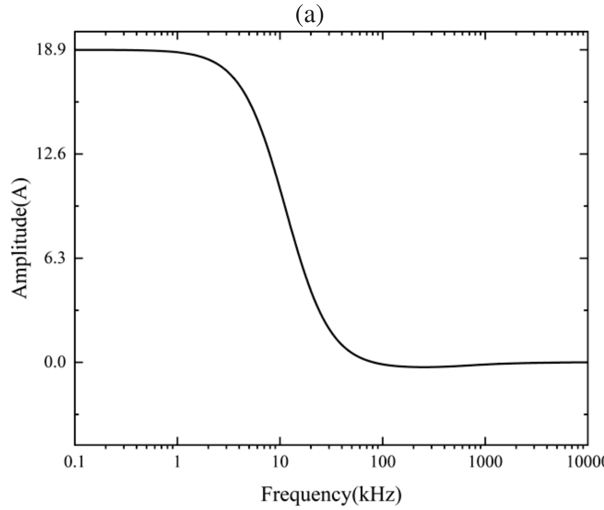

(b)

Fig. 5. Injected lightning current waveform and magnetic field waveform at the observation point. (a) Magnetic field waveform at position P3 and the injected current and (b) frequency component of lightning current component A.

As shown in Fig. 5 (a), the high amplitude of the magnetic field caused by **P** can be explained in two ways. First, in the EFIE, the scalar potential term causes the electric field to increase, which leads to an increase in the thin-line current in the solution. Second, the addition of a potential matrix considers the current in the capacitor branch. The current in the capacitor increases the amplitude of the thin-line current when it flows into the node.

However, before the actual non-thin wire conductive structure was meshed, the inside of the structure was not filled with air. The capacitance term in PEEC could not be introduced at this time. By comparing the results of PEEC and FIT, it was found that the consistency between the FIT and PEEC was higher when the capacitance term was not considered. At this point, **P** caused the magnetic field calculation results to be too large.

C. Analysis of the influence of FFT and mesh density on the results

Because the accuracy of the results highly depends on the mesh density and FFT operations, the influence of the related settings of the mesh density and FFT should be analyzed.

Simulation settings are listed in Table 1. Methods 1-3 were used to compare the impact of the mesh density on the results. In addition, Methods 4-8, which involved changing the sampling frequency and duration of the source, were used to compare the impact of FFT on the results.

In the simulation, five observation points were selected to analyze the amplitude of the results. The coordinates of these points were P1 (0.075, 0.250, 0.050), P2 (0.125, 0.150, 0.050), P3 (0.125, 0.250, 0.050), P4 (0.125, 0.350, 0.050), and P5 (0.175, 0.250, 0.050) (unit: m). The results for these five points are listed in Table 2. Because P3 is above the center of the plate, P1 and P2 are symmetrical, and P4 and P5 are symmetrical. The *x*-axis magnetic fields at P1, P2, P4, and P5 should be equal.

Under different mesh densities (Methods 1-3), this feature became more evident as the number of thin lines increased. In Method 3, the difference in the magnetic fields between the two pairs of symmetrical positions was considerably smaller than that of the FIT, which indirectly verified the accuracy of the results. At the same time, when comparing Methods 4-8, changes in the sampling frequency and waveform duration did not cause major changes in the results.

In addition to amplitude comparison, the magnetic field at the center point was compared, as shown in Fig. 6. Because the time-domain waveforms under different simulation settings were not very different, we compared the single-sided frequency spectra of the results in Fig. 6 (a), as shown in Fig. 6 (b).

Comparing the results of Methods 1-3 in Fig. 6 (b), the power spectra of different mesh densities were consistent. The duration of the excitation source and the sampling frequency affected the spectrum.

The effect of the duration on the result was small, as in Methods 4 and 6 in Fig. 6 (b). The reason for the small difference is that the FFT of the nonperiodic signal was obtained by extending the signal after truncation, and lightning current component A had less energy after 300 μs.

The sampling frequency had a greater impact on the spectrum than on the waveform time, as in Methods 4 and 5. As the sampling frequency increased, the spectrum gradually became consistent with that of the

Table 1: Simulation settings and time consumption

Method	Number of Sticks	Number of Nodes	Sampling Frequency (MHz)	Time of Waveform (μs)	Time (s)
Method 1	45	20	2	100	0.089338
Method 2	689	250	2	100	11.745
Method 3	4597	1584	2	100	1158.3
Method 4	689	250	10	300	176.47
Method 5	689	250	100	300	1818.31
Method 6	689	250	10	500	301.3620255
Method 7	689	250	500	100	3002.46
Method 8	689	250	2	500	57.7893795
	Number of Cells		**Frequency Range (MHz)**	**Time of Waveform (μs)**	
FIT	38080		0∼100	100	2 h 58 min

Table 2: Simulation results of different methods

Method	Peak Value of Magnetic Field Intensity of *X*-Axis (Ka/M)				
	P1	**P2**	**P3**	**P4**	**P5**
Method 1	239.06	247.63	236.39	235.76	231.37
Method 2	239.30	240.98	236.59	241.23	238.46
Method 3	238.32	238.24	233.69	238.25	238.31
Method 4	239.46	241.18	236.79	241.43	238.62
Method 5	239.46	241.18	236.79	241.43	238.62
Method 6	239.5	241.26	236.88	241.52	238.68
Method 7	239.27	240.95	236.55	241.19	238.44
Method 8	239.52	241.25	236.87	241.50	238.67
FIT	237.9	238.4	230.9	238.4	237.9

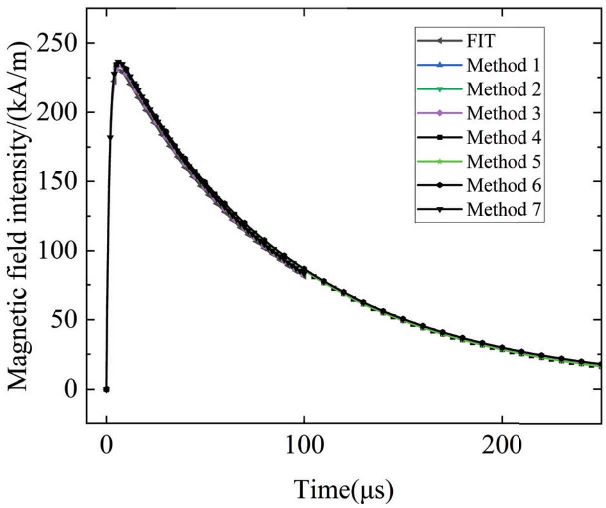

Fig. 6. Results of the FIT and PEEC methods. (a) Time-domain waveforms obtained using different methods and (b) frequency-domain waveforms obtained using different methods.

FIT. Although there were certain differences in the frequency domains between the different frequency methods, Table 2 and Fig. 6 (a) show that the peak value and time-domain waveform of the magnetic field were not significantly different. Therefore, the magnetic field results obtained using the simplified PEEC equation were accurate. In addition, the results indicated that the relevant settings and solution results of the entire FFT and IFFT processes were reliable.

From the perspective of computational time, the thin-line model under the PEEC method was considerably faster than that under the FIT. As shown in Table 1, the grid became denser and the calculation time increased; however, the time was significantly less than that taken by the FIT. Therefore, the line-network model was more efficient.

D. Surface current distribution

Next, the method for estimating the surface current distribution was verified by comparing it with the FIT. The average error caused by orthogonal decomposition (Error_{OD}) was also analyzed.

The Error_{OD} values calculated using equation (11) and the average current density $j_a(k)$ of the surface element calculated using equation (7) at different k values at 6 μs are shown in Fig. 7.

Figure 7 shows the average current density on the surface elements, which first increased and then decreased with increasing height. The maximum surface current was observed when k reached approximately 10 (at a height of approximately 10 mm). Error_{OD} first decreased and then increased with height, reaching a minimum value when k was approximately 3 (at a height of approximately 3 mm). The normal magnetic field component of the panel near this position was the smallest.

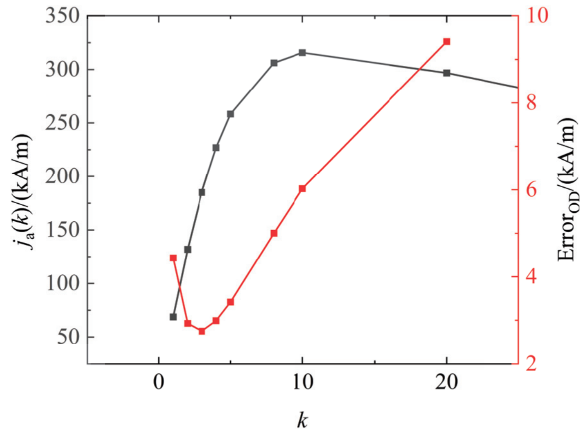

Fig. 7. Results of Error_{OD} and $j_a(k)$ at different heights.

As shown in section III, the magnitude of the magnetic field at k_{max} can be used to estimate the surface current rather than the tangential component and minimum height of Error_{OD}. We explain the reason for this estimation by presenting the results of the surface current distribution in Fig. 8. Surface currents were calculated using k=10 and k=3. FIT results were used for comparison, as shown in Fig. 9. Moreover, the maximum and minimum values of the color bars are kept consistent in Figs. 8 and 9.

As shown in Fig. 9, the lightning current flowed along the edges. In addition, results indicate that the current flowing through the edge was approximately 4.5×10^5 A/m. The currents at the injection and outflow points exceeded 8×10^5 A/m.

As shown in Fig. 8 (a), the tangential component may not be suitable for inverting the surface current distribution. Orthogonal decomposition of the plate-edge magnetic field would result in loss of the magnetic field in the normal direction, decreasing the current density on the edge surface.

When k=3, Error_{OD} was the smallest, the surface current at the injection point was greater than 6×10^5 A/m, and the edge surface current density was approximately 3×10^5 A/m, as shown in Fig. 8 (b). However, the estimated results for the surface current were too small, which indicates that the minimum height of Error_{OD} cannot be used to reflect the surface current distribution.

When k=10, $j_a(k)$ was largest, and the inversion results of the thin-wire model were closer to the FIT results. Therefore, FIT verified that the surface current density could be effectively inverted by determining the height with the maximum average current density.

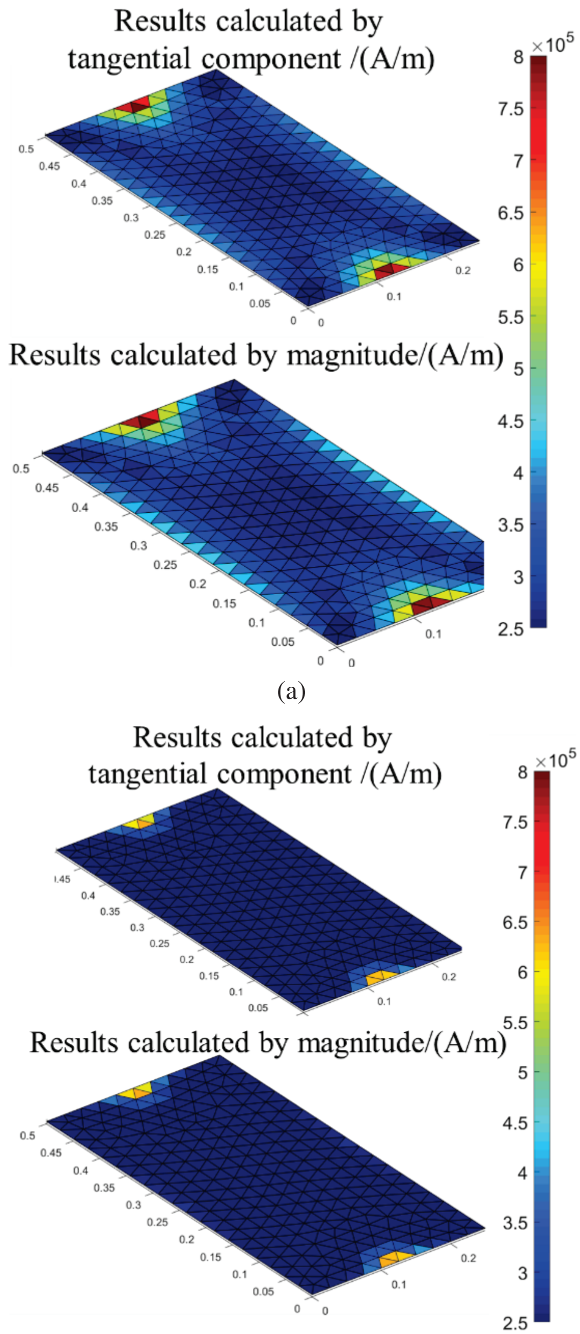

Fig. 8. Results of the current distribution. (a) Surface current distribution at k=10. The height of the magnetic field calculation point for each surface element is 10 mm. (b) Surface current distribution at k=3. The height of the magnetic field calculation point for each surface element is 3 mm.

According to the above analysis, the thin-line model did not exhibit a stronger magnetic field closer to the observation point of the current-carrying structure. Instead, as the distance decreased, it showed a trend of first increasing and then decreasing, as shown in Fig. 7.

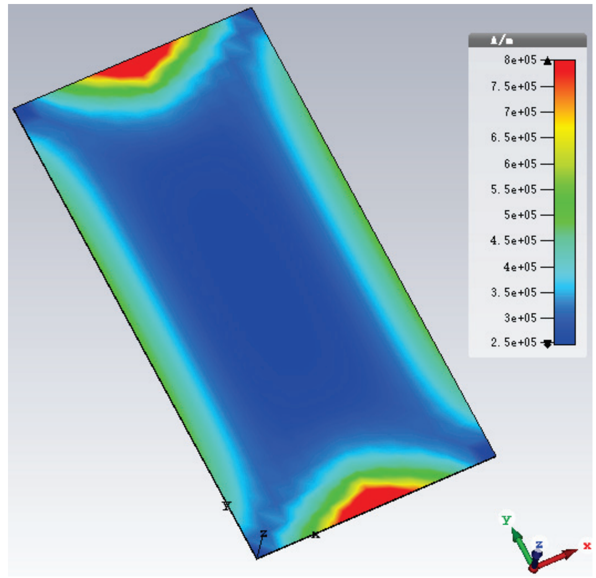

Fig. 9. FIT results of the lightning current distribution of the plate at 6 μs.

E. Current distribution inversion for a real case

In part D, an inversion method for the surface current distribution of the thin-line model is introduced. Although a flat plate is the basic unit of complex structures, there are many structures with large curvatures, such as aircraft wings and vertical tails. Therefore, lightning current distribution in an elliptical barrel was analyzed.

The long semi-axis of the elliptical barrel was 90 mm, the short semi-axis was 45 mm, and its length was 1.2 m. The lightning current was injected through four points and flowed out from four points, as shown in Fig. 10. The lightning current component A injected into the structure was 200 kA. Therefore, the current injected at each point was set as 50 kA.

The number of sticks and nodes and the calculation time for the elliptical barrel after being represented by a thin line are listed in Table 3. To avoid meshing the

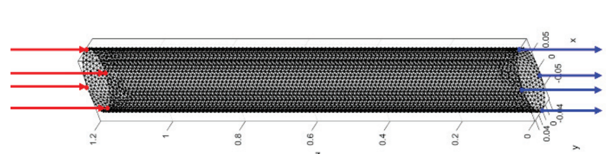

Fig. 10. Schematic diagram of elliptical barrel lightning current injection.

Table 3: Simulation results of different methods

Method	Number of Sticks	Number of Nodes	Sampling Frequency (MHz)	Time of Waveform (μs)	Calculation Time/s	Inversion Time (s)	
						Without Using Parallel Computing	Using Parallel Computing
PEEC	15970	5350	1	100	14653	26481	4074
	Number of Cells		Frequency Range (MHz)		Calculation Time (s)		
FIT	63648		0 100		72534		

1-mm-thick structure, the elliptical barrel was modeled as a 1-mm-thick surface. If the mesh step size was too small, the calculation time was very long.

According to Table 3, when the number of sticks and nodes was large, that is, when the number of surface elements was large, the inversion time was longer, which is equivalent to the calculation time. This is because the inversion process of every surface element must calculate the contribution of all line currents. The calculations of the current distribution for each element were independent of each other. Therefore, parallel computing technology was introduced with 12 workers, and the time required to invert the panel current was reduced sharply from 26481 to 4074 s.

The representation of the physical structure using the thin-wire model fixes the flow direction of the current, which may be one of the reasons for its high computational efficiency. Based on these comparisons, the use of PEEC under the thin-line model was more efficient than the use of FIT. This is possibly because magnetic field and surface current distribution of the entire calculation space were not obtained, unlike in FIT. Subsequently, magnetic field and surface current distribution results were obtained by post-processing the results. For complex models, the inversion time may be extremely long; however, as shown in Table 3, the inversion efficiency can be improved through parallel computing.

In addition, the surface current distribution at 6 μs is shown in Figs. 11 (a) and (b), and the Error_{OD} calculated using equation (11) and the average current density $j_a(k)$ calculated using equation (7) at different k values at 6 μs of the elliptical barrel are shown in Fig. 11 (c).

Figure 11 shows that even for a structure with a certain curvature, such as an ellipse, the surface current distribution obtained by the inversion method in this study was highly consistent with FIT. In addition, as shown in Fig. 11 (c), even when the model and structure thicknesses changed, the magnetic field calculation point position remained near k=10. The error caused by orthogonal decomposition was different from that shown in Fig. 7 and continued to increase.

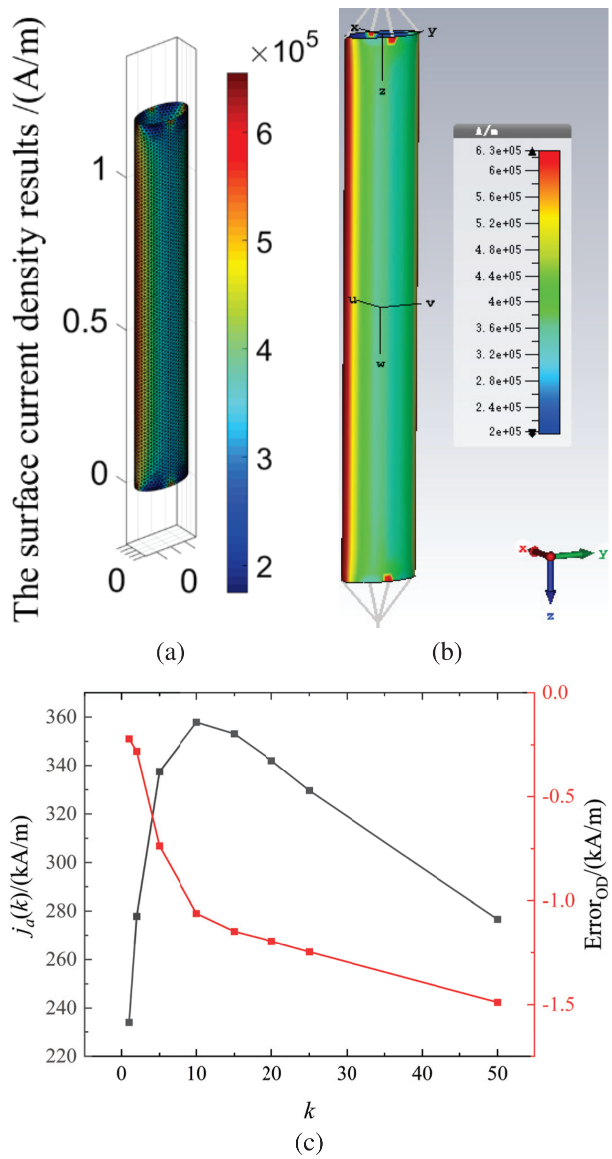

Fig. 11. Lightning current distribution results for the elliptical barrel: (a) PEEC results, (b) FIT results, and (c) Error_{OD} and $j_a(k)$ at different heights in the elliptical barrel case.

V. DUAL CHARACTERISTIC ANALYSIS UNDER THE PEEC FRAMEWORK

In sections III and IV, the PEEC equation is simplified by ignoring **P**, and surface current distribution inversion is discussed. For high frequencies and certain situations where electric field effects are considered, such as electromagnetic wave scattering and HIRF problems, it is necessary to consider the potential matrix. For some complex structures, nonsparse **P** and **L** matrices often require large amounts of memory storage and calculation processes.

Although Darney et al. analyzed the **P** and **L** characteristics of a 2D cross-section [21], the equation in three-dimensional (3D) space was not given. Therefore, the equation for the 3D thin lines was derived as follows:

$$L_{i,j} \cdot C_{i,j} = L_{i,j} / p_{i,j} \,. \tag{16}$$

However, equation (16) is not completely equal and cannot be established even at certain positions.

For some edge points, the length of the sticks when calculating the potential node was inconsistent with the length of the inductance sticks, such as the starting point of a long straight wire. Second, because the inductance matrix is defined based on sticks, its dimensions are $l \times l$, whereas the potential matrix is defined based on nodes, and its dimensions are $n \times n$. For a set of $\mathrm{L}_{i,j}$ and $\mathrm{C}_{i,j}$ with the same subscript, there may be no correspondence between the points and lines.

Simple mathematical operations were performed on the above equation to present it in graphical form:

$$\frac{L_{i,j} \cdot C_{i,j}}{\mu_0 \cdot \mu_r \cdot \varepsilon_0 \cdot \varepsilon_r \cdot < \overrightarrow{l_i}\,, \overrightarrow{l_j} >} \approx 1. \tag{17}$$

In particular, when l_i and l_j are perpendicular, the denominator of the above equation is zero and the equation does not hold.

To verify equation (17), a finite-length straight wire was used as a simple example. The wire was divided into several segments. The first 10 rows and first 10 columns of the **P** and **L** matrices were substituted into the above formula, and the results were compared when the numbers of Gaussian calculation points were different, as shown in Fig. 12.

Because **P** and **L** are symmetric matrices, and the nodes and sticks correspond exactly for long straight wires, the matrix shown in Fig. 12 was also symmetric. In addition, Gaussian calculations for the number of points can strengthen the relationship in equation (17). This is because the calculation results became more accurate as the number of calculation points increased. For Row 1 and Column 1, the addition of Gaussian calculation points did not significantly change the results. In addition, the first point in Row 1 and Column 1 did not satisfy equation (17). This is because $P_{1,1}$ or $C_{1,1}$ is an isolated point. When the

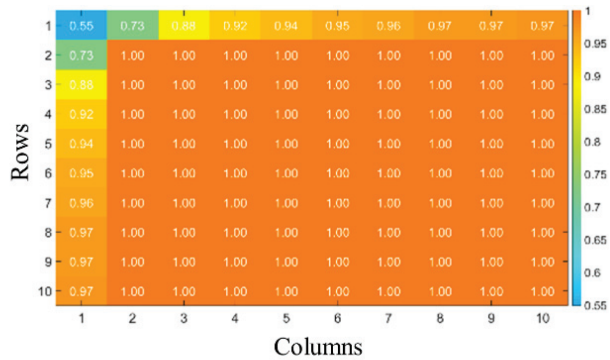

(a)

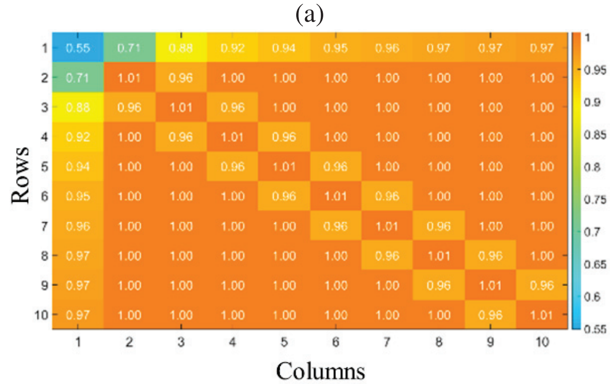

(b)

Fig. 12. Relationship between the **P** and **L** matrices: (a) number of Gaussian calculation points is 100 and (b) number of Gaussian calculation points is 2.

point is calculated, it is only half the integral path of len_1.

In addition, the matrix elements of the first 10 rows and columns of the **P** and **L** matrices in Method 2 shown in part B of section IV and in the literature [36] were compared. The plate in [36] was divided into a rectangular grid using equation (17), and the calculation results are shown in Fig. 13.

The rectangular mesh had more positions that complied with equation (17) because there were more finite-length straight-wire structures [36]. Compared to rectangular grids, triangular grids had fewer positions that satisfy equation (17). This is because a set of $L_{i,j}$ and $C_{i,j}$ with the same subscript mentioned above may not correspond to nodes and sticks. In addition, the NaN symbol in Fig. 13 indicates that the angle between l_i and l_j was $90°$.

The **P-L** relationship may help researchers understand the relationship between **P** and **L** while reducing memory storage. Because the matrix constructed using equation (17) has a large number, 1, as shown in Fig. 12, it is only necessary to construct a dense **P** or **L** and construct a sparse **P-L** relationship matrix by setting 1 to 0

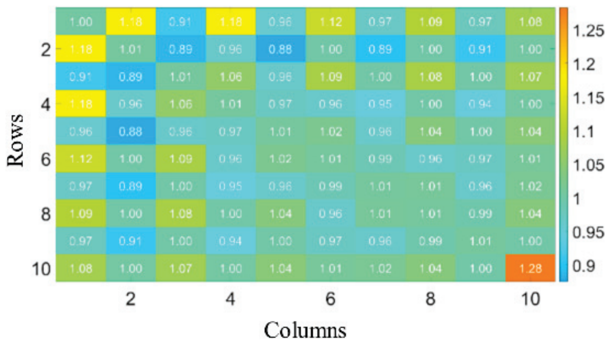

(a)

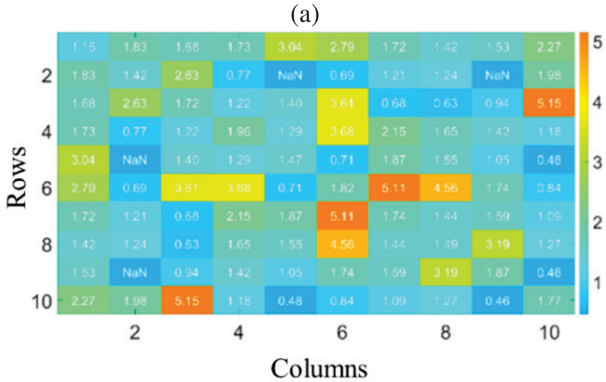

(b)

Fig. 13. Relationship between the **P** and **L** matrices of different grids: (a) rectangular grid and (b) triangular grid.

in the matrix, thereby establishing another dense matrix based on the sparse **P**-**L** relationship matrix. This operation can reduce the storage space of a dense matrix, thereby improving its performance.

VI. CONCLUSION

To address the question of lightning current distribution when a non-thin wire structure is equivalent to a thin-line model, this study developed the PEEC method and performed it in the frequency domain. A magnetic field calculation equation was derived, which is more convenient for experimental verification. An inversion method for the surface current density was then established. In addition, parallel computing technology was used to increase inversion efficiency. The method in this study is extremely efficient and can be extended to simulate lightning current distribution in complex structures. The accuracy of the results was close to that of the FIT. The main conclusions are as follows.

(1) Calculation efficiency of the thin-line model was considerably greater than that of the FIT. For flat and elliptical structures, the calculation results were highly consistent with those of the FIT.

(2) Influence of time delay and potential matrix on the solution results was analyzed. It was found that these influences depended on the frequency. The error gradually increased with an increase in frequency. When the scale of the problem was within $S = 60$, the error caused by the time delay was within 10%. Although there was a large difference in the results caused by the potential matrix, the results obtained by ignoring the potential matrix for non-thin conductor structures were more accurate when compared with the FIT.

(3) Surface current density of the thin-line model was effectively obtained by inverting the surface current through the maximum magnetic field position.

(4) For the thin-line model, as the height increased, the magnetic field first increased and then decreased. Even when the height was approximately 10 times the radius of the thin sticks, the magnetic field intensity was maximized for a flat plate or elliptical barrel.

ACKNOWLEDGMENTS

This study was supported by the National Key Laboratory of Electromagnetic Information Control and Effects (grant number 20240404 MJZ5-2N22 and 50909030401). We would like to thank the reviewers for their professional comments, which helped us improve the quality of the manuscript, as well as the editors.

REFERENCES

[1] Roger F. Harrington, *Field Computation by Moment Methods*. Oxford: Oxford University Press, 1996.

[2] J.-M. Jin, *The Finite Element Method in Electromagnetics*. Hoboken, NJ: John Wiley & Sons, 2015.

[3] T. Weiland, "A discretization model for the solution of Maxwell's equations for six-component fields," *Archiv Elektronik und Uebertragungstechnik*, vol. 31, pp. 116-120, Apr. 1977.

[4] A. E. Ruehli, "Inductance calculations in a complex integrated circuit environment," *IBM Journal of Research and Development*, vol. 16, no. 5, pp. 470-481, 1972.

[5] Y. Kane, "Numerical solution of initial boundary value problems involving Maxwell's equations in isotropic media," *IEEE Transactions on Antennas and Propagation*, vol. 14, no. 3, pp. 302-307, 1966.

[6] C. Tong, S. Qiu, X. Si, Z. Duan, Z. Li, and Y. Li, "Research on the lightning current distribution simulation and lightning test of a passenger aircraft's vertical tail," *Fiber Composites*, vol. 3, p. 5, 2021.

[7] K. Sun, X. Zhao, G. Zhang, and H. Zhang, "Numerical simulations of the lightning attachment points on airplane based on the fractal theory," *Acta Phys. Sin.*, vol. 63, no. 2, pp. 1-7, 2014.

[8] J. Yang, X. Qie, J. Wang, Y. Zhao, Q. Zhang, T. Yuan, Y. Zhou, and G. Feng, "Observation of the lightning induced voltage in the horizontal conductor and its simulation," *Acta Phys. Sin.*, vol. 57, p. 8, 2008.

[9] G. A. Rasek and S. E. Loos, "Correlation of direct current injection (DCI) and free-field illumination for HIRF Certification," *IEEE Transactions on Electromagnetic Compatibility*, vol. 50, no. 3, pp. 499-503, 2008.

[10] Y. Liu, Z. Fu, A. Jiang, Q. Liu, and B. Liu, "FDTD analysis of the effects of indirect lightning on large floating roof oil tanks," *Electric Power Systems Research*, vol. 139, pp. 81-86, 2016.

[11] M. R. Alemi, S. H. H. Sadeghi, and H. Askarian-Abyaneh, "A marching-on-in-time method of moments for transient modeling of a vertical electrode buried in a lossy medium," *IEEE Transactions on Electromagnetic Compatibility*, vol. 64, no. 6, pp. 2170-2178, 2022.

[12] C. Tong, Z. Duan, Y. Huang, S. Qiu, X. Si, Z. Li, and Z. Yuan, "Study of the B-dot sensor for aircraft surface current measurement," *Sensors*, vol. 22, no. 19, p. 7499, 2022.

[13] G. Gutiérrez, R. M. Castejón, H. Tavares, H. Galindo, E. P. Gil, M. R. Cabello, and S. G. García, "Validation of lightning simulation compared with measurements using DCI technique post-processed to be applied to a lightning threat," *IEEE Transactions on Electromagnetic Compatibility*, vol. 65, no. 1, pp. 281-291, 2023.

[14] K. S. H. Lee, *EMP Interaction: Principles, Techniques, and Reference Data: A Handbook of Technology from the EMP Interaction Notes*. London: Hemisphere Publishing Corporation, 1986.

[15] R. Mittra, *Numerical and Asymptotic Techniques in Electromagnetics*. New York: Springer, 1975.

[16] G. E. Bridges and L. Shafai, "Validity of the thin-wire approximation for conductors near a material half-space," *Digest on Antennas and Propagation Society International Symposium*, pp. 232-235, 1989.

[17] T. Bauernfeind, P. Baumgartner, O. Bíró, A. Hackl, C. Magele, W. Renhart, and R. Torchio, "Multi-objective synthesis of NFC-transponder systems based on PEEC method," *IEEE Transactions on Magnetics*, vol. 54, no. 3, pp. 1-4, 2018.

[18] P. Baumgartner, T. Bauernfeind, O. Bíró, A. Hackl, C. Magele, W. Renhart, and R. Torchio, "Multi-objective optimization of Yagi-Uda antenna applying enhanced firefly algorithm with adaptive cost function," *IEEE Transactions on Magnetics*, vol. 54, no. 3, pp. 1-4, 2018.

[19] R. Torchio, P. Alotto, P. Bettini, D. Voltolina, and F. Moro, "A 3-D PEEC formulation based on the cell method for full-wave analyses with conductive, dielectric, and magnetic media," *IEEE Transactions on Magnetics*, vol. 54, no. 3, pp. 1-4, 2018.

[20] G. Antonini, A. E. Ruehli, D. Romano, and F. Loreto, "The partial elements equivalent circuit method: The state of the art," *IEEE Transactions on Electromagnetic Compatibility*, vol. 65, no. 6, pp. 1695-1714, 2023.

[21] I. B. Darney, *Circuit Modelling for Electromagnetic Compatibility*. Raleigh, NC: Scitech Publishing, pp. 15-20, 2013.

[22] I. B. Darney, "Grounding, floating and screening," in *IET Conference Proceedings*, London, UK, 2000.

[23] R. Torchio, "PEEC modelling of large-scale fusion reactor magnets," thesis, Universita' Degli Studi Di Padova, 2016.

[24] I. B. Darney and C. M. Hewitt, *Darney's Circuit Theory and Modelling: Updated and Extended for EMC/EMI*. Raleigh, NC: Scitech Publishing, 2023.

[25] J. Parmantier, F. Issac, and V. Gobin, "Indirect effects of lightning on aircraft and rotorcraft," *Journal Aerospace Lab.*, vol. 5, no. 5, pp. 1-27, 2012.

[26] W. Ye, W. Liu, N. Xiang, K. Li, and W. Chen, "Analytical evaluation of partial elements in the full-wave PEEC formulation for thin-wire structure," *IEEE Transactions on Electromagnetic Compatibility*, vol. 65, no. 5, pp. 1410-1421, 2023.

[27] W. Ye, W. Liu, N. Xiang, K. Li, and W. Chen, "A full-wave PEEC model for thin-wire structure in the air and homogeneous lossy ground," *IEEE Transactions on Electromagnetic Compatibility*, vol. 65, no. 2, pp. 518-527, 2023.

[28] W. Ye, W. Liu, N. Xiang, K. Li, L. Cheng, B. Hu, Y. Zhou, and W. Chen, "A low-frequency approximation PEEC model for thin-wire grounding systems in half-space," *IEEE Transactions on Power Delivery*, vol. 38, no. 2, pp. 1297-1307, 2023.

[29] B. Li, Z. Du, Y. Du, Y Ding, Y Zhang, J. Cao, L. Zhao, and J. Chen, "An advanced wire-mesh model with the three-dimensional FDTD method for transient analysis," *IEEE Transactions on Electromagnetic Compatibility*, pp. 1-10, 2023.

[30] D. Prost, F. Issac, T. Volpert, W. Quenum, and J. P. Parmantier, "Lightning-induced current simulation using RL equivalent circuit: Application to an aircraft subsystem design," *IEEE Transactions on Electromagnetic Compatibility*, vol. 55, no. 2, pp. 378-384, 2013.

[31] Yinghua Lv, *Numerical Methods for Computing Electromagnetism*. Beijing: Tsinghua University Press, 2006.

[32] R. Torchio, P. Bettini, and P. Alotto, "PEEC-based analysis of complex fusion magnets during fast voltage transients with H-matrix compression," *IEEE Transactions on Magnetics*, vol. 53, no. 6, pp. 1-4, 2017.
[33] Z. Xiongfei, B. Shirong, L. Zhengxiang, N. Junsong, Z. Cheng, and C. Liu, "FDTD calculation of the current distribution of microstrip transmission line circuits," in *2012 International Conference on Computational Problem-Solving (ICCP),* Leshan, pp. 245-247, 2012.
[34] J. Cao, Y. Du, Y. Ding, B. Li, R. Qi, Y. Zhang, and Z. Li, "Lightning surge analysis of transmission line towers with a hybrid FDTD-PEEC method," *IEEE Transactions on Power Delivery*, vol. 37, no. 2, pp. 1275-1284, 2022.
[35] Y. Zhang, H. Chen, Y. Du, Z. Li, and Y. Wu, "Lightning transient analysis of main and sub-main circuits in commercial buildings using PEEC method," *IEEE Transactions on Industry Applications*, vol. 56, no. 1, pp. 106-116, Jan.-Feb. 2020.
[36] https://github.com/UniPD-DII-ETCOMP/PEEC-1D

Zemin Duan was born in Hefei, China, in 1955. He received a B.Sc. from Hefei University of Technology in 1982, and M.Sc. and Ph.D. from the Institute of Plasma Physics, Chinese Academy of Sciences, in 1990 and 1994, respectively. He is a professor at the School of Electrical Engineering, Hefei University of Technology, Chief Specialist of the AVIC Technology Foundation Establishment in Lightning Protection of Airplanes, member of the National Technical Committee for Standardization of Lightning Protection, China, and member of AAAF and SAE. He has been engaged in professional research on pulse power technology and lightning protection of aircraft for more than 20 years.

Chen Tong was born in Yangzhou, Jiangsu, China, in 1995. He received a B.S. in engineering from Hunan Institute of Technology in 2018. Since 2018, he has been studying for a doctorate at the School of Electrical Engineering and Automation, Hefei University of Technology. From 2019 to 2023, he was engaged in research related to aircraft lightning protection and surface lightning current calculation and measurement.

Yeyuan Huang was born in Hefei, Anhui, China, in 1989. He received a B.S. from Anhui University of Science and Technology. He received a Ph.D. from University of Science and Technology of China in 2021. From 2022 to 2023, he worked at the Anhui Provincial Key Laboratory of Aircraft Lightning Protection and the Aerospace Science and Technology Key Laboratory of Strong Electromagnetic Environment Protection Technology. During this time, he conducted research related to the protection of aircraft from high-intensity radiation fields.

Xinping Li was born in Ningyuan County, Hunan Province, in 1980. He received a Bachelor of Science degree in Mathematics and Applied Mathematics from Hunan Institute of Technology in 2004, a Master of Science degree in Probability Theory and Mathematical Statistics from Central South University in 2012, and a Master of Science degree in Computational Mathematics from Hunan University in 2021. Doctor of Science degree. He has been working in the School of Mathematics of Hunan University of Technology since 2004. He was hired as a lecturer in 2010 and an associate professor in 2023. He has published in *IEEE Geoscience and Remote Sensing Letters, Remote Sensing, Journal of Computational Physics, Journal of Function Space, Applied Mathematics Letters,* and *Statistics & Probability Letters.* Li is a director of the Hunan Provincial Operations Research Society and a member of the Chinese Society of Industrial and Applied Mathematics.

Shanliang Qiu was born in Hefei, Anhui, China, in 1983. He received the B.S. degree from Hefei University of Technology in 2005. In 2010, he received his Ph.D. from University of Science and Technology of China. He has been working at Anhui Provincial Key Laboratory of Aircraft Lightning Protection and Aerospace Science and Technology Key Laboratory of Strong Electromagnetic Environment Protection Technology since 2011. In the laboratory, he is mainly engaged in aircraft electrostatic discharge brushes and aircraft deposition electrostatic protection related work.

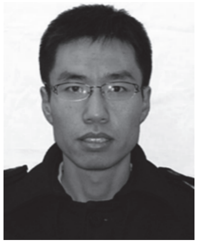

Xiaoliang Si was born in 1985 in Changchun, Jilin Province. He is a Ph.D. and an associate researcher. His main research direction is the strong electromagnetic environment protection technology for aircraft.

Yan Wei is currently studying for his Ph.D. in the Lightning Protection Laboratory of Aircraft at Hefei University of Technology. His main research interests are lightning discharge and electrostatic electromagnetic environmental effects. He is engaged in aircraft electrostatic discharge brushes and aircraft deposition electrostatic protection related work.

Yao Ling was born in Anqing, Anhui, China, in 1996. She received a B.S. in engineering from Qingdao University of Science and Technology in 2018. Since 2018, she has been studying for a doctorate in School of Electrical Engineering and Automation, Hefei University of Technology. From 2019 to 2023, she has been engaged in research related to aircraft lightning protection.